

SISSA

Scuola
Internazionale
Superiore di
Studi Avanzati

Physics Area – PhD course in
ASTROPHYSICS

Fundamental properties
of the dark and the luminous matter
from Low Surface Brightness discs

Candidate:
Di Paolo Chiara

Advisor:
Salucci Paolo

Academic year 2019-20



Look at obstacles as opportunities for improvement.

(Buffycats)

Contents

Introduction	5
I	9
1 Dark matter particles and scenarios	11
1.1 DM phenomenon in the particles framework	11
1.1.1 Weakly interacting massive particles (WIMP)	11
1.1.2 Scalar fields and fuzzy dark matter	13
1.1.3 Self-interacting dark matter (SIDM)	14
1.1.4 Warm dark matter particle (WDM)	14
1.1.5 Primordial black holes (PBH)	15
1.2 In search for the dark particle	15
1.3 Issues with the main DM scenario and its simplest solutions . . .	16
1.3.1 Issues with other DM candidates	18
2 The dark and the luminous matter distribution in disc/LSB galaxies	19
2.1 The contributions to the circular velocity rotation curves	20
2.1.1 The stellar disc	20
2.1.2 The gaseous disc	21
2.1.3 The stellar bulge	21
2.1.4 The DM halo	22
2.1.5 Rotation curves modeling	23
2.2 The universal rotation curve (URC)	24
3 Low Surface Brightness (LSB) galaxies: observational properties of the luminous matter	27
3.1 Main LSBs observational properties	27
3.2 LSBs evolution	32
3.3 The LSBs environment	34
3.4 Further LSBs observations	34
4 LSBs mass modeling and scaling laws involving luminous and dark matter	35
4.1 LSBs sample	35
4.2 Mass modeling results from previous works on individual LSB galaxies	36

4.3	LSBs mass modelling results from the URC method	40
4.4	LSBs scaling laws	43
4.4.1	Structural relationships	43
4.4.2	Comparison between the results from individual and stacked (URC) LSBs analysis	46
4.5	Angular momentum	47
4.6	The compactness in LSBs	48
4.7	The LSBs universal rotation curve	50
5	Low Surface Brightness galaxies and the gravitational acceleration	53
5.1	Test for g and g_b	53
5.2	The GGBX relationship	56
5.3	Consequences	60
6	Hints for a direct interaction between luminous and dark matter from structural properties of the LSBs	61
6.1	The collisional DM scenario	62
6.2	Future observations and predictions	63
	Conclusions	65
II		69
7	PAPER 1: “The universal rotation curve of low surface brightness galaxies IV: the interrelation between dark and luminous matter”	71
8	PAPER 2: “The Radial Acceleration Relation (RAR): Crucial Cases of Dwarf Disks and Low-surface-brightness Galaxies”	99
9	PAPER 3: “Phase-space mass bound for fermionic dark matter from dwarf spheroidal galaxies”	113

Introduction

What we can observe by means of telescopes is the light emitted by stars, dust and gas, but they are only the tip of an iceberg. According to the latest observational data, the Universe contains: only $\sim 5\%$ ordinary matter, $\sim 27\%$ dark matter and $\sim 68\%$ dark energy (e.g. [Ade et al., 2014, Aghanim et al., 2018]).

Dark matter (DM) is a type of matter hypothesized to account for effects that appear to be the result of invisible mass. The existence and properties of dark matter can be inferred from its gravitational effects on visible matter and radiation and from the observations of the large-scale structure of the universe [Faber and Gallagher, 1979, Trimble, 1987]. Astrophysicists hypothesized dark matter because of discrepancies between the mass of large astronomical objects determined from their gravitational effects and the mass calculated from the “luminous matter” they contain (stars, gas and dust). Many observations have indicated the presence of dark matter in the universe, including the rotational speeds of galaxies in the 1960s–1970s [Faber and Gallagher, 1979, Rubin et al., 1980, Bosma, 1981a, Bosma, 1981b], gravitational lensing of background objects by galaxy clusters such as the Bullet Cluster [Clowe et al., 2004, Markevitch et al., 2004], the temperature distribution of hot gas in galaxies and clusters of galaxies [Rees and Ostriker, 1977, Cavaliere and Fusco-Femiano, 1978], and more recently the pattern of anisotropies in the cosmic microwave background (CMB) [Hinshaw et al., 2009, Ade et al., 2016]. Particularly, detailed analysis of the anisotropies in the CMB observed by WMAP and Planck shows that around five-sixths of the total matter is in a form which does not interact significantly with ordinary matter or photons [Hinshaw et al., 2009, Ade et al., 2016]. Furthermore, the theory of Big Bang nucleosynthesis (BBN), which accurately predicts the observed abundance of the chemical elements, indicates that the vast majority of dark matter in the universe cannot be baryons [Copi et al., 1995]. Then, large astronomical searches for gravitational microlensing, have shown that only a small fraction of the dark matter in the Milky Way can be hidden in dark compact objects composed of ordinary (baryonic) matter which emit little or no electromagnetic radiation [Alcock et al., 2000]. The excluded range of object masses is from half the Earth’s mass up to 30 solar masses [Tisserand et al., 2007, Wyrzykowski et al., 2011]. All this points to the non baryonic nature of dark matter.

Despite the evidences about the DM existence, this mysterious component of the Universe is made primarily of a not yet characterized type of particle. The search for this particle, by a variety of methods, is one of the major efforts in particle physics today [Bertone et al., 2005].

Beside the DM, another relevant mystery in the Universe is the *Dark energy*. It is a hypothetical form of energy which permeates all of space and tends to

accelerate the expansion of the universe [Carroll et al., 1992], as indicated by observation since the 1990s. Adding the cosmological constant Λ to cosmology’s standard FLRW (Friedmann-Lemaître-Robertson-Walker) metric leads to the so-called Λ -CDM model, which also involves the most favourite candidate for the dark matter, namely the collisionless Cold Dark Matter (CDM).

The Λ -CDM model has been referred to as the Standard Model of Cosmology because of its precise agreement with observations on large scale structures (see e.g. [Kolb and Turner, 1990, Mukhanov, 2005, Ellis et al., 2012, Aghanim et al., 2018]).

In this work, we focus our attention on the DM distribution in galaxies and its relation with the luminous matter (LM) distribution. Particularly, we deal with the structural properties of DM and LM in disc galaxies, rotating objects with a rather simple kinematics, devoting special attention to the Low Surface Brightness (LSB) galaxies. They are rotating disc systems which emit an amount of light per area smaller than normal spirals, with a face-on central surface brightness $\mu_0 \gtrsim 23 \text{ mag arcsec}^{-2}$ in the B band [Impey and Bothun, 1997]. They are usually locally more isolated than other kinds of galaxies (e.g. [Bothun et al., 1993, Rosenbaum et al., 2009]) and likely evolving very slowly with very low star formation rates, characterised by sporadic small-amplitude events (e.g. [Das et al., 2009, Galaz et al., 2011], [Schombert and McGaugh, 2014, Lei et al., 2018]). This is suggested by colors, metallicities, gas fractions and extensive population synthesis modelling (e.g. [van der Hulst et al., 1993, McGaugh, 1994, de Blok et al., 1995, Bell et al., 2000, Schombert and McGaugh, 2014]). As we see in radio synthesis observations, LSB galaxies have extended gas discs with low gas surface densities and high M_{HI}/L ratios (e.g. [van der Hulst et al., 1993, Du et al., 2019]), where M_{HI} is the mass of the HI gaseous disc and L is the luminosity. The low metallicities make the gas cooling difficult and in turn the stars difficult to form (e.g. [McGaugh, 1994]). LSBs are required to be dominated by DM, as shown by the analysis of their Tully-Fisher relation (e.g. [Zwaan et al., 1995]), of their individual (e.g. [de Blok et al., 2001], [de Blok and Bosma, 2002]) and stacked rotation curves (RCs) [Di Paolo et al., 2019a]. Overall, the LSBs result to be a different laboratory than the normal spirals to test the properties of the dark and the luminous matter.

This thesis is divided into two parts:

- **PART 1**, mainly drawn from the REVIEW “Fundamental properties of the dark and the luminous matter from Low Surface Brightness discs” (Di Paolo & Salucci, to be submitted). It is based on:
 - a)* the review of previous works by various authors on DM (Chapter 1), disc galaxies (Chapter 2) and LSBs (Chapter 3);
 - b)* the presentation of the recent main results on LSB disc galaxies published in [Di Paolo et al., 2019a] (Chapter 4) and [Di Paolo et al., 2019b] (Chapter 5), contextualized in the large DM phenomenon puzzle (Chapter 6);
- **PART 2**, which includes the works, above discussed, as appeared in the journals. The published papers are:

- a)* PAPER 1 (Chapter 7): “The universal rotation curve of low surface brightness galaxies IV: the interrelation between dark and luminous matter” [Di Paolo et al., 2019a];
- b)* PAPER 2 (Chapter 8): “The Radial Acceleration Relation (RAR): Crucial Cases of Dwarf Disks and Low-surface-brightness Galaxies” [Di Paolo et al., 2019b];
- c)* PAPER 3 (Chapter 9): “Phase-space mass bound for fermionic dark matter from dwarf spheroidal galaxies” [Di Paolo et al., 2018].

Part I

Chapter 1

Dark matter particles and scenarios

After accepting the existence of dark matter, there is a spontaneous question: what is the nature of dark matter? Several possibilities have been proposed.

Since dark matter has not yet been observed directly, if it exists, it must barely interact with ordinary baryonic matter and radiation, except through gravity. Or likely it has not been revealed till now because the experimental researches could have not been set in order to reveal "the" DM particle. At any rate, it remains unknown whether it consists of a single particle species or a larger collection of fields, like in case of the Standard Model. Among few indications, probably DM particles are extremely long-lived or stable, with a lifetime comparable to the age of the Universe, as suggested by the large cosmic abundance of DM which must have been generated very early in the history of Universe and survived unchanged until today (for a quantitative discussion see Chapter 5 in [Kolb and Turner, 1990]) at least out of the innermost galactic regions.

1.1 DM phenomenon in the particles framework

In the following, only few simple, but fundamentally different, categories of DM particle candidates are presented. For a complete discussion of the various DM models and existing constraints, see e.g. [Bergstrom, 2000, Bertone et al., 2005, Garrett and Duda, 2011, Bauer and Plehn, 2017, Profumo, 2017].

1.1.1 Weakly interacting massive particles (WIMP)

Weakly interacting massive particles (WIMPs) are hypothetical particles that are thought to interact via gravity and any other force (or forces), potentially not part of the standard model itself, which is as weak as or weaker than the weak nuclear force, but also non-vanishing in its strength. WIMP particles make up the so called **collisionless cold dark matter**, which is involved in the Λ CDM N-body simulations.

In more detail, WIMPs fit the model of a relic dark matter particle from the early Universe, when all particles were in a state of thermal equilibrium.

For sufficiently high temperatures ($T \gg m_{WIMP}$), such as those existing in the early Universe, the dark matter particle and its antiparticle would have been both forming from and annihilating into lighter particles of the Standard Model ($DM+DM \rightleftharpoons SM+SM$). As the Universe expanded and cooled ($T \lesssim m_{WIMP}$), the DM density is exponentially suppressed ($\propto \exp[-m_{WIMP}/T]$), the average thermal energy of these lighter particles decreased and eventually became insufficient to form a dark matter particle-antiparticle pair. The annihilation of the dark matter particle-antiparticle pairs ($DM+DM \rightleftharpoons SM+SM$), however, would have continued, and the number density of dark matter particles would have begun to decrease exponentially. Eventually, however, the number density would become so low that the dark matter particle and antiparticle interaction would cease, and the number of dark matter particles would remain (roughly) constant as the Universe continued to expand. Particles with a larger interaction cross section would continue to annihilate for a longer period of time, and thus would have a smaller number density when the annihilation interaction ceases. Based on the current estimated abundance of dark matter in the Universe, it is required a self-annihilation cross section of $\langle\sigma v\rangle \simeq 3 \times 10^{-26} \text{cm}^3 \text{s}^{-1}$, which is roughly what is expected for a new particle in the 100 GeV mass range that interacts via the electroweak force.

Because supersymmetric extensions of the standard model of particle physics readily predict a new particle with these properties, this apparent coincidence is known as the “WIMP miracle”, and a stable supersymmetric partner has long been a prime WIMP candidate [Steigman and Turner, 1985, Kolb and Turner, 1990, Jungman et al., 1996, Munoz, 2017]. WIMP-like particles are also predicted by Grand Unified Theory (GUT) [Ross, 1985, Arcadi, 2016] or models with additional dimensions [Servant and Tait, 2003, Hooper and Profumo, 2007], where one or more of the many newly predicted particles could play the role of DM.

We highlight that because of their large mass, WIMPs would be relatively slow moving. They are defined cold dark matter (CDM), characterized by non-relativistic velocities since its decoupling time. Their relatively low velocities would be insufficient to overcome the mutual gravitational attraction, and as a result, WIMPs would tend to clump together. They could generate small structures (galaxies) and then they would be able to aggregate among themselves to form larger structures (bottom-up theory). See Fig. 1.1.

In the current Λ -cold dark matter (Λ CDM) paradigm, the non-relativistic DM can be described by a collisionless fluid, whose particles interact only gravitationally and very weakly with the Standard Model particles [Jungman et al., 1996, Bertone, 2010]. The N-body simulations in the Λ CDM give rise to structures of virialized DM halos with a universal spherically averaged density profile $\rho_{NFW}(r)$ [Navarro et al., 1997]:

$$\rho_{NFW}(r) = \frac{\rho_s}{(r/r_s)(1+r/r_s)^2} \quad , \quad (1.1)$$

where the density ρ_s and the scale radius r_s are parameters which vary from halo to halo in a strongly correlated way [Wechsler et al., 2006]. Eq. 1.1 is the so called **Navarro-Frenk-White (NFW) profile**. A very important quantity involved in such profile is the *concentration* parameter $c = r_s/R_{vir}$,

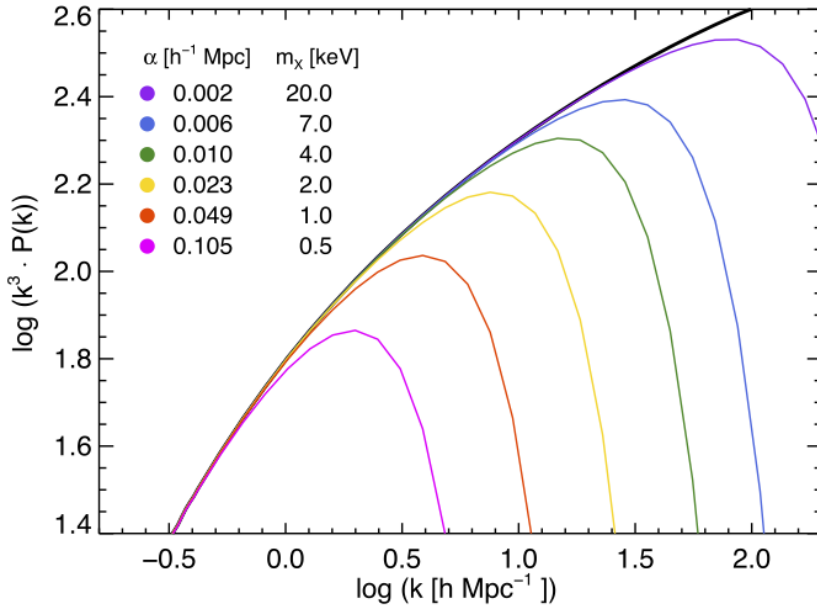


Figure 1.1: Linear power spectra for Λ CDM (*black line*) and Λ WDM (*coloured lines*) scenarios. The WDM models are labelled by their thermal relic mass and corresponding value of the damping scale, α , in the legend. The WDM transfer function is given by $[P_{WDM}/P_{CDM}]^{1/2} = [1 + (\alpha k)^{2.24}]^{-4.46}$; k is the wavenumber. Image reproduced from [Kennedy et al., 2014].

where R_{vir} is the virial radius¹, which practically encloses the whole mass of the DM halo. The concentration parameter is a weak function of the halo mass [Klypin et al., 2011], but it is a very important quantity in determining the density shape at intermediate radii. Finally, we highlight the *cusp* shape $\propto r^{-1}$ of the NFW profile for inner galactic radii and the behaviour $\propto r^{-3}$ for the outer radii. See Fig. 1.2.

WIMPs are often considered one of the main candidates for cold dark matter. However, they have not been detected till now. Furthermore, the CDM is challenged by the observations at small scales (see e.g. [Naab and Ostriker, 2017, Bullock and Boylan-Kolchin, 2017]). This issue will be dealt with in the end of this chapter.

1.1.2 Scalar fields and fuzzy dark matter

Scalar fields like axions were introduced in order to solve the strong CP problem in particle physics [Duffy and van Bibber, 2009]. Furthermore, beyond these, other scalar fields as axion-like particles were introduced, motivated by string theory [Kane et al., 2015]. In order to be DM, these scalars are required to be non-relativistic and abundantly produced in very early Universe and to be (subsequently or always) decoupled from ordinary matter.

¹The virial radius R_{vir} is defined as the radius at which the average DM mass density within this radius is 100 times the critical density of the Universe.

Among the scalar fields, ultra-light axions (ULA) seems to be particularly interesting from the point of view of DM phenomenology [Weinberg, 1978, Hu et al., 2000, Ringwald, 2012, Hui et al., 2017, Bernal et al., 2017]. Indeed, these hypothetical particles, of mass $m_a \sim 10^{-22}$ eV, can mimic the behaviour of the cold dark matter (CDM). Once in galaxies, however, the inter-particle distance is much smaller than their de Broglie wave length: the particles move collectively as a wave and their equation of state can lead to cored configurations like those observed. This is the so called **fuzzy DM** scenario. The particles behave as Bose-Einstein condensate (BEC) and the capability to detect scalar field dark matter with the LIGO experiment is under analysis [Li et al., 2017]. Moreover, promising approach for detecting ULA might be by testing the shape of small scale matter power spectrum, as for example through the observations of Lyman- α forest [Iršič et al., 2017, Nori et al., 2019], 21-cm astronomy [Nebrin et al., 2019], gravitational lensing [Vegetti and Koopmans, 2009, Bayer et al., 2018] or careful study of galactic kinematics [Simon et al., 2019]. On the other hand, existence of axions is currently being probed through possible coupling with electromagnetic fields [Sikivie, 1983, Asztalos et al., 2010, Graham et al., 2015].

1.1.3 Self-interacting dark matter (SIDM)

In astrophysics and particle physics, self-interacting dark matter (SIDM) assumes that dark matter has self-interactions, in contrast to the collisionless dark matter assumed by the Λ -CDM model. SIDM was postulated in 2000 to resolve a number of conflicts between observations and N-body simulations (of cold collisionless dark matter only) on the galactic scale and smaller [Spergel and Steinhardt, 2000]. According to the SIDM model, DM particles scatter elastically with each other and are heated by elastic collisions within the dense inner halo and leave the region: the central and nearby densities are then reduced, turning an original cusp into a core. The collision rate is negligible during the early Universe when structures form. SIDM, therefore, retains the success of large-scale structure formation of the Λ -CDM scenario and affects the dark structures on small scales only once they are already virialized. See [Zavala et al., 2013, Tulin et al., 2013, Bellazzini et al., 2013, Boddy et al., 2014, Vogelsberger et al., 2014, Elbert et al., 2015, Kaplinghat et al., 2015].

1.1.4 Warm dark matter particle (WDM)

Warm dark matter (WDM) particle decouples from the cosmological plasma when it is still mildly relativistic. It seems to overcome the problem on small scales (typical of the collisionless CDM) and, if we take into account the possibility of a fermionic DM particle, it could also solve the cusp problem. Indeed, given the mass \sim keV of a WDM particle, its de-Broglie scale length is of the order \sim tens kpc, that is close to optical scale length in galaxies. Thus, a quantum pressure emerges [Destri et al., 2013, de Vega et al., 2013, Lovell et al., 2014, de Vega and Sanchez, 2017] and it can shape the inner DM density profile with the possibility of forming a core distribution. A strong lower limit has been put on the mass of the fermionic DM particle, taking into account the smallest dwarf spheroidal (dSph) satellites of the Milky Way. Considerations on the phase-space density and on the dynamical friction lead to a final lower bound

of $m \gtrsim 100$ eV [Di Paolo et al., 2018] (for detailed discussions, see PAPER 3 in Chapter 9).

The WDM particles can be created in the early Universe as thermal relics (with the same mechanisms described in the previous section for the WIMP particle, see Fig. 1.1) or it can be non-resonantly produced [Dodelson and Widrow, 1994, Shi and Fuller, 1999, Kusenko, 2009]. In the latter case, the DM candidate is the **sterile neutrino**, which is required in extensions to the standard model to explain the small neutrino mass through the seesaw mechanism [Asaka et al., 2005, Ma, 2006]. The sterile neutrino might be detected from the annihilation product: a monochromatic line at $2m_{WDM} \simeq keV$ [Boyarsky et al., 2007, Bulbul et al., 2014, Boyarsky et al., 2014]. For an up-to-date review of viable sterile neutrino DM models see, e.g., [Drewes, 2013, Adhikari et al., 2017, Boyarsky et al., 2019].

1.1.5 Primordial black holes (PBH)

In 2015-2017 the idea that dark matter was composed of primordial black holes (PBH), made a comeback following results of gravitation wave measurements which detected the merger of intermediate mass black holes. It was proposed that the intermediate mass black holes causing the detected merger formed in the hot dense early phase of the universe due to denser regions collapsing. Their behaviour on large scale is expected to be similar to the CDM particles, however their nature is fundamentally different. Indeed, their production is generally linked to the inflation.

1.2 In search for the dark particle

Many experiments to detect and study dark matter particles, primarily WIMP, are being actively undertaken, but none has yet succeeded [Bertone et al., 2005]. See e.g. [Arcadi et al., 2018] for a detailed review. Fundamentally, there are three possible ways to detect DM particles, that we resume below:

i) indirect detection, which refers to the observation of annihilation or decay products of DM particles far away from Earth. Indirect detection efforts typically focus on locations where DM is thought to accumulate the most: in the centers of galaxies and galaxy clusters, as well as in the smaller satellite galaxies of the Milky Way. Typical indirect searches look for excess gamma rays, which are predicted both as final-state products of annihilation, or are produced as charged particles interact with ambient radiation via inverse Compton scattering. The spectrum and intensity of a gamma ray signal depends on the annihilation products, and must be computed on a model-by-model basis. The γ -ray flux with an energy of E from dark matter annihilation in a distant source within a solid angle $\Delta\Omega$ is given by $\Phi(E, \Delta\Omega) \propto [(\langle\sigma v\rangle/m_{DM}^2) \sum_f b_f dN_\gamma/dE] J_{\Delta\Omega}$, where $\langle\sigma v\rangle$ is the thermally averaged annihilation cross-section, m_{DM} is the mass of a single dark matter particle, and b_f and dN_γ/dE denote the branching fraction of the annihilation into the final state f and the number of photons per energy, respectively. Beyond the physical processes and the DM particle mass, the γ -ray flux also depends on the spatial DM distribution in the source through the J -factor $= \int_{\Delta\Omega} \int_{l_{os}} dl \Delta\Omega \rho^2(l, \Omega)$ in case of an annihilation process or the D -factor $= \int_{\Delta\Omega} \int_{l_{os}} dl \Delta\Omega \rho(l, \Omega)$ in case of a decay process [Gunn et al., 1978, Bergstrom et al., 1998, Geringer-Sameth et al., 2015]. These factors correspond

to the line-of-sight (*los*) integrated dark matter density squared for annihilation and the dark matter density for decay, respectively, within solid angle $\Delta\Omega$. Experiments have placed bounds on DM annihilation and decay, via the non-observation of an annihilation and decay signal. For constraints on the cross-sections see (e.g.) Fig. 2 in [Hoof et al., 2018] (Fermi-LAT), Fig. 8 in [Archambault et al., 2017] (VERITAS), Fig. 1 in [Abdallah et al., 2016] (H.E.S.S.), Fig. 5 in [Cui et al., 2018] (AMS-02), Fig. 4 in [Iovine et al., 2019] (IceCube and ANTARES);

ii) direct detection, which refers to the observation of the effects of a DM particle - nucleus collision as the dark matter passes through a detector in an Earth laboratory. Since the WIMP carries no electric charge, in most scenarios it will not interact with the atomic electrons but will instead elastically scatter off the atomic nucleus. The momentum transfer gives rise to a nuclear recoil which might be detectable [Goodman and Witten, 1985, Schumann, 2019]. Although most DM particles encountering the Sun or the Earth are expected to pass through without any effect, it is hoped that a large number of dark matter crossing a sufficiently large detector will interact often enough to be seen, at least a few events per year. There are currently no confirmed detections of dark matter from direct detection experiments (e.g. XENON1T, CDMSlite, DAMA, DAMA0, COUPP, PICO60(C₃F₈), PICASSO, PANDAX-II, SuperCDMS, CDEX, KIMS, CRESST-II, PICO60(CF₃I), DS50, COSINUS, DarkSide-50), but only limits on the DM-Standard Model particle cross-section. See (e.g.) Fig. 12-13 in [Schumann, 2019], Fig. 1 in [Kang et al., 2019];

iii) collider production, an alternative approach to the detection of dark matter particles in nature, which attempts to produce DM in a laboratory. Experiments with the Large Hadron Collider (LHC) may be able to detect dark matter particles produced in collisions of the LHC proton beams. In this case, the DM particle may be detected indirectly as missing energy and momentum that escape the detectors [Kane and Watson, 2008]. See the constraints on the DM particle mass (e.g.) in Fig.3 in [Trevisani, 2018]. Constraints on dark matter also exist from the LEP experiment using a similar principle, but probing the interaction of dark matter particles with electrons rather than quarks [Fox et al., 2011].

1.3 Issues with the main DM scenario and its simplest solutions

The particle that till now has caught more attention as DM candidate is the lightest supersymmetric particle, the lightest *neutralino* (see e.g. [Bergstrom, 1999]), which behaves as a CDM (WIMP) particle in the evolving Universe. However this particle has never been produced either detected. Moreover, there are astrophysical evidences that the CDM has some issues in reproducing the observed structures. Indeed, despite the fact that the N-body simulations in the Λ CDM scenario produce results well in agreement with the large scale structure (especially when $\gtrsim 1$ Mpc) in the Universe, we discover an overabundance of too small structures not observed by recent surveys. This is the so-called **missing satellite problem** (e.g [Klypin et al., 1999, Moore et al., 1999, Zavala et al., 2009, Papastergis et al., 2011, Klypin et al., 2015]). A possible explanation for this

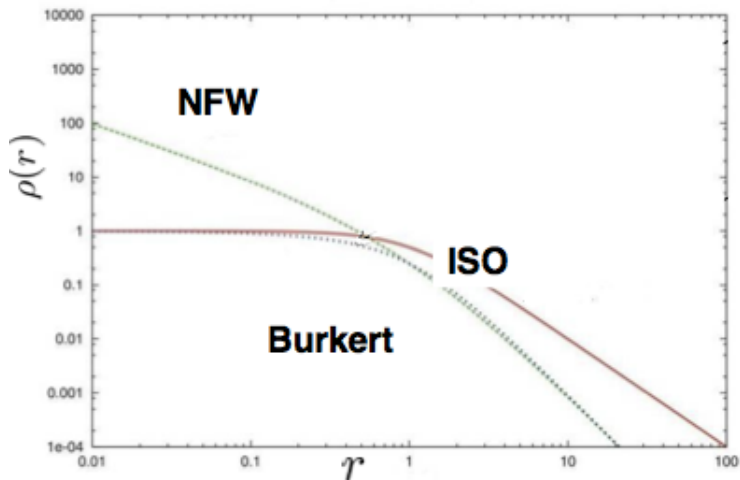


Figure 1.2: Typical NFW density profile, with cusped halo in the center. Burkert and isothermal (ISO) profiles are also represented as possible cored density distributions. Note that the NFW and Burkert outer density profiles are $\propto r^{-3}$, in agreement with observations; while, the isothermal outer density profile appears $\propto r^{-2}$, but this is inconsistent with the observations.

discrepancy is the existence of dark satellites that failed to accrete gas and form stars either because of the expulsion of gas in the supernovae-driven winds or because of gas heating by the intergalactic ionizing background. However, larger haloes (among the smallest predicted by the Λ CDM) have deeper potential wells and should, in the absence of strong feedback, be able to retain gas and form stars, nevertheless we do not observe the large number predicted by the N-body simulations. This is the so called **too big to fail problem** (e.g. [Ferrero et al., 2012, Boylan-Kolchin et al., 2012, Garrison-Kimmel et al., 2014, Papastergis et al., 2015]).

Furthermore, the cusped DM halo predicted from the N-body simulations is in contrast with the observed cored profiles, well described by the Burkert profile (see Eq. 2.7 in Chapter 2). See Fig. 1.2. This is the so called **cusp-core problem** (e.g. [Salucci, 2001, de Blok and Bosma, 2002, Gentile et al., 2004, Gentile et al., 2005, Simon et al., 2005, Del Popolo and Kroupa, 2009, Oh et al., 2011, Weinberg et al., 2015]), that is well known in spirals of any luminosity (see [Salucci, 2019]).

A solution proposed to the Λ CDM contrasts is the introduction of the effect of **baryonic matter feedbacks** on the DM distribution (e.g. [Navarro et al., 1996a, Read and Gilmore, 2005, Mashchenko et al., 2006, Pontzen and Governato, 2014, Di Cintio et al., 2014]): the baryonic feedback generated by supernovae explosion blows the existing gas to the outer galactic regions, modifying the total gravitational potential, then the initial collisionless DM density can get its central cusp erased.

However, this process seems to be unable to produce the observed cored DM distribution in dwarf and large spirals, in details for $R_d \lesssim 0.5$ kpc and

$R_d \gtrsim 5$ kpc [Di Cintio et al., 2014]. Furthermore, the halo response to the stellar feedback is shown to be a strong function of the star formation threshold [Dutton et al., 2019, Benítez-Llambay et al., 2019], rising doubts on the ability to form cored DM distributions. Finally, the stellar feedback inefficiency in modifying the inner DM halo distribution seems to be evident in large LSBs [Kuzio de Naray and Spekkens, 2011], due to the fact that they are very slowly evolving system and to their huge radial extension with respect to normal spirals (see Fig. 4.1).

1.3.1 Issues with other DM candidates

It is interesting to note that also the alternative scenarios to the Λ CDM run in difficulties after some simple considerations. The ULA is challenged in the production of DM core radius with size $\gtrsim 10kpc$ [Hui et al., 2017], in contrast with the large observed sizes (see e.g. the bottom panel in Fig. 4.2). The SIDM, which is strongly constrained by clusters observations [Banerjee et al., 2019], requires a strong and improbable velocity dependence in the cross section between the dark particles. Then, despite the possibility to form core in the inner galactic region, some challenges for the WDM emerge at high redshift [Iršič et al., 2017]. Finally, concerning the PBHs, increasingly strong limits on their abundance can be inferred from the microlensing observations: a survey of about a thousand supernova detected no gravitational lensing events, although about 8 would be expected if intermediate mass primordial black holes accounted for the majority of dark matter [Zumalacárregui and Seljak, 2018]. Furthermore, CMB and several other probes, together seem to disfavour PBHs from constituting all of the DM (see e.g. [Capela et al., 2013, Niikura et al., 2019]), at least the PBHs intended as the very massive celestial objects (much larger than $1 M_\odot$) responsible for the observed gravitational waves.

Chapter 2

The dark and the luminous matter distribution in disc/LSB galaxies

One important way to investigate the DM properties is to study its distribution in galaxies. This is quite relatively simple in rotational supported systems, such as spiral galaxies, since they have a rather simple kinematics. Instead, it is more difficult to investigate the DM distribution in elliptical galaxies. In this case, we are talking about systems dominated by random motions rather than by rotational motions and the analysis of the matter distribution involves the velocity dispersion $\sigma(r)$ rather than the circular velocity $V(r)$. The kinematics is more uncertain and, furthermore, the analysis is complicated by the presence of the nuisance anisotropy parameter, which is font of degeneracy (see e.g. Section 4.4 in [Salucci, 2019]).

Concerning rotating disc galaxies, one method to infer the dark matter distribution is to model their circular velocity rotation curves $V(r)$ (see Fig. 2.1), taking into account that it rises as result of different matter components contributing to the whole gravitational potential:

$$V_{tot}^2(r) = r \frac{d}{dr} \phi_{tot}(r) = V_d^2(r) + V_{HI}^2(r) + V_{bu}^2(r) + V_h^2(r) \quad , \quad (2.1)$$

with the Poisson equation relating the surface (spatial) densities to the corresponding gravitational potentials. V_d , V_{HI} , V_{bu} and V_h are the contribution to the total velocity rotation curve $V_{tot}(r)$ by the stellar disc, the gaseous disc, the bulge and the dark matter halo, respectively ([Faber and Gallagher, 1979, Rubin et al., 1985] and e.g. [Salucci, 2019]). Once we know the contributions from the observed luminous matter (i.e. V_d , V_{HI} and V_{bu}), by fitting the observed rotation curve $V(r)$ with the model $V_{tot}^2(r)$ in Eq. 2.1, we obtain information about the V_h component, which involves dark matter halo parameters. Thus, in order to infer the DM distribution, it is necessary to know the luminous matter components V_d , V_{HI} and V_{bu} .

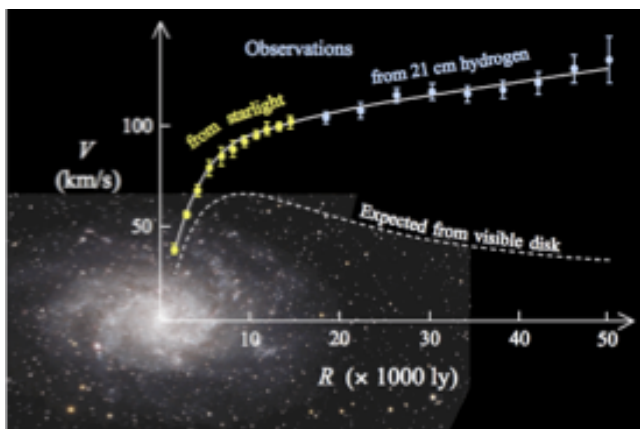


Figure 2.1: Velocity rotation curve of a typical spiral galaxy [Corbelli and Salucci, 2000]: predicted based on the visible matter (*dashed line*) and observed (*solid line*). The distance is from the galactic core.

2.1 The contributions to the circular velocity rotation curves

In the following, the contribution to circular velocity rotation curves $V_{tot}(r)$ from the stellar disc, the stellar bulge, the gaseous disc and the DM halo, are described.

2.1.1 The stellar disc

Caveat some occasional cases not relevant for the present topic, the stars in rotating systems are mainly distributed in a **thin disc** with surface luminosity [Freeman, 1970]:

$$\mu(R) = \mu_0 e^{-R/R_d} \quad (2.2)$$

where μ_0 is the central value and R_d is the disc scale length (see Fig. 2.2 and also e.g. Fig. 1 in [McGaugh and Bothun, 1994], Fig. 7-11 in [Wyder et al., 2009]). The light profile does not depend on galaxy luminosity; thus, the disc length R_d sets a consistent reference scale in all objects. Moreover we are used to take the optical radius $R_{opt} = 3.2R_d$ as the stellar disc size, including the 83% of the total luminosity¹. The contribution to the circular velocity from the stellar disc component is given by:

$$V_d^2(r) = \frac{1}{2} \frac{G M_d}{R_d} (3.2 r/R_{opt})^2 (I_0 K_0 - I_1 K_1) \quad , \quad (2.3)$$

where I_n and K_n are the modified Bessel functions computed at $1.6x$, with $x = r/R_{opt}$.

¹Noticeably the total luminosity and the half-light radius $R_{1/2}$ enclosing half of the latter are good tags of the objects. The disc scale length and the half-light radius are simply related by the equation $R_{1/2} = 1.68 R_d$.

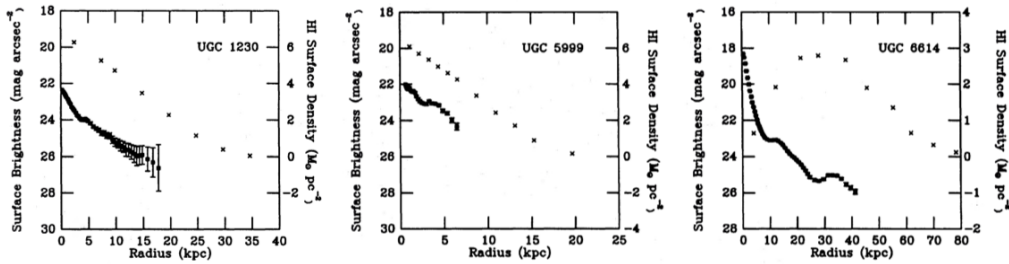


Figure 2.2: The radial surface brightness distribution in R and the radial HI surface density distributions of three LSB galaxies (UGC1230, UGC5999, UGC6614). The image is reproduced from [van der Hulst et al., 1993].

2.1.2 The gaseous disc

Furthermore, a **gaseous HI disc** is usually present in rotating disc galaxies. The contribution to the circular velocity V_{HI} is obtained from the HI surface density $\Sigma_{HI}(R)$ by solving the Poisson equation (Section (5a) in [Kent, 1986]). Typical gas distributions are shown in Fig. 2.2. Very approximately, in the external region, the gaseous HI disc shows a Freeman distribution (see e.g. Fig. 2.2 and also Fig. 2 in [van der Hulst et al., 1993]) with a scale length about three times larger than that of the stellar disc ([Evoli et al., 2011, Wang et al., 2014]):

$$\Sigma_{HI}(R) = \Sigma_{HI,0} e^{-R/3R_d} \quad . \quad (2.4)$$

The contribution of the gaseous disc to the circular velocity is:

$$V_{HI}^2(R) = \frac{1}{2} \frac{GM_{HI}}{3R_D} (1.1 R/R_{opt})^2 (I_0 K_0 - I_1 K_1) \quad , \quad (2.5)$$

where M_{HI} is the gaseous disc mass (correcting by a factor 1.3 in order to account for the He abundance), I_n and K_n are the modified Bessel functions computed at $0.53x$.

Anyway, in first approximation this component can be neglected in terms of mass modelling. In fact, the gas contribution is usually a minor component to the circular velocities, since the inner regions of galaxies are dominated by the stellar component and in the external regions, where the gas component overcomes the stellar one, the DM contribution is largely the most important [Evoli et al., 2011].

On the other hand, the HI disc is usually important as tracers of the galaxies gravitational field, precisely because of its extension in the outer region where we lack stellar observations. See Fig. 2.1.

Finally, inner H_2 and CO discs are also present, but they are negligible with respect to the stellar and HI ones [Gratier et al., 2010, Corbelli and Salucci, 2000].

2.1.3 The stellar bulge

Large disc galaxies are characterised by the presence of a central **bulge**, which usually appear as a round ellipsoid, where old and new stars are crammed

tightly together within few parsecs. Assuming that the innermost velocity measurements are obtained at a radius r_{in} , usually larger than the edge of the bulge, we can consider the bulge as a point mass. Its contribution V_{bu} to the circular velocity, relevant in the inner galactic region, can be expressed by the simple functional form:

$$V_{bu}^2(r) = \alpha_{bu} V_{in}^2 \left(\frac{r}{r_{in}} \right)^{-1} , \quad (2.6)$$

where α_b is a parameter which can vary from 0.2 to 1 (e.g. see [Yegorova and Salucci, 2007]), V_{in} and r_{in} are the values of the first velocity measurement closer to the galactic center.

2.1.4 The DM halo

Since the luminous component is not able to fit the whole rotation curve ([Rubin et al., 1980, Bosma, 1981b] and also [Bertone and Hooper, 2018]), we need to add a contribution by a **spherical dark matter halo**. The density profiles $\rho(r)$ that are usually tested are:

i) the *NFW profile*, which is the result from the N-body simulation in the Λ -CDM scenario described in Eq. 1.1, characterised by a central *cusp* $\propto r^{-1}$ and by an external tail $\propto r^{-3}$ (see Fig. 1.2);

ii) the *cored profile*, characterised by a central constant density $\rho(r) = const.$ within a core radius r_0 and by an external tail whose negative slope can vary according to the specific adopted model. In particular a very successful empirical model is the **Burkert profile** [Burkert, 1995]:

$$\rho_{DM}(r) = \frac{\rho_0 r_0^3}{(r + r_0)(r^2 + r_0^2)} , \quad (2.7)$$

where ρ_0 is the central mass density and r_0 is the core radius. This profile is characterised by an external tail $\propto r^{-3}$ (see Fig. 1.2). Its mass distribution is:

$$\begin{aligned} M_{DM}(r) &= \int_0^r 4\pi \tilde{r}^2 \rho_{DM}(\tilde{r}) d\tilde{r} = \\ &= 2\pi \rho_0 r_0^3 [\ln(1 + r/r_0) \\ &\quad - tg^{-1}(r/r_0) + 0.5 \ln(1 + (r/r_0)^2)] . \end{aligned} \quad (2.8)$$

The contribution to the total circular velocity is given by:

$$V_h^2(r) = G \frac{M_{DM}(r)}{r} . \quad (2.9)$$

The Burkert profile represents the (empirical) family of cored distributions, which includes e.g. the pseudo-isothermal, degenerate fermionic particles (see also PAPER 3 in Chapter 9), Bynney-Tremaine profile. To discriminate among them the correct one is, currently, very difficult (see Fig.7 in [Salucci, 2019] and the references therein).

Particularly, among the family of cored distributions cited above, the **pseudo-isothermal profile** is often used. It takes the form:

$$\rho(r) = \rho_0 \frac{r_0^2}{(r^2 + r_0^2)} \quad , \quad (2.10)$$

where ρ_0 is the central constant density and r_0 is the core radius. This profile is characterised by an external tail $\propto r^{-2}$ (see Fig. 1.2) and implies constant velocities when $r \gg R_{opt}$, which however disagrees with the RC profiles at very outer radii that show a decline with radius [Shankar et al., 2006].

iii) the **Zhao halos profile** [Zhao, 1996], which can assume both the form of a cusped or a cored profile:

$$\rho(r) = \frac{\rho_0}{(r/r_0)^\gamma (1 + (r/r_0)^\alpha)^{\frac{\beta+\gamma}{\alpha}}} \quad . \quad (2.11)$$

However it involves a large number of parameters: the density ρ_0 , the radius r_0 , the α , β and γ parameters, which control the slope and the curvature of the profile. This seems in disagreement with observations in spirals, ellipticals and spheroidals that suggest that DM halos are one (two)-parameters family (as described in the previous DM halo profiles). See also the discussion in Section 6 in [Salucci, 2019].

It is worth emphasizing that the tail of the cored Burkert profile, $\propto r^{-3}$ (as well as the NFW case), is in agreement with the weak lensing observations, which allow us to estimate the DM distribution of mass in the outer region of galaxies [Schneider, 1996, Hoekstra and Bhuvnesh, 2008, Zu and Mandelbaum, 2015, Donato et al., 2009].

Furthermore, we highlight that the cored Burkert profile well reproduces, in cooperation with the velocity components of the luminous matter, the individual circular velocities of spirals [Salucci and Burkert, 2000], dwarf discs [Karukes and Salucci, 2017] and low surface brightness systems [Di Paolo et al., 2019a] (PAPER 1 in Chapter 7), giving better results than the cusp profile (Dehqani et al. in prep.).

2.1.5 Rotation curves modeling

When modeling the rotation curves (RCs), in order to know the contribution from the stellar component (disc and bulge), it is usually assumed that the observed density of stars is proportional to the R-band light by taking into account a *guessed mass to light ratio* M_*/L . Then, the contribution from the gaseous disc can be evaluated from the resolved HI surface density and the contribution from the DM halo (usually including two unknown parameters) is given by the RC best fit.

Another way of considering the contribution to $V(r)$ by the luminous matter is the *maximum disc model*, based on the M_*/L tuning so that gas and luminous stars account for as much as of the galaxy's rotation as possible.

Furthermore, we can leave some *free parameters* (as e.g. M_d or M_*/L) in the luminous contribution to the circular velocity and find them directly by the

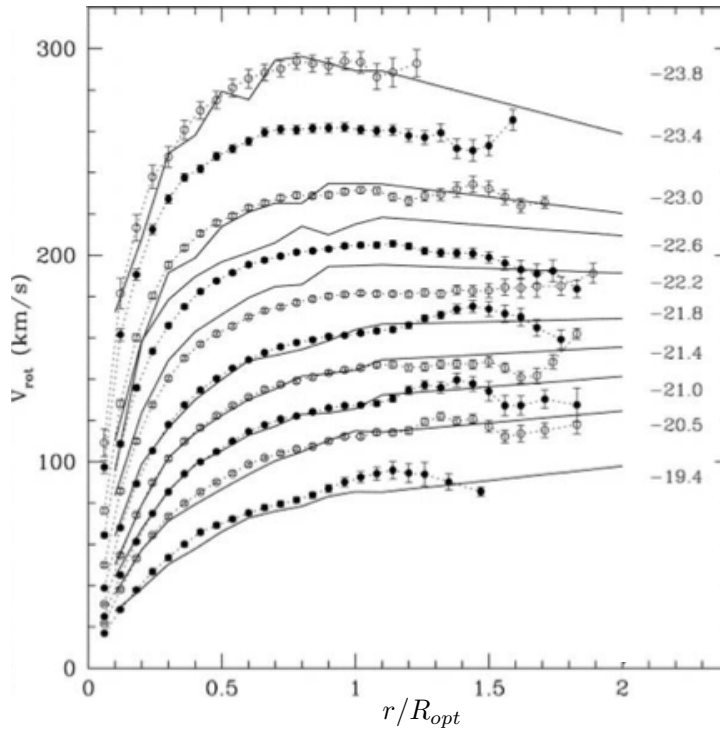


Figure 2.3: Coadded rotation curves from 3100 normal spirals, obtained by plotting together the results by [Persic et al., 1996] and [Catinella et al., 2006]. The galaxies magnitude M_I are indicated on the right of the rotation curves.

RC best fit.

When the rotation curves of disc galaxies are modelled, they can be studied individually or by means of a stacked analysis, such as the “*universal rotation curve method*”, described in the Sections 2.2-4.3.

2.2 The universal rotation curve (URC)

A very interesting feature of spiral galaxies is that the bigger they are, the more luminous they are and the higher rotational velocities they show. Moreover, when their RCs, with the radial coordinate normalised with respect to their optical radius R_{opt} ², are put together, they appear to follow a *universal trend* (first shown in Fig. 4 in [Rubin et al., 1985], then in [Persic and Salucci, 1991, Persic et al., 1996, Rhee, 1996, Roscoe, 1999, Catinella et al., 2006, Noordermeer et al., 2007, Salucci et al., 2007, López Fune, 2018] and e.g. [Salucci, 2019]). From small to large galaxies, the RCs have higher and higher velocities and profiles that gradually change. See also Fig. 2.3-2.4. By means of the “*universal rotation curve (URC) method*”, a stacked analysis which involves groupings of similar

²The details of this choice are expressed at length in [Persic et al., 1996].

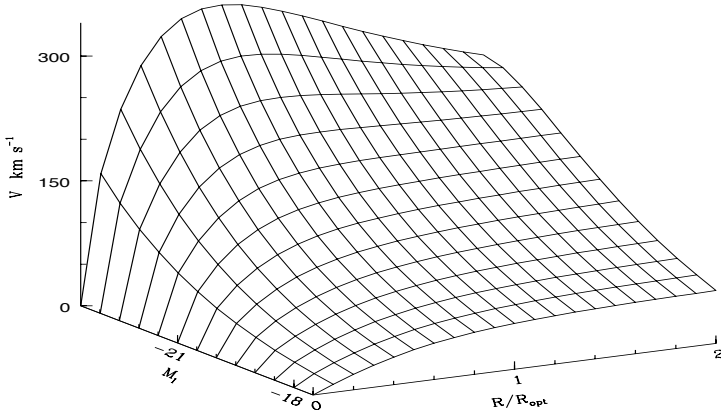


Figure 2.4: Universal rotation curve (URC) for spiral galaxies in the local volume [Persic et al., 1996]. The velocity (V) rotation curves are expressed as function of the normalised radii R/R_{opt} and of the galaxies magnitude M_I .

RCs and their mass modelling, it is possible to construct an analytic function that gives a good description of all the rotation curves of the local spiral galaxies within a spherical volume $\simeq (100 \text{ Mpc})^3$. The URC method was applied for the first time in [Persic and Salucci, 1991]. This was followed by a series of three works: [Persic et al., 1996] (Paper I), [Salucci et al., 2007] (Paper II) and [Karukes and Salucci, 2017] (Paper III), where the URC method gave deeper results related to *normal spirals*, also called *high surface brightness* (HSB) spirals, and *dwarf disc* (*dd*) galaxies. A subsequent work confirmed the above results with up to 3100 disc galaxies and highlighted the existence of *tight scaling relations* among the properties of spirals with different size [Lapi et al., 2018].

The statistical approach of the URC analysis, based on the mass modeling of stacked and suitably normalised RCs of similar luminosity, has some relevant advantages over the individual fit of the RCs. Indeed, it increases the signal-to-noise ratio, smoothing out small-scale fluctuations induced by bad data and/or by physical features as spiral warps. Thus, it is possible to work on a large sample of RCs, also including those curves characterised by a brute-force fit if analysed individually. Furthermore, the considered stacked analysis leads us to prefer a cored Burkert profile for the DM halo, giving rise to very good fit of the RCs alongside the Freeman stellar disc (e.g. [Karukes and Salucci, 2017, Di Paolo et al., 2019a]).

Let us underline that the concept of *universality* in the RCs means that all of them can be described by the same analytical function as long as expressed in terms of the normalised radius and of one global parameter of the galaxies, such as magnitude, luminosity, mass or velocity at the optical radius ($V_{opt} \equiv V(R_{opt})$). Therefore, the *universal rotation curve* (URC) is the circular velocity at a certain radius r given by (e.g.) $V(r/R_{opt}, L)$, where L is the galaxy’s luminosity. See Fig. 2.4. Obviously, the URC does not change even using, instead

of R_{opt} , any other radial coordinate proportional to the stellar disc scale length R_d ³.

The URC is a very powerful tool since, given the observation of few properties (such as R_d and L) of a certain galaxy, it is possible to deduce its rotation curve and all its properties.

In this work, we investigate the concept of the URC, the resulting mass models and the scaling relations in *Low Surface Brightness* (LSB) disc galaxies. We compare the found scaling relations to the results obtained in previous works by individual modelling of the LSBs RCs and to the results of other disc galaxies of a different Hubble type, namely the spiral galaxies and the dwarf disc galaxies.

³The results of the paper remain unchanged for any chosen radial coordinate if expressed in units of λR_d , with any λ value ranging from 1 to 4.

Chapter 3

Low Surface Brightness (LSB) galaxies: observational properties of the luminous matter

LSB galaxies (see Fig. 3.1-3.2-3.3) are rotating disc systems which emit an amount of light per area smaller than normal spirals, with a face-on central surface brightness $\mu_{0,B} \gtrsim 23 \text{ mag arcsec}^{-2}$ in the B band (e.g. [Impey and Bothun, 1997]) and/or $\mu_{0,R} \gtrsim 21 \text{ mag arcsec}^{-2}$ in the R band (see e.g. Fig. 2.2 and also Fig. 1 in [McGaugh and Bothun, 1994], Fig. 7 in [Wyder et al., 2009]). The $\mu_{0,B}$ value is systematically fainter than the canonical $\mu_{0,B} = 21.65 \text{ mag arcsec}^{-2}$ of normal spirals [Freeman, 1970, van der Kruit, 1987]. The LSBs are characterised by diffuse, low-density exponential stellar discs [de Blok et al., 1996, Burkholder et al., 2001, O'Neil et al., 2004], with typical average values $\Sigma_* \simeq 12.3 M_\odot/\text{pc}^2$ (see e.g. Tab.2 in [Lei et al., 2019]), on average about 3 - 4 times lower than than in HSB spiral galaxies, reaching sometimes also values $\simeq 10$ times lower.

3.1 Main LSBs observational properties

The observed LSBs cover the full population of galaxies, ranging from small ($\simeq 10^7 M_\odot$) to very large (more than $10^{10} M_\odot$) stellar disc mass M_d (see e.g. Fig. 3.4 - 4.2 - 4.7), from small to large size, with stellar disc scale lengths R_d spanning from fraction of kpc to tens of kpc (see e.g. Fig. 4.1). Their typical magnitudes are: $-20 \lesssim M_B \lesssim -10$ (see e.g. 3.5 and Tab. 2 in [Du et al., 2019]), $-15 \lesssim M_V \lesssim -9$ (see e.g. Fig. 10 in [Cohen et al., 2018], Tab. E1 in [Prole et al., 2019]), $-14 \lesssim M_R \lesssim -23$ (see e.g. Fig. 2 in [Minchin et al., 2004]).

The LSB disc galaxies includes several morphologies (see e.g. Fig. 3.1-3.2-3.3, Tab.1 in [Honey et al., 2016], Tab.1 in [Honey et al., 2018]), from irregulars to spirals. They span from dwarfs to giant galaxies; the latter are often made of a HSB disc embedded in a larger LSB disc extended till $\simeq 100$ kpc, as

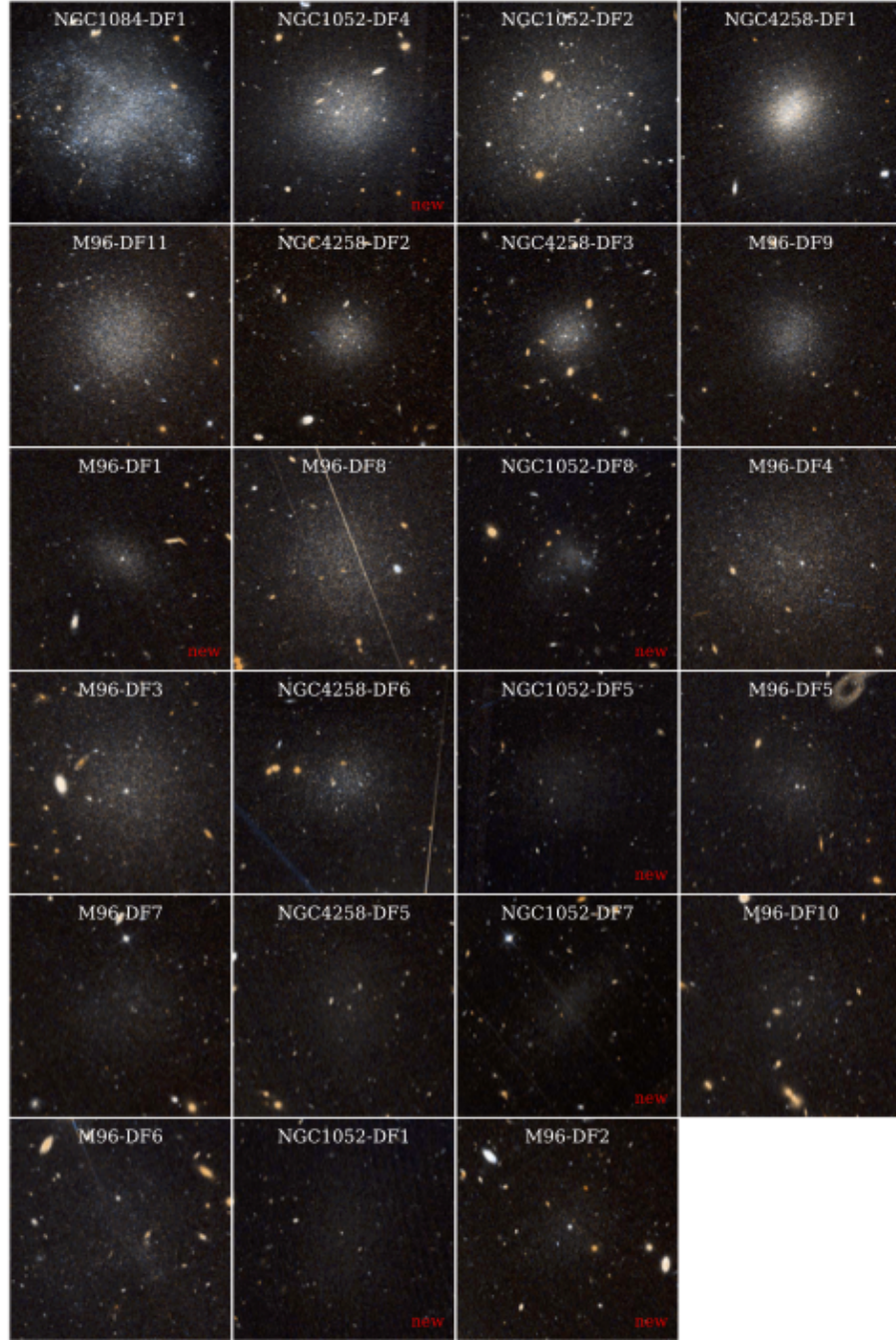


Figure 3.1: LSB galaxies. From left to right and top to bottom, the galaxies are ordered by effective surface brightness in the V606-band. Image reproduced from [Pahwa and Saha, 2018].

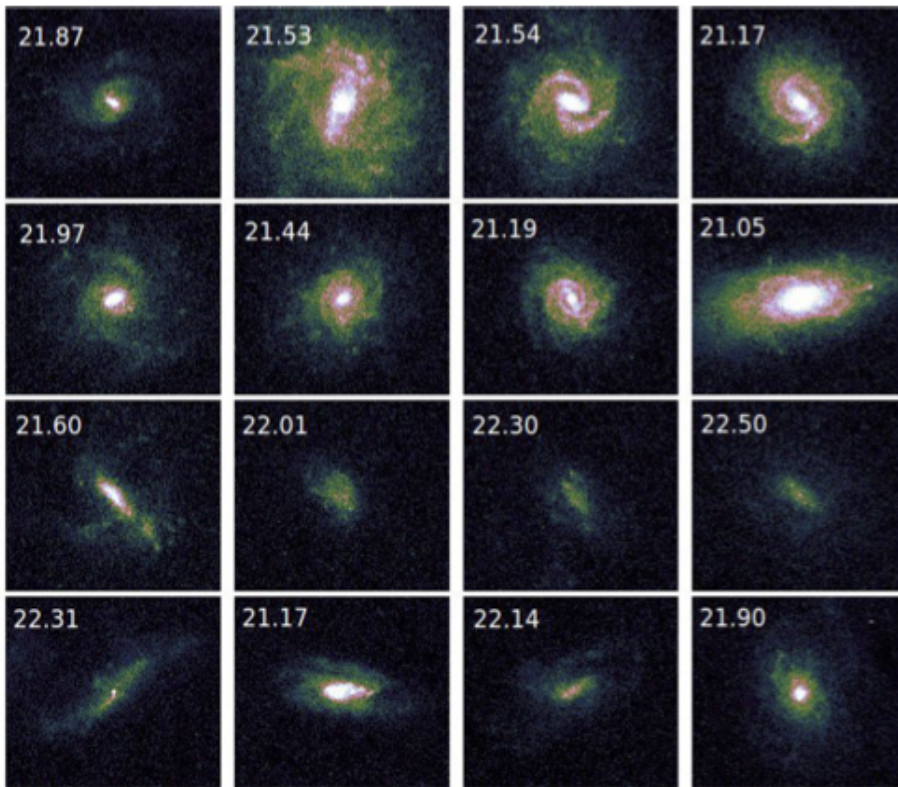


Figure 3.2: A few representative galaxies of different morphologies of LSB galaxies in r-band. The disc central surface brightness (in units of mag arcsec^{-2}) is indicated on the top of each galaxy. The colour scale is same for all panels. Image reproduced from [Cohen et al., 2018].

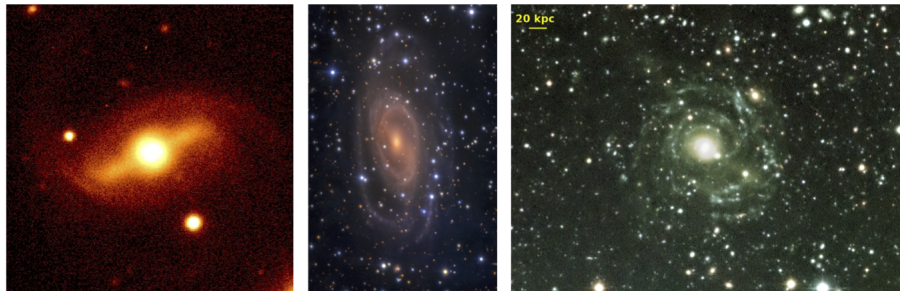


Figure 3.3: *First panel:* R-band image of the barred LSB galaxy UM163, reproduced from [Honey et al., 2016]. *Second panel:* image of UGC 1378 reproduced from [Saburova et al., 2019], a giant low-surface brightness (gLSB) discy galaxy. UGC 1378 has both a high surface brightness and an extended low surface brightness discs. *Third panel:* image of the giant LSB galaxy Malin 1 (u, g, i, z in blue, green, yellow, red, respectively) reproduced from [Boissier et al., 2016].

in Malin1 [Bothun et al., 1987, Impey and Bothun, 1989, Boissier et al., 2016] (see Fig. 3.3). Most LSBs are without bars, but a small fraction of them show bars (e.g [Honey et al., 2016], see Fig. 3.2-3.3). The largest LSBs usually show a central bulge (e.g. [Das, 2013]). The LSB galaxies generally results to be bluer than normal spirals (HSBs), with typical B-V color approximately in the range [0.49; 0.52], lower than the typical average value $B-V \simeq 0.75$ of the HSBs spirals. See Fig. 3.5 and also e.g. the results reported in Fig. 7-11 in [Wyder et al., 2009] and in [McGaugh and Bothun, 1994, de Blok et al., 1996, Schombert and McGaugh, 2014, Pahwa and Saha, 2018, Du et al., 2019]. Despite the characteristic blue color of the LSB galaxies, sometimes it is possible to observe them also as red objects (see Fig. 3.5 and also e.g. [O'Neil et al., 2000]).

An LSBs peculiarity is the lack of correlation between their surface brightness μ_0 and colors versus other galaxies properties, as the disc mass, the luminosity, the disc scale length (e.g. [McGaugh and Bothun, 1994], see also e.g Fig. 6 in [Bothun et al., 1997], Fig. 8 - 11 in [Pahwa and Saha, 2018]).

Radio synthesis observations show that LSB galaxies have extended gas discs with masses M_{HI} ranging on average between 10^8 and $10^{10} M_{\odot}$ (see e.g. [O'Neil et al., 2000, Pahwa and Saha, 2018, Lei et al., 2019]), usually comparable with the stellar disc mass M_d (see Fig. 3.4 and also e.g. Tab. 2 in [Lei et al., 2019]). The LSBs show large values of M_{HI}/L ratios (e.g. [van der Hulst et al., 1993, O'Neil et al., 2000, Du et al., 2019]), which can result to be several times higher than in normal spirals. See 3.5. Typical values of M_{HI}/L_B in LSBs range from $\simeq 0.1$ to $\simeq 10$ [Burkholder et al., 2001, O'Neil et al., 2004, Du et al., 2019], reaching sometimes extremely high values like 50 [O'Neil et al., 2000]. The reason for these values can be found both in the large mass of the LSBs gaseous disc and its characteristic low density, which likely prevents an efficient star formation (e.g. [Das et al., 2009, Galaz et al., 2011]). Indeed, the typical HI surface density values in the LSB galaxies are $\Sigma_{HI} \simeq 5 M_{\odot} pc^{-2}$ (see Fig. 2.2 - 3.6 and also e.g. [de Blok et al., 1996, Lei et al., 2019]), on average lower (less than half) than the values found in comparable high surface brightness galaxies. Accord-

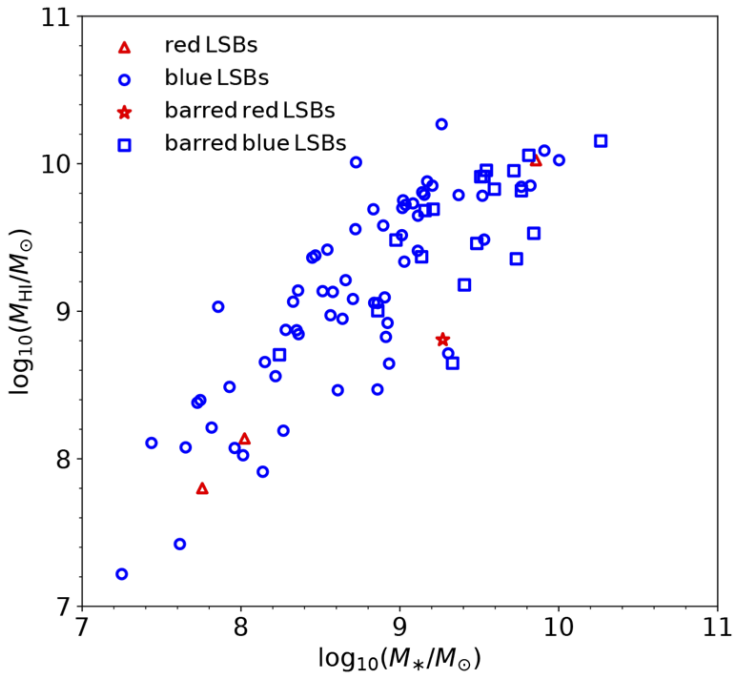


Figure 3.4: Mass of the stellar disc M_* versus the HI mass M_{HI} , reproduced from [Pahwa and Saha, 2018].

ing to the Kennicutt criteria [Kennicutt, 1989, Kennicutt, 1998], the HI surface densities in LSBs appear to be systematically below the star formation threshold (see e.g. Fig. 5 in [van der Hulst et al., 1993] and also [Schmidt, 1959, Kennicutt, 1998, Boissier et al., 2016]), implying that the gas is not stable to collapse and form stars [van der Hulst et al., 1993, Martin and Kennicutt, 2001, Blitz and Rosolowsky, 2004, Robertson and Kravtsov, 2008, Wyder et al., 2009]. As result, the star formation rate (SFR) in LSBs is very low, usually $\lesssim 0.1 M_\odot yr^{-1}$, at least one order of magnitude lower than in HSB spirals (see e.g. [de Blok et al., 1996, van den Hoek et al., 2000], Tab. 3 in [Lei et al., 2018], Tab. 2 in [Lei et al., 2019]). Typical values of the star formation surface densities are $\Sigma_{SFR} \lesssim 10^{-3} M_\odot yr^{-1} kpc^{-2}$ as reported in Fig. 3.6. See also Tab. 3 in [Lei et al., 2018]. The low star formation in LSBs can be also due to a low star formation efficiency (only a few percent than in HSB), as pointed by [Lei et al., 2018], noting that the LSBs have much lower SFR and Σ_{SFR} than star-forming galaxies, despite both of them have similar HI surface densities (see Fig. 10 in [Lei et al., 2018]).

It is worth to note that the LSBs are characterised by low metallicity ($< 1/3$ solar abundance, see e.g. Fig.8 in [McGaugh and Bothun, 1994] and also [Liang et al., 2010, Bresolin and Kennicutt, 2015, Honey et al., 2016]), with a consequent lack of large amounts of molecular gas (due to inefficient cooling), and by low dust content [Matthews and Gao, 2001, O'Neil and Schinnerer, 2003, Hinz et al., 2007, Wyder et al., 2009], which are important factor in determining the slow evolution of LSB galaxies.

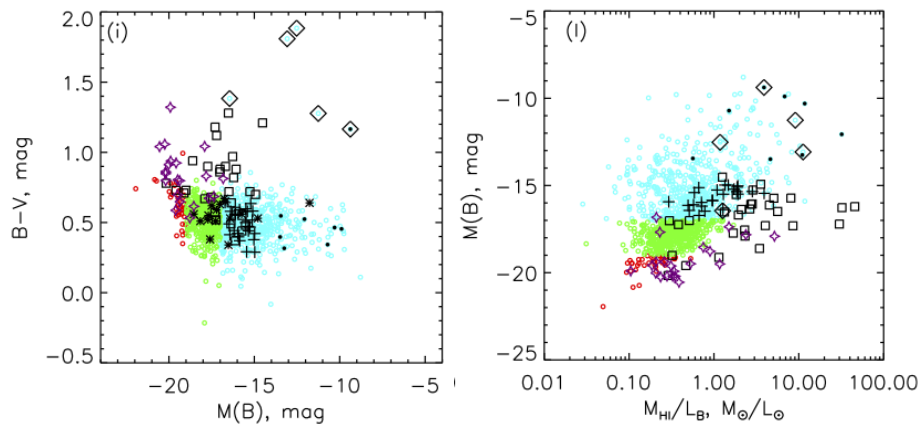


Figure 3.5: Properties of LSB galaxies sample from [Du et al., 2019, O’Neil et al., 2000, McGaugh and Bothun, 1994, de Block et al., 1995], represented by *open circles, open squares, open triangles, asterisks* respectively, compared with HSB galaxies (*purple stars*) from [Ponomareva et al., 2017]. The *cyan, green and red open circles* represent dwarf, moderate-luminosity and giant LSBs in the [Du et al., 2019] sample. The over-plotted black plus symbols represent candidates of Ultra Diffuse Galaxies in the [Du et al., 2019] sample. The LSBs which have very red color ($B-V > 1.0$ mag) but are low in luminosity ($M(B) > -17.0$ mag) and gas-rich ($M_{HI}/L_B > 1.0$) are over-marked by open diamonds. The image is reproduced from [Du et al., 2019].

3.2 LSBs evolution

The typical observed very blue colors of LSBs suggest that young stars are the dominant population, while the old stars do not make a substantial contribution (e.g. [Wyder et al., 2009, Schombert and McGaugh, 2014]). These properties, together with the observed low $H\alpha$ emission (e.g [Schombert et al., 2013]) and the high gas fractions, indicate a history of nearly constant star formation, compared to the declining star formation models which match the properties of HSB spirals and irregulars (e.g. [Vorobyov et al., 2009, Schombert and McGaugh, 2014]). Furthermore, the LSBs typical very low content in metal and dust, which are normally produced during the star formation process, also suggests that they formed relatively few stars over a Hubble time (see e.g [Wyder et al., 2009, Vorobyov et al., 2009]). The LSB stellar population appears to be uniformly distributed in the stellar disc, since there is no significant color gradient in the color images of the bars (when present) [Honey et al., 2016]. Likely the star formation is characterised by sporadic small-amplitude events (e.g [Schombert and McGaugh, 2014]). Overall, the LSBs seems not to be the faded remnants of HSBs that have ceased star formation, as also suggested by the absence of correlation between μ_0 and colors with other galaxies properties (see e.g. [Bothun et al., 1997]). Rather LSBs are likely slowly evolving galaxies (e.g. [Vorobyov et al., 2009, Schombert and McGaugh, 2014]).

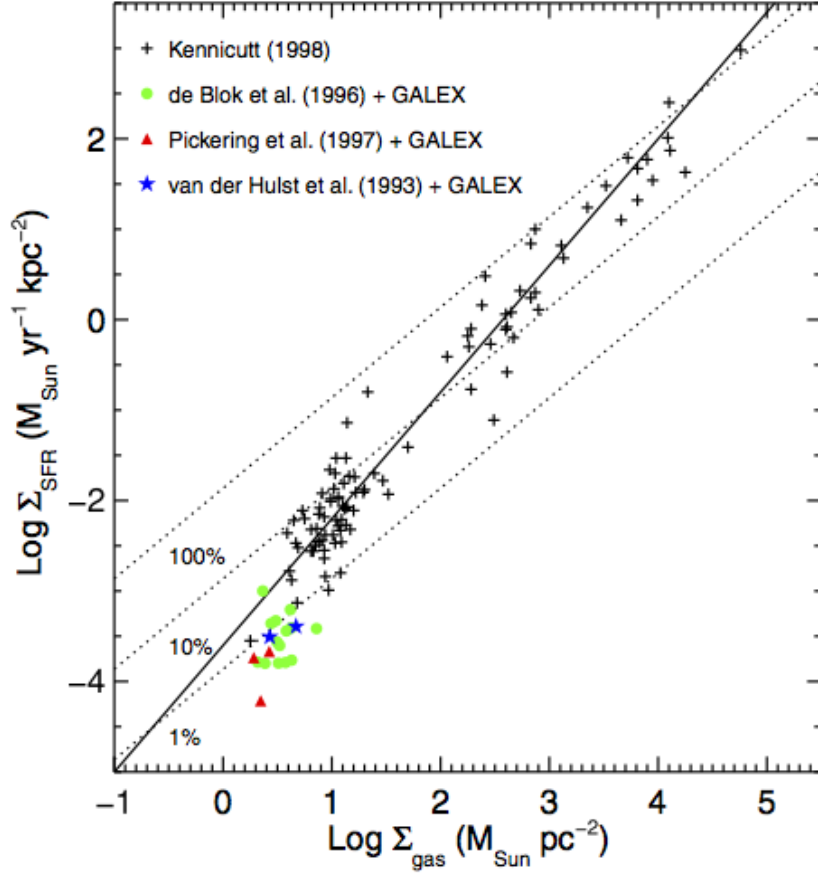


Figure 3.6: Star formation rate (SFR) surface density as a function of the total hydrogen gas surface density. The colored symbols indicate the sample of 19 LSB galaxies from [Wyder et al., 2009] with SFRs measured from the UV with no correction for dust attenuation. The gas surface densities are derived from the HI data from [de Blok et al., 1996] (green circles), [Pickering et al., 1997] (red triangles), and [van der Hulst et al., 1993] (blue stars) and assume that the molecular fraction is negligible. The black pluses indicate the sample of higher surface brightness galaxies from [Kennicutt, 1998] while the solid line is the power-law fit to these points. The LSB galaxies tend to lie below the extrapolation of the power-law fit to the higher surface brightness sample. The three *dotted lines* show the star formation efficiency (SFE) of 100%, 10%, 1% in a timescale of $10^8 yr$. Image reproduced from [Wyder et al., 2009].

3.3 The LSBs environment

The LSB galaxies are generally isolated systems, located on the edges of large-scale structure [Bothun et al., 1997, Rosenbaum and Bomans, 2004, Galaz et al., 2011, Kovács et al., 2019], in or near large-scale voids. Likely, forming them in underdense regions minimizes the external processes like tidal interactions and mergers, which are able to increase the gas density. The isolated environments are especially characterising the giant LSBs [Rosenbaum et al., 2009], while the smaller LSB dwarf and irregular galaxies are found in both underdense regions [Pustilnik et al., 2011] as well as more crowded environments [Merritt et al., 2014, Davies et al., 2016]. At any rate, beyond the systems isolation, another way to keep the gas at low densities may also be to form LSBs within high spin parameter halos (e.g. [Dalcanton et al., 1997a, Boissier et al., 2003, Di Cintio et al., 2019]). The collapse of the disc is suppressed by high angular momentum, leading to a galaxy with a larger disc size, lower gas surface density and lower surface brightness than a low-spin galaxy of the same mass.

3.4 Further LSBs observations

It is important to note that LSBs seem to be not rare; they comprise $\gtrsim 50\%$ of the general galaxy population (e.g. [McGaugh et al., 1995, Bothun et al., 1997, Dalcanton et al., 1997b, Trachternach et al., 2006, Greco et al., 2018, Honey et al., 2018]), with some cosmological implications (see e.g. Section 5 in [Bothun et al., 1997], Tab. 4 in [Minchin et al., 2004]).

However, the LSBs detection is challenging, due to their lower surface brightness than their HSB counterparts. Thus, LSBs are more difficult to detect against the sky [Disney, 1976, Williams et al., 2016], observational capability and selection effects inevitably lead a bias to our understanding of the galaxy formation and evolution. The first LSB galaxies samples were mainly composed of LSBs in the bright end of surface brightness (e.g. [Schombert et al., 1992, McGaugh and Bothun, 1994, de Blok et al., 1995, Impey et al., 1996]). Afterwards, LSB galaxies that have fainter surface brightness ($\mu_{0,B} \simeq 24\text{--}28 \text{ mag arcsec}^{-2}$) were discovered (see e.g. [Williams et al., 2016, Trujillo and Fliri, 2016]). Since the LSBs are mostly rich in HI gas, a promising investigation could come from the radio observations (e.g. [Giovanelli et al., 2005]). Till now, more than 10000 LSB galaxies has been revealed (e.g. [Zhong et al., 2008]), mostly in the local universe ($z \lesssim 0.1 - 0.2$ [Williams et al., 2016]).

Chapter 4

LSBs mass modeling and scaling laws involving luminous and dark matter

In this chapter we analyse a LSBs sample giving the results obtained in previous works by the mass modelling of the rotation curves of individual objects and the results obtained by means of the URC method (stacked analysis). The latter is used to know the scaling laws between the luminous and the dark matter properties. The found relationships are compared to those of galaxies of different morphology. Finally, the universal rotation curve (URC) is established for the LSB galaxies.

4.1 LSBs sample

Given the relevance of the URC method, in this work we show the result from the analysis applied to a LSBs sample. In [Di Paolo et al., 2019a] (PAPER 1 in Chapter 7), we consider 72 rotating disc galaxies classified as "low surface brightness" in literature (see Tab. B1 and Fig. I1-I2-I3-I4-I5 in [Di Paolo et al., 2019a] in Chapter 8 for the references and for the RCs plots, respectively; the data are available online as supplementary material in [Di Paolo et al., 2019a]). In the very majority of cases the authors classify a galaxy as LSB when the face-on central surface brightness $\mu_0 \gtrsim 23 \text{ mag arcsec}^{-2}$ in the B band. We select our sample according to the following criteria:

- i)* the rotation curves extend to at least $\simeq 0.8 R_{opt}$ (when V_{opt} is not available from observation, it can be extrapolated since from $\simeq 1/2 R_{opt}$ to $2 R_{opt}$, the RCs are linear in radius with a small value of the slope);
- ii)* the RCs are symmetric, smooth (e.g. without strong signs of non circular motions) and with an average fractional internal uncertainty lesser than 20%. In short we eliminated RCs that in no way can be mass-modelled without huge uncertainties;
- iii)* the galaxy disc scale length R_d and the inclination function $1/\sin i$ are known within 30% uncertainty.

The selected LSBs have optical velocities V_{opt} spanning from ~ 24 km/s to

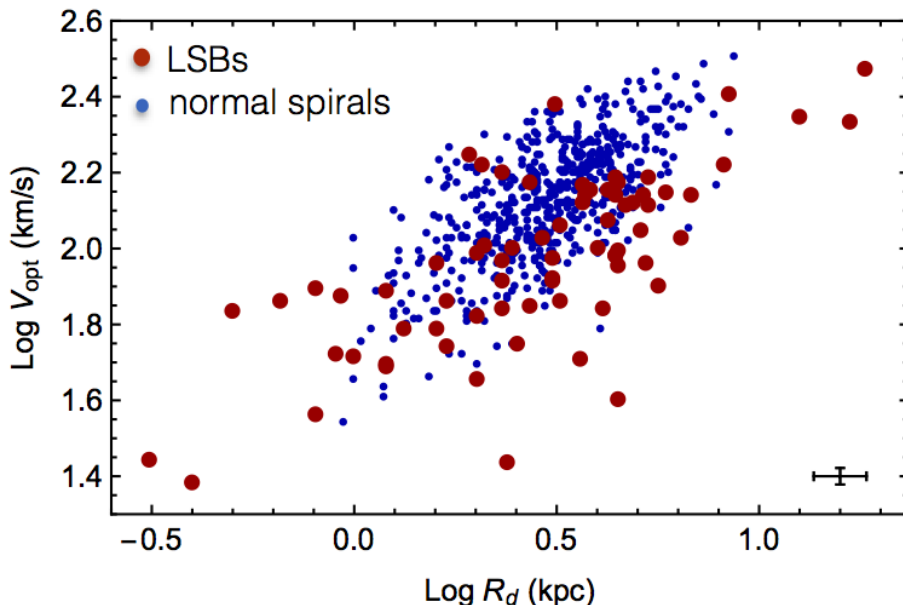


Figure 4.1: Optical velocity versus disc scale lengths in LSB galaxies (*red*) and in normal spirals (*blue*) [Persic et al., 1996]. The typical fractional uncertainties are 5% in V_{opt} and 15% in R_d , as shown in the right-down corner.

~ 300 km/s, covering the values of the full population. In Fig. 4.1, the values of the stellar disc scale lengths R_d and the optical velocities V_{opt} measured in LSBs are shown and compared to those measured in normal spirals. A larger spread in the former case is clearly recognizable. This feature will be used later to explain the need of introducing a new structural variable, the *compactness*, in order to better describe the LSBs.

The sample of rotation curves consists of 1614 independent (r, V) measurements. When the RCs, expressed in normalised radial units, are put together, see Fig. 4.13, they show an universal trend analogous to that of the normal spirals (Fig. 2.4). Then, given the observed trend in LSBs and the relevance of the URC method, we search our sample of LSBs for a universal rotation curve and for the related scaling relations among the galaxy’s structural parameters. The results are shown in Sections 4.3-4.4-4.7, after a brief report in Section 4.2 of the individual RCs analysis of the same LSB sample performed in previous works.

4.2 Mass modeling results from previous works on individual LSB galaxies

The LSB galaxies were investigated some years ago by individual modelling of their rotation curves. Most of the authors of the previous studies tested the cusped NFW profile and a cored profile in order to describe the DM halo. The cored profile usually involved was the pseudo-isothermal one (see Eq. 2.10).

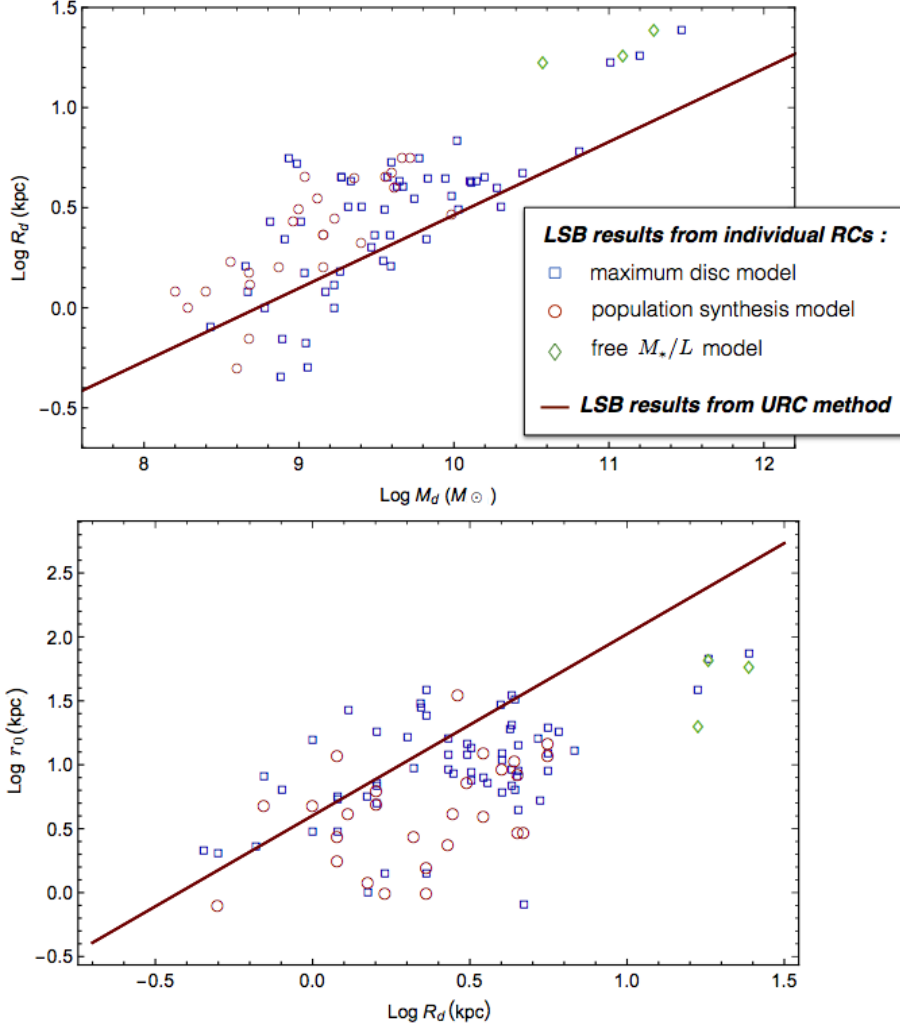


Figure 4.2: Data evaluated in previous works from individual modelling of the LSBs rotation curves, taking into account the maximum disc model (*blue squares*), the population synthesis model (*red circles*) and the free stellar mass to light ratio M_*/L (*green diamonds*) for the disc contribution as indicated in Section 4.2. The data are compared to the relationships found from the stacked analysis of the URC method (*red lines*) [Di Paolo et al., 2019a], involving also the LSBs galaxies with the shown data. In the *upper panel* the stellar disc scale length vs the mass of the stellar disc data are reported and compared to Eq. 4.6; in the *lower panel* the core radius of the DM halo vs the stellar disc scale length data are reported and compared to Eq. 4.2.

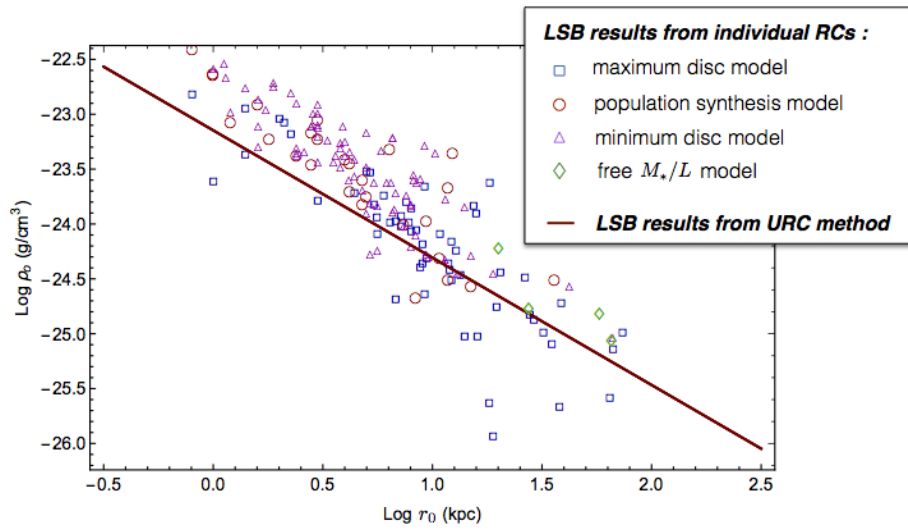


Figure 4.3: Data evaluated in previous works from individual modelling of the LSBs rotation curves, taking into account the maximum disc model (*blue squares*), the population synthesis model (*red circles*), the free stellar mass to lighth ratio M_*/L (*green diamonds*) and the minimum disc model (*magenta triangles*) for the disc contribution as indicated in Section 4.2. The data are compared to the relationships found from the stacked analysis of the URC method (*red lines*) [Di Paolo et al., 2019a], involving also the LSB galaxies with the shown data. The central density of the DM halo vs the core radius data are reported and compared to Eq. 4.4.

This density profile is part of the family of cored distribution (see Subsection 2.1.4) and, in the inner galactic region, can be easily compared to a Burkert distribution (Eq. 2.7) with the same ρ_0 value provided the relationship $r_{0,Burk} \simeq 2r_{0,pseudo-iso}$ exists. Concerning the contribution from the stellar disc, most of the authors considered the maximum disc model, the minimum disc model and the fixed stellar mass to light ratio M_*/L from the population synthesis model.

In most cases, despite the different method adopted to describe the stellar disc, the cored DM profiles give rise to better fits than the cusped ones (e.g. [de Blok and Bosma, 2002, Marchesini et al., 2002, Swaters et al., 2003, Kuzio de Naray et al., 2006, Kuzio de Naray et al., 2008]). Furthermore, sometimes the NFW fits point to unphysical parameters in disagreement with the predictions from the Λ CDM numerical models (see e.g. Fig. 10 in [de Blok and Bosma, 2002], Fig. 15 in [Swaters et al., 2003], Fig. 21 in [Pickering et al., 1997]).

In the following we compare the available data in literature to our results obtained by means of the URC method (we anticipate here the scaling laws found in [Di Paolo et al., 2019a] and later shown in Section 4.4).

In the upper panel of Fig. 4.2, we show the relation between the stellar disc scale lengths R_d and the masses of the stellar discs M_d . The data obtained by involving the maximum disc model in the RCs fits are taken from [de Blok and McGaugh, 1997, Pickering et al., 1997, van Zee et al., 1997, Swaters et al., 2000, de Blok and Bosma, 2002, Swaters et al., 2003]. The data obtained by considering M_*/L from the population synthesis model are taken from [Carignan and Puche, 1990, de Blok and Bosma, 2002, Kuzio de Naray et al., 2008]. Furthermore, we also include the results from [Pickering et al., 1997], which involve a free M_*/L in the RCs fit.

In the lower panel of Fig. 4.2, we show the relation between the DM halo core radius r_0 and the stellar disc scale lengths R_d . The results from the maximum disc analysis include the data from [Pickering et al., 1997, van Zee et al., 1997, de Blok and McGaugh, 1997, Swaters et al., 2000, de Blok and Bosma, 2002, Swaters et al., 2003, Kuzio de Naray et al., 2008], while the results from the population synthesis model include data from [de Blok and Bosma, 2002, Carignan and Puche, 1990, Kuzio de Naray et al., 2008]. The results from the free M_*/L analysis obtained by [Pickering et al., 1997] are also reported.

Finally, in Fig. 4.3, the relation between the central DM halo density ρ_0 and the core radius r_0 is shown. We include data from [Pickering et al., 1997, de Blok and McGaugh, 1997, Swaters et al., 2000, de Blok and Bosma, 2002, Swaters et al., 2003, Kuzio de Naray et al., 2008] for the maximum disc model analysis, data from [de Blok and Bosma, 2002, Carignan and Puche, 1990, Kuzio de Naray et al., 2008] for fixed M_*/L from the population synthesis method. Furthermore we include the data from free M_*/L analysis obtained by [Pickering et al., 1997] and the data from the minimum disc model obtained by [Pickering et al., 1997, de Blok and McGaugh, 1997, Swaters et al., 2003, de Blok and Bosma, 2002, Marchesini et al., 2002, Swaters et al., 2003, Kuzio de Naray et al., 2006, Kuzio de Naray et al., 2008].

It is worth to note that the large LSB galaxy Malin 1 (see e.g. [Bothun et al., 1997]) is not part of our study because it seems to deserve separate considerations. Malin 1 appears as a HSB disc embedded in a remarkably extended, optically faint, and gas-rich outer structure beyond its normal disc (see Fig. 3.3) [Barth, 2007, Boissier et al., 2016]. There are also some other complex structures that require a separate and accurate study [Saburova et al., 2019] like e.g. the giant LSB disc galaxy UGC 1378 (see Fig. 3.3) or the the Large Magellanic

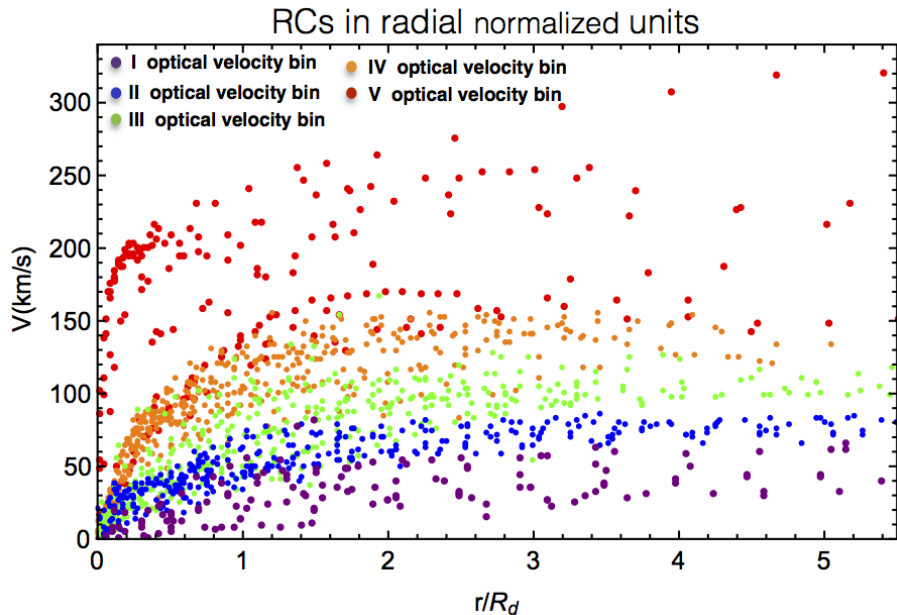


Figure 4.4: LSBs rotation curves (in normalised radial units) grouped in five optical velocity bins. In this and in the following figures, *purple*, *blue*, *green*, *orange* and *red* colors are referred to the rotation curves of the I, II, III, IV and V optical velocity bins, respectively. The average optical velocity in each bin is: $\langle V_{opt} \rangle = 43, 73, 101, 141, 206 \text{ km/s}$, respectively. [Di Paolo et al., 2019a].

Cloud [Nidever et al., 2019].

4.3 LSBs mass modelling results from the URC method

In [Di Paolo et al., 2019a] (PAPER 1 in Chapter 7), we apply the URC method to the 72 rotating disc galaxies introduced in the above sections. Among the first steps, the URC method [Persic et al., 1996] requires to make the galaxies RCs as similar as possible (in radial extension, amplitude and profile) by introducing the normalisation of their coordinates and an eventual galaxies binning. Let us notice that the justification for these starting steps comes from the analogous process performed in spirals and from a *qualitative* inspection of LSB RCs. Finally, the goodness of the results will show the goodness of the method.

In the following we briefly describe the URC method, applied to our LSB sample (for further details see [Di Paolo et al., 2019a]). The 72 RCs are arranged in 5 optical velocity bins according to their increasing V_{opt} as in Fig. 4.4; then, by normalising the radial units with respect to their disc scale length R_d , their radial extensions are made more similar. Indeed, most of the data are extended up to $\simeq 5.5R_d$. Furthermore, the RCs are comparable also in their amplitude when expressed in double normalised units, by dividing their

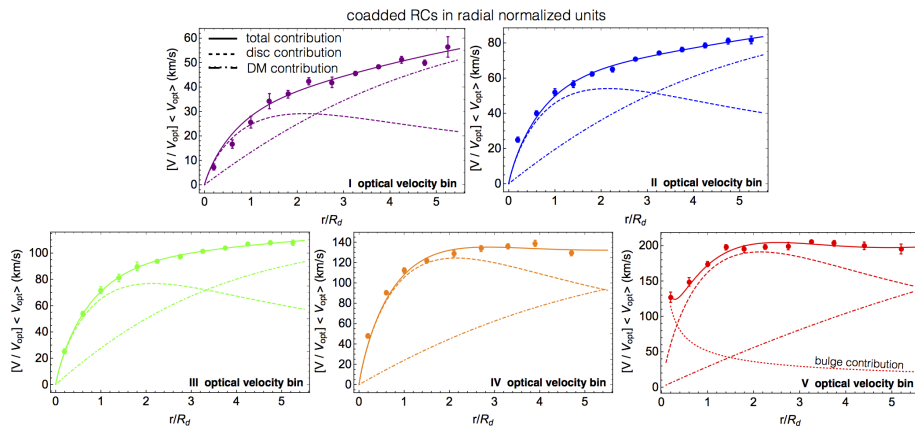


Figure 4.5: In each of the five panels the velocity best-fit models to the corresponding coadded RCs are shown. The *dashed*, *dot-dashed*, *dotted* and *solid* lines indicate the stellar disc, the DM halo, the stellar bulge and the model contribution to the circular velocities.

amplitude V with respect to their own optical velocity V_{opt} .

Overall, the optical velocity binning and the double normalisation makes the RCs more similar in each of the five optical velocity bins. After that all the RCs are double normalised, we perform a *radial binning* in each of the five *optical velocity bins* and we evaluate the average velocity value in each radial bin, giving rise to five *coadded* rotation curves.

In short, the above coadded RCs can be considered as the average rotation curves of galaxies of similar properties as, e.g., V_{opt} . Particularly, the binning in five groups is suggested by the fact that, since the sample includes 72 objects, 10-15 galaxies are the minimum number in each optical velocity bin in order to create suitable coadded RCs (that will be described in the next paragraphs) and to eliminate statistically observational errors and small non circularities from the individual RCs. Similarly to the velocity binning process, we have chosen the number of the normalised radial bins as a compromise between having a large number of data for each radial bin and a large number of radial bins for each coadded RC. Reasonable variations of the positions and amplitudes of the radial bins do not affect the resulting coadded RCs.

It is worth emphasizing the advantages of these RCs: their building erases the peculiarities and much reduces the observational errors of the individual RCs. This yields to a universal description of the kinematics of LSBs by means of 5 extended and smooth RCs whose values have an uncertainty at the level of 5% – 15%.

Then, by multiplying the previous coadded RCs by the corresponding $\langle V_{opt} \rangle$ (evaluated in each optical velocity bin from the individual galaxies), we obtain the coadded RCs shown in Fig. 4.5. The difference in the profiles corresponding to galaxies with different optical velocities is evident. This is explained by the very different luminous and dark mass distributions in LSBs of different sizes and optical velocities, as shown in the following by means of the *mass modelling*.

We model the coadded RCs data, as in normal spirals [Salucci et al., 2007],

with an analytic function $V(r)$ which includes the contributions from the stellar disc V_d and from the DM halo V_h ; for the fifth optical velocity bin (related to the largest LSBs) we also introduce a bulge component V_{bu} ([Morelli et al., 2012, Das, 2013]). The analytic functions take the expressions used in the previous section: Eq. 2.3 for the stellar exponential disc (leaving the mass of the stellar disc M_d as a free parameter), Eq. 2.6 for the stellar bulge, Eq. 2.8-2.9 for the spherical DM halo, finally the total RCs amplitude $V(r)$ is given by the sum in quadrature of the various contribution according to Eq. 2.1.

Let us stress that in first approximation the inclusion in the model of a HI gaseous disc component can be neglected. In fact, the gas contribution is usually a minor component to the circular velocities, since the inner regions of galaxies are dominated by the stellar component and in the external regions, where the gas component overcomes the stellar one, the DM contribution is largely the most important [Evoli et al., 2011]. A direct test in [Di Paolo et al., 2019a](Appendix F) shows that our assumption does not affect the mass modelling in this work.

Concerning the dark matter component, the presence of cored profiles in LSBs is well known from individual rotation curves (see e.g. [de Blok et al., 2001, de Blok and Bosma, 2002, Kuzio de Naray et al., 2008], [Bullock and Boylan-Kolchin, 2017]). In [Di Paolo et al., 2019a], we model the DM halo profile by means of the *cored Burkert profile* ([Burkert, 1995, Salucci and Burkert, 2000]). This halo profile has an excellent record in fitting the actual DM halos around disc systems of any luminosity and Hubble Types (see [Salucci, 2019]; [Lapi et al., 2018], [Memola et al., 2011], [Salucci et al., 2012]). In addition, the Burkert profile is in agreement with weak lensing data at virial distances [Donato et al., 2009].

It is however worth noticing that there is no sensible difference, in the mass modelling inside R_{opt} , in adopting different cored DM density profiles [Gentile et al., 2004]. Then, the Burkert density profile is adopted in modelling the LSBs rotation curves.

By fitting the five coadded RCs by means of the URC model described above, we obtain for each coadded RC the best values of three free parameters: the mass of the stellar disc M_d , the central constant density of the DM halo ρ_0 and its core radius r_0 . The evaluation of these parameters allows us also to evaluate the baryonic and the DM contribution to the total velocity rotation curves $V(r)$, as shown in Fig. 4.5.

In Fig. 4.5 we realise that, in the inner regions of the LSB galaxies, the stellar component (dashed line) is dominant; while, on the contrary, in the external regions, the DM component (dot-dashed) is the dominant one. Moreover, the transition radius¹ between the region dominated by the baryonic matter and the region dominated by the dark matter increases with the normalised radius when we move from galaxies with the lowest V_{opt} to galaxies with the highest V_{opt} . A similar behaviour was also observed in normal spiral galaxies ([Persic et al., 1996, Lapi et al., 2018]).

Particularly, we can quantify the baryonic fraction as function of the radial coordinate through the ratio between the baryonic contribution to the circular velocity and the total contribution:

$$f_b(r) = V_b^2(r)/V^2(r) \quad , \quad (4.1)$$

¹The *transition radius* is the radius where the DM component, dot-dashed line, overcomes the luminous component, dashed line.

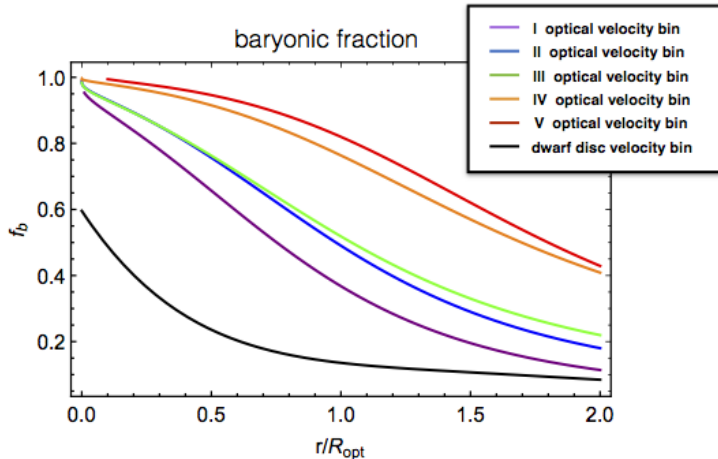


Figure 4.6: Baryonic fraction as function r/R_{opt} , derived by the URCs of *dd* (black line, with $\langle V_{opt} \rangle = 40 \text{ km/s}$) [Karukes and Salucci, 2017] and of LSBs (purple, blue, green, orange and red, with: $\langle V_{opt} \rangle = 43, 73, 101, 141, 206 \text{ km/s}$) [Di Paolo et al., 2019a].

where the baryonic contribution $V_b^2(r) = V_d^2(r) + V_{HI}^2(r) + V_{bu}^2(r)$ takes into account the stellar disc, (eventually) the gaseous disc and stellar bulge respectively. The total contribution $V^2(r) = V_b^2(r) + V_h^2(r)$ includes the baryonic plus the dark matter component. The baryonic fraction as function of the normalised radius r/R_{opt} is shown in Fig. 4.6, where the coloured curves refer to the five LSBs coadded RCs and the black one refers to the unique coadded RC for the dwarf disc galaxies studied by [Karukes and Salucci, 2017].

4.4 LSBs scaling laws

The mass models provided us with the structural parameters of the five coadded RCs. They allow us to build the scaling relations characterising the LSB galaxies and to retrieve the properties from the individual RCs by means of a *denormalisation* method, described in detail in [Di Paolo et al., 2019a]. The resulting structural properties are reported in Tab. G1-G2 in [Di Paolo et al., 2019a] in Chapter 8. In the following, our results are compared to those obtained in the URC analysis of normal spirals [Lapi et al., 2018] and dwarf disc galaxies [Karukes and Salucci, 2017].

4.4.1 Structural relationships

A particularly relevant relationship is shown in Fig. 4.7 (left panel): the stellar disc scale length and the DM core radius of the five velocity models are strongly correlated. The best linear fit in logarithmic scale is:

$$\text{Log } r_0 = 0.60 + 1.42 \text{ Log } R_d \quad , \quad (4.2)$$

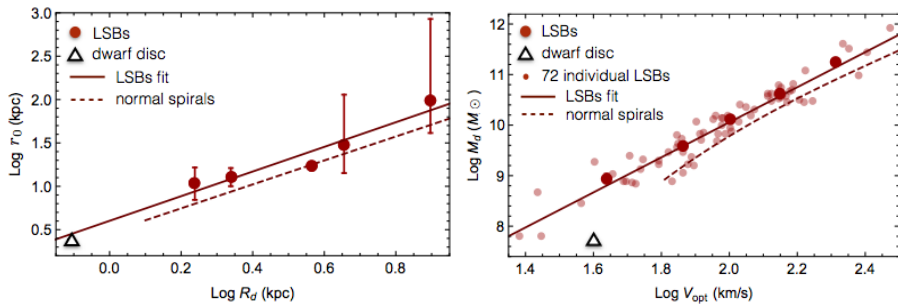


Figure 4.7: Relationship between the DM halo core radius and the stellar disc scale length (*left panel*) and relationship between the stellar disc mass and the optical velocity (*right panel*). The *large points* refer to the values of the five velocity bins, while the *small points* refer to the values of each LSB galaxy. The LSBs best fit (*solid line*) is compared to that of the normal spirals (*dashed line*) (e.g. [Lapi et al., 2018]). The black empty triangle represents the relationship in dwarf disc galaxies [Karukes and Salucci, 2017].

The found result is comparable to that of previous works ([Persic et al., 1996, Karukes and Salucci, 2017, Lapi et al., 2018]) and highlights a relevant entanglement between the luminous matter and the dark matter in galaxies of different type.

Then in Fig. 4.7 (right panel) the relation between the stellar disc mass and the optical velocity is shown. The LSB data are well fitted by:

$$\text{Log } M_d = 3.12 + 3.47 \text{ Log } V_{opt} \quad . \quad (4.3)$$

This relationship, analogous to the Tully-Fisher relation, is also comparable to the normal spirals' one (with an average difference of 0.2 dex), while it differs a bit from the dwarf disc data (0.7 dex).

Next, in Fig. 4.8 (left panel) we show the relation between the DM halo central density and the core radius, which indicates that the highest mass densities are in the smallest galaxies, as also found in normal spirals [Salucci et al., 2007]. We find:

$$\text{Log } \rho_0 = -23.15 - 1.16 \text{ Log } r_0 \quad . \quad (4.4)$$

It is worth to note that the LSB best fit line lies 0.2 dex below the HSB one. Despite the error-bars, probably this could be linked to an original DM density lower in LSBs than in HSBs. Moreover, we find that the central surface density follows the relationship:

$$\text{Log } \Sigma_0 = \text{Log } (\rho_0 r_0) \simeq 1.9 \quad , \quad (4.5)$$

Σ_0 is expressed in units of M_\odot/pc^2 . See Fig. 4.8 (right panel). Remarkably, this relationship extends itself over 18 blue magnitudes and in objects spanning from dwarf to giant galaxies ([Spano et al., 2008, Gentile et al., 2009, Donato et al., 2009, Plana et al., 2010, Salucci et al., 2012, Li et al., 2019, Chan, 2019]).

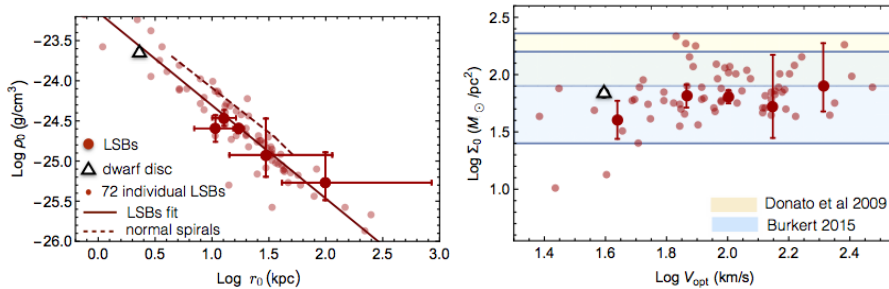


Figure 4.8: *Left* panel: the relationship between the central DM halo mass density and its core radius. *Right* panel: surface density $\Sigma_0 = \rho_0 R_c$ versus their optical velocities V_{opt} (LSBs in red points). Also shown the scaling relation obtained by [Donato et al., 2009] (yellow shadowed area) and [Burkert, 2015] (light blue shadowed area). The black empty triangle represents the dwarf discs [Karukes and Salucci, 2017].

This result is hard to explain, unless a fine-tuned process in galaxy formation or some unknown interaction exists, because it is a priori difficult to envisage such relation (Eq. 4.5) across galaxies that have experienced significantly different evolutionary histories, including numbers of mergers, baryon cooling or feedback from supernova-driven winds [Gentile et al., 2009].

We find positive correlation between the mass of the stellar disc M_d and the stellar disc scale length R_d (Fig. 4.9), described by the best fitting equation:

$$\text{Log } R_d = -3.19 + 0.36 \text{Log } M_d \quad (4.6)$$

Analogously, we find a positive correlation also between the mass of DM halo M_{vir} ² and the core radius r_0 (Fig. 4.9), described by the following best fitting equation:

$$\text{Log } r_0 = -5.32 + 0.56 \text{Log } M_{\text{vir}} \quad (4.7)$$

Then, we consider the baryonic fraction (complementary to the DM fraction) relative to the entire galaxies, namely, the ratio between the stellar mass $M_* \equiv M_d$ in LSBs and the virial mass M_{vir} , that practically represents the whole dark mass of a galaxy. Fig. 4.10 shows that the lowest fraction of baryonic content is in the smallest galaxies (with the smallest stellar disc mass M_d). We note that this ratio increases going towards larger galaxies and then reaches a plateau from which it decreases for the largest galaxies. This finding is in agreement with the inverse “U-shape” of previous works relative to normal spirals [Lapi et al., 2018]. Furthermore, our result seems to follow a trend similar to that found in [Moster et al., 2010, Moster et al., 2013], concerning all Hubble

²The virial mass M_{vir} is evaluated according to the usual relation $M_{\text{vir}} = \frac{4}{3} \pi 100 \rho_{\text{crit}} R_{\text{vir}}^3$, where R_{vir} is the virial radius and $\rho_{\text{crit}} = 9.3 \times 10^{-30} \text{g/cm}^3$ is the critical density of the Universe.

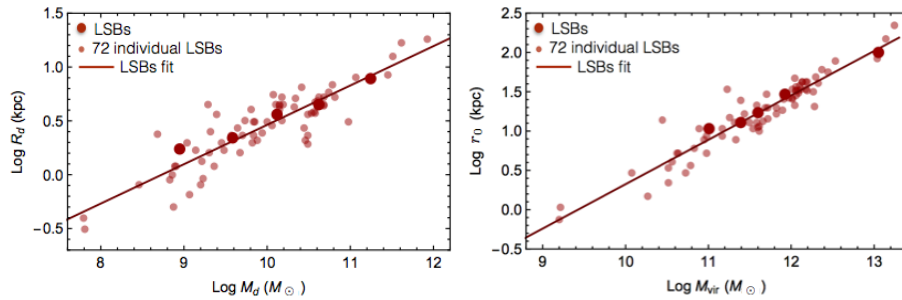


Figure 4.9: *Left panel:* relationship between the stellar disc scale length and the stellar disc mass. *Right panel:* relationship between the DM halo core radius and the virial mass.

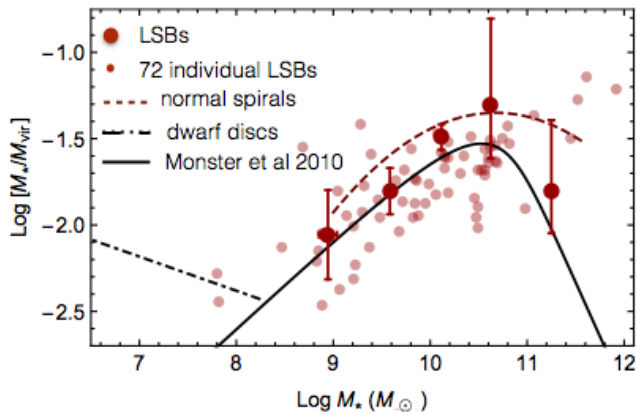


Figure 4.10: Fraction of baryonic matter in LSBs versus their mass in stars (*points*) compared with that of normal spirals (*dashed line*) [Lapi et al., 2018], of other Hubble Types (*black solid line*) [Moster et al., 2010] and of dwarf discs (*black dot-dashed line*) [Karukes and Salucci, 2017].

Types ³, including a large number of elliptical galaxies for higher M_* . Our result points to a less efficient star formation in the smallest LSBs.

4.4.2 Comparison between the results from individual and stacked (URC) LSBs analysis

Overall, the relationships found from the URC method in [Di Paolo et al., 2019a] are quite in agreement with the results found in previous works by means of individual modelling of the LSBs rotation curves (see Fig. 4.2-4.3). The differences are mainly due to the two involved DM profiles, Burkert in the URC analysis and pseudo-isothermal in the individual RCs analysis. Indeed, their differences affect the evaluation of the galaxies structural parameters, especially when the

³In [Moster et al., 2010], the stellar mass M_* can indicate the mass enclosed in a disc and/or in a bulge).

RCs data are extended up to $\simeq 2 R_{opt}$ (as in the LSB sample case).

Moreover, in most cases, the authors of the individual RCs analysis made use of maximum disc model, population synthesis model or minimum disc model, in order to take into account the stellar component, while in the URC method we leave a free parameter (the mass of the stellar disc M_d , assuming an exponential Freeman disc) linked to the stellar disc contribution. Consequently, also the DM halo parameters are affected by the above choice in the RCs fit, giving different final results.

Then, the scatter between our URC results and the previous ones from individual RCs analysis has also to be found in the low statistics: the URC method involved 72 galaxies and they are compared to the results of only ~ 30 of them analysed individually⁴.

Finally, we should also consider that the spread of data in the plots of Fig. 4.2-4.3 can be due to the relevance of a new parameter, the *compactness*, that will be dealt with in Section 4.6.

4.5 Angular momentum

The LSB data allow us to evaluate the specific angular momentum (per unit mass) of the stellar component j_* by means of the relation $j_* = 2f_R R_d V_{opt}$ (see [Romanowsky and Fall, 2012]), where $f_R = \int dx x^2 e^{-x} V(x R_d) / 2V_{opt}$ is the shape factor (of order unity). In Fig. 4.11 (right panel), we show the relationship between j_* and mass of the stellar disc M_d :

$$\text{Log } j_* = -3.51 + 0.62 \text{ Log } M_d \quad . \quad (4.8)$$

The LSB relation is in agreement with the results obtained for normal spirals [Lapi et al., 2018] and with the relation with fixed slope $j_* \propto M^{2/3}$ for pure discs (*black line*) by [Romanowsky and Fall, 2012].

Then, we can evaluate the specific angular momentum of the DM halo j_h . It is defined as (see [Mo et al., 1998, Mo et al., 2010]) $j_h = \sqrt{2} \lambda R_h V_h$, where $R_h \equiv R_{vir}$, V_h is given by the relation $V_h^2 = G M_{vir} / R_{vir}$ and λ is the spin parameter of the host DM halo, with an average value $\langle \lambda \rangle \approx 0.0035$ nearly independent of mass and redshift (from numerical simulation [Barnes and Efstathiou, 1987, Bullock et al., 2001, Macciò et al., 2007, Zjupa and Springel, 2017]). Particularly, the fraction between the j_* and j_h allow us to find the amount of the halo angular momentum retained by the stellar component:

$$f_j = \frac{j_*}{j_h} \simeq 0.55 \quad . \quad (4.9)$$

This quantity is nearly constant in the whole LSB sample, with individual values ranging from 0.45 to 0.7. According to the standard and the simplest theory of disc formation, the sharing and conservation of angular momentum between baryons and DM should imply $f_j \approx 1$ (see e.g. [Romanowsky and Fall, 2012]). However, the found value for LSBs is lower, as well as the result from normal spirals $f_j \simeq 0.8$ [Lapi et al., 2018]. From a theoretical perspective, f_j values

⁴Sometimes, the same galaxies are studied by different authors and with multiple approaches in treating the stellar disc contribution. This is the reason of a number of data > 30 referred to the individual analysis in Fig. 4.2-4.3.

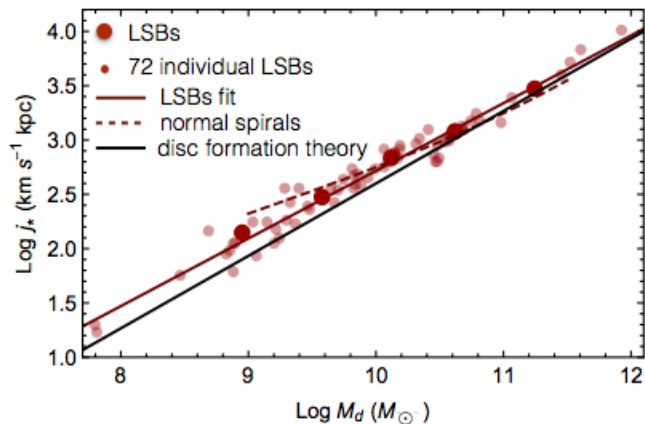


Figure 4.11: LSBs stellar specific angular momentum (*points*) and best fit (*solid red line*) compared to the normal spirals results (*red dashed line*) [Lapi et al., 2018] and to the relation $j_* \propto M_d^{2/3}$ for pure discs (*black line*) by [Romanowsky and Fall, 2012].

below 1 can be due to inhibited collapse of the high angular momentum gas located in the outermost region ([Fall, 1983, Shi et al., 2017]). Likely, in spirals the inhibition is due to the stellar feedback processes (similarly also in Elliptical galaxies, where the processes are especially strong and the biased collapse is also involved) [Shi et al., 2017, Posti et al., 2018]. Probably, in LSBs the inhibition of the high angular momentum gas collapse is mainly due to the very low gas surface density and the (consequently) slow star formation, without involving the very external region of galaxies.

4.6 The compactness in LSBs

We note that the above relationships show a large scatter, on average $\sigma \simeq 0.34$ dex, more than three times the value ($\sigma \simeq 0.1$ dex in [Lapi et al., 2018], [Yegorova and Salucci, 2007]) found in normal spiral galaxies for the respective relations.

We can reduce the scatter in the LSBs scaling relations and proceed with the URC building by introducing a new parameter, the *compactness* of the stellar mass distribution C_* . This parameter was first put forward in [Karukes and Salucci, 2017] to cope with a similar large scatter in the above scaling relations of the *dd* galaxies. In short the large scatter in the previous relationships is due to the fact that galaxies with the same stellar disc mass M_d (or V_{opt}) can have a very different size for R_d (i.e. $\text{Log } R_d$ can vary almost 1 dex). We define this effect with the fact that LSBs have a different “stellar compactness” C_* ; see Fig. 4.1 and Fig. 4.9 (left panel). We define C_* starting from Eq. 4.6 (see left panel in Fig. 4.9) and, according to [Karukes and Salucci, 2017], we set the stellar compactness through the following relation:

$$C_* = \frac{10^{(-3.19+0.36 \text{Log } M_d)}}{R_d} \quad , \quad (4.10)$$

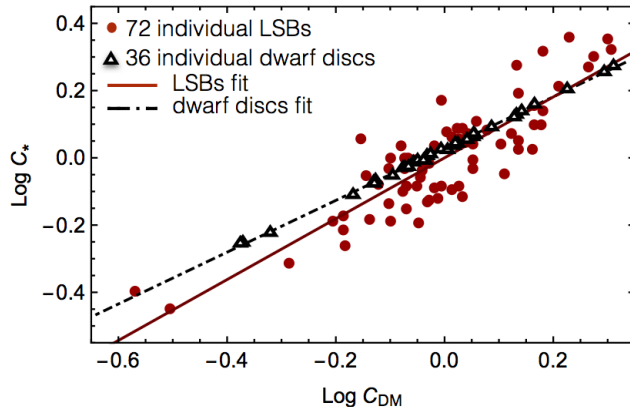


Figure 4.12: Relationship between the compactness of the stellar disc and the compactness of the DM halo (*red points*). The black triangles refer to the dwarf discs of [Karukes and Salucci, 2017]. The solid and the dot-dashed lines are the best fit relations for LSBs and dwarf discs.

where, let us remind, R_d is measured from photometry. By means of Eq. 4.10, C_* measures, for a galaxy with a fixed M_d , the deviation between the observed R_d and the “expected” R_d value from Eq. 4.6 (obtained by using the best fit line in Fig. 4.9). In short, at fixed M_d , galaxies with the smallest R_d have a high compactness ($\text{Log } C_* > 0$), while galaxies with the largest R_d have low compactness ($\text{Log } C_* < 0$).

The previous average scatter $\sigma \simeq 0.34$ dex of the 2D relations is reduced to $\sigma \simeq 0.06$ dex when we also add the third variable C_* . The resulting scatter is smaller than the typical values obtained for normal spirals (see [Di Paolo et al., 2019a] for further details).

Finally, in analogy to C_* , we evaluate also the *compactness of the DM halo* C_{DM} , i.e. we investigate the case in which the galaxies with the same virial (dark) mass M_{vir} exhibit different core radius r_0 . The M_{vir} vs r_0 relationship is shown in Fig.4.9(right panel) alongside with the best fit linear relation, described by Eq. 4.7. Then, according to [Karukes and Salucci, 2017], we define the compactness C_{DM} of the DM halo as:

$$C_{DM} = \frac{10^{(-5.32+0.56 \text{Log } M_{vir})}}{r_0} \quad , \quad (4.11)$$

taking into account Eq. 4.7. Thus, at fixed M_{vir} , galaxies with smaller r_0 have higher compactness ($\text{Log } C_{DM} > 0$), while galaxies with larger r_0 have lower compactness ($\text{Log } C_{DM} < 0$).

Then, we plot the compactness of the stellar disc versus the compactness of the DM halo in Fig. 4.12. We note that C_* and C_{DM} are strictly related: galaxies with high C_* , also have high C_{DM} . The logarithmic data are well fitted by the linear relation:

$$\text{Log } C_* = 0.00 + 0.90 \text{Log } C_{DM} \quad . \quad (4.12)$$

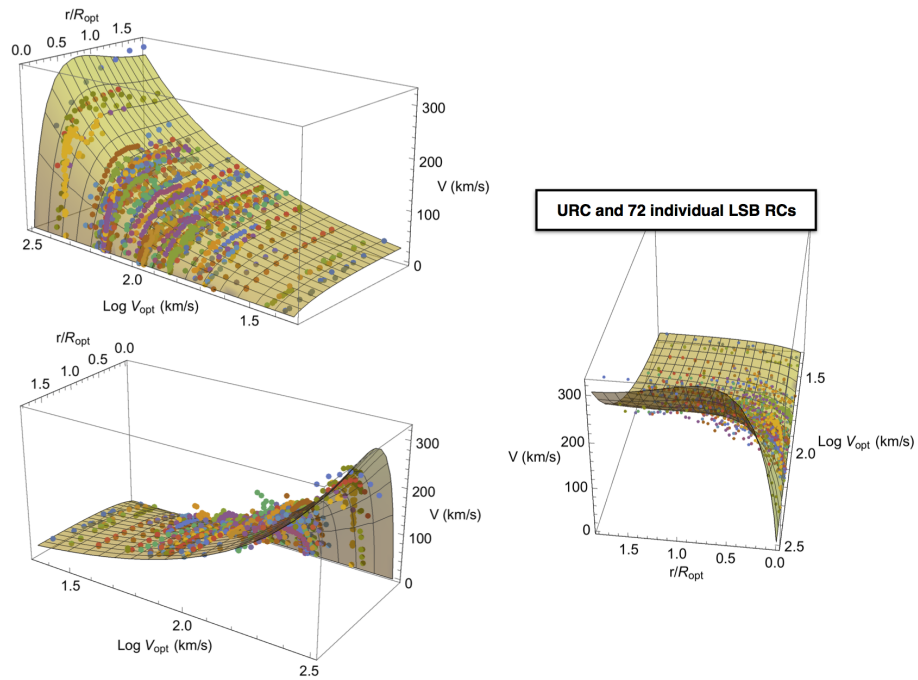


Figure 4.13: LSBs universal rotation curve (URC), with compactness $\text{Log } C_* = 0$, and the individual 72 LSBs rotation curves.

The results are in very good agreement with those obtained for *dd* galaxies [Karukes and Salucci, 2017], whose best-fitting relation is given by: $\text{Log } C_* = 0.77 \text{Log } C_{DM} + 0.03$. In the figure we realize that the average difference between the two relationships is just about 0.1 dex.

This result is remarkable because the same relation is found for two very different types of galaxies (LSBs and *dds*). The strong relationship between the two *compactnesses* certainly indicates that the stellar and the DM distributions follow each other very closely.

4.7 The LSBs universal rotation curve

Finally, we establish $V_{URC}(r; R_{opt}, V_{opt}, C_*)$, the URC-LSB in physical units, as in [Persic et al., 1996] but with the inclusion of the new parameter C_* . Straightforwardly, we find a universal function $V_{URC}(r/R_{opt}, V_{opt}, C_*)$.

This is easily evaluated by expressing M_d , R_d , r_0 and ρ_0 as function of V_{opt} and C_* from the analysis of the LSBs data. The above quantities put in Eq. 2.1, which involves Eq. 2.3-2.8-2.9, give rise to the analytic expression for the

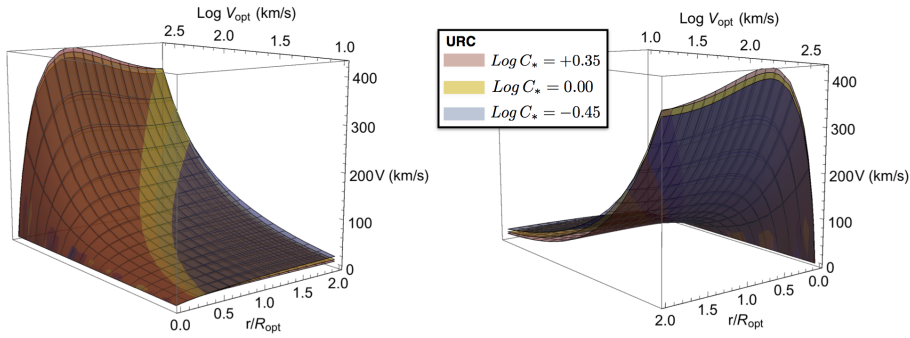


Figure 4.14: Universal rotation curves (URC) in physical velocity units for three different values of stellar compactness; low ($\text{Log } C_* = -0.45$), standard ($\text{Log } C_* = 0.00$) and high ($\text{Log } C_* = +0.35$) stellar compactness, respectively in *blue*, *yellow* and *red* colors. The figure in the second panel corresponds to that of the first panel when rotated by 180° around the velocity axis.

universal rotation curve (expressed in physical units):

$$\begin{aligned}
 V^2(x, V_{opt}, C_*) &= 2.2 x^2 \times 10^{f_1(V_{opt}, C_*)} \times [I_0 K_0 - I_1 K_1] & (4.13) \\
 &+ 1.25/x \times 10^{f_2(V_{opt}, C_*)} \times \\
 &\{ -tg^{-1}[3.2 x \times 10^{f_3(V_{opt}, C_*)}] \\
 &+ \ln[1 + 3.2 x \times 10^{f_3(V_{opt}, C_*)}] \\
 &+ 0.5 \ln[1 + 10.24 x^2 \times 10^{2 f_3(V_{opt}, C_*)}] \} \quad ,
 \end{aligned}$$

where I_n, K_n are the modified Bessel functions evaluated at $1.6x$, with $x = r/R_{opt}$, and $f_1(V_{opt}, C_*) = 9.79 + 2.39 \text{Log } V_{opt} + 0.05 \text{Log } C_*$, $f_2(V_{opt}, C_*) = -0.55 + 2.65 \text{Log } V_{opt} - 1.67 \text{Log } C_*$, $f_3(V_{opt}, C_*) = 0.35 - 0.58 \text{Log } V_{opt} + 0.65 \text{Log } C_*$. In Fig. 4.13 we plot the URC (Eq. 4.13) considering $\text{Log } C_* = 0$, corresponding to the case in which all the LSBs data in Fig. 4.9 were lying on the regression line (or, analogously, the case in which the spread of LSBs data in Fig. 4.1 was small). The curve shown in Fig. 4.13 is in good agreement with the LSBs rotation curves data. On average, the uncertainty between the velocity data and the URC velocity predicted values is $\Delta V/V \simeq 19\%$, which can be reduced to $\Delta V/V \simeq 8\%$, when the observational errors, the systematics, the small non circularities and the prominent bulge component are taken into account in the individual RCs. This result, approximately equal to that found in normal spirals [Persic et al., 1996], highlights the success of the URC method also in LSBs galaxies.

Finally, in Fig. 4.14 we show the URC obtained with three significant different values of stellar compactness. The central yellow surface has $\text{Log } C_* = 0.00$ (standard case) and the other two surfaces have $\text{Log } C_* = -0.45$ (the minimum value achieved in the LSB sample) and $\text{Log } C_* = +0.35$ (the maximum one). The three surfaces appear similar: the differences between the URC with $\text{Log } C_* = 0.00$ and the URC with the appropriate values of C_* for each individual object lie within the URC errorbars for most of the objects. See Fig.

I1-I2-I3-I4-I5 in [Di Paolo et al., 2019a] in Chapter 8, where all the 72 RCs are plotted alongside their URC fit highlighting the success of the URC method on individual rotation curves, as also for *dd* galaxies in [Gammaldi et al., 2018] and for HSB spirals in [Yegorova and Salucci, 2007] by means of the radial Tully-Fisher relation (see also [Fune, 2018]).

Completing our analysis, we have discovered the relevance of C_* in the LSB galaxies. By resumming:

- i)* the compactness is linked to the spread in the $V_{opt} - R_d$ plot (Fig 4.1). Galaxies at fixed V_{opt} can have smaller R_d (higher C_*) or larger R_d (lower C_*) than the average. The range of $\text{Log } R_d$ at fixed V_{opt} can reach almost 1 dex;
- ii)* the compactness is a main source for the large scatter ($\sigma \simeq 0.34$) in the 2D scaling relations (see Fig. 4.7-4.8);
- iii)* the profiles of the various RCs can be affected by the compactness (see e.g. Fig. 4.4). Thus, the spread in the profiles of the RCs in each velocity bin, is not only due to the large width of the optical velocity bins, but it is also due to the different values of the galaxies compactness.

Taking all this into account, we point out that in the URC-LSB building procedure, having an improved statistic, the optimal approach would be considering from the start to bin the available RCs in C_* (obtained by the spread of data in the $V_{opt} - R_d$ plot in Fig. 4.1) contemporaneously to V_{opt} . Moreover, with a sufficiently higher statistics, we can also increase the number of the velocity bins and characterise each of them with a smaller V_{opt} range to reach the performance of [Persic et al., 1996].

Finally, the LSBs URC provides us with the best observational data to test specific density profiles (e.g. NFW, WDM, Fuzzy DM) or alternatives to dark matter (e.g. MOND). Any mass model under test must reproduce scaling relations among the luminous matter and the DM properties not only dependent on the optical velocity V_{opt} , as in the normal spirals case, but also dependent on the stellar compactness C_* .

Chapter 5

Low Surface Brightness galaxies and the gravitational acceleration

The LSB galaxies, together with the dwarf disc galaxies, turn out to be important in order to establish a universal relation between the radial gravitational acceleration g , its baryonic component g_b and the normalised galactic radius $x \equiv r/R_{opt}$ where they are evaluated. The relation that we found shows that the result obtained in [McGaugh et al., 2016], involving a relationship between the only two quantities g and g_b , is a limiting case of a more extended relation and can be interpreted in terms of the distribution of the luminous and the dark matter in galaxies.

5.1 Test for g and g_b

In [Di Paolo et al., 2019b] (PAPER 2 in Chapter 8), the relation between the radial gravitational acceleration g and its baryonic component g_b in LSBs and in dwarf discs is analysed. It is found that the two quantities must be related also to the radial coordinate $x \equiv r/R_{opt}$ where they are evaluated, differently from the result found few years ago by [McGaugh et al., 2016], hereafter McG+16.

In rotating systems, the galaxy gravitational potential Φ_{tot} and the radial acceleration $g(r)$ of a point mass at distance r are linked by the following relationship:

$$g(r) = \frac{V^2(r)}{r} = \left| -\frac{d\Phi_{tot}(r)}{dr} \right| , \quad (5.1)$$

with $V(r)$ the circular velocity. The baryonic component of the radial acceleration is given by:

$$g_b(r) = \frac{V_b^2(r)}{r} = \left| -\frac{d\Phi_b(r)}{dr} \right| , \quad (5.2)$$

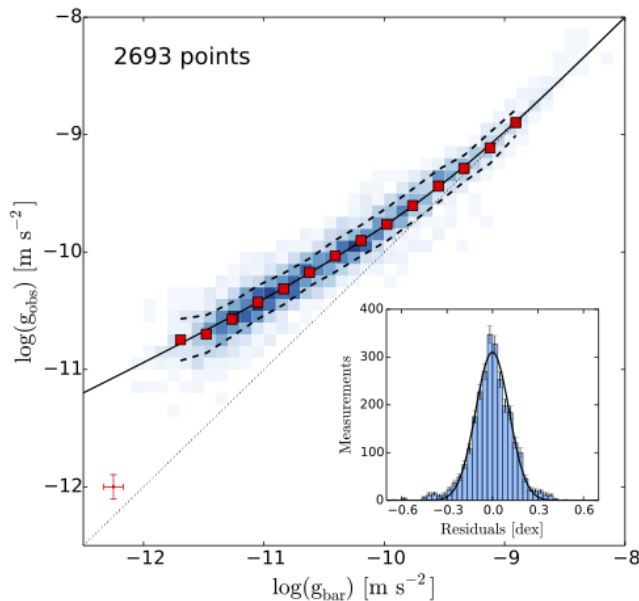


Figure 5.1: Relationship between the total acceleration g and its baryonic component g_b in disc galaxies found in [McGaugh et al., 2016]. Image reproduced from [McGaugh et al., 2016].

where V_b is the baryonic contribution to the circular velocity (see the previous section).

Obviously we have:

$$g_h(r) = g(r) - g_b(r) \quad , \quad (5.3)$$

where g_h refers to the dark matter contribution to the radial acceleration g . Notice that all these quantities depend on radius.

Particularly, in our work, we consider that in each galaxy with rotation curve $V(r)$, we have: $g(r) = V^2(r)/r$ and $g_b(r) = f_b(r)g(r)$, where $f_b(r)$ is the baryonic fraction assumed to be the same in galaxies belonging to the same optical velocity bin as in the URC method (see Fig. 4.6 in the previous section). Notice that $g(r)$ is totally observed, $g_b(r)$ has a part derived from the rotation curve.

The emerging g vs g_b results, obtained for *dd* and LSB galaxies, are shown in Fig 5.2 and compared to the McG+16 results coming from the analysis of 153 galaxies, mainly normal spirals. McG+16 found that the radial acceleration $g(r)$ shows an anomalous feature: it correlates at any radius and in any object, with its component generated from the baryonic matter $g_b(r)$ in a way that it is *i*) very different from the $g = g_b$ relationship expected in the Newtonian case with the presence of the only baryonic matter and *ii*) of difficult understanding in the standard Newtonian + dark matter halos scenario. In more detail, the

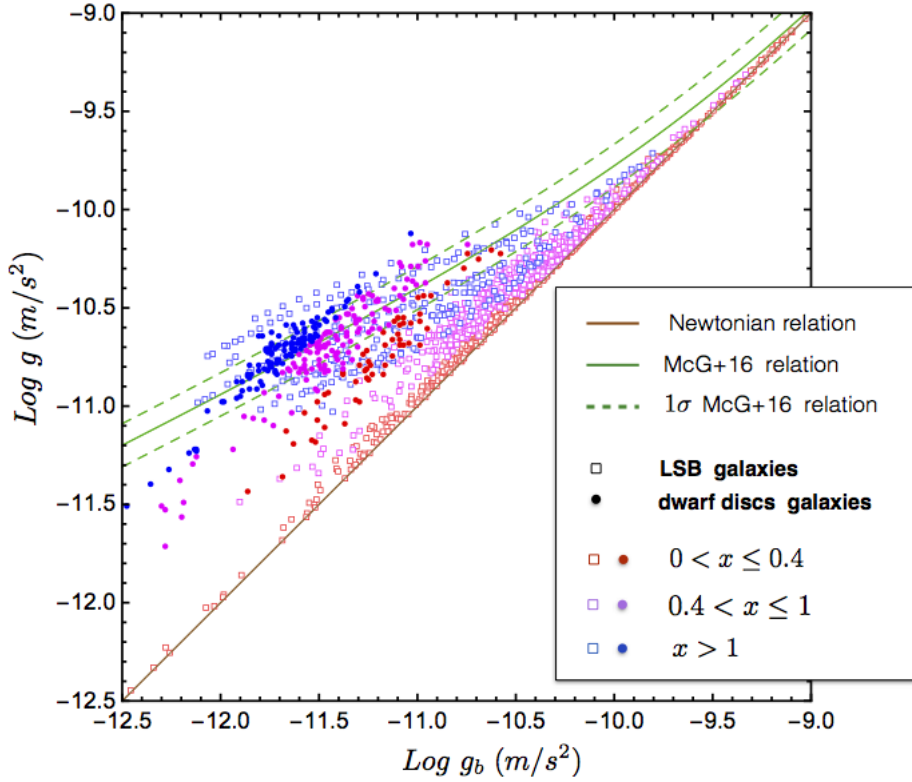


Figure 5.2: Relationship between the total acceleration g and its baryonic component g_b . $x = r/R_{opt}$. Red, magenta and blue points correspond to radial bins with increasing distance from galactic center (see legend). Also shown: the McGaugh et al. (2016) relationship (green line) [McGaugh et al., 2016] with its 1σ errorbars of 0.11 dex (dashed green lines); the Newtonian relationship $\text{Log } g = \text{Log } g_b$ (brown line).

pairs (g_b, g) found in their data analysis, are fitted by the following relationship:

$$g(r) = \frac{g_b(r)}{1 - \exp\left(-\sqrt{\frac{g_b(r)}{\tilde{g}}}\right)} \quad , \quad (5.4)$$

with $\tilde{g} = 1.2 \times 10^{-10} \text{ m s}^{-2}$. See Fig. 5.1. At high accelerations, $g \gg \tilde{g}$, Eq. 5.4 converges to the Newtonian relation $g = g_b$; while, at lower accelerations, $g < \tilde{g}$, Eq. 5.4 strongly deviates from the latter ([McGaugh et al., 2016, Li et al., 2018]). An analogous result is also found in [Salucci, 2018] (hereafter S18), analysing normal spirals with the same method described in the LSBs case.

In Fig. 5.2, we realise that the universality of the $g(g_b)$ relation, holding in normal spirals (McG+16, S18) breaks down in our samples. The scatters of *dd* and LSB data with respect to the McG+16 relation are 0.17 dex and 0.31 dex respectively. The data relative to inner radii of galaxies (red data) are the closest to the equality line $\text{Log } g = \text{Log } g_b$, while data relative to more external radii (blue data) of galaxies tend to depart from the equality line towards the region covered by McG+16 relation, with $\text{Log } g > \text{Log } g_b$. This is intrinsically related to the mass distribution in galaxies: the higher is the baryonic fraction f_b , the more g is close to g_b , and reversely the lower is f_b , the more g overcomes g_b . This interpretation will be deeply deal with in the following.

5.2 The GGBX relationship

We realise that a relationship between g and g_b necessarily must involve also the position x , where the two accelerations are measured, and the Hubble type of the objects. This is shown in our new 3D relationship, Eq. 5.5, (hereafter *GGBX* relation) among the $\text{Log } g - \text{Log } g_b - x$ quantities. Starting from the McG+16 relation (in order to have a straightforward comparison), we added new terms to find the best fitting model for LSB data. The best and simplest model that we found is:

$$\begin{aligned} \text{Log } g_{LSB}(x, \text{Log } g_b) &= (1 + ax) \text{Log } g_b \\ &+ b x \text{Log} [1 - \exp(-\sqrt{g_b(x)/\tilde{g}})] + cx + dx^2 \quad , \end{aligned} \quad (5.5)$$

where the fitting parameters a, b, c, d assume the best-fit values -0.95, 1.79, -9.01, -0.05 respectively. The scatter of LSB data from the fitting surface is considerably reduced, down to 0.05 dex, i.e. to a sixth of the scatter from the McG+16 relation. Let us notice that the model used in Eq. 5.5 is just an empirical function used to fit the data that recovers $\text{Log } g \rightarrow \text{Log } g_b$ when $x \rightarrow 0$.

In the case of *dd* galaxies, by simply applying translations and/or dilatations to Eq. 5.5 along the three involved axes, we obtain the following best fitting model:

$$\text{Log } g_{dd}(x, \text{Log } g_b) = \text{Log } g_{LSB} \left(\frac{x}{l} + h, \frac{\text{Log } g_b}{m} + n \right) + q \quad . \quad (5.6)$$

We found a perfect fit of the data when the fitting parameters l, h, m, n, q assume the best-fit values 0.49, 2.41, 0.74, 1.72, 1.19 respectively. The scatter

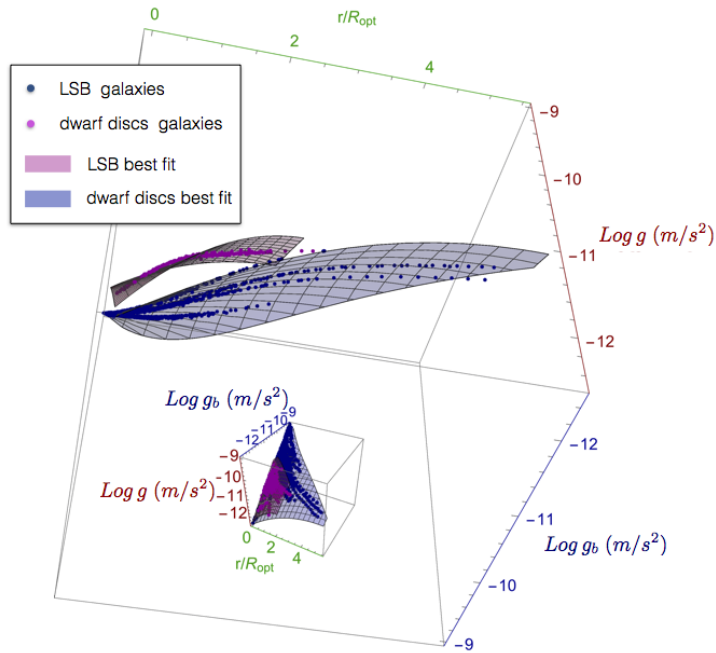


Figure 5.3: Relation among total acceleration g , baryonic acceleration g_b and normalised radii r/R_{opt} , from different angles. The *magenta* and *blue points* refer to *dd* and LSB galaxies data respectively. The *surfaces* are the results from the best fitting models.

of *dd* with respect to the fitting surface is considerably reduced, with a value of 0.03 dex, i.e. about a fifth of the scatter from the McG+16 relation.

We show in Fig. 5.3 the *dd* and LSB data in the $g - g_b - x$ space, with their best fitting surfaces from Eq. 5.5-5.6. The result is extremely remarkable. It shows a precise relation linking the total and baryonic acceleration, the galactocentric distance r/R_{opt} and even the morphology of galaxies. We highlight that all our results are intrinsically related to the *mass distribution in galaxies*, depending on the variation of the baryonic fraction $f_b(r)$ along the *galactocentric radius* and on the fact that $f_b(r)$ changes when we consider galaxies of different size and different Hubble Type.

In order to have a physical interpretation of the previous results, it's useful to study what happens in single galaxies when we consider their $g(r)$ and $g_b(r)$. Fig. 5.4 shows one *dd* galaxy and five LSB galaxies belonging to five different families (optical velocity bins) characterised by an increasing size. We note that:

i) larger galaxies, with larger optical velocity, achieve higher values of both the total and the baryonic acceleration (as also found in McG+16 and S18);

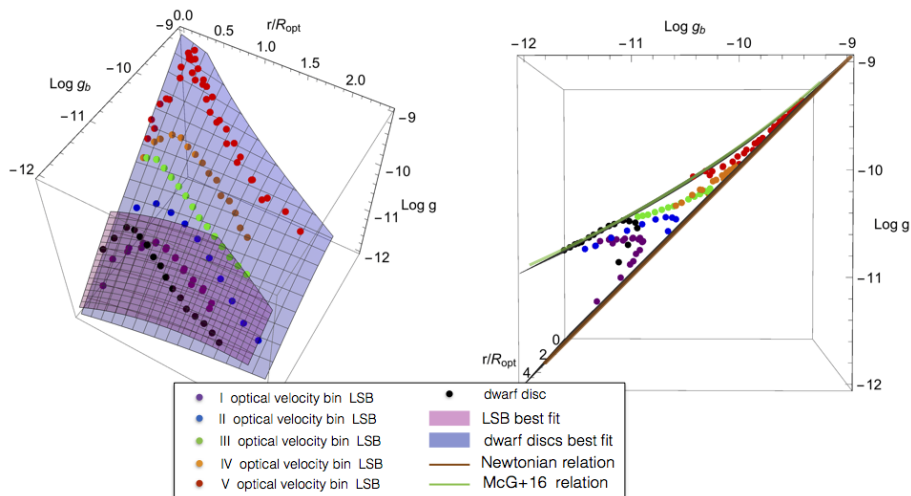


Figure 5.4: Relation among total acceleration g (in $m s^{-2}$), baryonic acceleration g_b (in $m s^{-2}$) and normalised radii r/R_{opt} , for one *dd* galaxy (black) and five LSB galaxies belonging to five different families (purple, blue, green, orange and red refer to galaxies families with increasing V_{opt}). The magenta and blue surfaces are the results from the *dd* and LSB fitting models (left panel); the uppermost green and the lowest brown surfaces are the McG+16 and the Newtonian relations (right panel).

ii) both the total and the baryonic acceleration, g and g_b , increase going from smaller to larger radii till $r \sim R_d$ ($= R_{opt}/3.2$) and decrease going beyond the stellar disc scale length. This is a direct consequence of the baryonic and the dark matter mass distribution in galaxies. Fig. 5.5 shows the behaviour of the baryonic component of the gravitational acceleration $g_b = f_b g$, of the dark matter halo component $g_h = (1 - f_b) g$ and of the total acceleration g as function of normalised radius r/R_{opt} . Because of the gravitational potential generated by the exponential stellar disc distribution and by the cored dark matter distribution, we expect to observe an increase of each acceleration component g_i ($i = b, h$) going from inner to external radii till the achievement of the typical scale radius R_i , which includes the bulk of the i -component at higher density. Beyond the typical scale radius, we expect that g_i decreases because of the lower and lower density of the i -component. This means that the baryonic component increases till the peak associated to the stellar disc scale length R_d and decreases for larger radii. Similarly, the dark matter component shows the peak around the halo core radius r_0 . Finally the relation for the total acceleration $\text{Log } g - r/R_{opt}$ comes simply from the sum of the previous components.

Note that the peak in $\text{Log } g - r/R_{opt}$ relation is usually close to R_d especially in large galaxies, as highlighted in the last panel of Fig.5.5. This is due to the high density and high fraction of the stellar component with respect to the DM one, i.e. due to the dominance of g_b (and g_b peak) over g_h (and g_h peak), in the region of available observable data. Instead, in small galaxies (see the first two panels in Fig.5.5), the peak in the $\text{Log } g - r/R_{opt}$ relation usually lies between the

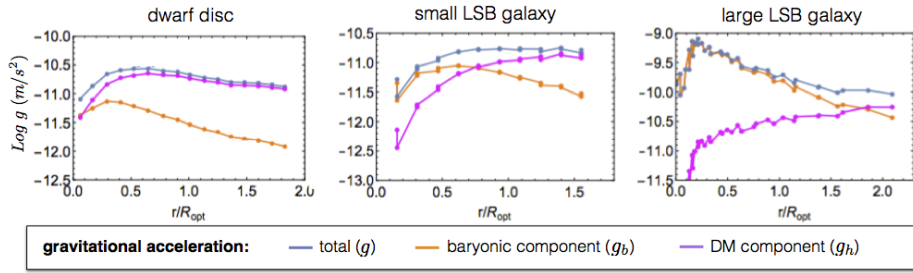


Figure 5.5: Relations between the normalised radii and the components of gravitational acceleration: $r/R_{opt} - \text{Log } g_b$ (orange line and points), $r/R_{opt} - \text{Log } g_h$ (magenta), $r/R_{opt} - \text{Log } g$ (blue), where g_b is the baryonic acceleration component, g_h is the dark matter halo component and g is the total acceleration. The results in the three panels are shown respectively for a dwarf disc galaxy ($V_{opt} = 55 \text{ km/s}$), for a small LSB galaxy ($V_{opt} = 37 \text{ km/s}$) and a large LSB galaxy ($V_{opt} = 240 \text{ km/s}$).

stellar and the dark matter typical scale lengths, R_d and $r_0 \sim R_{opt}$, because the dark matter density and fraction are quite relevant, i.e. both the g_b and the g_h peaks are important contributions and are responsible for the resulting smoothed peak of $\text{Log } g - r/R_{opt}$ relation. We underline that small galaxies are denser than the large ones and their DM core radius r_0 is close to the optical radius R_{opt} (see e.g. results in [Karukes and Salucci, 2017, Di Paolo et al., 2019a]);

iii) the deviation between g and g_b is more evident in smaller galaxies (compare the pictures of Fig. 5.5). This is again obviously due to the distribution of baryonic and dark matter; it is sufficient to see that the *transition radius*¹ between the region dominated by baryons and dark the region dominated by DM is located in very inner region if we consider small galaxies, while it lies in the most external region of the galaxies if we consider large galaxies (see Fig. 4.5). Indeed, we expect that the higher is the baryonic fraction f_b the more g is similar to g_b and, on the other hand, the higher is the DM fraction, the more g is detached from g_b with the additional relevant contribution by dark matter to the baryonic one ($g \gg g_b$);

iv) the variation of the difference between $\text{Log } g$ and $\text{Log } g_b$, evaluated in the radial range which spans from the innermost to the outermost observable region of a galaxy, is especially high when the baryonic fraction $f_b(r)$ decreases visibly in the same radial range (see Fig. 4.6-5.5). In simple words, a high decrease of baryonic fraction $f_b(r)$ implies a more and more relevant contribution of DM to the total gravitational acceleration g and obviously a more and more relevant deviation of g from g_b going from smaller to larger radii.

¹The *transition radius* is the radius where the DM component (dot-dashed line in Fig. 4.5), overcomes the luminous component, (dashed line in Fig. 4.5).

5.3 Consequences

From an analysis on individual galaxies, like those related to Fig. 5.4, a *boomerang* shape emerges in the $\text{Log } g - \text{Log } g_b - r/R_{opt}$ space. This can be easily interpreted in light of Fig. 5.5 and of the explanations given above: the peaks of the boomerangs, relative to single galaxies, are associated approximately to the disc scale length R_d of the stellar component. In the second picture of Fig. 5.4, if we move along the boomerangs from the $g \simeq g_b$ region to the upper region, where $g > g_b$, we are moving from the inner to the external radii of galaxies. Thus, the first side (the lowest) and the second side (the highest) of each boomerang are approximately related to the galactic region inside and outside R_d respectively.

Specifically, we note a *narrow boomerang* shape, related to large LSB galaxies (e.g. red points in the second picture of Fig. 5.4), due to a slight decrease of $f_b(r)$ around $R_d = R_{opt}/3.2$, as shown in Fig 4.6. Indeed, this corresponds to a slight increase of DM distribution, which gives a relatively small contribution to the gravitational acceleration and implies that $\text{Log } g$ slightly overcomes $\text{Log } g_b$, giving rise to a narrow boomerang. On the other hand, we find a *wide boomerang shape* in small LSB galaxies (e.g. purple points in the second picture of Fig. 5.4) due to a strong decrease of $f_b(r)$ around R_d . In fact, this corresponds to a fast increase of the dark matter fraction around R_d and, thus, to a relatively high contribution by DM to the gravitational acceleration, with the direct consequence that $\text{Log } g$ quickly overcomes $\text{Log } g_b$ (giving rise to a wide boomerang).

Moreover, taking into account the *dd* sample, we note that $g \gg g_b$ already starting from the inner galactic region, with $r < R_d$ (e.g. black points in the second picture of Fig. 5.4). The reason is the high fraction of dark matter in the innermost region of dwarf discs, as shown in [Karukes and Salucci, 2017]; thus the dark matter is already relevant in the innermost galactic region, giving an important contribution to the gravitational acceleration also in the inner region of galaxies, so that $g \gg g_b$. We also note a wide boomerang shape easily explainable with the same argumentation used above for the small LSB galaxies.

As consequence of the above observations, we deduce that:

- i)* first of all, in order to see the two boomerang sides it is necessary to have enough observative data both inside and outside the disc scale length R_d ;
- ii)* the narrow or wide boomerang shape (related to the slow or fast decrease of the baryonic fraction $f_b(r)$) are typical of large or small galaxies, respectively. Thus it's much simpler to recognise the boomerang shape (in the $\text{Log } g - \text{Log } g_b - r/R_{opt}$ space) in dwarf galaxies;
- iii)* given one spiral and one LSB, both with the same V_{opt} , they can show very different $f_b(r)$. Thus, a fixed value of g_b can often be found, in the spiral and in the LSB, at very different radii and can corresponds to very different values of g . This mainly explains the failure of the McG+16 relation in LSBs.

Chapter 6

Hints for a direct interaction between luminous and dark matter from structural properties of the LSBs

The analysis of the matter distribution in galaxies leads us to realise the profound interconnection which is present between the luminous component and the dark component, which are linked by tight scaling relations (see e.g. Section 4.4 and [Lapi et al., 2018]). Furthermore, galaxies of different morphologies seem to follow analogous scaling relations despite their different star formation history, as shown in Section 4.4.

It is especially of relevance the $r_0 - R_d$ relationship (left panel in Fig. 4.7), where the DM core radius r_0 and the stellar disc scale length R_d are derived in totally independent ways: the former by means of accurate mass modelling of galaxy kinematics, while the latter is directly derived from galaxy photometry. The strong correlation we see in Fig. 4.7 can hardly be arisen spuriously and is of difficult explanation in a collisionless DM scenario unless a fine-tuning in the baryonic-feedback process exists in galaxies with different size, morphology and star formation history (see also e.g. [Dutton et al., 2019]). Moreover, the difficulties are enhanced when we take into account the case of the largest LSBs (see the discussion in Section 1.3 and Chapter 3).

In the light of the above considerations, alongside the lack of detection of a collisionless DM particle (the WIMP particle, which is the main candidate in the Λ CDM scenario, has not yet been detected), we are motivated to suppose that the dark and the luminous components can have interacted in a direct way, other than through gravity, over the Hubble time in the inner regions of galaxies (Salucci et al. in prep.). Furthermore, this hypothesis could easily explain other observations related to the DM halo properties and other general open problems in astrophysics and cosmology, as shown in the next subsection.

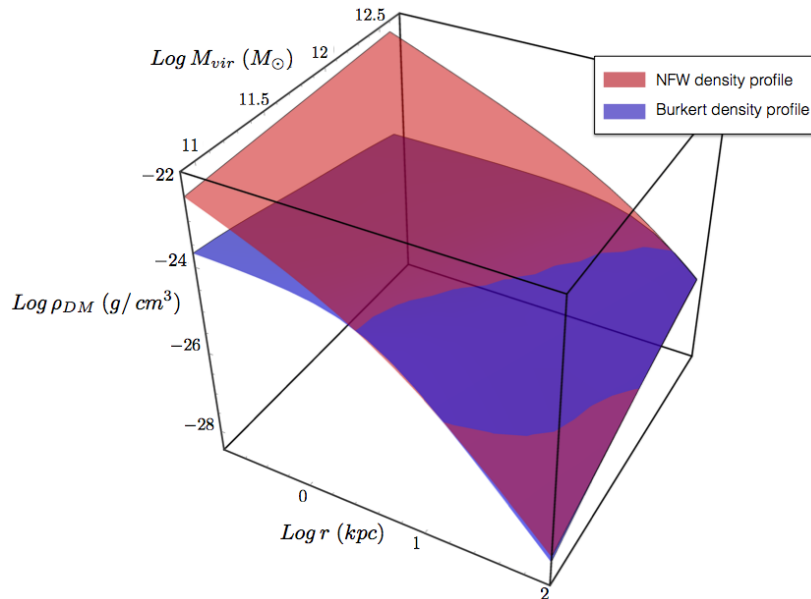


Figure 6.1: Original (*red*) and present-day (*blue*) DM density profile ρ_{DM} around galaxies as a function of radius r and halo mass M_{vir} .

6.1 The collisional DM scenario

In our collisional DM scenario, the DM particle - nucleon interactions (or/and similar ones) have left behind, at galactic scales, a number of imprints including the formation of cores in the DM density distribution and a strong entanglement between the distributions of the dark and luminous components. Remarkably, we can estimate how much dark mass has been involved in this process to form the DM halo profiles we detect now around galactic stellar discs.

The following arguments are made for spiral galaxies, however we expect them to be also valid for LSBs, since their scaling relationships are almost identical to those of the normal spirals.

Halos around spirals were formed at high redshifts in a free fall time of about $10^{7-8.5} yr$, i.e. in a time much smaller than the collisional time (here assumed $10^{10} yr$). So as soon as it gets virialized, the halo has a NFW profile [Navarro et al., 1996b]. We can recover it by looking at the outermost regions of the dark halos: [Salucci et al., 2007] have found that, for $r > 2r_0$, i.e., *outside* the region inside which the collisional interactions have mostly taken place in the past 10 Gyr, the DM density profile is well reproduced by

$$\rho_{DM,cusp}(r, c, M_{vir}) = \frac{M_{vir}}{4\pi R_{vir}} \frac{c^2 g(c)}{\tilde{x}(1 + c\tilde{x})^2} \quad , \quad (6.1)$$

where R_{vir} is the virial mass, $\tilde{x} = r/R_{vir}$ is the radial coordinate, M_{vir} is the virial mass enclosed in R_{vir} , $c \simeq 14 (M_{vir}/(10^{11} M_{\odot}))^{-0.13}$ is the *concentration* parameter and $g(c) = [\ln(1 + c) - c/(1 + c)]^{-1}$ (see [Salucci et al., 2007]). See Fig. 6.1. This result is not surprising since we know from N-Body simulations

that the NFW halo profile is the final virialized realization of any self gravitating collisionless particle (e.g. [Lapi and Cavaliere, 2011]), as the present DM particles. This allows us to obtain the primordial distribution of the DM halo by considering Eq. 6.1 to hold since the center of the galaxy. In this way we obtain the density distribution of the DM halo before that the DM-LM interaction takes place. In Fig. 6.1 one can see the primordial and the present dark halos density distributions for the whole family of spirals. In each object the amount of DM removed within the core radius $\sim r_0$ over the Hubble time is:

$$\Delta M_{DM}(r_0) = 4\pi \int_0^{r_0} (\rho_{DM,cusp}(r, M_{vir}) - \rho_{DM}(r, M_{vir})) r^2 dr \quad . \quad (6.2)$$

The amount of dark mass removed inside $\sim r_0$ by the dark-luminous collisional interactions ranges from 40 % to 90 % the primordial one (Salucci et al. in prep.). It is remarkable that the dark mass which has been removed from the core region is only 1/100 of the (present) halo mass. All the intriguing features we discover in the mass distributions of spirals are created by acting on a small fraction of the whole amount of the dark halo particles.

This means that, if the DM particles are captured in the stellar disc or scattered beyond the core radius, given the small fraction of the involved DM, it is difficult to discriminate the two possibilities of interactions by the only consideration of the matter distribution.

At any rate, one of the dynamical predictions of our scenario is that cores in the DM density distribution are formed from the center out to the external regions, as the time from the galaxy virialization goes by. Thus galaxies of fixed virial mass, if observed at high red-shift z , should have smaller core radius than those observed at $z \sim 0$.

Moreover, we expect to observe some continuing interactions especially on the edge of the stellar disc in $z \sim 0$ galaxies.

It is interesting to note that the DM-LM interaction can likely also contribute to solve some other open problems in astrophysics, as pointed in the following.

We could consider the DM-LM interaction, in the inner region of large galaxies (especially the ellipticals), as a possible catalyst able to accelerate the process of the central massive black hole (BH) formation (an open problem nowadays). Indeed, if the DM was captured by a forming massive BH in its initial stage, it could exert further gravitational attraction on the surrounding matter, making the BH accretion faster than in presence of the only baryonic matter.

Another consideration could be that, if the DM can be captured by the densest stellar objects, such as stellar BH, the mass of the involved objects could be enhanced with respect the value expected from the stellar evolution theory.

6.2 Future observations and predictions

In this scenario, we consider the DM-LM interaction that can lead to a completely new kind of particle, but obviously we need strong proofs in order to assess such interactions. On experimental point of view, without entering the very complex issue of specifying the DM particle and predicting the detection rates, it is important to stress that the interaction of such particle with the

ordinary matter could be revealed. However, since the locations and the types of this interaction are so numerous, we will specify only few particular cases by claiming that also in the situations not considered below some signature of the proposed interaction will occur (Salucci et al. in prep.).

We expect, in primis, that an indirect evidence of the particle will show up from anomalies in the internal properties of the stars and in their photon-neutrino emissions that would result in strong tension with the predictions of the standard theory of stellar structure and evolution.

Furthermore, the open channel between the dark and the SM particles yields other possibilities of detection through observations and experiments. As examples, out of many possibilities, the LM-DM interaction that would occur on the surface of neutron stars and on the accretion discs on BHs could produce cosmic positrons and, therefore, to be a component of the PAMELA and AMS detected positron excess [Adriani et al., 2009, Accardo et al., 2014]. On this regard we should stress that any kind of DM-DM particles annihilation process would produce a peaked gamma ray spectrum, never observed till now. The positron/electron excess instead, with a cut-off spectrum, is perfectly in line with any complex DM-SM particles interaction, where any kind of known particles will definitely end up into electrons/positrons, neutrinos and gammas.

The interactions we propose could also produce diffuse energetic photons detected by VHE gamma rays experiments such as Fermi telescope. The Moon and the Earth atmosphere may also be source of DM generated radiation.

Moreover, such collisional particle, could be created in accelerators and detected as missing momentum or missing masses in the particle flow of the interaction. At collider we must be open to the possibility that the interaction can be of a completely different nature. A complete new sector coupled to electroweak (EW) fields, for example, could be responsible for the DM-SM particles interaction. New searches are ongoing in CMS/Atlas experiments enlarging the analysis to more complex and different scenarios. Given this we can surely say that exclusions made by LHC and underground experiments are not yet conclusive for the actual DM particle we propose.

Obviously, future observations at low and high redshifts [Kaviraj, 2020] will allow us to deep the knowledge on the evolution of the luminous and the dark matter distribution, giving decisive proof on the DM scenario we have started to develop here. Interesting probes come from the near future *radio astronomy*, analysing the 21-cm emission line from the HI regions and thus providing us with new insights on the matter distribution over a broad range of scales and redshifts. The future results will be able to constraint the clustering properties of DM and eventually to find possible deviation (e.g. [Sitwell et al., 2014, Carucci et al., 2015]) or confirmation of the standard Λ -CDM scenario.

Conclusions

For a century, astronomical observations have been pointing to the existence of a large amount of matter, namely the DM, beyond the standard luminous (baryonic) matter. However the DM puzzle is still unresolved. In this work, we have reviewed the main concepts concerning the knowledge of the DM properties, with the related achievements and issues (Chapter 1). Then, we focused on the Low Surface Brightness (LSB) galaxies recalling the results on their properties collected over the last three decades (Chapter 3).

In this work, the LSBs are studied by means of the universal rotation curve (URC) method (like in [Persic et al., 1996]). It consists of a stacked analysis which allows us to give a universal description of disc galaxies, with a dependence on few parameters, such as the optical radius R_{opt} and the optical velocity V_{opt} . The analysis leads to a good description of the LSBs rotation curves by involving in their mass modelling the contribution from a Freeman stellar disc and a Burkert cored DM halo. The obtained universal rotation curve (Fig. 4.13-4.14) is described by Eq. 4.13 and is affected by an error $\Delta V/V \simeq 8\%$, highlighting the success of the URC method. The goodness of the result can be also realised on the individual rotation curves in Fig. I1-I2-I3-I4-I5 in [Di Paolo et al., 2019a] in Chapter 8.

Furthermore, the URC method allow us to infer tight scaling relations among the luminous and the dark matter distribution properties as in [Persic et al., 1996, Karukes and Salucci, 2017, Lapi et al., 2018]. Among the scaling relations we highlight Eq. 4.2 involving the stellar disc scale length R_d and the DM core radius r_0 , Eq. 4.4 involving the DM halo central density ρ_0 and r_0 , Eq. 4.8-4.9 related to the angular momentum in galaxies. These relations are almost identical to those of the normal spirals (high surface brightness, HSB) and of the dwarf disc galaxies. The found results seem hard to be explained unless a fine-tuned process in galaxy formation or some unknown interaction exists, across galaxies that have experienced different evolutionary histories.

Particularly, the found scaling relations also need the involvement of the compactness C_* , a new parameter which is related to the spread of the $V_{opt} - R_d$ data (Fig. 4.1) and that results necessary for describing the LSB galaxies, as well as the dwarf disc galaxies [Karukes and Salucci, 2017]. The dependence of the scaling laws on this new quantity (beyond R_{opt} and V_{opt}) gives rise to a new challenge for the N-body+hydrodynamical simulations in reproducing the observed galaxies properties.

We have also analysed the relation between the gravitational acceleration relation g and its component g_b due to the presence of the only baryonic matter. The analysis on LSBs (and on dwarf disc galaxies) leads to the necessity of also

involving the galactic radius $x \equiv r/R_{opt}$ where g and g_b are evaluated. A deeper analysis shows that the found *GGBX* relationship (and the $g - g_b$ relationship found in previous work [McGaugh et al., 2016]) can be easily interpreted in light of the luminous and dark matter distribution in galaxies.

Finally, we take into account that the most favoured Λ CDM scenario has some relevant problems to cope with and that the solutions invoked in the previous years can hardly solve them (Section 1.3). Nevertheless, regarding the cusp-core problem, optimistic ideas on the ability of the feedback process to flatten the DM cusped halos, preserving the Λ CDM scenario, also exist. E.g., in [Dutton et al., 2019], despite the halo response is a strong function of the star formation threshold in galaxies of different size, the authors rely on the possibility that such threshold might derive from large differences in the gas fractions and star formation rates. At any rate, the LSBs take the challenges at higher levels. These galaxies show a cored DM halo distribution characterised by r_0 values which are correlated to R_d values according to Eq. 4.2, like galaxies of different morphology. However, taking into account the very low HI gas density of the LSBs, the high M_{HI}/L , the extremely low star formation rate characterised by sporadic events, the extremal extension of the stellar disc (especially for the most luminous LSBs) and other peculiarities described in Chapter 3, some doubts can arise about the ability of the baryonic feedback to flatten the DM halo cusps (e.g. [Kuzio de Naray and Spekkens, 2011]) and to produce results in agreement with Eq. 4.2. The above issue, plus the difficulty in explaining the observed strong entanglement (well described by scaling laws) between the luminous matter (LM) and the dark matter distribution in galaxies of different morphology and different star formation history, plus the undetected WIMP particle, lead us to suppose the existence of a direct LM-DM interaction, other than through gravity.

The *LM-DM interaction* might be a necessary key to understand the DM phenomenon, to reproduce the *observed core* in the galactic DM halo and the empirical relationships between the galactic properties. Probably this kind of particle is not the "only one", but it needs to be mixed to other particles, likely to the still known candidates.

In conclusion, further studies are needed in order to have a better understanding about the LSBs, the galaxy formation/evolution and the DM phenomenon. In particular, we need:

- a) to enlarge the LSBs rotation curves sample and their resolution in order to have a better knowledge of the LSB galaxies properties and of the LM and the DM relationship, which may give us informations on the LM-DM interaction;
- b) to study the giant LSBs, special objects which are often made of a HSB disc embedded in a large LSB disc. Likely, dwarf and giant LSBs can have different evolution history (e.g. [Matthews et al., 2001]);
- c) to analyse some extreme cases of LSBs which show some peculiarities making them different from most of the *standard* LSB discs. Indeed, most of them are very blue, but some of them are also very red (e.g. [Burkholder et al., 2001]); most LSBs have low metal content, but some of them show near solar abundances [Bell et al., 2000]; they can be dwarfs, but also giants with different properties than other LSBs (e.g. [Boissier et al., 2016]), also with bulges and

AGN (e.g. [Mishra et al., 2018]);

d) to enlarge the observations at low and high redshifts. This will allow us to deep the knowledge on the evolution of the luminous and the dark matter distribution, giving decisive proof on the DM scenario. Particularly, the future observations will be useful to test the number of the small (LSB) galaxies giving informations about the small-scale problems in the Λ CDM scenario.

Likely, decisive observations will come in the future from measurements from radio telescopes like ALMA and SKA and from optical telescopes like VLT and ELT.

Part II

Chapter 7

PAPER 1: “The universal rotation curve of low surface brightness galaxies IV: the interrelation between dark and luminous matter”

The universal rotation curve of low surface brightness galaxies – IV. The interrelation between dark and luminous matter

Chiara Di Paolo,^{1,2,3★} Paolo Salucci^{1,2,3★} and Adnan Erkurt⁴

¹Physics, SISSA/ISAS, Via Bonomea 265, I-34136 Trieste, Italy

²INFN Sez. Trieste, Via A. Valerio 2, I-34127 Trieste, Italy

³IFPU, Via Beirut 2-4, I-34151 Trieste, Italy

⁴Physics, Istanbul University, Beyazit, 34452 Fatih/Istanbul, Turkey

Accepted 2019 September 17. Received 2019 August 2; in original form 2018 October 4

ABSTRACT

We investigate the properties of the baryonic and the dark matter components in low surface brightness (LSB) disc galaxies, with central surface brightness in the B band $\mu_0 \geq 23$ mag arcsec⁻². The sample is composed of 72 objects, whose rotation curves show an orderly trend reflecting the idea of a universal rotation curve (URC) similar to that found in the local high surface brightness (HSB) spirals in previous works. This curve relies on the mass modelling of the co-added rotation curves, involving the contribution from an exponential stellar disc and a Burkert cored dark matter halo. We find that the dark matter is dominant especially within the smallest and less luminous LSB galaxies. Dark matter haloes have a central surface density $\Sigma_0 \sim 100 M_\odot \text{pc}^{-2}$, similar to galaxies of different Hubble types and luminosities. We find various scaling relations among the LSBs structural properties which turn out to be similar but not identical to what has been found in HSB spirals. In addition, the investigation of these objects calls for the introduction of a new luminous parameter, the stellar compactness C_* (analogously to a recent work by Karukes & Salucci), alongside the optical radius and the optical velocity in order to reproduce the URC. Furthermore, a mysterious entanglement between the properties of the luminous and the dark matter emerges.

Key words: galaxies: fundamental parameters – galaxies: kinematics and dynamics – dark matter.

1 INTRODUCTION

Dark matter (DM) is the main actor in cosmology. It is believed to constitute the great majority of the mass and to rule the processes of structure formation in the Universe.¹ The so-called Lambda cold dark matter (Λ CDM) scenario, in which one assumes a weakly interacting massive particle (WIMP) that decouples from the primordial plasma when non-relativistic, successfully reproduces the structure of the cosmos on large scales (Kolb & Turner 1990). However, some challenges to this scenario emerge at small galactic scales, such as the ‘missing satellite problem’ (e.g. Klypin et al. 1999; Moore et al. 1999; Zavala et al. 2009; Papastergis et al. 2011; Klypin et al. 2015) and the ‘too-big-to-fail problem’ (e.g. Boylan-Kolchin, Bullock & Kaplinghat 2012; Ferrero, Navarro & Sales 2012; Garrison-Kimmel et al. 2014; Papastergis et al. 2015). Moreover, the galactic inner DM density profiles generally appear to be cored, rather than cuspy as predicted in the Λ CDM scenario (e.g.

Salucci 2001; de Blok & Bosma 2002; Gentile et al. 2004, 2005; Simon et al. 2005; Del Popolo & Kroupa 2009; Oh et al. 2011; Weinberg et al. 2015), in spirals of any luminosity (see Salucci 2019). In ellipticals and dwarf spheroidals (dSphs) the question is still uncertain (Salucci 2019).

These issues suggest to study different scenarios from the ‘simple’ Λ CDM, such as warm DM (e.g. de Vega et al. 2013; Lovell et al. 2014), self-interacting DM (e.g. Vogelsberger et al. 2014; Elbert et al. 2015), or to introduce the effect of the baryonic matter feedbacks on the DM distribution (e.g. Navarro, Eke & Frenk 1996; Read & Gilmore 2005; Mashchenko, Couchman & Wadsley 2006; Di Cintio et al. 2014; Pontzen & Governato 2014).

One important way to investigate the properties of DM in galaxies is to study rotation-supported systems, such as spiral galaxies, since they have a rather simple kinematics. The stars are mainly distributed in an exponential thin disc with scale length R_d (Freeman 1970). Notice that related to this scale length, in this paper, we will use the optical radius R_{opt} , defined as the radius encompassing 83 per cent of the total luminosity and proportional to the stellar disc scale length: $R_{\text{opt}} = 3.2R_d$ (the details of this choice are expressed at length in Persic, Salucci & Stel 1996). In order to explain the

* E-mail: cdipaolo@sissa.it (CDP); salucci@sissa.it (PS)

¹In this paper we adopt the scenario of DM in Newtonian gravity, leaving to other works the investigation in different frameworks.

observed rotation curves (RCs) of disc systems, it is necessary to assume the presence of a spherical DM halo surrounding the galaxies (Faber & Gallagher 1979; Rubin et al. 1985; Salucci 2019).

A very interesting feature of spiral galaxies is that the bigger they are, the more luminous they are and the higher rotational velocities they show. Moreover, when their RCs, with the radial coordinate normalized with respect to their optical radius R_{opt} , are put together, they appear to follow a *universal trend* (first shown in fig. 4 in Rubin et al. 1985, then in Persic & Salucci 1991, Persic et al. 1996, Rhee 1996, Roscoe 1999, Catinella, Giovanelli & Haynes 2006, Noordermeer et al. 2007, Salucci et al. 2007, López Fune 2018, and Salucci 2019). From small to large galaxies, the RCs have higher and higher velocities and profiles that gradually change. See also the top panel in Fig. A1 in Appendix A.

By means of the ‘*universal rotation curve* (URC) method’, which involves groupings of similar RCs and their mass modelling, it is possible to construct an analytic function that gives a good description of all the RCs of the local spiral galaxies within a spherical volume $\simeq (100 \text{ Mpc})^3$. The URC method was applied for the first time in Persic & Salucci (1991). This was followed by a series of three works: Persic et al. (1996) (Paper I), Salucci et al. (2007) (Paper II), and Karukes & Salucci (2017) (Paper III), where the URC method gave deeper results related to *normal spirals*, also called high surface brightness (HSB) spirals, and *dwarf disc* (*dd*) galaxies. A subsequent work confirmed the above results with up to 3100 disc galaxies and highlighted the existence of *tight scaling relations* among the properties of spirals with different size (Lapi, Salucci & Danese 2018).

Let us underline that the concept of *universality* in the RCs means that all of them can be described by the same analytical function as long as expressed in terms of the normalized radius and of one global parameter of the galaxies, such as magnitude, luminosity, mass, or velocity at the optical radius ($V_{\text{opt}} \equiv V(R_{\text{opt}})$). Therefore, the URC is the circular velocity at a certain radius r given by $V(r/R_{\text{opt}}, L)$, where L is the galaxy’s luminosity. See the bottom panel in Fig. A1 in Appendix A. Obviously, the URC does not change even using, instead of R_{opt} , any other radial coordinate proportional to the stellar disc scale length R_d .²

The URC is a very powerful tool since, given the observation of few properties (such as R_d and L) of a certain galaxy, it is possible to deduce its RC and all its properties.

In this paper (IV), we investigate the concept of the URC, the resulting mass models, and the scaling relations in *low surface brightness* (LSB) disc galaxies, comparing them to the results of other disc galaxies of a different Hubble type.

LSB galaxies are rotating disc systems which emit an amount of light per area smaller than normal spirals. They are locally more isolated than other kinds of galaxies (e.g. Bothun et al. 1993; Rosenbaum & Bomans 2004) and likely evolving very slowly with very low star formation rates. This is suggested by colours, metallicities, gas fractions, and extensive population synthesis modelling (e.g. van der Hulst et al. 1993; McGaugh 1994; de Blok, van der Hulst & Bothun 1995; Bell et al. 2000). As we see in radio synthesis observations, LSB galaxies have extended gas discs with low gas surface densities and high M_{HI}/L ratios (e.g. van der Hulst et al. 1993), where M_{HI} is the mass of the H I gaseous disc. The low metallicities make the gas cooling difficult and in turn the stars difficult to form (e.g. McGaugh 1994). LSBs are required to

be dominated by DM, as shown by the analysis of their Tully–Fisher relation (e.g. Zwaan et al. 1995) and of their individual RCs (e.g. de Blok, McGaugh & Rubin 2001; de Blok & Bosma 2002).

The LSB sample used in this work involves 72 galaxies selected from literature, whose optical velocities span from ~ 24 to $\sim 300 \text{ km s}^{-1}$, covering the values of the full population. Our analysis of LSBs by means of the URC method is triggered by the result shown in Fig. 1, from which we can see that the LSBs RCs gradually change very orderly from small to large galaxies (or equally from objects with small to large optical velocities V_{opt}). Following the URC method, the sample of galaxies is divided in different velocity bins, according to their increasing values of V_{opt} . A double normalization of all the RCs is performed with respect to: (i) their own R_{opt} , along the radial axis, and (ii) their own V_{opt} , along the velocity axis. In these specific coordinates, in each velocity bin, the RCs are all alike. Then, the double-normalized co-added RCs, a kind of average RC for each velocity bin, are constructed. The analysis continues with their *mass modelling*, yielding the distribution of luminous and DM in structures with different V_{opt} . This is followed by the denormalization process, which gives the structural parameters of each object of the sample, and allows us to obtain the related scaling relations for the LSBs. The internal scatter of the found scaling relationships is larger (three times or more) than the analogous ones in normal spirals. A similar finding also emerged in the case of *dd* galaxies (Karukes & Salucci 2017). Remarkably, the scatter in the *dd* relationships was reduced after the introduction of a new quantity, the *compactness* of the luminous matter distribution C_* , that indicates how the values of R_d vary in galaxies with the same stellar disc mass. Therefore, such results statistically suggest the introduction of the compactness also in the analogous LSBs scaling relationships. The previous steps lead to the construction of the URC for the LSBs, which is one of the main goals of this work. Finally, in analogy to Karukes & Salucci (2017), we also investigate the compactness of the DM distribution C_{DM} and its relation to C_* .

The structure of this paper is as follows: in Section 2, we describe our sample of LSB galaxies; in Sections 3–5, the URC method and the analysis of the LSBs structural properties are described in detail; in Section 6 we obtain the LSBs scaling relations and we compare them to those of other disc systems; in Sections 7–8, the concept of *compactness* is introduced and the URC-LSB is built; finally, in Section 9, we comment on our main results.

The distances are evaluated from the recessional velocity assuming $H_0 = 72 \text{ km s}^{-1} \text{ Mpc}^{-1}$.

2 THE LSB SAMPLE AND THE ROTATION CURVES UNIVERSAL TREND

We consider 72 rotating disc galaxies classified as ‘low surface brightness’ in literature (see Table B1 in Appendix B). In the very majority of cases the authors classify a galaxy as LSB when the face-on central surface brightness $\mu_0 \gtrsim 23 \text{ mag arcsec}^{-2}$ in the *B* band. We select our sample according to the following criteria:

- (i) the RCs extend to at least $\simeq 0.8 R_{\text{opt}}$ (when V_{opt} is not available from observation, it can be extrapolated since from $\simeq 1/2 R_{\text{opt}}$ to $2 R_{\text{opt}}$, the RCs are linear in radius with a small value of the slope);
- (ii) the RCs are symmetric, smooth (e.g. without strong signs of non-circular motions) and with an average fractional internal uncertainty lesser than 20 per cent. In short we eliminated RCs that in no way can be mass-modelled without huge uncertainties;

²The results of the paper remain unchanged for any chosen radial coordinate if expressed in units of λR_d , with any λ value ranging from one to four.

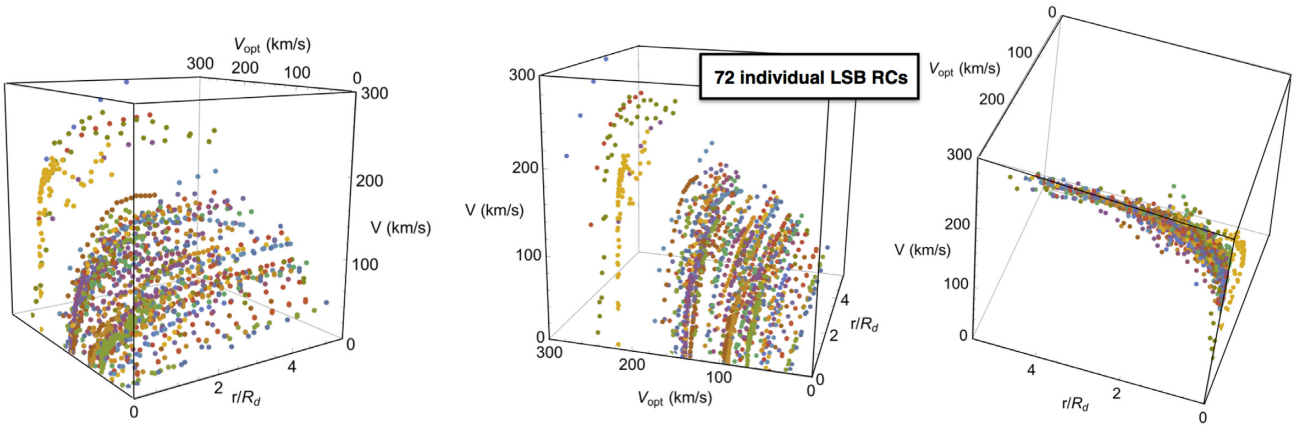


Figure 1. LSBs RCs (each one in different colour) ordered according to increasing optical velocities V_{opt} . Note that the radial coordinate is normalized with respect to the disc scale length R_d . A *universal trend* is recognizable analogous to that emerged in normal spirals (see Fig. A1 in Appendix A).

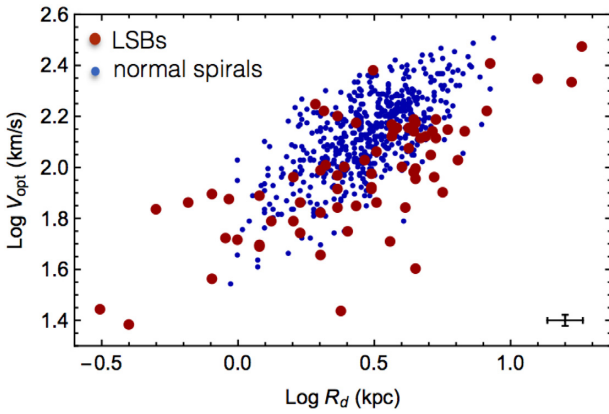


Figure 2. Optical velocity versus disc scale lengths in LSB galaxies (*red*) and in normal spirals (*blue*) (Persic et al. 1996). The typical fractional uncertainties are 5 per cent in V_{opt} and 15 per cent in R_d , as shown in the bottom right corner.

(iii) the galaxy disc scale length R_d and the inclination function $1/\sin i$ are known within 30 per cent uncertainty.

The selected 72 LSBs have optical velocities V_{opt} spanning from ~ 24 to ~ 300 km s^{-1} ; the sample of RCs consists of 1614 independent (r, V) measurements. When the RCs, expressed in normalized radial units, are put together, see Fig. 1, they show a universal trend analogous to that of the normal spirals (Fig. A1 in Appendix A). Then, given the observed trend in LSBs and the relevance of the URC method, we search our sample of LSBs for a URC and for the related scaling relations among the galaxy’s structural parameters.

In Fig. 2, the values of the stellar disc scale lengths R_d and the optical velocities V_{opt} measured in LSBs are shown and compared to those measured in normal spirals. A larger spread in the former case is clearly recognizable. This feature will be used later to explain the need of introducing a new structural variable: the *compactness*.

Finally, it is useful to stress that previous studies on individual LSB galaxies reveal in the mass profiles of these objects the presence of an exponential stellar disc, an extended gaseous disc at very low density (e.g. de Blok, McGaugh & van der Hulst 1996), and the presence of a spherical DM halo, likely with a core profile (e.g. de Blok et al. 2001; de Blok & Bosma 2002; Kuzio de Naray, S. & de Blok 2008).

3 THE CO-ADDED ROTATION CURVES OF LSB GALAXIES

The individual RCs (in normalized radial units) shown in Fig. 1 motivate us to proceed, also in LSB, with the URC method, analogously to what has been done on the HSB spiral galaxies (Persic et al. 1996; Lapi et al. 2018) and dwarf discs (Karukes & Salucci 2017). It is useful to anticipate here that the average scatter of the RCs data from a fitting surface (as the URC in Fig. 15) is $\Delta V/V \simeq 8$ per cent (taking into account the observational errors, the systematics, and the small non-circularities in the motion). This small value gives an idea of the universality of the LSBs RCs expressed in normalized radial units.

Among the first steps, the URC method (Persic et al. 1996) requires to make the galaxies RCs as similar as possible (in radial extension, amplitude, and profile) by introducing the normalization of their coordinates and an eventual galaxies binning. Let us notice that the justification for these starting steps comes from the analogous process performed in spirals and from a qualitative inspection of LSB RCs. Finally, the goodness of the results will show the goodness of the method.

The characteristics of the RCs in physical and normalized units are visible in Fig. 3:

- (i) in the first panel, the RCs are expressed in physical units; they appear to be different in radial extension, amplitude, and profile;
- (ii) in the second panel, the RCs are expressed in normalized radial units with respect to their disc scale length R_d . Their radial extensions are made more similar. Indeed, most of the data are extended up to $\simeq 5.5R_d$;
- (iii) in the third panel, the RCs are expressed in double-normalized units with respect to their disc scale length R_d and optical velocity V_{opt} , along the radial and the velocity axis, respectively. The RCs in such specific units are comparable also in their amplitude.

Overall, the double normalization makes the 72 RCs more similar, apart from their profiles. However, when these RCs are arranged in five optical velocity bins according to their increasing V_{opt} as in Fig. 4, we realize that the *double-normalized* RCs profiles belonging to one of these bins are very similar among themselves but clearly different from those of the RCs in other optical velocity bins (see Fig. 5).

We have chosen to build five V_{opt} bins as a compromise between having a large number of data for each co-added RC and a large

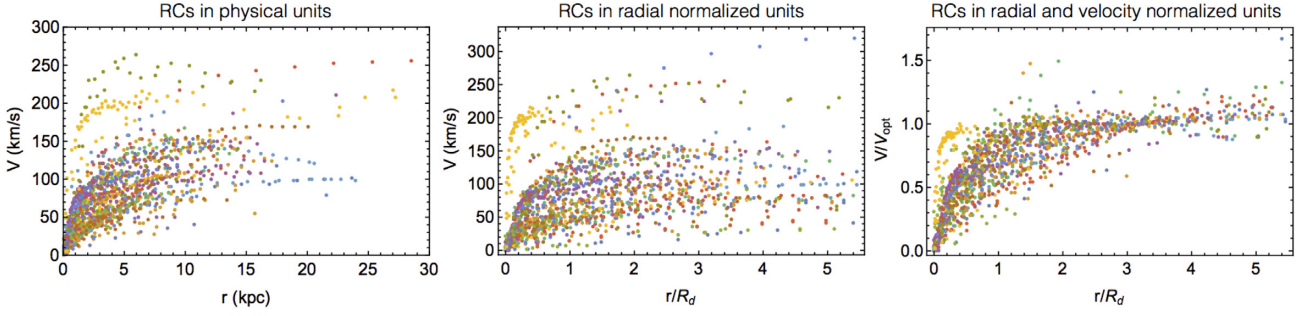


Figure 3. LSBs RCs (each one in different colour) in physical units (*first panel*), in normalized radial units (*second panel*), and in double-normalized radial and velocity units (*third panel*). See also Appendix C.

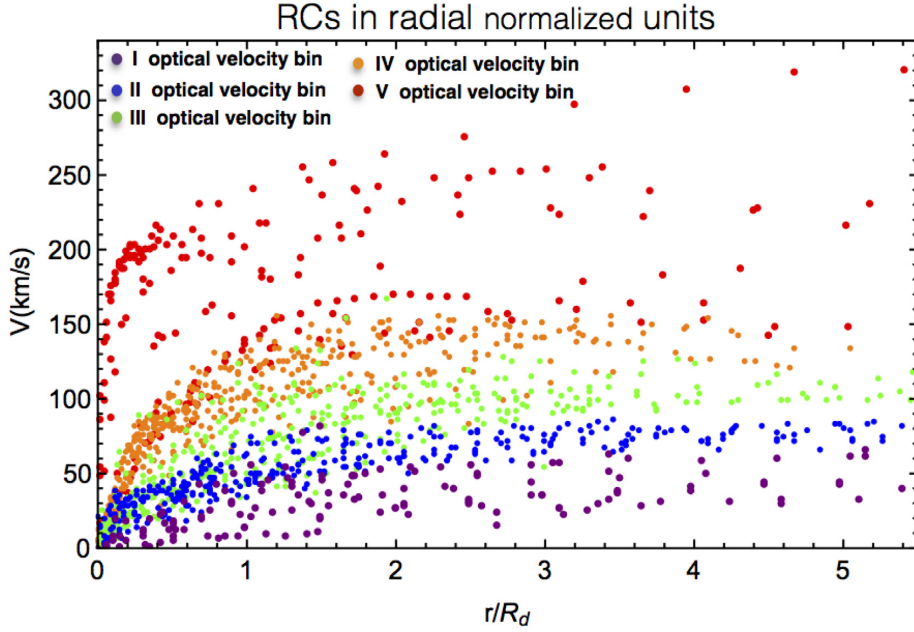


Figure 4. LSBs RCs (in normalized radial units) grouped in five optical velocity bins. In this and in the following figures, *purple*, *blue*, *green*, *orange*, and *red* colours are referred to the RCs of the I, II, III, IV, and V optical velocity bins, respectively.

number of co-added RCs. Particularly, the binning in five groups is suggested by the fact that, since the sample includes 72 objects, 10–15 galaxies are the minimum number in each optical velocity bin in order to create suitable co-added RCs (that will be described in the next paragraphs) and to eliminate statistically observational errors and small non-circularities from the individual RCs.

In detail, the number of galaxies in each bin, the span in V_{opt} , the average optical velocity $\langle V_{\text{opt}} \rangle$, the average stellar disc scale length $\langle R_d \rangle$, the number of galaxies and of the (r, V) data are all reported in Table 1.

We also point out Fig. D1 in Appendix D, where the RCs, grouped in their velocity bins, are compared in physical and double-normalized units.

After that all the RCs are double normalized, we perform the *radial binning* in each of the five *optical velocity bins*. Similar to the velocity binning process, we have chosen $\simeq 11$ normalized radial bins as a compromise between having a large number of data for each radial bin and a large number of radial bins for each co-added RC. Moreover, we required that the inner radial bins (for $r \leq 2R_d$) and the outer radial bins (for $r > 2R_d$) included a minimum of 13 and five measurements, respectively. In detail, for the I, the II, and the III optical velocity bins, the radial *normalized* coordinate is divided in

12 bins: the first five have a width of 0.4 and the remaining a width of 0.5. For the IV and the V velocity bins, for statistical reasons, we adopt a different division of the radial coordinate. In the IV velocity bin we adopt three radial bins of width 0.4, five of width 0.6, and the last one of width 1. In the V velocity bin, we adopt five, four, and two radial bins of widths 0.4, 0.5, and 0.8, respectively. The number of data per radial bin is reported in Tables E1–E2 in Appendix E. Reasonable variations of the positions and amplitudes of the radial bins do not affect the resulting co-added RCs.

Therefore, for each of the five V_{opt} bins, in every k -radial bin we built there are N_k double-normalized velocities v_{ik} , with i running from 1 to N_k . Their average value is given by $V_k = \frac{\sum_{i=1}^{N_k} v_{ik}}{N_k}$, as in Persic et al. (1996). Then, by repeating this for all the radial bins of each of the five V_{opt} bins, we obtain the five double-normalized *co-added* RCs shown in Fig. 5. The *standard error of the mean* we consider in this work is

$$\delta V_k = \sqrt{\frac{\sum_{i=1}^{N_k} (v_{ik} - V_k)^2}{N_k(N_k - 1)}}. \quad (1)$$

In short, the above co-added RCs can be considered as the average RCs of galaxies of similar properties as e.g. V_{opt} . It is

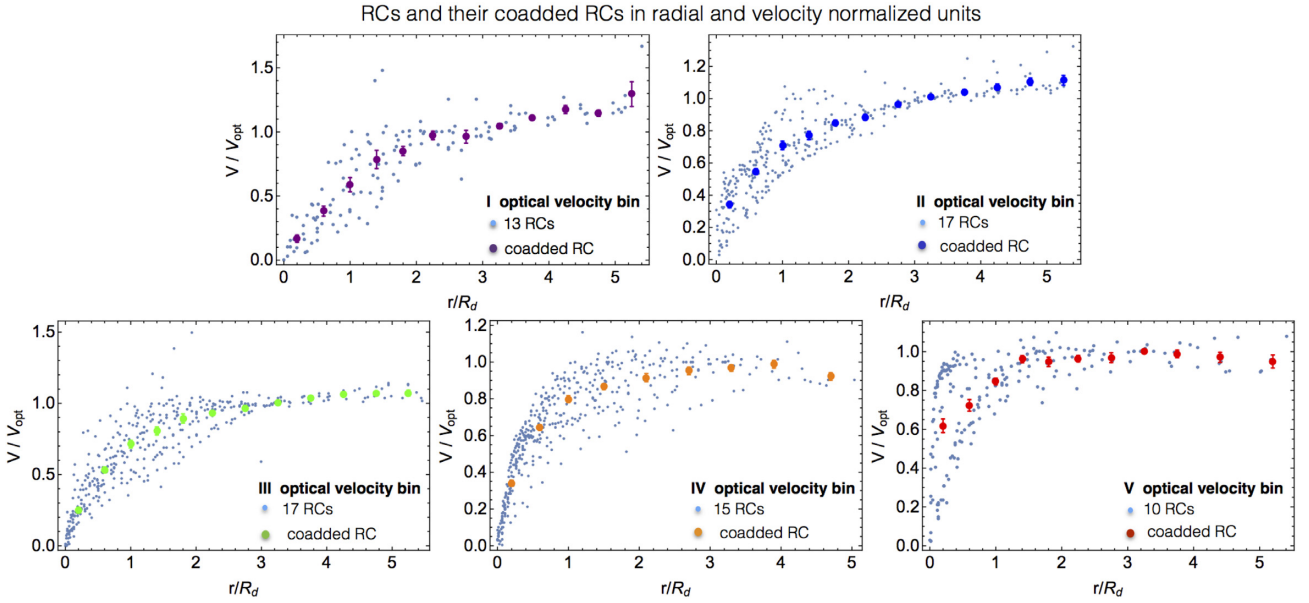


Figure 5. In each of the five panels: LSBs double-normalized RCs for each of the five optical velocity bins (*grey points*). Also shown are the corresponding co-added RCs (*larger coloured points*) for each of these five bins. Notice that part of the scatter in the five profiles will be eliminated by introducing the compactness in the URC. See Section 7.

Table 1. LSB velocity bins. Columns: (1) i - velocity bin; (2) range values for V_{opt} ; (3) number of LSB galaxies in each velocity bin; (4) average value of V_{opt} evaluated from the individual galaxies; (5) average value of R_d evaluated from the individual galaxies; (6) number of (r, V) data from the individual galaxies.

V_{opt} bin	V_{opt} range km s^{-1}	N. galaxies	$\langle V_{\text{opt}} \rangle$ km s^{-1}	$\langle R_d \rangle$ kpc	N. data
(1)	(2)	(3)	(4)	(5)	(6)
1	24–60	13	43.5	1.7	151
2	60–85	17	73.3	2.2	393
3	85–120	17	100.6	3.7	419
4	120–154	15	140.6	4.5	441
5	154–300	10	205.6	7.9	210

worth emphasizing the advantages of these RCs: their building erases the peculiarities and also reduces the observational errors of the individual RCs. This yields to a universal description of the kinematics of LSBs by means of five extended and smooth RCs whose values have an uncertainty at the level of 5–15 per cent. In Fig. 6 the five co-added RCs are shown together.

(i) in the first panel, they are expressed in double-normalized units covering a very small region in the $(V/V_{\text{opt}}, R/R_{\text{opt}})$ plane;

(ii) in the second panel, they are expressed in physical velocity units. These co-added RCs are obtained by multiplying the previous co-added RCs by the corresponding $\langle V_{\text{opt}} \rangle$ (reported in Table 1).

(iii) in the third panel, the co-added RCs are expressed in physical units both along the velocity and the radial axes. They are obtained by multiplying the previous co-added RCs by the corresponding $\langle R_d \rangle$ reported in Table 1.

In Fig. 6 the difference in the profiles corresponding to galaxies with different optical velocities is evident.³

³This is explained by the very different luminous and dark mass distributions in LSBs of different sizes and optical velocities, as shown in the next section.

All the data shown in Fig. 6 can be recast by means of Tables E1–E2 (in Appendix E) and Table 1.

4 THE MASS MODELLING OF THE CO-ADDED ROTATION CURVES

In this section we investigate the co-added RCs, normalized along the radial axis (see second panel in Fig. 6), whose data are listed in Tables E1–E2 in Appendix E. We model the co-added RCs data, as in normal spirals (Salucci et al. 2007), with an analytic function $V(r)$ which includes the contributions from the stellar disc V_d and from the DM halo V_h :

$$V^2(r) = V_d^2(r) + V_h^2(r). \quad (2)$$

Let us stress that in first approximation the inclusion in the model of a HI gaseous disc component can be neglected. In fact, the gas contribution is usually a minor component to the circular velocities, since the inner regions of galaxies are dominated by the stellar component and in the external regions, where the gas component overcomes the stellar one, the DM contribution is largely the most important (Evoli et al. 2011). A direct test in Appendix F shows that our assumption does not affect the mass modelling obtained in this paper.

We describe the stellar and the DM component. The first one is given by the well-known Freeman disc (Freeman 1970), whose surface density profile is

$$\Sigma_d(r) = \frac{M_d}{2\pi R_d^2} \exp(-r/R_d), \quad (3)$$

where M_d is the disc mass. Equation (3) leads to (Freeman 1970):

$$V_d^2(r) = \frac{1}{2} \frac{G M_d}{R_d} \left(\frac{r}{R_d} \right)^2 (I_0 K_0 - I_1 K_1), \quad (4)$$

where I_n and K_n are the modified Bessel functions computed at $1.6x$, with $x = r/R_{\text{opt}}$.

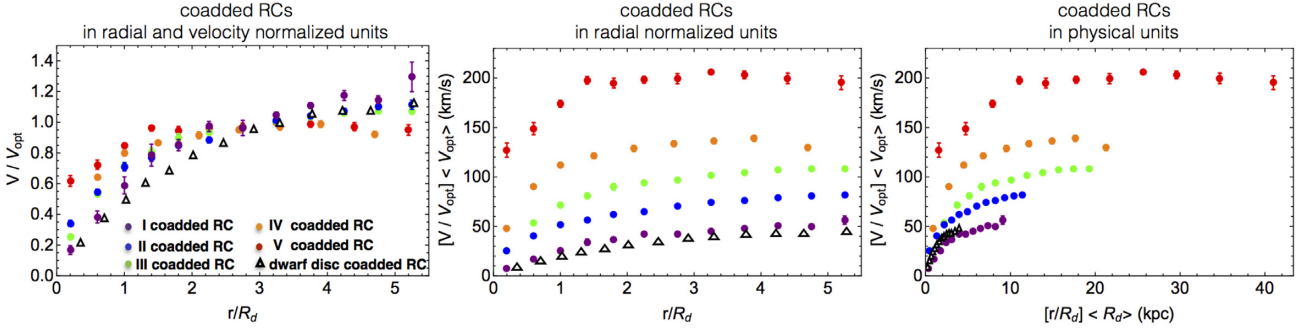


Figure 6. Co-added RCs for the five velocity bins in double-normalized units (*first panel*), in physical velocity units (*second panel*), and in physical units along both the velocity and radial axes (*third panel*). The black empty triangles are the co-added RC for the dwarf disc galaxies (Karukes & Salucci 2017).

Finally, for the fifth optical velocity bin we will introduce a bulge component (Das 2013).

Concerning the DM component, the presence of cored profiles in LSBs is well known from individual RCs (see e.g. de Blok et al. 2001; de Blok & Bosma 2002; Kuzio de Naray et al. 2008, Bullock & Boylan-Kolchin 2017). In this paper, we model the DM halo profile by means of the *cored Burkert profile* (Burkert 1995; Salucci & Burkert 2000). This halo profile has an excellent record in fitting the actual DM haloes around disc systems of any luminosity and Hubble Types (see Memola, Salucci & Babic 2011; Salucci et al. 2012; Lapi et al. 2018; Salucci 2019). In addition, the Burkert profile is in agreement with weak lensing data at virial distances (Donato et al. 2009).

It is however worth noticing that there is no sensible difference, in the mass modelling inside R_{opt} , in adopting different cored DM density profiles (Gentile et al. 2004). Then, we adopt the following density profile (Burkert 1995):

$$\rho_{\text{DM}}(r) = \frac{\rho_0 R_c^3}{(r + R_c)(r^2 + R_c^2)}, \quad (5)$$

where ρ_0 is the central mass density and R_c is the core radius. Its mass distribution is

$$\begin{aligned} M_{\text{DM}}(r) &= \int_0^r 4\pi \tilde{r}^2 \rho_{\text{DM}}(\tilde{r}) d\tilde{r} \\ &= 2\pi \rho_0 R_c^3 [\ln(1 + r/R_c) \\ &\quad - t g^{-1}(r/R_c) + 0.5 \ln(1 + (r/R_c)^2)]. \end{aligned} \quad (6)$$

The contribution to the total circular velocity is given by

$$V_h^2(r) = G \frac{M_{\text{DM}}(r)}{r}. \quad (7)$$

We fit the five co-added RCs by means of the URC model described above, which, for each co-added RC, is characterized by three free parameters, M_d , ρ_0 , and R_c , all set to be larger than zero. Other limits for the priors of the fitting arise from the amplitude and the profile of the co-added RCs themselves. We require that: $10^6 M_\odot \lesssim M_d \lesssim 10^{12} M_\odot$ from the galaxies luminosities, $R_c \lesssim 200 \frac{R_{\text{opt}}}{30 \text{ kpc}}$ kpc to avoid solid body RCs in all objects, and $10^{-26} \lesssim \rho_0 \lesssim 10^{-22} \text{ g cm}^{-3}$ (the lower limit guarantees that the dark component is able to fit the RC allied with the luminous component, the upper limit is to make the DM contribution important but not larger than the RCs amplitudes). Notice that these limits agree well with the outcomes of the modelling of individual RCs as found in literature.

The resulting best-fitting values for the three free parameters (M_d , ρ_0 , R_c) are reported in Table 2 and the best-fitting velocity models

are plotted alongside the co-added RCs in Fig. 7.

In the case of the V velocity bin, we introduce a central bulge (whose presence is typical in the largest galaxies) (Das 2013). We adopt for the bulge velocity component the simple functional form:

$$V_b^2(r) = \alpha_b V_{\text{in}}^2 \left(\frac{r}{r_{\text{in}}} \right)^{-1}, \quad (8)$$

where $V_{\text{in}} = 127 \text{ km s}^{-1}$ and $r_{\text{in}} = 0.2 \langle R_d \rangle \simeq 1.6 \text{ kpc}$ are the values of the first velocity point of the V co-added RC. Since r_{in} is larger than the edge of the bulge, we consider the latter as a point mass. α_b is a parameter which can vary from 0.2 to 1 (e.g. see Yegorova & Salucci 2007). By fitting the V co-added RC we found: $\alpha_b = 0.8$; the other best-fitting parameters M_d , ρ_0 , R_c are reported in Table 2.

In Fig. 7 we realize that, in the inner regions of the LSB galaxies, the stellar component (dashed line) is dominant, while, on the contrary, in the external regions, the DM component (dot-dashed) is the dominant one. Moreover, the transition radius⁴ between the region dominated by the baryonic matter and the region dominated by the DM increases with normalized radius when we move from galaxies with the lowest V_{opt} to galaxies with the highest V_{opt} . A similar behaviour was also observed in normal spiral galaxies (Persic et al. 1996; Lapi et al. 2018).

5 DENORMALIZATION OF THE CO-ADDED ROTATION CURVES

The mass models found in the previous section provided us with the structural parameters of the five co-added RCs. Now, we retrieve the properties from the individual RCs by means of the *denormalization* method. It relies on the facts that, in each velocity bin, (i) all the double-normalized RCs are similar to their co-added double-normalized RC (see Fig. 5) and that (ii) we have performed extremely good fits of the co-added RCs (see Fig. 7). Thus, the relations existing for the co-added RCs are assumed to approximately hold also for the individual RCs that form each of the five co-added ones.

The first relation that we apply in the denormalization process is shown in Fig. 8; the stellar disc scale length and the DM core radius of the five velocity models are strongly correlated. The best linear fit in logarithmic scale is

$$\text{Log } R_c = 0.60 + 1.42 \text{ Log } R_d. \quad (9)$$

⁴The *transition radius* is the radius where the DM component, dot-dashed line, overcomes the luminous component, dashed line.

Table 2. Relevant parameters of the five co-added RCs. Columns: (1) i - velocity bin; (2) average value of V_{opt} ; best-fitting value of (3) ρ_0 ; (4) R_c ; (5) M_d ; (6) estimated halo virial mass according to equation (13); (7) fraction of baryonic component at R_{opt} (equation 11); (8) k values defined according to equation (10).

Vel. bin	$\langle V_{\text{opt}} \rangle$ km s $^{-1}$	ρ_0 $10^{-3} M_{\odot} \text{pc}^{-3}$	R_c kpc	M_d $10^{11} M_{\odot}$	M_{vir} $10^{11} M_{\odot}$	$\alpha(R_{\text{opt}})$	k
(1)	(2)	(3)	(4)	(5)	(6)	(7)	(8)
1	43.5	3.7 ± 1.4	10.7 ± 4.3	$(8.8 \pm 1.8) \times 10^{-3}$	1.0 ± 0.4	0.37	0.36
2	73.3	5.1 ± 1.1	12.8 ± 3.0	$(3.8 \pm 0.3) \times 10^{-2}$	2.4 ± 0.9	0.49	0.44
3	100.6	3.7 ± 0.5	17.1 ± 1.9	$(13.0 \pm 0.5) \times 10^{-2}$	4.0 ± 1.3	0.52	0.47
4	140.6	$1.7^{+1.8}_{-1.1}$	30^{+40}_{-22}	$(4.2 \pm 0.4) \times 10^{-1}$	8.4 ± 3.5	0.76	0.63
5	205.6	$0.8^{+0.7}_{-0.4}$	99^{+213}_{-87}	1.7 ± 0.1	112 ± 55	0.82	0.70

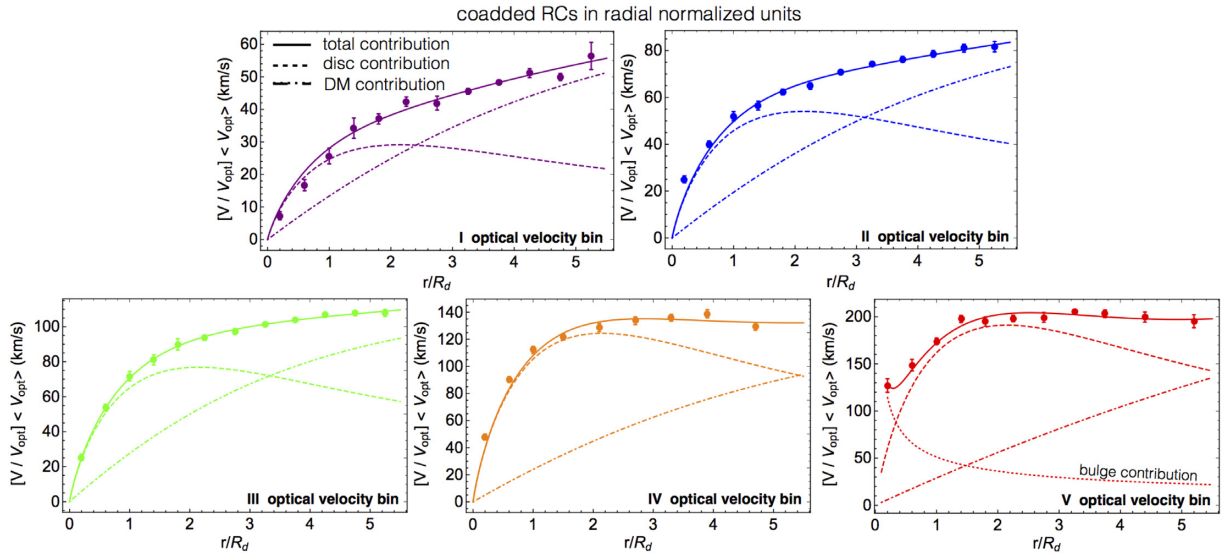


Figure 7. In each of the five panels the velocity best-fitting models to the corresponding co-added RCs are shown. The *dashed*, *dot-dashed*, *dotted*, and *solid* lines indicate the stellar disc, the DM halo, the stellar bulge, and the model contribution to the circular velocities.

The errors in the fitting parameter are shown in Table H1 in Appendix H. The relation expressed by equation (9) means that in each galaxy we can evaluate R_c from its measured R_d . It is worth noting that a similar relation exists also in normal spirals (Fig. 8).

The second relation we use for the denormalization assumes that for galaxies belonging to each V_{opt} bin:

$$\frac{G M_d}{V_{\text{opt}}^2 R_{\text{opt}}} = k, \quad (10)$$

where the k values are reported in Table 2. R_{opt} and V_{opt} are measured for all the galaxies, thus equation (10) allows us to evaluate the stellar disc mass M_d for each of them.

As the third step in the denormalization process we evaluate at R_{opt} , for each of the five co-added RCs, the fraction of the baryonic matter:

$$\alpha(R_{\text{opt}}) = \frac{V_d^2(R_{\text{opt}})}{V^2(R_{\text{opt}})}. \quad (11)$$

The $\alpha(R_{\text{opt}})$ values are reported in Table 2; we assume that all the galaxies included in each optical velocity bin take the same value for $\alpha(R_{\text{opt}})$. Then, for each galaxy, we write the DM mass inside the optical radius as:

$$M_{\text{DM}}(R_{\text{opt}}) = [1 - \alpha(R_{\text{opt}})] V_{\text{opt}}^2 R_{\text{opt}} G^{-1}. \quad (12)$$

Finally, by considering equations (6)–(12) together with the result

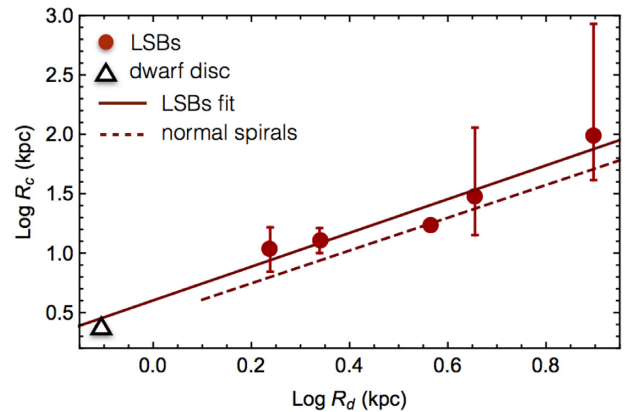


Figure 8. Relationship between the DM halo core radius and the stellar disc scale length (*points*) and its best fit (*solid line*) compared to that of the normal spirals (*dashed line*) (e.g. Lapi et al. 2018). The black empty triangle represents the relationship in dwarf disc galaxies (Karukes & Salucci 2017).

from the first denormalization step, we evaluate the central density of the DM halo ρ_0 for each galaxy.

The structural parameters of the dark and luminous matter of the galaxies of our sample, inferred by the denormalization procedure, are reported in Tables G1–G2 in Appendix G. Moreover, we have the basis to infer other relevant quantities of the galaxies structure

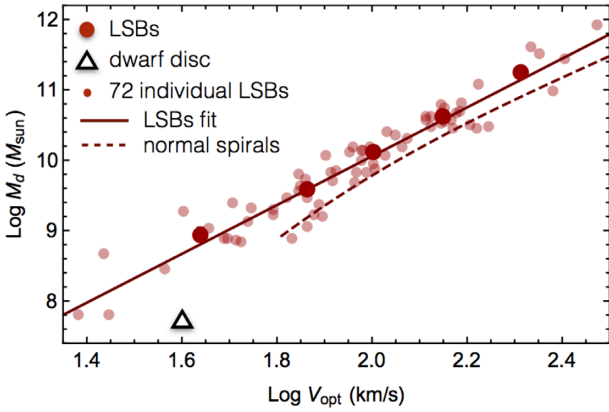


Figure 9. Relationship between the stellar disc mass and the optical velocity. The *large points* refer to the values of the five velocity bins, while the *small points* refer to the values of each LSB galaxy. The *solid* and the *dashed* lines are the best fit for LSBs and normal spirals (e.g. Lapi et al. 2018). The black triangle represents the dwarf discs (Karukes & Salucci 2017).

that will be involved, in the next section, in building the scaling relations. The virial mass M_{vir} that practically encloses the whole mass of a galaxy is evaluated according to:

$$M_{\text{vir}} = \frac{4}{3} \pi 100 \rho_{\text{crit}} R_{\text{vir}}^3, \quad (13)$$

where R_{vir} is the virial radius and $\rho_{\text{crit}} = 9.3 \times 10^{-30} \text{ g cm}^{-3}$ is the critical density of the Universe. The DM central surface density Σ_0 is evaluated by the product ρ_0 and R_c . The M_{vir} and Σ_0 values for the objects in our sample are shown in Tables G1–G2 in Appendix G.

6 THE SCALING RELATIONS

In this section, we work out the scaling relations among the structural properties of dark and luminous matter in each LSB galaxy. Let us stress that for many of the scaling relations we have no a priori insight of how they should be; in this case, the goal is to find a statistically relevant relationship. Then we fit the observational data with the simple power-law model. The errors on the fitting parameters of the various scaling relations and their standard scatters are reported in Table H1 in Appendix H. Hereafter, the masses are expressed in M_{\odot} , the radial scale length in kpc, the velocities in km s^{-1} , and the mass densities in g cm^{-3} .

We start with the relation between the stellar disc mass and the optical velocity. Fig. 9 shows that the LSB data are well fitted by

$$\text{Log } M_d = 3.12 + 3.47 \text{Log } V_{\text{opt}}. \quad (14)$$

This relation holding for the LSBs is similar but not identical to the normal spirals’ one. See the comparison with Lapi et al. (2018) in Fig. 9.

Next, in Fig. 10 (left-hand panel) we show the relation between the DM halo central density and the core radius, which indicates that the highest mass densities are in the smallest galaxies, as also found in normal spirals (Salucci et al. 2007). We find:

$$\text{Log } \rho_0 = -23.15 - 1.16 \text{Log } R_c. \quad (15)$$

Moreover, we find that the central surface density follows the relationship (see Fig. 10, right-hand panel):

$$\text{Log } \Sigma_0 = \text{Log } (\rho_0 R_c) \simeq 1.9, \quad (16)$$

Σ_0 is expressed in units of M_{\odot}/pc^2 .

Remarkably, this relationship extends itself over 18 blue magnitudes and in objects spanning from dwarf to giant galaxies (Spano et al. 2008; Donato et al. 2009; Gentile et al. 2009; Plana et al. 2010; Salucci et al. 2012; Chan 2019; Li et al. 2019).

Then, we consider the baryonic fraction (complementary to the DM fraction) relative to the entire galaxies, namely, the ratio between the stellar mass $M_* \equiv M_d$ in LSBs and the virial mass M_{vir} , that practically represents the whole dark mass of a galaxy. Fig. 11 shows that the lowest fraction of baryonic content is in the smallest galaxies (with the smallest stellar disc mass M_d). We note that this ratio increases going towards larger galaxies and then reaches a plateau from which it decreases for the largest galaxies. This finding is in agreement with the inverse ‘U-shape’ of previous works relative to normal spirals (Lapi et al. 2018). Furthermore, our result seems to follow a trend similar to that found in Moster et al. (2010), concerning all Hubble Types.⁵ The result points to a less efficient star formation in the smallest LSBs.

Finally, we work out the relationships needed to establish $V_{\text{URC}}(R; R_{\text{opt}}, V_{\text{opt}})$, the URC-LSB in physical units (as in Persic et al. 1996). Straightforwardly, we are looking for the universal function $V_{\text{URC}}(r/R_{\text{opt}}, V_{\text{opt}})$,⁶ able to reproduce analytically the LSBs RCs in Fig. 1.

This implies that M_d , R_d , R_c , and ρ_0 have to be expressed as a function of V_{opt} . Thus, we use equation (14) and the following relations, obtained after the denormalization process:

$$\begin{aligned} \text{Log } R_d &= -1.65 + 1.07 \text{Log } V_{\text{opt}} \\ \text{Log } R_c &= -1.75 + 1.51 \text{Log } V_{\text{opt}} \\ \text{Log } \rho_0 &= -22.30 - 1.16 \text{Log } V_{\text{opt}}, \end{aligned} \quad (17)$$

see Fig. 12. We note that the above relations (equations 14–17) show a large scatter, on average $\sigma \simeq 0.34$ dex, more than three times the value ($\sigma \simeq 0.1$ dex in Yegorova & Salucci 2007 and Lapi et al. 2018) found in normal spiral galaxies for the respective relations. This poses an issue to the standard procedure (Persic et al. 1996) to build the URC in physical units.

In the previous sections we have found a universal function to reproduce the double-normalized RC of LSBs $V(r/R_{\text{opt}})/V(R_{\text{opt}})$. Now we are looking for a universal function to reproduce the RC in physical units $V(r)$. In spiral galaxies this is simple since M_d , R_d , R_c , and ρ_0 are closely connected.

7 THE COMPACTNESS AS THE THIRD PARAMETER IN THE URC

We can reduce the scatter in the LSBs scaling relations and proceed with the URC building by introducing a new parameter: the *compactness* of the stellar mass distribution C_* . This parameter was first put forward in Karukes & Salucci (2017) to cope with a similar large scatter in the above scaling relations of the *dd* galaxies. In short the large scatter in the previous relationships is due to the fact that galaxies with the same stellar disc mass M_d (or V_{opt}) can have a very different size for R_d (i.e. $\text{Log } R_d$ can vary almost 1 dex). We define this effect with the fact that LSBs have a different ‘stellar compactness’ C_* ; see Figs 2 and 13.

⁵In Moster et al. (2010), the stellar mass M_* can indicate the mass enclosed in a disc and/or in a bulge.

⁶Hereafter, we express the normalized radial coordinate in terms of the optical radius R_{opt} , instead of R_d , in order to facilitate the comparison with previous works on the URC.

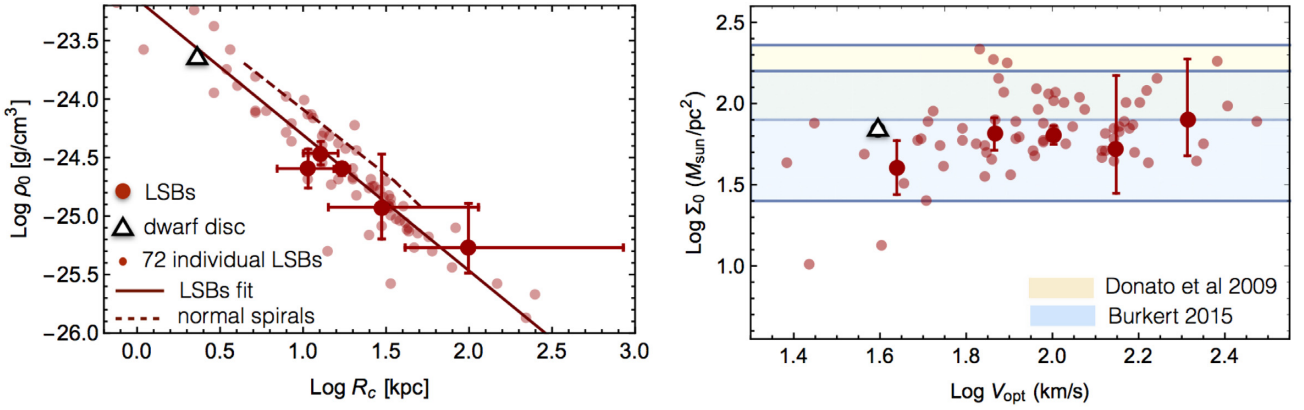


Figure 10. Left-hand panel: the relationship between the central DM halo mass density and its core radius. Right-hand panel: surface density $\Sigma_0 = \rho_0 R_c$ versus their optical velocities V_{opt} (LSBs in red points). Also shown is the scaling relation obtained by Donato et al. (2009) (yellow shadowed area) and Burkert (2015) (light blue shadowed area). The black empty triangle represents the dwarf discs (Karukes & Salucci 2017).

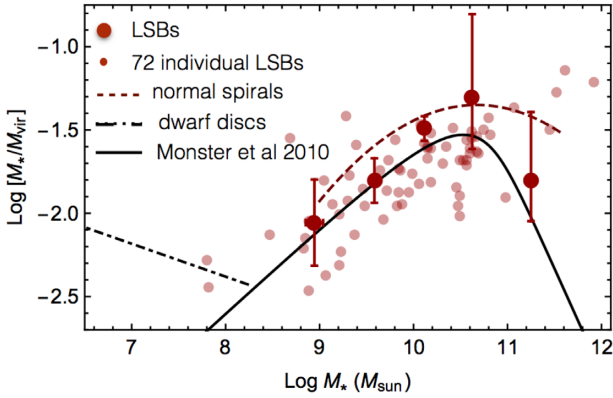


Figure 11. Fraction of baryonic matter in LSBs versus their mass in stars (points) compared with that of normal spirals (dashed line) (Lapi et al. 2018), of other Hubble Types (black solid line) (Moster et al. 2010), and of dwarf discs (black dot-dashed line) (Karukes & Salucci 2017).

We define C_* , starting from the best-fitting linear relation (see Fig. 13):

$$\text{Log } R_d = -3.19 + 0.36 \text{Log } M_d \quad (18)$$

and, according to Karukes & Salucci (2017), we set the stellar compactness through the following relation:

$$C_* = \frac{10^{(-3.19+0.36 \text{Log } M_d)}}{R_d}, \quad (19)$$

where, let us remind, R_d is measured from photometry. By means of equation (19), C_* measures, for a galaxy with a fixed M_d , the deviation between the observed R_d and the ‘expected’ R_d value from equation (18) (obtained by using the best-fitting line in Fig. 13). In short, at fixed M_d , galaxies with the smallest R_d have a high compactness ($\text{Log } C_* > 0$), while galaxies with the largest R_d have low compactness ($\text{Log } C_* < 0$).

The $\text{Log } C_*$ values for the galaxies of our sample are shown in Tables G1–G2 in Appendix G and span from -0.45 to 0.35 .

By introducing the compactness we reduce the scatter in the relations needed to establish the analytical function of the URC-LSB in physical units. This is highlighted in Fig. 14, where the data

are shown alongside their best-fitting plane.

$$\begin{aligned} \text{Log } M_d &= 2.52 + 3.77 \text{Log } V_{\text{opt}} - 1.49 \text{Log } C_* \\ \text{Log } R_d &= -2.27 + 1.38 \text{Log } V_{\text{opt}} - 1.55 \text{Log } C_* \\ \text{Log } R_c &= -2.62 + 1.96 \text{Log } V_{\text{opt}} - 2.20 \text{Log } C_* \\ \text{Log } \rho_0 &= -20.95 - 1.84 \text{Log } V_{\text{opt}} + 3.38 \text{Log } C_*. \end{aligned} \quad (20)$$

We find that, by using equation (20), the internal scatter of data with respect to the planes is always reduced compared to the case in which M_d , R_d , R_c , and ρ_0 were expressed only in terms of V_{opt} . The previous average scatter $\sigma \simeq 0.34$ dex of the 2D relations (equations 14–17), in the 3D relations (equation 20), is reduced to $\sigma \simeq 0.06$ dex smaller than the typical values obtained for normal spirals.

We now evaluate the analytic expression for the URC (expressed in physical units). By using equation (2) alongside equations (4), (6), and (7) and expressing M_d , R_d , R_c , and ρ_0 as in equation (20), we obtain:

$$\begin{aligned} V^2(x, V_{\text{opt}}, C_*) &= 2.2 x^2 \times 10^{f_1(V_{\text{opt}}, C_*)} \\ &\times [I_0 K_0 - I_1 K_1] + 1.25/x \times 10^{f_2(V_{\text{opt}}, C_*)} \\ &\times \{-t g^{-1}[3.2 x \times 10^{f_3(V_{\text{opt}}, C_*)}]\} \\ &+ \ln[1 + 3.2 x \times 10^{f_3(V_{\text{opt}}, C_*)}] \\ &+ 0.5 \ln[1 + 10.24 x^2 \times 10^{2 f_3(V_{\text{opt}}, C_*)}], \end{aligned} \quad (21)$$

where I_n , K_n are the modified Bessel functions evaluated at $1.6x$, with $x = r/R_{\text{opt}}$ and

$$\begin{aligned} f_1(V_{\text{opt}}, C_*) &= 9.79 + 2.39 \text{Log } V_{\text{opt}} + 0.05 \text{Log } C_* \\ f_2(V_{\text{opt}}, C_*) &= -0.55 + 2.65 \text{Log } V_{\text{opt}} - 1.67 \text{Log } C_* \\ f_3(V_{\text{opt}}, C_*) &= 0.35 - 0.58 \text{Log } V_{\text{opt}} + 0.65 \text{Log } C_*. \end{aligned} \quad (22)$$

Finally, we plot in Fig. 15 the URC (equations 21–22) considering $\text{Log } C_* = 0$, corresponding to the case in which all the LSBs data in Fig. 13 were lying on the regression line (or, analogously, the case in which the spread of LSBs data in Fig. 2 was small). The curve shown in Fig. 15 is in good agreement with the LSBs RCs data. On average, the uncertainty between the velocity data and the URC velocity predicted values is $\Delta V/V \simeq 19$ per cent, which can be reduced to $\Delta V/V \simeq 8$ per cent, when the observational errors, the systematics, the small non-circularities, and the prominent bulge

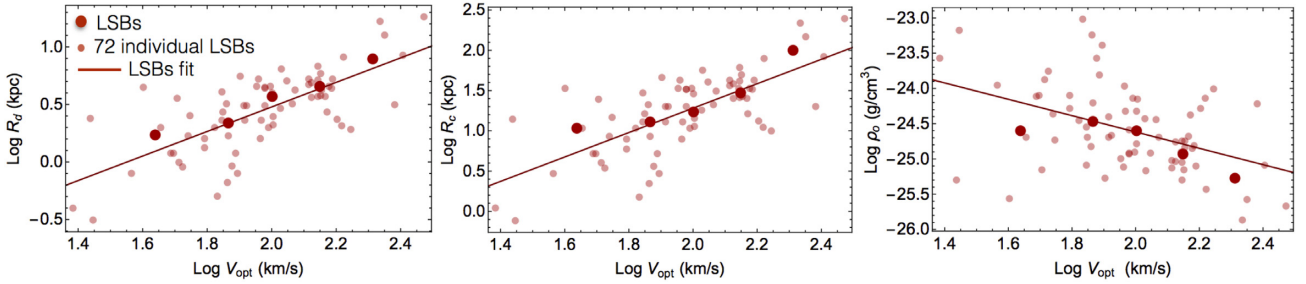


Figure 12. LSBs relationships between (a) the stellar disc scale length, (b) the DM core radius, and (c) the central DM core density versus the optical velocity (first, second, and third panel).

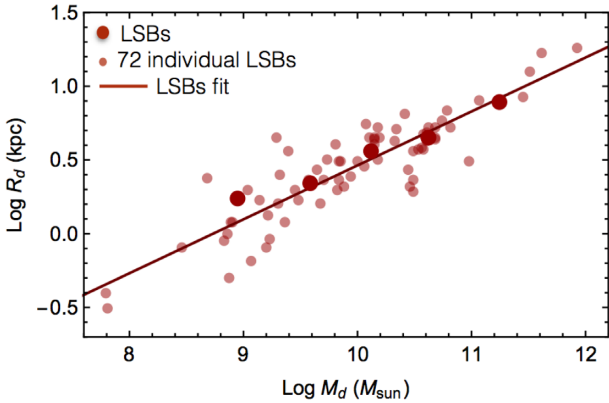


Figure 13. Relationship between the stellar disc scale length and the stellar disc mass.

component⁷ (as in ESO534–G020) are taken into account in the individual RCs. This result, approximately equal to that found in normal spirals (Persic et al. 1996), highlights the success of the URC method also in LSBs galaxies. The smallness of the uncertainty achieved in the URC-LSB (physical) is evident in Appendix I, where the individual RCs are tested. As a gauge we point out that F583-4, NGC 4395, UGC5005, F568V1, ESO444–G074 have a value of $\Delta V/V \simeq 8$ per cent. Moreover, in Appendix I, the individual RCs are tested by assuming (i) $\text{Log } C_* = 0$ and (ii) their values of C_* (reported in Tables G1–G2 in Appendix G).

Finally, in Fig. 16 we show the URC obtained with three significant different values of stellar compactness. The central yellow surface has $\text{Log } C_* = 0.00$ (standard case) and the other two surfaces have $\text{Log } C_* = -0.45$ (the minimum value achieved in the LSB sample) and $\text{Log } C_* = +0.35$ (the maximum one). The three surfaces appear similar, however when we normalize them with respect to V_{opt} along the velocity axis, their profiles appear different, see Fig. 17. Nevertheless, the differences between the URC with $\text{Log } C_* = 0.00$ and the URC with the appropriate values of C_* for each individual object lie within the URC error bars for most of the objects (see Appendix I).

7.1 The relevance of C_* in LSB galaxies

Completing our analysis, we have discovered the relevance of C_* in the LSB galaxies. By resuming, this work shows that:

⁷The bulge component is taken into account in the co-added RCs modelling, but not in the final URC, going beyond the scope of the paper.

(i) the compactness is linked to the spread in the $V_{\text{opt}}-R_d$ plot (Fig. 2). Galaxies at fixed V_{opt} can have smaller R_d (higher C_*) or larger R_d (lower C_*) than the average. The range of $\text{Log } R_d$ at fixed V_{opt} can reach almost 1 dex;

(ii) the profiles of the various RCs can be affected by the compactness (see e.g. Fig. 17). Thus, the spread in the profiles of the RCs in each velocity bin (see Figs 4–5) is not only due to the large width of the optical velocity bins,⁸ but it is also due to the different values of the galaxies compactness.

(iii) the compactness is the main source for the large scatter ($\sigma \simeq 0.34$) in the 2D scaling relations (see Figs 9–14).

Taking all this into account, we point out that in the URC-LSB building procedure, having an improved statistic, the optimal approach would be considering from the start to bin the available RCs in C_* (obtained by the spread of data in the $V_{\text{opt}}-R_d$ plot in Fig. 2) contemporaneously to V_{opt} . Moreover, with a sufficiently higher statistics, we can also increase the number of the velocity bins and characterize each of them with a smaller V_{opt} range to reach the performance of Persic et al. (1996).

Finally, we stress that in the LSBs there is no one-to-one correspondence among the optical velocity, the optical radius, the luminosity, the virial mass, and other galaxies quantities. Then, if we order the RCs normalized in radial units, according to quantities different from the optical velocity (as in Fig. 1), they would not lie on a unique surface but, according to the spread of the stellar compactness among the objects, will give rise to a spread of RC data lying on different surfaces.

8 THE CORRELATION BETWEEN THE COMPACTNESS OF THE STELLAR AND THE DM MASS DISTRIBUTIONS

Following Karukes & Salucci (2017), we evaluate also the compactness of the DM halo C_{DM} , i.e. we investigate the case in which the galaxies with the same virial (dark) mass M_{vir} exhibit different core radius R_c .

The M_{vir} versus R_c relationship is shown in Fig. 18 alongside the best-fitting linear relation, described by

$$\text{Log } R_c = -5.32 + 0.56 \text{Log } M_{\text{vir}}. \quad (23)$$

⁸Given the limited number of available RCs, each optical velocity bin includes galaxies with a certain range in V_{opt} , causing the corresponding RCs to have (moderately) different profiles, analogously to normal spirals.

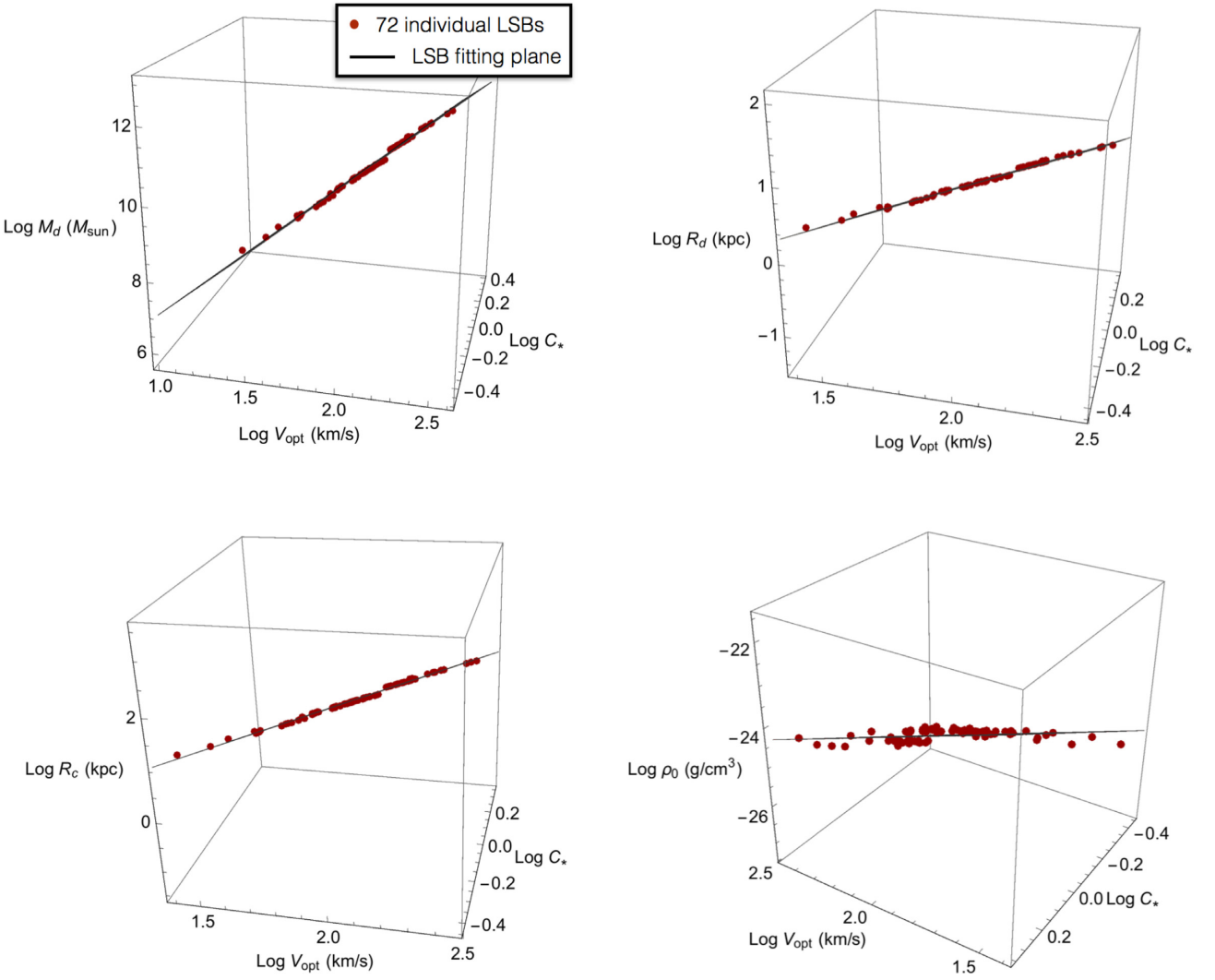


Figure 14. In the panels we show the relationships between (a) the stellar disc mass, (b) the stellar disc scale length, (c) the DM core radius, and (d) the central DM core density versus the optical velocity and the compactness of the stellar distribution. The errors in the distance of galaxies, which propagates on R_c , M_d , R_d , ρ_0 , are negligible in the above for 3D relationships.

Then, according to Karukes & Salucci (2017), we define the compactness C_{DM} of the DM halo as:

$$C_{DM} = \frac{10^{(-5.32+0.56 \text{Log } M_{vir})}}{R_c}. \quad (24)$$

Thus, at fixed M_{vir} , galaxies with smaller R_c have higher compactness ($\text{Log } C_{DM} > 0$), while galaxies with larger R_c have lower compactness ($\text{Log } C_{DM} < 0$).

The values obtained for $\text{Log } C_{DM}$ are reported in Tables G1–G2 in Appendix G and span from -0.57 to 0.30 .

Then, we plot the compactness of the stellar disc versus the compactness of the DM halo in Fig. 19. We note that C_* and C_{DM} are strictly related: galaxies with high C_* , also have high C_{DM} . The logarithmic data are well fitted by the linear relation:

$$\text{Log } C_* = 0.00 + 0.90 \text{Log } C_{DM}. \quad (25)$$

The results are in very good agreement with those obtained for *dd* galaxies (Karukes & Salucci 2017), whose best-fitting relation is given by $\text{Log } C_* = 0.77 \text{Log } C_{DM} + 0.03$. In the figure we realize

that the average difference between the two relationship is just about 0.1 dex.

This result is remarkable because the same relation is found for two very different types of galaxies (LSBs and *dds*). The strong relationship between the two compactness certainly indicates that the stellar and the DM distributions follow each other very closely. In a speculative way, given the very different distribution of luminous matter in an exponential thin disc and the distribution of DM in a spherical cored halo, such strong correlation in equation (25) might point to a non-standard interaction between the baryonic and the DM, a velocity-dependent self-interaction in the dark sector, or a fine-tuned baryonic feedback (e.g. Di Cintio et al. 2014; Chan et al. 2015).

9 CONCLUSIONS

We analysed a sample of 72 LSB galaxies selected from literature, whose optical velocities V_{opt} span from ~ 24 to $\sim 300 \text{ km s}^{-1}$. Their RCs, normalized in the radial coordinate with respect to the stellar disc scale length R_d (or the optical radius R_{opt}) and ordered according

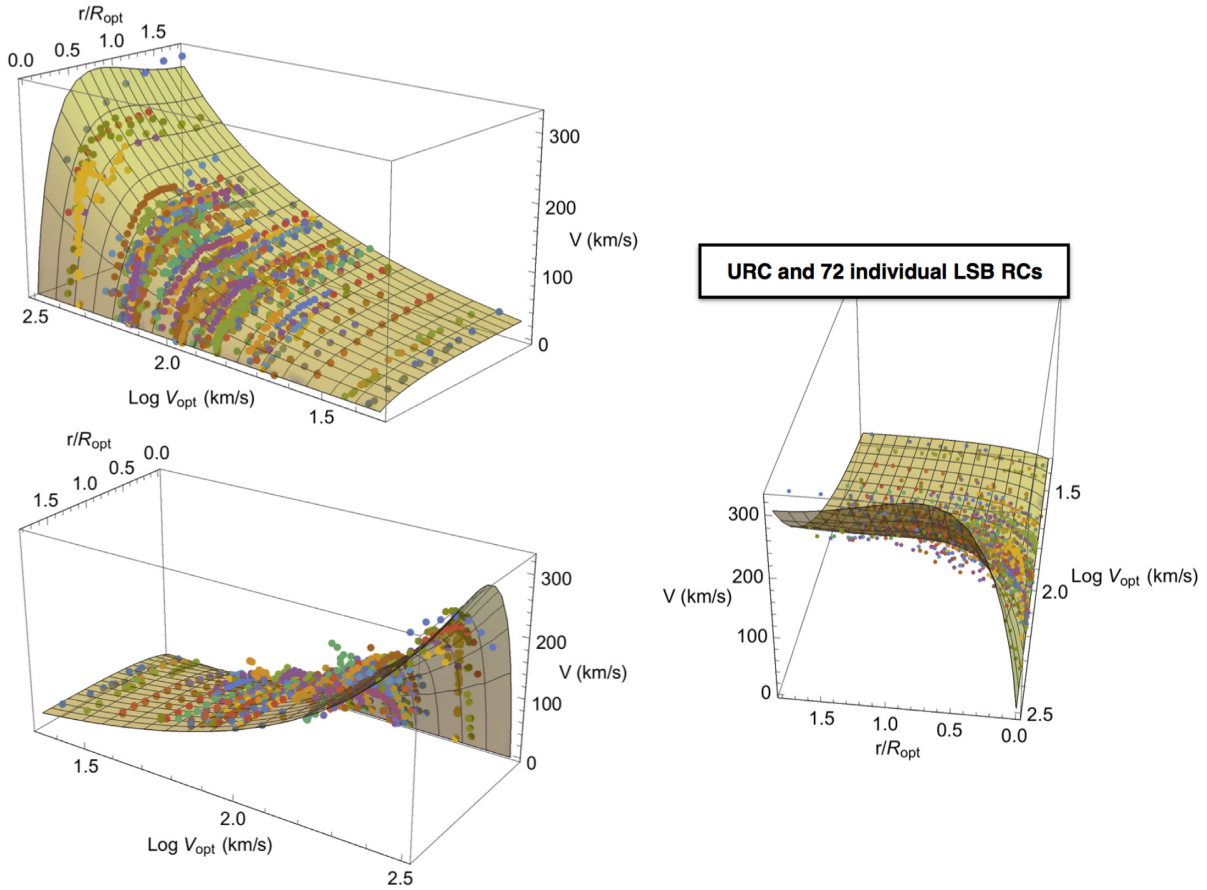


Figure 15. LSBs URC, with compactness $\text{Log } C_* = 0$, and the individual 72 LSBs RCs.

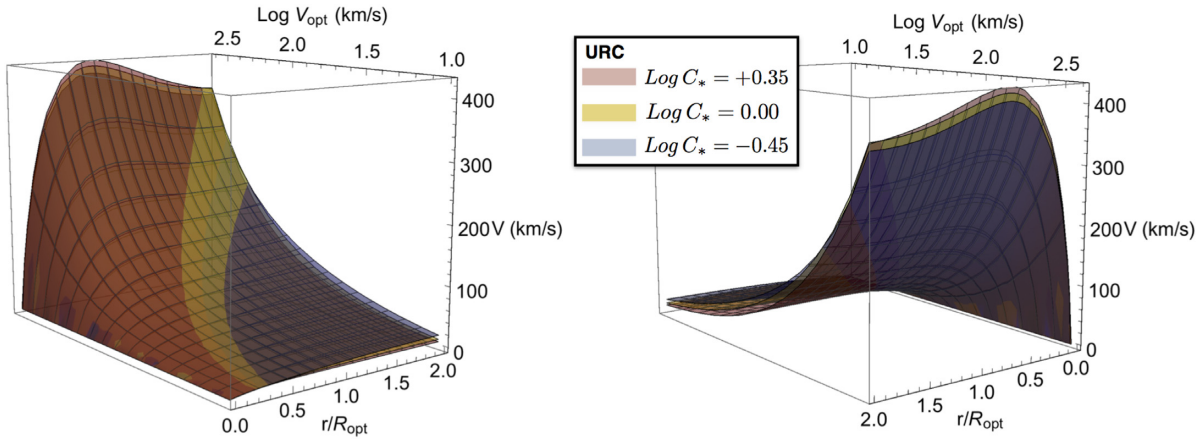


Figure 16. URC in physical velocity units for three different values of stellar compactness: low ($\text{Log } C_* = -0.45$), standard ($\text{Log } C_* = 0.00$), and high ($\text{Log } C_* = +0.35$) stellar compactness, respectively, in *blue*, *yellow*, and *red* colours. The figure in the second panel corresponds to that of the first panel when rotated by 180° around the velocity axis.

to the increasing optical velocity V_{opt} , follow a universal trend (Fig. 1), analogously to the normal (HSB) spirals. This led us to build the URC of LSBs as in Persic et al. (1996), i.e. to find an analytic expression to reproduce any circular velocity by means of only few observable parameters (e.g. R_{opt} and V_{opt}).

The building of the URC allows us to obtain the properties of the stellar and DM distribution and to evaluate the scaling relations valid for the whole population of objects. The analysis on the LSBs

RCs leads us to a scenario which is very similar qualitatively, but not quantitatively, to that of the normal spirals. In detail, in both cases, we observe that the main contribution to the circular velocity, in the innermost galactic region, is given by the stellar disc component, while, in the external region it is given by a cored DM spherical halo. Moreover, the fraction of DM that contributes to the RCs is more relevant as lower V_{opt} is, i.e. in smaller galaxies (Fig. 7).

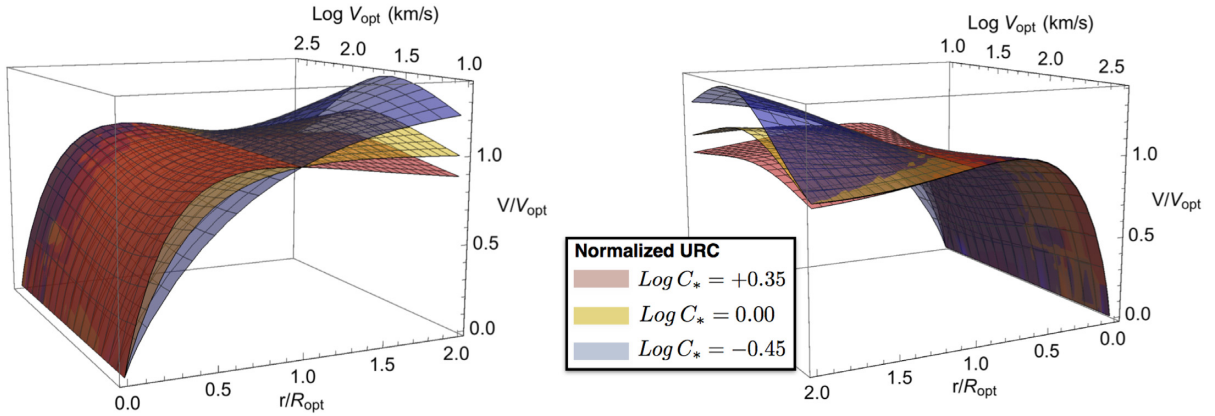


Figure 17. URC in double-normalized units for three values of the stellar compactness: $\text{Log } C_* = -0.45, 0.00, +0.35$, respectively, in *blue, yellow, and red* colours. Notice that the figure in the second panel corresponds to that of the first panel rotated of 180° around the velocity axis.

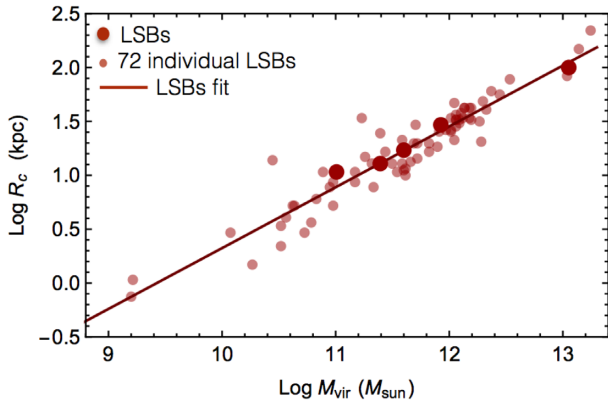


Figure 18. Relationship between the DM halo core radius and the virial mass.

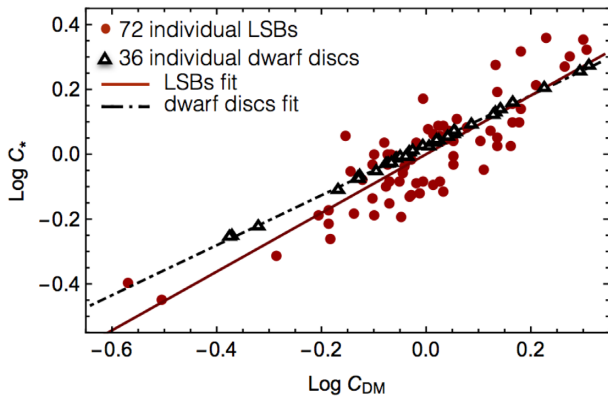


Figure 19. Relationship between the compactness of the stellar disc and the compactness of the DM halo (*red points*). The black triangles refer to the dwarf discs of Karukes & Salucci (2017). The solid and the dot-dashed lines are the best-fitting relations for LSBs and dwarf discs.

The scaling relations among the galactic properties seem to follow a similar trend in LSB galaxies and HSB spirals (Figs 8–10).

On the other side, there is a clear difference: we realize the presence of a large scatter in the LSBs relationships with respect to that found in normal spirals (see Lapi et al. 2018). Such difference can be traced back to the large spread of the $V_{\text{opt}}-R_d$ data (see Fig. 2) or, analogously, to the large spread of the R_d-M_d relationship

in Fig. 13. This finding leads us to introduce the concept of *compactness* of the luminous matter distribution C_* , involved for the first time in Karukes & Salucci (2017) to cope with a similar issue in the case of *dd* galaxies.

We have that in galaxies with a fixed value for M_d , the smaller the R_d , the higher the C_* . By considering C_* in the scaling relations, the scatter is much reduced (it becomes smaller than that of the normal spirals). By involving this new parameter, we proceed with the building of the analytic universal expression to describe all the LSBs RCs (in physical units, km s^{-1} versus kpc). The resulting URC, $V(r; R_{\text{opt}}, V_{\text{opt}}, C_*)$ in equations (21)–(22), well describes all the RCs of our sample (Figs 15 and 11–15). The average scatter of the RCs data from the fitting surface in Fig. 15 achieves the small value of $\Delta V/V \simeq 0.08$, taking into account the observational errors, the systematics, and the small non-circularities in the motion. This result remarks the success of the method leading to the URC and of the relevance of C_* in the RCs profiles (Fig. 17) and in the scaling relations, which has been discovered in building the URC.

With larger statistics, one should subdivide the RCs according to the galaxies C_* and V_{opt} .

An important finding concerns the compactness of the DM distribution C_{DM} , indicating galaxies with the same virial mass and different core radius (Fig. 18). We find a strong correlation between C_* and C_{DM} as also found in Karukes & Salucci (2017) (Fig 19): *the distributions of stellar disc and of its enveloping DM halo are entangled*. In a speculative way, this finding appears to be of very important relevance for the nature of DM. In fact, the strong correlation between C_* and C_{DM} may hint to the existence of non-standard interactions between the luminous matter and the DM, or non-trivial self-interaction in the DM sector or a (hugely) fine-tuned baryonic feedback on the collisionless DM distribution.

Finally, the LSBs URC provides us with the best observational data to test specific density profiles (e.g. NFW, WDM, Fuzzy DM) or alternatives to DM (e.g. MOND). The normal spirals' URC, in connection with the normal spirals' R_{opt} versus V_{opt} relationship, is a function of V_{opt} : $V_{\text{URC(ns)}}(r/R_{\text{opt}}, V_{\text{opt}})$ (*ns* stands for normal spirals). Therefore, to represent *all* the normal spirals' individual RCs it is sufficient to evaluate $V_{\text{URC(ns)}}(r/R_{\text{opt}}, V_{\text{opt}})$ for a reasonable number j of V_{opt} values, homogeneously spread in the spirals V_{opt} range. Any mass model under test must reproduce the V_{opt} -dependent URC. Instead, the LSBs URC, in connection with the LSBs R_{opt} versus V_{opt} and C_* relationship, is a function of *two* galaxy structural properties: V_{opt} and C_* . In this case, to represent *all* the LSBs RCs we have to build $V_{\text{URC(LSB)}}(r/R_{\text{opt}}, V_{\text{opt}}, C_*)$. We need a large sample of RCs

of galaxies of different V_{opt} and C_* yielding a reasonable number of RCs in each of the more numerous (V_{opt} ; C_*) bins we have to employ. The galaxies model under test must reproduce a much complex (observational driven) URC than that of normal spirals which depends on just the structural parameter V_{opt} .

ACKNOWLEDGEMENTS

We thank E. Karukes and A. Lapi for useful discussions. We thank Brigitte Greinöcker for improving the text. We thank the referee for her/his several inputs that have improved the paper.

REFERENCES

- Bell E. F., Barnaby D., Bower R. G., de Jong R. S., Harper D. A., Hereld M., Loewenstein R. F., Rauscher B. J., 2000, *MNRAS*, 312, 470
- Bothun G. D., Schombert J. M., Impey C. D., Sprayberry D., McGaugh S. S., 1993, *AJ*, 106, 530
- Boylan-Kolchin M., Bullock J. S., Kaplinghat M., 2012, *MNRAS*, 422, 1203
- Bullock J. S., Boylan-Kolchin M., 2017, *ARA&A*, 55, 343
- Burkert A., 1995, *ApJ*, 447, L25
- Burkert A., 2015, *ApJ*, 808, 158
- Carignan C., Puche D., 1990, *AJ*, 100, 641C
- Catinella B., Giovanelli R., Haynes M. P., 2006, *ApJ*, 640, 751
- Chan M., 2019, *Sci. Rep.*, 9, 3570
- Chan T. K., Kereš D., Oñorbe J., Hopkins P. F., Muratov A. L., Faucher-Giguère C.-A., Quataert E., 2015, *MNRAS*, 454, 2981
- Das M., 2013, *J. Astrophys. Astron.*, 34, 19
- de Blok W. J. G., van der Hulst J., Bothun G., 1995, *MNRAS*, 274, 235
- de Blok W. J. G., Bosma A., 2002, *A&A*, 385, 816
- de Blok W. J. G., McGaugh S. S., 1997, *MNRAS*, 290, 533
- de Blok W. J. G., McGaugh S. S., van der Hulst J. M., 1996, *MNRAS*, 283, 18
- de Blok W. J. G., McGaugh S. S., Rubin V. C., 2001, *AJ*, 122, 2381
- de Vega H. J., Moreno O., Moya de Guerra E., Ramón Medrano M., Sánchez N. G., 2013, *Nucl. Phys. B.*, 866, 177
- Del Popolo A., Kroupa P., 2009, *A&A*, 502, 733
- Di Cintio A., Brook C. B., Macciò A. V., Stinson G. S., Knebe A., Dutton A. A., Wadsley J., 2014, *MNRAS*, 437, 415
- Donato F. et al., 2009, *MNRAS*, 397, 1169
- Elbert O. D., Bullock J. S., Garrison-Kimmel S., Rocha M., Oñorbe J., Peter A. H. G., 2015, *MNRAS*, 453, 29
- Evoli C., Salucci P., Lapi A., Danese L., 2011, *ApJ*, 743, 45
- Faber S. M., Gallagher J. S., 1979, *ARA&A*, 17, 135
- Ferrero I., Abadi M. G., Navarro J. F., Sales L. V., Gurovich S., 2012, *MNRAS*, 425, 2817
- Freeman K. C., 1970, *ApJ*, 160, 811
- Garrison-Kimmel S., Boylan-Kolchin M., Bullock J. S., Kirby E. N., 2014, *MNRAS*, 444, 222
- Gentile G., Salucci P., Klein U., Vergani D., Kalberla P., 2004, *MNRAS*, 351, 903
- Gentile G., Burkert A., Salucci P., Klein U., Walter F., 2005, *ApJ*, 634, L145
- Gentile G., Famaey B., Zhao H., Salucci P., 2009, *Nature*, 461, 627
- Karukes E. V., Salucci P., 2017, *MNRAS*, 465, 4703
- Klypin A., Kravtsov A. V., Valenzuela O., Prada F., 1999, *ApJ*, 522, 82
- Klypin A., Karachentsev I., Makarov D., Nasonova O., 2015, *MNRAS*, 454, 1798
- Kolb E. W., Turner M. S., 1990, *The Early Universe*. Addison Wesley, Redwood City, CA
- Kuzio de Naray R., McGaugh S. S., de Blok W. J. G., Bosma A., 2006, *ApJS*, 165, 461
- Kuzio de Naray R., McGaugh S. S., de Blok W. J. G., 2008, *ApJ*, 676, 920
- Lapi A., Salucci P., Danese L., 2018, *ApJ*, 859, 2
- Li P., Lelli F., McGaugh S. S., Starkman N., Schombert J. M., 2019, *MNRAS*, 482, 5106
- López Fune E., 2018, *MNRAS*, 475, 2132
- Lovell M. R., Frenk C. S., Eke V. R., Jenkins A., Gao L., Theuns T., 2014, *MNRAS*, 439, 300
- Marchesini D., D'Onghia E., Chincarini G., Firmani C., Conconi P., Molinari E., Zacchei A., 2002, *ApJ*, 575, 801
- Mashchenko S., Couchman H. M. P., Wadsley J., 2006, *Nature*, 442, 539
- McGaugh S. S., 1994, *ApJ*, 426, 135
- Memola E., Salucci P., Babić A., 2011, *A&A*, 534, A50
- Moore B., Ghigna S., Governato F., Lake G., Quinn T., Stadel J., Tozzi P., 1999, *ApJ*, 524, L19
- Morelli L., Corsini E. M., Pizzella A., Dalla Bontà E., Coccato L., Méndez-Abreu J., Cesetti M., 2012, *MNRAS*, 423, 962
- Moster B., Somerville R., Maubetsch C., van den Bosch F., Macciò A., Naab N., Oser L., 2010, *ApJ*, 710, 903
- Navarro J. F., Eke V. R., Frenk C. S., 1996, *MNRAS*, 283, L72
- Noordermeer E., van der Hulst J. M., Sancisi R., Swaters R. S., van Albada T. S., 2007, *MNRAS*, 376, 1513
- Oh S.-H., de Blok W. J. G., Brinks E., Walter F., Kennicutt J. R. C., 2011, *AJ*, 141, 193
- Palunas P., Williams T. B., 2000, *AJ*, 120, 2884
- Papastergis E., Martin A. M., Giovanelli R., Haynes M. P., 2011, *ApJ*, 739, 38
- Papastergis E., Giovanelli R., Haynes M. P., Shankar F., 2015, *A&A*, 574, A113
- Persic M., Salucci P., 1991, *ApJ*, 368, 60
- Persic M., Salucci P., Stel F., 1996, *MNRAS*, 281, 27
- Pickering T. E., Impey C. D., van Gorkom J. H., Bothun G. D., 1997, *AJ*, 114, 1858
- Pickering T. E., van Gorkom J. H., Impey C. D., Quillen A. C., 1999, *AJ*, 118, 765
- Pizzella A., Corsini E. M., Sarzi M., Magorrian J., Méndez-Abreu J., Coccato L., Morelli L., Bertola F., 2008, *MNRAS*, 387, 1099
- Plana H., Amram P., Mendes de Oliveira C., Balkowski C., 2010, *AJ*, 139, 1
- Pontzen A., Governato F., 2014, *Nature*, 506, 171
- Read J. L., Gilmore G., 2005, *MNRAS*, 356, 107
- Rhee M. H., 1996, PhD thesis, Univ. Groningen
- Roscoe D. F., 1999, *Pramana*, 53, 1033
- Rosenbaum S. D., Bomans D. J., 2004, *A&A*, 422, L5
- Rubin V. C., Burstein D., Ford J. W. K., Thonnard N., 1985, *ApJ*, 289, 81
- Salucci P., 2001, *MNRAS*, 320, L1
- Salucci P., Martins C. F., Lapi A., 2010, <http://www.sissa.it/ap/dmg/dmaw/presentation.html>
- Salucci P., 2019, *A&AR*, 27, 2
- Salucci P., Burkert A., 2000, *ApJ*, 537, L9
- Salucci P., Lapi A., Tonini C., Gentile G., Yegorova I., Klein U., 2007, *MNRAS*, 378, 41
- Salucci P., Wilkinson M. I., Walker M. G., Gilmore G. F., Grebel E. K., Koch A., Frigerio Martins C., Wyse R. F. G., 2012, *MNRAS*, 420, 2034
- Simon J. D., Bolatto A. D., Leroy A., Blitz L., Gates E. L., 2005, *ApJ*, 621, 757
- Spano M., Marcellin M., Amram P., Carignan C., Epinat B., Hernandez O., 2008, *MNRAS*, 383, 297
- Swaters R. A., Madore B. F., Trewella M., 2000, *ApJ*, 531, L107
- Swaters R. A., Madore B. F., van den Bosch F. C., Balcells M., 2003, *ApJ*, 583, 732
- van Zee L., Haynes M. P., Salzer J. J., Broeils A. H., 1997, *AJ*, 113, 1618
- van den Bosch F. C., Swaters R. A., 2001, *MNRAS*, 325, 1017
- van der Hulst J. M., Skillman E. D., Smith T. R., Bothun G. D., McGaugh S. S., de Blok W. J. G., 1993, *AJ*, 106, 548
- Vogelsberger M., Zavala J., Simpson C., Jenkins A., 2014, *MNRAS*, 444, 3684
- Weinberg D. H., Bullock J. S., Governato F., Kuzio de Naray R., Peter A. H. G., 2015, *Proc. Natl. Acad. Sci.*, 112, 12249
- Yegorova I. A., Salucci P., 2007, *MNRAS*, 377, 507
- Zavala J., Jing Y. P., Faltenbacher A., Yepes G., Hoffman Y., Gottlöber S., Catinella B., 2009, *ApJ*, 700, 1779
- Zwaan M. A., van der Hulst J. M., de Blok W. J. G., McGaugh S. S., 1995, *MNRAS*, 273, L35

SUPPORTING INFORMATION

Supplementary data are available at [MNRAS](#) online.

LSBdata.txt

Please note: Oxford University Press is not responsible for the content or functionality of any supporting materials supplied by the authors. Any queries (other than missing material) should be directed to the corresponding author for the article.

APPENDIX A: UNIVERSALITY IN NORMAL SPIRALS

Fig. A1, from Persic et al. (1996) and Catinella et al. (2006), allows us to appreciate the *universality* of the RCs in normal spirals after the radial normalization. Let us point out the trend of the RCs from small to large galaxies.

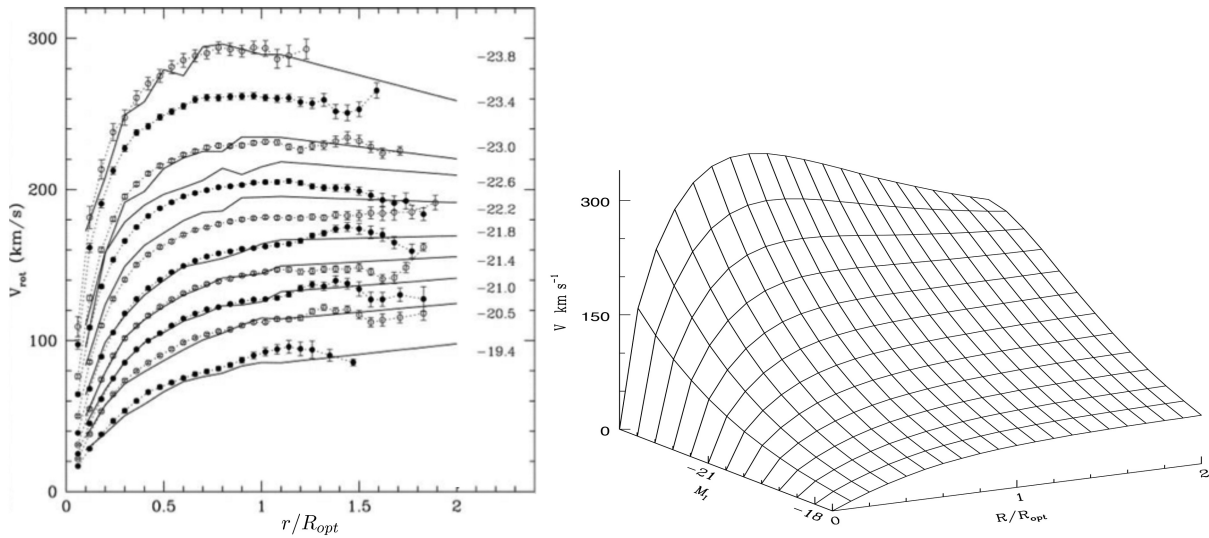


Figure A1. Top panel: co-added RCs from 3100 normal spirals, obtained by plotting together the results by Persic et al. (1996) and Catinella et al. (2006) (originally in the slides by Salucci 2010). Also indicated are the absolute I-magnitudes. Bottom panel: URC (Persic et al. 1996).

APPENDIX B: LSB GALAXIES SAMPLE AND REFERENCES

In Table B1, we report the list of the LSB galaxies of this work with their related references.

APPENDIX C: ROTATION CURVES IN PHYSICAL UNITS

In Fig. C1, the 72 LSB RCs are shown in physical units. Here, all the data are included, while the first panel of Fig. 3 includes only data with $r \leq 30$ kpc.

Table B1. LSB sample: galaxy names and references of their RCs and photometric data. Note that some galaxies have multiple RC data.

Galaxy	Reference	Galaxy	Reference
NGC 100	de Blok & Bosma (2002)	UGC 11557	Swaters et al. (2003)
NGC 247	Carignan & Puche (1990)	UGC 11583	de Blok et al. (2001)
NGC 959	Kuzio de Naray et al. (2008)	UGC 11616	de Blok et al. (2001)
NGC 2552	Kuzio de Naray et al. (2008)	UGC 11648	de Blok et al. (2001)
NGC 2552	de Blok & Bosma (2002)	UGC 11748	de Blok et al. (2001)
NGC 2552	Swaters et al. (2003)	UGC 11819	de Blok et al. (2001)
NGC 2552	van den Bosch & Swaters (2001)	ESO 186–G055	Pizzella et al. (2008)
NGC 3274	de Blok & Bosma (2002)	ESO 206–G014	Pizzella et al. (2008)
NGC 3274	Swaters et al. (2003)	ESO 215–G039	Palunas & Williams (2000)
NGC 3347B	Palunas & Williams (2000)	ESO 234–G013	Pizzella et al. (2008)
NGC 4395	de Blok & Bosma (2002)	ESO 268–G044	Palunas & Williams (2000)
NGC 4395	van den Bosch & Swaters (2001)	ESO 322–G019	Palunas & Williams (2000)
NGC 4455	de Blok & Bosma (2002)	ESO 323–G042	Palunas & Williams (2000)
NGC 4455	Marchesini et al. (2002)	ESO 323–G073	Palunas & Williams (2000)
NGC 4455	van den Bosch & Swaters (2001)	ESO 374–G003	Palunas & Williams (2000)
NGC 5023	de Blok & Bosma (2002)	ESO 382–G006	Palunas & Williams (2000)
NGC 5204	Swaters et al. (2003)	ESO 400–G037	Pizzella et al. (2008)
NGC 5204	van den Bosch & Swaters (2001)	ESO 444–G021	Palunas & Williams (2000)
NGC 7589	Pickering et al. (1997)	ESO 444–G047	Palunas & Williams (2000)
UGC 628	de Blok & Bosma (2002)	ESO 488–G049	Pizzella et al. (2008)
UGC 634	van Zee et al. (1997)	ESO 509–G091	Palunas & Williams (2000)
UGC 731	de Blok & Bosma (2002)	ESO 534–G020	Pizzella et al. (2008)
UGC 731	Swaters et al. (2003)	F561-1	de Blok et al. (1996)
UGC 731	van den Bosch & Swaters (2001)	F563-V1	de Blok et al. (1996)
UGC 1230	de Blok & Bosma (2002)	F563-V2	Kuzio de Naray et al. (2006)
UGC 1230	van der Hulst et al. (1993)	F563-V2	de Blok et al. (1996)
UGC 1281	Kuzio de Naray et al. (2006)	F565-V2	de Blok et al. (1996)
UGC 1281	de Blok & Bosma (2002)	F568-1	Swaters, Madore & Trewhella (2000)
UGC 1551	Kuzio de Naray et al. (2008)	F568-3	Kuzio de Naray et al. (2006)
UGC 2684	van Zee et al. (1997)	F568-3	de Blok et al. (2001)
UGC 2936	Pickering et al. (1999)	F568-3	Swaters et al. (2000)
UGC 3137	de Blok & Bosma (2002)	F568-6	Pickering et al. (1997)
UGC 3174	van Zee et al. (1997)	F568-V1	Swaters et al. (2000)
UGC 3371	de Blok & Bosma (2002)	F571-8	Marchesini et al. (2002)
UGC 3371	van den Bosch & Swaters (2001)	F571-8	de Blok et al. (2001)
UGC 4115	de Blok et al. (2001)	F571-V1	de Blok et al. (1996)
UGC 4278	de Blok & Bosma (2002)	F574-1	Swaters et al. (2000)
UGC 5005	de Blok & McGaugh (1997)	F574-2	de Blok et al. (1996)
UGC 5272	Kuzio de Naray et al. (2008)	F579-V1	de Blok et al. (2001)
UGC 5272	de Blok & Bosma (2002)	F583-1	Kuzio de Naray et al. (2008)
UGC 5716	van Zee et al. (1997)	F583-1	Marchesini et al. (2002)
UGC 5750	Kuzio de Naray et al. (2006)	F583-1	de Blok et al. (2001)
UGC 5750	de Blok & Bosma (2002)	F583-1	de Blok et al. (1996)
UGC 5999	van der Hulst et al. (1993)	F583-4	Kuzio de Naray et al. (2006)
UGC 7178	van Zee et al. (1997)	F583-4	de Blok et al. (2001)
UGC 8837	de Blok & Bosma (2002)	F730-V1	de Blok et al. (2001)
UGC 9211	van den Bosch & Swaters (2001)	PGC 37759	Morelli et al. (2012)
UGC 11454	de Blok et al. (2001)		

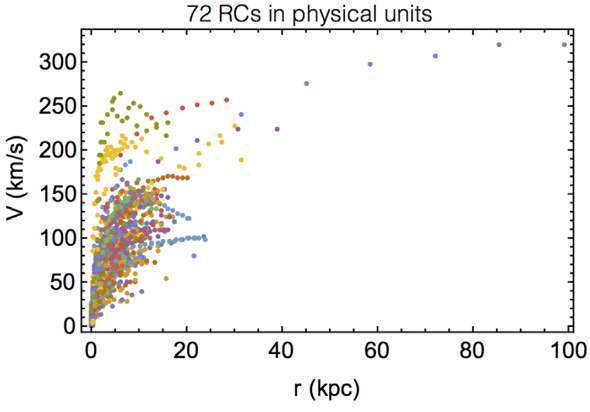


Figure C1. The 72 LSB RCs in physical units (all data).

APPENDIX D: ROTATION CURVES IN VELOCITY BINS

In Fig. D1 we show the LSBs RCs separately in the five velocity bins, both in physical units and in double-normalized units (i.e. along the radial and the velocity axes).

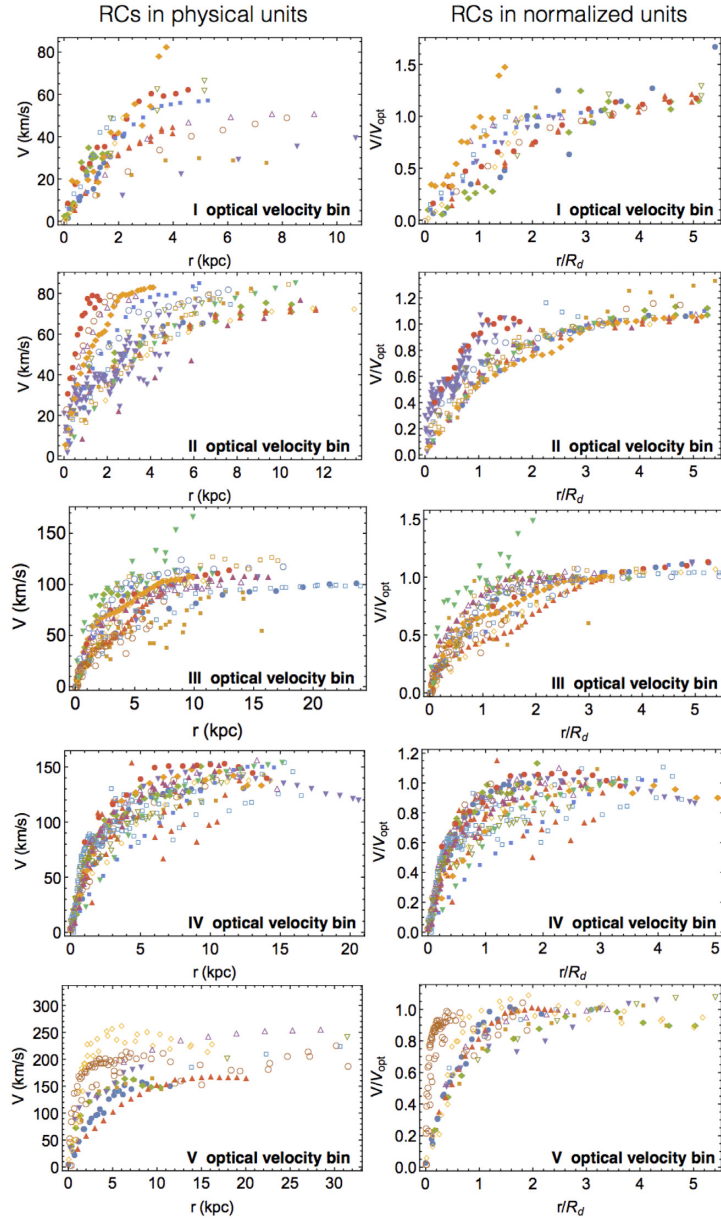


Figure D1. LSBs RCs belonging to each of the five optical velocity bins.

APPENDIX E: CONSTRUCTION OF THE CO-ADDED ROTATION CURVES

In Tables E1–E2 we show the data related to the five co-added RCs obtained in Section 3. In detail, the first column describes the centre of the radial bins represented by the coloured points in Figs 5–7. The second column indicates the number of RCs data (grey points in Fig. 5) belonging to each radial bin. Finally, the third and the fourth columns show the velocity data and their error bars in physical units, related to the co-added RCs in the second panel of Fig. 6 and in Fig. 7.

Table E1. RCs for each optical velocity bin of LSB galaxies. Columns: (1) centre of the radial bin; (2) number of data in each bin; (3) co-added velocity for each bin; (4) velocity error. In order to express the radial coordinate in physical units, the data of the first column relative to each velocity bin must be multiplied by the respective average value of disc scale length ($\langle R_D \rangle$), reported in Table 1.

r/R_D	N. data	V km s ⁻¹	Error bar km s ⁻¹
(1)	(2)	(3)	(4)
I velocity bin			
0.2	15	7.3	1.2
0.6	19	16.7	1.7
1.0	18	25.6	2.4
1.4	19	34.2	3.1
1.8	13	37.1	1.6
2.25	13	42.4	1.4
2.75	10	41.9	2.1
3.25	13	45.5	0.9
3.75	5	48.4	0.7
4.25	5	51.1	1.4
4.75	5	49.9	1.1
5.25	5	56.4	4.2
II velocity bin			
0.2	62	25.0	1.5
0.6	70	40.0	1.3
1.0	39	52.0	1.9
1.4	26	56.5	1.9
1.8	26	62.3	1.2
2.25	23	64.8	1.3
2.75	23	70.7	0.8
3.25	16	74.3	0.5
3.75	15	76.3	1.2
4.25	12	78.6	1.4
4.75	12	81.0	1.6
5.25	9	81.7	2.1
III velocity bin			
0.2	86	25.3	1.8
0.6	56	53.7	1.9
1.0	46	71.8	2.7
1.4	45	81.1	2.8
1.8	35	89.9	3.2
2.25	39	93.6	1.3
2.75	29	97.2	1.7
3.25	20	101.3	0.5
3.75	10	104.0	0.8
4.25	8	106.9	1.0
4.75	10	107.8	1.4
5.25	6	107.9	2.0

Table E2. It continues from Table E1.

r/R_D	N. data	V km s ⁻¹	Error bar km s ⁻¹
(1)	(2)	(3)	(4)
IV velocity bin			
0.2	141	47.9	2.2
0.6	81	90.4	2.0
1.0	54	112.2	2.6
1.5	58	121.8	2.2
2.1	41	128.6	3.1
2.7	28	133.7	2.9
3.3	17	136.0	2.5
3.9	9	138.9	3.0
4.7	8	129.5	2.8
V velocity bin			
0.2	71	127.1	7.2
0.6	32	148.7	6.1
1.	23	173.9	3.5
1.4	14	197.6	3.7
1.8	16	194.8	4.9
2.25	14	198.2	3.4
2.75	5	199.3	5.2
3.25	9	205.5	1.5
3.75	6	203.2	4.0
4.4	8	199.6	5.3
5.2	5	195.2	6.9

APPENDIX F: THE GAS COMPONENT IN THE ROTATION CURVES

The gas disc component in galaxies is an additional component to the stellar disc and the DM halo giving a contribution to the circular velocities. At any rate, by performing a suitable test, it is possible to realize that the gas is (moderately) important only in the first optical velocity bin, where, in any case, in the inner regions the stellar component overcomes the gaseous one, while in the external region the DM component overcomes the gaseous one; thus, the gas component gives a modest contribution to the RC. In Fig. F1, for the first velocity bin co-added RC, we compare the mass–velocity model fit that includes the contribution from a H I disc with the velocity–mass model which does not. The estimated masses of the stellar disc and of the DM halo show, in the two cases, only a moderate change.

By modelling the co-added RC of the first V_{opt} bin by means of the stellar/H I disc + DM halo model we get:

$$M_d = 8.0 \times 10^8 M_\odot;$$

$$r_0 = 10.7 \text{ kpc};$$

$$\rho_0 = 3.2 \times 10^{-3} M_\odot \text{ pc}^{-3};$$

$$M_{\text{vir}} = 8.2 \times 10^{10} M_\odot;$$

$$M_{\text{HI}} = 1.0 \times 10^9 M_\odot.$$

By removing the gaseous disc, we get:

$$M_d = 8.8 \times 10^8 M_\odot;$$

$$r_0 = 10.7 \text{ kpc};$$

$$\rho_0 = 3.7 \times 10^{-3} M_\odot \text{ pc}^{-3};$$

$$M_{\text{vir}} = 1.0 \times 10^{11} M_\odot.$$

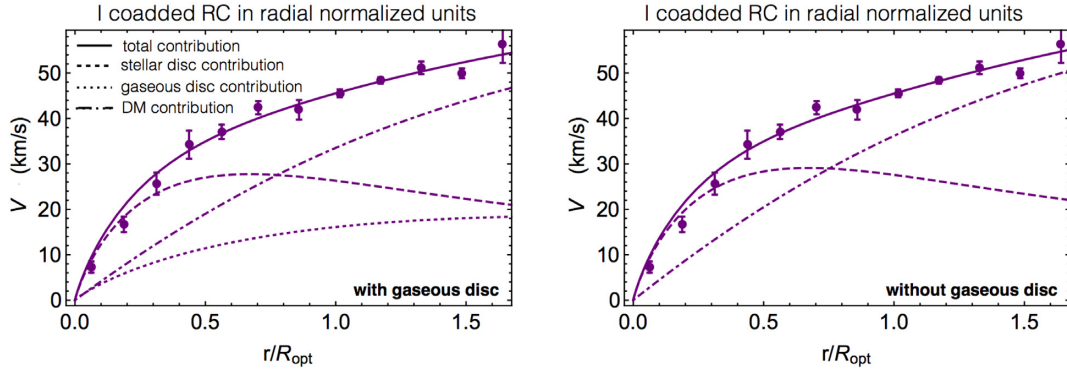


Figure F1. I velocity bin RC best fitted with gas (*left-hand panel*) and without gas (*right-hand panel*). The *dashed*, *dot-dashed*, *dotted*, and *solid* lines stand for the stellar disc, the DM halo, the gaseous disc, and the total contributions to the RC.

We remind that M_d , r_0 , ρ_0 , M_{HI} (all quantities inferred by the fit) are the stellar disc mass, the DM halo core radius, the central core mass density, the HI gaseous disc mass (including the correction for the helium contribution), respectively. M_{vir} is the virial mass. The differences in the values of M_d , r_0 , ρ_0 , M_{vir} , when we include gas or we exclude the gaseous component, are inside the error bars reported in Table 2 related to the fit without the HI disc.

APPENDIX G: STRUCTURAL PROPERTIES OF LSB GALAXIES

In Tables G1–G2 we report: the names of the LSB galaxies in our sample alongside their distances D , the stellar disc scale lengths R_d , and the optical velocities V_{opt} (all taken from literature). Furthermore, the table shows the values of the stellar disc mass M_d , the DM core radius R_c , the central density of the DM halo ρ_0 , the virial mass M_{vir} , the central surface density $\Sigma_0 = \rho_0 R_c$, the compactness of the stellar mass distribution C_* , and that of the DM mass distribution C_{DM} , all evaluated in this work.

Table G1. Individual properties of LSBs. Columns: (1) galaxy name; (2) distance; (3) disc scale length; (4) optical velocity; (5) disc mass; (6) core radius; (7) central DM density; (8) virial mass; (9) central surface density; (10) compactness of stellar mass distribution; (11) compactness of the DM mass distribution.

Name	D Mpc	R_d kpc	V_{opt} km s^{-1}	M_d $10^7 M_\odot$	R_c kpc	$\text{Log } \rho_0$ g cm^{-3}	M_{vir} $10^9 M_\odot$	$\text{Log } \Sigma_0$ $M_\odot \text{pc}^{-2}$	$\text{Log } C_*$	$\text{Log } C_{\text{DM}}$
(1)	(2)	(3)	(4)	(5)	(6)	(7)	(8)	(9)	(10)	(11)
UGC4115	7.8	0.4	24.2	6.3	1.1	-23.57	1.6	1.63	0.06	-0.15
F563V1	51.0	2.4	27.3	48	14	-25.30	27	1.01	-0.40	-0.57
UGC11583	5.9	0.3	27.9	6.5	0.7	-23.17	1.6	1.88	0.17	-0.00
UGC2684	8.2	0.8	36.7	29	2.9	-23.95	12	1.69	-0.00	-0.10
F574-2	66.0	4.5	40.0	192	33	-25.57	171	1.13	-0.45	-0.50
F565V2	36.0	2.0	45.2	110	11	-24.69	76	1.51	-0.19	-0.21
UGC5272	6.1	1.2	48.8	77	5.2	-24.11	42	1.77	-0.02	-0.04
UGC8837	5.1	1.2	49.6	79	5.2	-24.10	44	1.78	-0.02	-0.03
F561-1	63.0	3.6	50.8	250	25	-25.15	244	1.41	-0.31	-0.28
UGC3174	11.8	1.0	51.7	72	4.0	-23.88	36	1.89	0.04	0.04
NGC 4455	6.8	0.9	53.0	68	3.4	-23.75	33	1.96	0.08	0.08
UGC1281	5.5	1.7	55.0	138	8.5	-24.36	96	1.74	-0.08	-0.05
UGC1551	20.2	2.5	55.8	211	15	-24.73	182	1.61	-0.18	-0.14
UGC9211	12.6	1.3	61.9	165	5.9	-24.10	66	1.84	0.06	0.01
F583-1	1.6	1.6	62.0	201	7.8	-24.29	90	1.77	0.00	-0.03
UGC5716	24.1	2.0	66.4	288	11	-24.45	150	1.75	-0.03	-0.04
UGC7178	24.0	2.3	69.9	367	13	-24.54	210	1.74	-0.06	-0.04
ESO400-G037	37.5	4.1	69.9	651	29	-25.09	502	1.55	-0.21	-0.18
NGC 3274	0.47	0.5	68.0	75	1.5	-23.01	18	2.33	0.35	0.30
F583-4	49.0	2.7	70.5	438	16	-24.69	275	1.69	-0.10	-0.08
F571V1	79.0	3.2	72.4	549	21	-24.83	382	1.66	-0.14	-0.10
NGC 5204	4.9	0.7	73.1	115	2.2	-23.24	33	2.27	0.30	0.27
UGC731	8.0	1.7	73.3	298	8.5	-24.20	147	1.90	0.04	0.05
NGC 959	7.8	0.9	75.3	172	3.6	-23.57	60	2.15	0.21	0.21
NGC 100	11.2	1.2	77.2	233	5.2	-23.81	96	2.07	0.15	0.16
NGC 5023	4.8	0.8	78.4	160	2.9	-23.38	52	2.25	0.27	0.27
UGC5750	56.0	5.6	80.0	1171	46	-25.27	1125	1.56	-0.26	-0.18
UGC3371	12.8	3.1	82.0	681	20	-24.69	494	1.78	-0.09	-0.02

Table G1 – *continued*

Name	D Mpc	R_d kpc	V_{opt} km s^{-1}	M_d $10^7 M_{\odot}$	R_c kpc	$\text{Log } \rho_0$ g cm^{-3}	M_{vir} $10^9 M_{\odot}$	$\text{Log } \Sigma_0$ $M_{\odot} \text{pc}^{-2}$	$\text{Log } C_*$	$\text{Log } C_{\text{DM}}$
(1)	(2)	(3)	(4)	(5)	(6)	(7)	(8)	(9)	(10)	(11)
NGC 4395	3.5	2.3	82.3	509	13	−24.40	312	1.89	−0.00	0.05
UGC11557	23.8	3.1	83.7	710	20	−24.67	520	1.80	−0.08	−0.01
UGC1230	51.0	4.5	90.0	1278	34	−24.99	1027	1.71	−0.15	−0.07
ESO206–G014	60.3	5.2	91.3	1531	42	−25.12	1338	1.67	−0.19	−0.10
NGC 2552	10.1	1.6	92.0	475	7.8	−23.97	213	2.09	0.14	0.18
UGC4278	10.5	2.3	92.6	691	13	−24.32	386	1.96	0.04	0.10
UGC634	35.0	3.1	95.1	984	20	−24.59	662	1.88	−0.03	0.05
ESO488–G049	23.0	4.4	95.3	1410	33	−24.92	1159	1.76	−0.13	−0.03
UGC5005	52.0	4.4	95.5	1406	33	−24.92	1153	1.77	−0.13	−0.03
UGC3137	18.4	2.0	97.7	669	11	−24.14	350	2.06	0.10	0.17
F574-1	96.0	4.5	99.0	1546	34	−24.91	1306	1.79	−0.12	−0.01
F568-3	77.0	4.0	100.5	1416	29	−24.78	1130	1.84	−0.08	0.02
ESO322–G019	45.2	2.5	100.7	878	14	−24.32	528	2.01	0.05	0.14
F563V2	61.0	2.1	101.3	755	11	−24.15	412	2.07	0.10	0.18
NGC 247	2.5	2.9	106.6	1156	18	−24.42	784	2.00	0.02	0.13
ESO444–G021	60.7	6.4	107.4	2603	56	−25.17	2760	1.75	−0.19	−0.05
F579V1	85.0	5.1	111.5	2223	40	−24.92	2134	1.85	−0.12	0.03
F568V1	80.0	3.2	115.8	1505	21	−24.44	1119	2.04	0.02	0.16
ESO374–G003	43.2	4.2	118.3	2084	31	−24.70	1856	1.97	−0.05	0.11
F568-1	85.0	5.3	130.0	4218	43	−25.13	1354	1.67	−0.03	−0.10
UGC628	65.0	4.7	130.0	3740	36	−25.02	1132	1.71	0.00	−0.07
UGC11616	72.8	4.9	133.2	4094	38	−25.04	1282	1.71	−0.00	−0.07
ESO186–G055	60.1	3.6	133.2	3041	25	−24.76	813	1.81	0.08	0.00
ESO323–G042	59.7	4.4	138.7	4020	33	−24.91	1221	1.78	0.04	−0.02
PGC37759	193.2	6.8	139.4	6195	60	−25.30	2318	1.65	−0.08	−0.12
ESO234–G013	60.9	3.7	139.4	3425	26	−24.74	949	1.84	0.08	0.02
F571-8	48.0	5.2	139.5	4765	42	−25.05	1577	1.73	−0.00	−0.05
F730V1	144.0	5.8	141.6	5523	49	−25.15	1953	1.71	−0.03	−0.07
UGC11648	46.7	3.8	142.2	3620	27	−24.74	1022	1.85	0.09	0.03
ESO215–G039	61.3	4.2	142.9	4037	31	−24.83	1208	1.82	0.06	0.01
ESO509–G091	72.8	3.7	146.8	3735	25	−24.68	1050	1.89	0.11	0.06

Table G2. It continues from Table G1.

Name	D Mpc	R_d kpc	V_{opt} km s^{-1}	M_d $10^7 M_{\odot}$	R_c kpc	$\text{Log } \rho_0$ g cm^{-3}	M_{vir} $10^9 M_{\odot}$	$\text{Log } \Sigma_0$ M_{\odot}/pc^2	$\text{Log } C_*$	$\text{Log } C_{\text{DM}}$
(1)	(2)	(3)	(4)	(5)	(6)	(7)	(8)	(9)	(10)	(11)
ESO444–G047	62.4	2.7	148.4	2809	16	−24.38	662	2.01	0.19	0.13
UGC11454	92.1	4.5	150.3	4787	34	−24.85	1525	1.85	0.06	0.03
UGC5999	45.0	4.4	153.0	4851	33	−24.82	1540	1.87	0.07	0.04
UGC11819	59.2	5.3	154.6	6578	43	−25.10	1490	1.70	0.04	−0.08
ESO382–G006	65.4	2.3	160.0	3097	13	−24.29	449	2.01	0.27	0.13
ESO323–G073	69.6	2.1	165.3	2923	11	−24.14	398	2.08	0.32	0.18
NGC 3347B	46.2	8.1	167.0	11760	78	−25.43	3369	1.63	−0.05	−0.14
ESO268–G044	49.9	1.9	175.6	3057	10	−24.01	406	2.16	0.36	0.23
ESO534–G020	226.7	16.7	216.6	40638	218	−25.86	17351	1.64	−0.17	−0.18
NGC 7589	115.0	12.6	224.0	32831	146	−25.58	13657	1.75	−0.08	−0.07
UGC11748	73.1	3.1	240.7	9418	20	−24.22	1911	2.26	0.32	0.31
UGC2936	43.6	8.4	255.0	28363	82	−25.09	10784	1.99	0.07	0.12
F568-6	201.0	18.3	297.0	83839	249	−25.67	49173	1.89	−0.10	0.01

APPENDIX H: ERRORS AND SCATTER IN THE SCALING RELATIONS

In Table H1, the errors on the best-fitting parameters of the scaling relations evaluated in this work are shown. The standard scatter σ of individual galaxies data of the various scaling relations is also reported. In the 2D scaling relations, it is evaluated according to:

$\sigma = \sqrt{\sum_{i=1}^N (y_i - f(x_i))^2 / N}$, where $N = 72$, y_i and x_i are the logarithmic data in the y and x axes, respectively, and f is the considered scaling function (a line). In the 3D scaling relations, the standard scatter is evaluated according to: $\sigma = \sqrt{\sum_{i=1}^N (z_i - \tilde{f}(x_i, y_i))^2 / N}$, where z_i , y_i , x_i are the logarithmic data in the z , y , and x axes, respectively, and \tilde{f} is the considered scaling function (a plane).

APPENDIX I: LSB ROTATION CURVES WITH THEIR URC

We show in Figs I1–I5 the LSBs RCs data together with their URC, taking into account equations (21) and (22) and the values of $R_{\text{opt}} \equiv 3.2 R_d$, V_{opt} , and C_* reported in Tables G1–G2 in Appendix G. We also show the URC for the case $\text{Log } C_* = 0$ in Figs I1–I5. In comparing the URC model with the 72 individual RCs, in 21 of them we have assumed a random systematic error running from $\simeq 3$ per cent to $\simeq 16$ per cent in their amplitudes (velocity measurements). In Table II, the changes applied are specified. Removing such systematics improves fits which were already successful. Let us stress that the URC can help determining how well an individual RC correctly reflects the mass distribution of the galaxy.

Table H1. Errors and scatters on the various scaling relations. Columns: (1) relation; (2)–(4) error bars on the *first*, *second*, and *third* (when present) fitting parameters; (5) standard scatter of the 72 individual galaxies data from the scaling relations.

Fitted relation (1)	Δa (2)	Δb (3)	Δc (4)	σ (5)
Equation (9): $\text{Log } R_c(\text{Log } R_d)$	0.15	0.26	–	–
Equation (14): $\text{Log } M_d(\text{Log } V_{\text{opt}})$	0.25	0.12	–	0.24
Equation (15): $\text{Log } \rho_0(\text{Log } R_c)$	0.07	0.05	–	0.21
Equation (17): $\text{Log } R_d(\text{Log } V_{\text{opt}})$	0.25	0.13	–	0.24
Equation (17): $\text{Log } R_c(\text{Log } V_{\text{opt}})$	0.36	0.18	–	0.34
Equation (17): $\text{Log } \rho_0(\text{Log } V_{\text{opt}})$	0.56	0.28	–	0.54
Equation (18): $\text{Log } R_d(\text{Log } M_d)$	0.23	0.02	–	0.16
Equation (20): $\text{Log } M_d(\text{Log } V_{\text{opt}}, \text{Log } C_*)$	0.06	0.03	0.04	0.06
Equation (20): $\text{Log } R_d(\text{Log } V_{\text{opt}}, \text{Log } C_*)$	0.02	0.01	0.02	0.02
Equation (20): $\text{Log } R_c(\text{Log } V_{\text{opt}}, \text{Log } C_*)$	0.03	0.02	0.02	0.03
Equation (20): $\text{Log } \rho_0(\text{Log } V_{\text{opt}}, \text{Log } C_*)$	0.15	0.07	0.10	0.13
Equation (23): $\text{Log } R_c(\text{Log } M_{\text{vir}})$	0.26	0.02	–	0.15
Equation (24): $\text{Log } C_*(\text{Log } C_{\text{DM}})$	0.01	0.06	–	0.15

Downloaded from https://academic.oup.com/mnras/article-abstract/490/4/5451/5574405 by guest on 11 February 2020

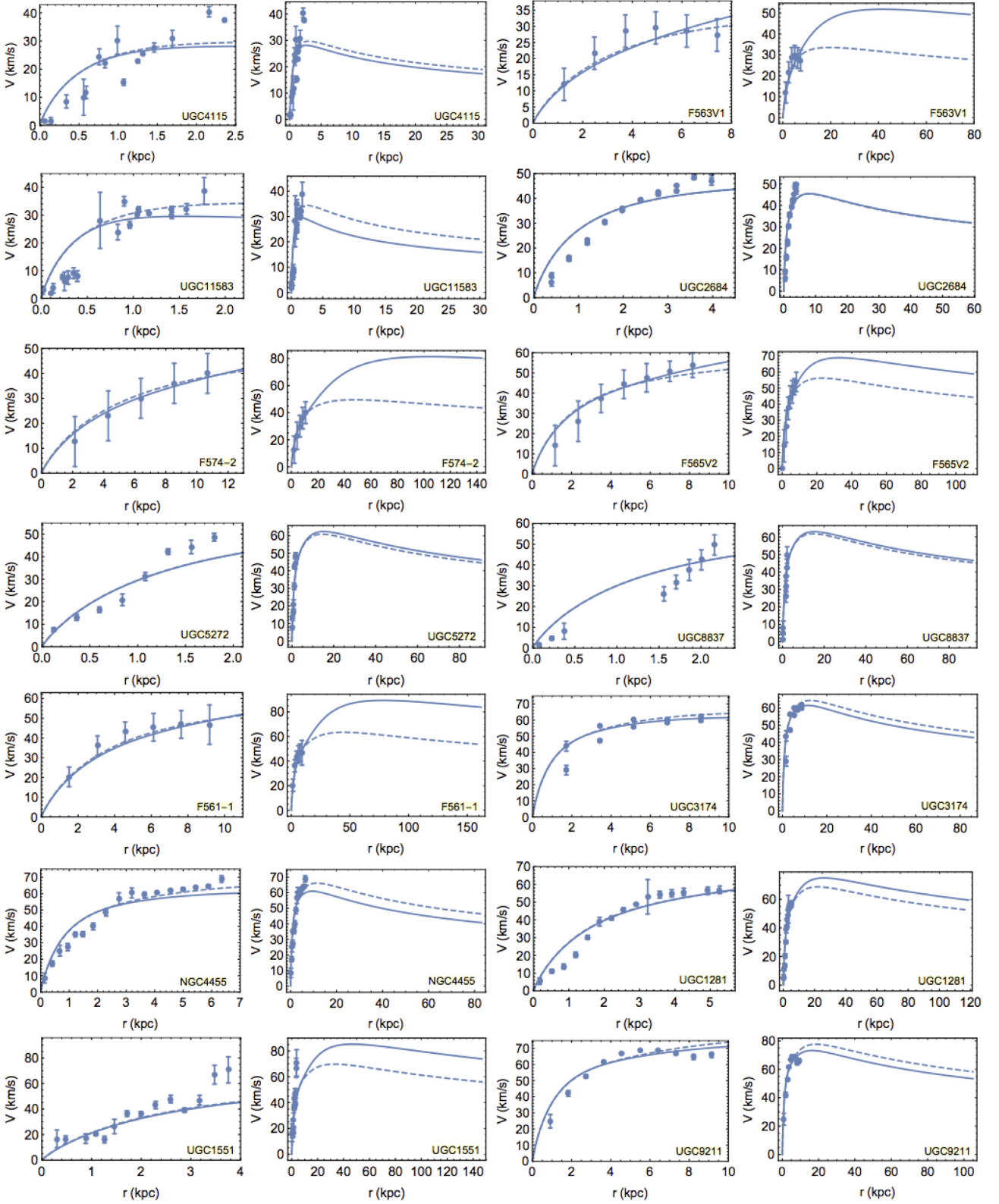


Figure II. LSBs RCs data with their URC given by equations (21)–(22). The *solid* line is obtained for the $\text{Log } C_*$ values reported in Tables G1–G2 in Appendix G and is compared with the *dashed* line obtained for $\text{Log } C_* = 0$. For each galaxy, we show the URC fit up to the farthest measurements (*left*) and up to the virial radius (*right*).

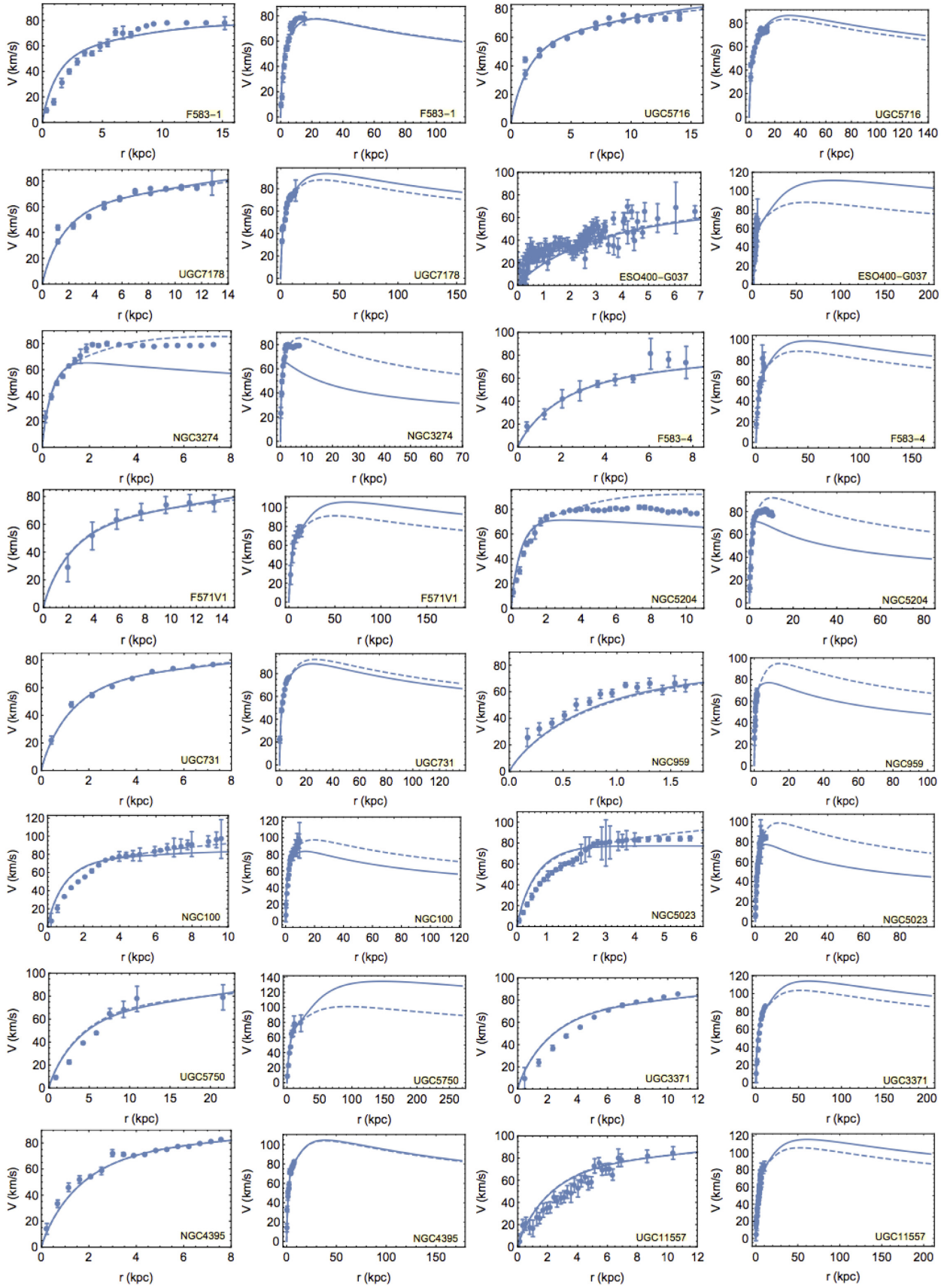


Figure 12. It continues from Table II.

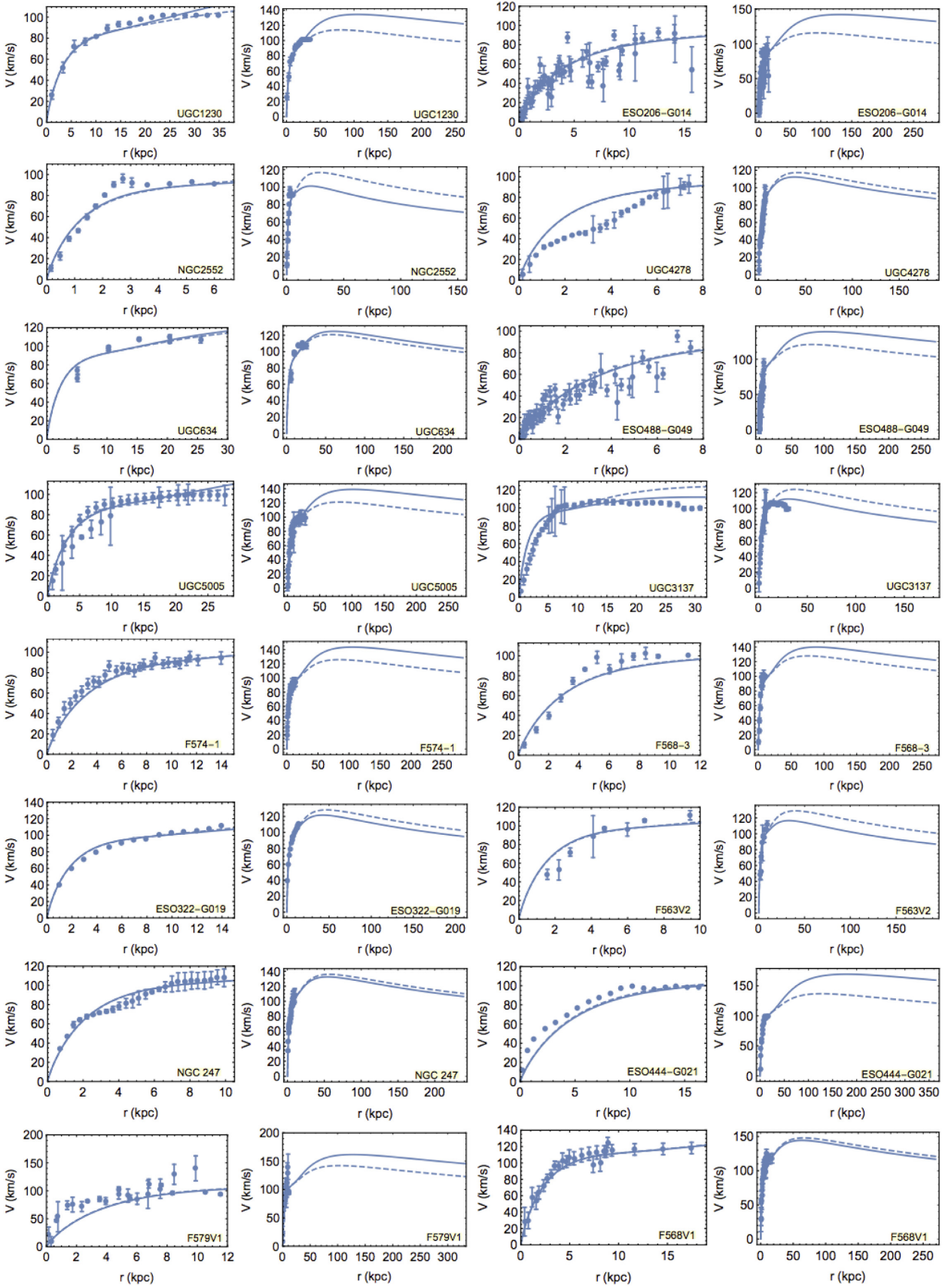


Figure I3. It continues from Table I2.

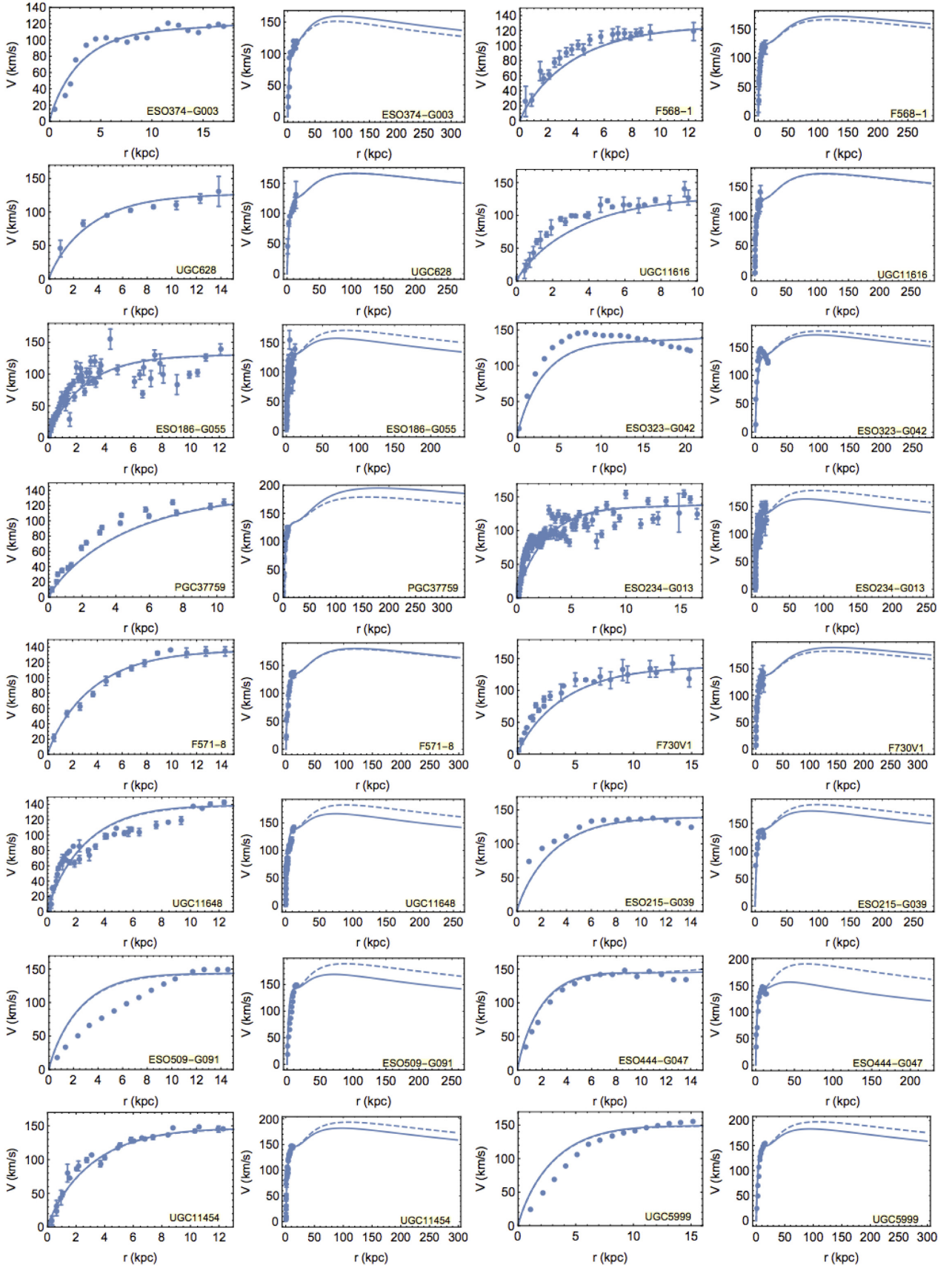


Figure 14. It continues from Table 13.

Downloaded from https://academic.oup.com/mnras/article-abstract/490/4/5451/5574405 by guest on 11 February 2020

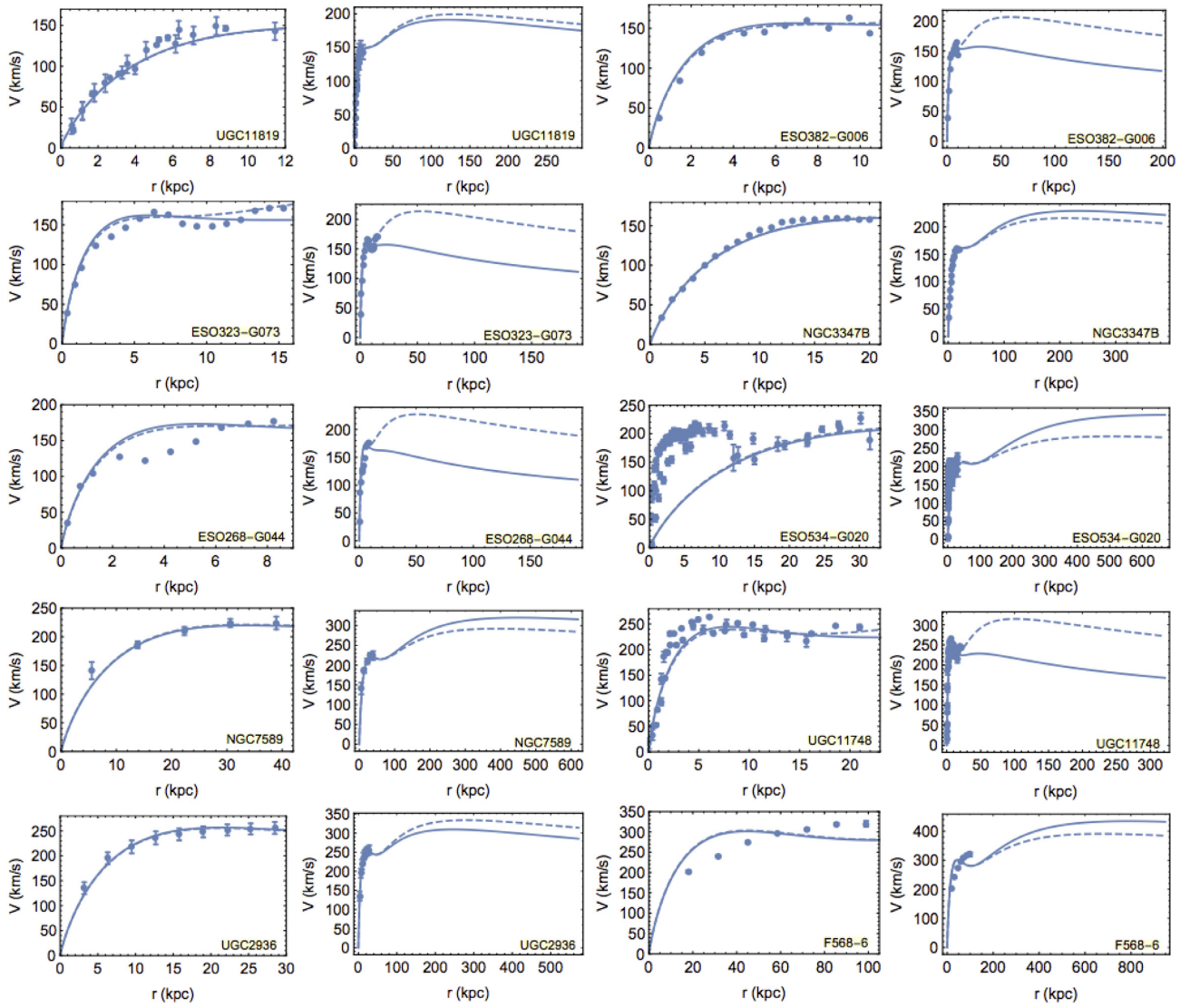


Figure 15. It continues from Table 14.

Table II. List of galaxies in which we have left the amplitude of the RC to freely vary by f per cent. Columns: (1) galaxy name; (2) correction to the velocity values of the RCs data, expressed in f per cent.

Name (1)	f per cent (2)
UGC2684	+ 10.9
F565V2	+ 8.8
F561-1	- 7.9
UGC3174	- 9.7
UGC1551	- 14.3
UGC9211	+ 4.8
F583-1	- 8.1
ESO400-G037	- 7.1
NGC 959	- 15.9
F574-1	- 8.1
ESO444-G021	- 9.3
F579V1	- 16.1
ESO374-G003	- 5.9
F568-1	- 9.2
UGC11616	- 7.5
PGC37759	- 10.8
F730V1	- 9.2
ESO215-G039	- 10.5
UGC11454	- 3.3
NGC 3347B	- 6.0
ESO268-G044	- 5.7

This paper has been typeset from a $\text{\TeX}/\text{\LaTeX}$ file prepared by the author.

Chapter 8

PAPER 2: “The Radial Acceleration Relation (RAR): Crucial Cases of Dwarf Disks and Low-surface-brightness Galaxies”



The Radial Acceleration Relation (RAR): Crucial Cases of Dwarf Disks and Low-surface-brightness Galaxies

C. Di Paolo¹, P. Salucci^{1,2}, and J. P. Fontaine³

¹SISSA/ISAS, Via Bonomea 265, I-34136 Trieste, Italy

²INFN, Sezione di Trieste, Via Valerio 2, I-34127 Trieste, Italy

³GSSI, Viale Francesco Crispi 7, I-67100 L'Aquila, Italy

Received 2018 October 11; revised 2019 January 15; accepted 2019 January 16; published 2019 March 11

Abstract

McGaugh et al. have found, in a large sample of disk systems, a tight nonlinear relationship between the total radial accelerations g and their components g_b that have arisen from the distribution of the baryonic matter. Here, we investigate the existence of such a relation in Dwarf Disk Spirals and Low Surface Brightness (LSB) galaxies on the basis of Karukes & Salucci and Di Paolo & Salucci. We have accurate mass profiles for 36 Dwarf Disk Spirals and 72 LSB galaxies. These galaxies have accelerations that cover the McGaugh range but also reach out to one order of magnitude below the smallest accelerations present in McGaugh et al. and span different Hubble Types. We found, in our samples, that the g versus g_b relation has a very different profile and also other intrinsic novel properties, among those, the dependence on a second variable: the galactic radius, normalized to the optical radius R_{opt} , at which the two accelerations are measured. We show that the new far from trivial g versus $(g_b, r/R_{\text{opt}})$ relationship is a direct consequence of the complex coordinated mass distributions of the baryons and the dark matter (DM) in disk systems. Our analysis shows that the McGaugh et al. relation is a limiting case of a new universal relation that can be very well framed in the standard “DM halo in the Newtonian Gravity” paradigm.

Key words: dark matter – galaxies: fundamental parameters – galaxies: kinematics and dynamics – galaxies: structure

1. Introduction

A recent study (McGaugh et al. 2016), hereafter referred to as **McG+16**, claims an empirical discovery that would challenge the idea of dark matter (DM) halos surrounding galaxies, or, at least, it would revolutionize our knowledge about the nature of the huge mass discrepancy therein. The standard paradigm relies on collisionless nonluminous particles constituting about 25% of the mass energy of the universe and playing a crucial role in the birth and the evolution of its structures.

The relation, in rotating systems, between the galaxy gravitational potential Φ_{tot} and the radial acceleration $g(r)$ of a point mass at distance r is

$$g(r) = \frac{V^2(r)}{r} = \left| -\frac{d\Phi_{\text{tot}}(r)}{dr} \right|, \quad (1)$$

where $V(r)$ is the circular velocity. The baryonic component of the radial acceleration is given by:

$$g_b(r) = \frac{V_b^2(r)}{r} = \left| -\frac{d\Phi_b(r)}{dr} \right|, \quad (2)$$

where

$$V_b^2(r) = V_d^2(r) + V_{\text{HI}}^2(r) + V_{\text{bu}}^2(r) \quad (3)$$

is the baryonic contribution to the circular velocity. In Equation (3), the velocities $V_i = |-r d\Phi_i(r)/dr|^{1/2}$ are the solutions of the separated Poisson equations: $\nabla^2\Phi_i(r) = 4\pi G\rho_i$. ρ_i is equal to the stellar disk, the HI disk and the bulge mass densities and Φ_i are the gravitational potentials of the i -components. Obviously we have:

$$g_h(r) = g(r) - g_b(r), \quad (4)$$

where g_h refers to the DM contribution to the radial acceleration g .

McG+16 investigated 153 galaxies across a wide range of Hubble types and luminosities with new high-quality data from the Spitzer Photometry and Accurate Rotation Curves database. The analysis includes (see Lelli et al. 2016 for details):

- (i) near-infrared ($3.6 \mu\text{m}$) observations that trace the distribution of stellar masses under the assumption of $0.5 M_{\odot}/L_{\odot}$ for the value of the stellar mass to light ratio in this band;
- (ii) the 21 cm observations that trace the distribution of the atomic gas and the velocity fields.

They found that the radial acceleration $g(r)$ shows an anomalous feature. It correlates at any radius and in any object, with its component generated from the baryonic matter $g_b(r)$ in a way that it is:

- (i) very different from the $g = g_b$ relationship expected in the Newtonian case with the presence of the only baryonic matter;
- (ii) claimed to be of difficult understanding in the standard Newtonian + DM halos scenario.

In detail, the McGaugh relationship (see Figures 1 and 3 in **McG+16**) relies on 153 objects for a number of 2693 independent circular velocity measurements. Each of them yields the pairs (g_b, g) , well fitted by:

$$\text{Log } g(r) = \text{Log} \left(\frac{g_b(r)}{1 - \exp\left(-\sqrt{\frac{g_b(r)}{\bar{g}}}\right)} \right), \quad (5)$$

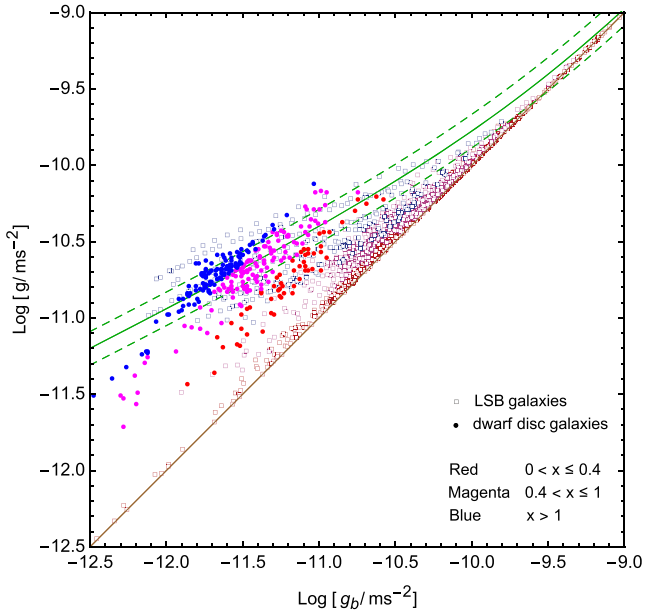


Figure 1. Relationship between the total acceleration g and its baryonic component g_b . $x = r/R_{\text{opt}}$. Red, magenta, and blue points correspond to radial bins with increasing distance from the galactic center (see the legend). Also shown are the McGaugh et al. (2016) relationship (solid green line) with its 1σ errorbars of 0.11 dex (dashed green lines) and the Newtonian relationship $\text{Log } g = \text{Log } g_b$ (brown line). See also Figure 6 in Appendix A for LSB data with very low values of $\text{Log } g$ and $\text{Log } g_b$.

with $\tilde{g} = 1.2 \times 10^{-10} \text{ ms}^{-2}$. At high accelerations, $g \gg \tilde{g}$, Equation (5) converges to the Newtonian relation $g = g_b$; while, at lower accelerations, $g < \tilde{g}$, Equation (5) strongly deviates from the latter (McGaugh et al. 2016; Li et al. 2018).

A recent investigation of the McG+16 relationship has been performed by Salucci (2018a, 2018b) (hereafter S18) in three very large samples of *normal spirals* by exploiting three specifically devised methods of deriving g_h (as shown in Equation (4)). In these works, the stellar mass distribution is estimated kinematically by means of the mass modeling of the rotation curves, rather than being estimated from spectrophotometry as in McG+16. The outcome is a $g(g_b)$ relationship, with an rms of 0.15 dex and with a quite small systematical difference of 0.2 dex from Equation (5) (Salucci 2018b). These results, totally framed in the DM scenario and obtained by means of novel methods of mass modeling, confirm the McG+16 relationship in normal Spirals.

Recently, Karukes & Salucci (2017) and Di Paolo & Salucci (2018) have obtained the radial distribution of the total, baryonic matter and DM for 36 dwarf spirals, yielding 315 acceleration measurements, and 72 Low Surface Brightness (LSB) galaxies, yielding 1601 acceleration measurements (see also Appendix A for further details). These accelerations occupy a region in the $g-g_b$ plane (see Figure 1) compatible with that covered by previous works, but that, in addition:

- (a) reaches smaller values along the vertical axis, considering our smallest value of $\text{Log } g/\text{m s}^{-2} \simeq -12.5$ (-14.5 , see Appendix A) and the McG+16 smallest unbinned value of $\text{Log } g/\text{m s}^{-2} \simeq -11.4$;
- (b) pertains to different Hubble Types than the bulk of the objects in McG+16; it is worth specifying that the sample of McG+16 (153 rotating objects) has dwarf and LSB disks alongside a large number of normal Spirals. In our

work, we have only dwarf disks (here called DD) and LSB galaxies.

A very important element of our analysis is the baryonic fraction $f_b(r)$, which varies in galaxies of different dimensions and Hubble Types. It is pivotal to frame our data and those of McG+16 and S18 within the standard “DM halo in the Newtonian Gravity” paradigm. Moreover, we will understand why the McG+16 relation is only a limit of a more complex universal relation.

Let us define the distribution of stars in disk galaxies, by means of their surface brightness, which is almost always given, in disk systems, by $\mu(r) = \mu(0) + 1.086 r/R_d$ (Freeman 1970), where R_d is the exponential disk scale length ($\mu(0)$ is variable object by object). In this work, the accelerations are in meters per second squared and the distances are in kiloparsecs. The optical radius R_{opt} is defined as the radius encompassing 83% of the total luminosity; $R_{\text{opt}} = 3.2 R_d$. The optical velocity V_{opt} is the circular velocity measured at R_{opt} . Let us note that in this paper, we will use alternatively the quantities x and $r/R_{\text{opt}} \equiv x$. In addition, our system of coordinates is r, φ, z .

The work is organized as follows: In Section 2, we describe the dwarf disks and LSBs samples. In Section 3, we briefly describe the universal rotation curve (URC) method used in our analysis. In Section 4, we build the g versus g_b relation followed, in Section 5, by a 3D analysis that involves the baryonic fraction $f_b(r)$ and the additional variable x . Finally, in Section 6, we report the consequences of our results.

2. The DD and LSB Samples

The sample of dwarf disks (Karukes & Salucci 2017) that we use in this work is drawn from the Local Volume catalog (Karachentsev et al. 2013). The faintest objects are 3 magnitudes fainter with respect to the sample of spirals of McG+16 and S18. These galaxies explore quite smaller mass scales than the normal Spirals. The criteria adopted to select the objects are described in Karukes & Salucci (2017). In detail, the sample consists of 36 galaxies (two among them are in common with the LSB sample) whose structural properties span the intervals: $-19.9 \lesssim M_K \lesssim -14.2$, $0.18 \text{ kpc} \lesssim R_d \lesssim 1.63 \text{ kpc}$, and $17 \text{ km s}^{-1} \lesssim V_{\text{opt}} \lesssim 61 \text{ km s}^{-1}$. All galaxies are bulgeless disk systems in which the rotation, corrected for the pressure support, totally balances the gravitational force.

The sample of LSBs consists of 72 disk galaxies. They are objects that emit an amount of light per area much smaller than normal spirals (McGaugh 1994; Impey & Bothun 1997; de Blok et al. 1996) and do not lay on the $L \propto R_d^2$ relationship of the latter. The sample of rotation curves is selected from the literature (A. Erkurt et al. 2019, in preparation)⁴ and characterized by objects whose optical velocities V_{opt} span from ~ 24 to $\sim 300 \text{ km s}^{-1}$.

For both DD and LSB samples, the available photometry and kinematics are of sufficient quality to allow us to obtain a proper mass modeling, by means of the technique of the URC (Persic et al. 1996).

⁴ In Appendix F, we provide the references for the RC data and other galactic properties (see Tables 1 and 2).

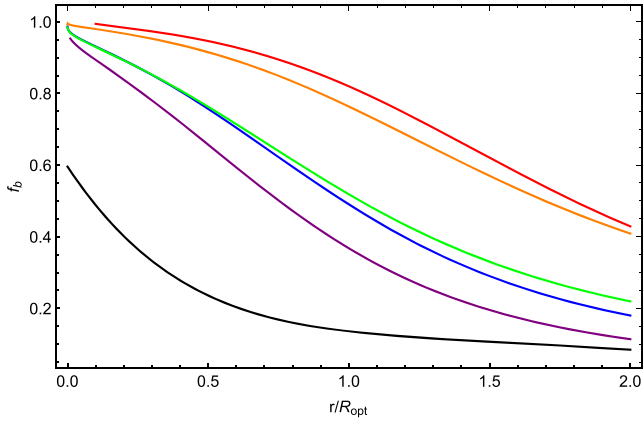


Figure 2. Baryonic fraction as a function of r/R_{opt} , derived by the URCs of DD (black line, with $\langle V_{\text{opt}} \rangle = 40 \text{ km s}^{-1}$; Karukes & Salucci 2017) and of LSBs (purple, blue, green, orange, and red, with $\langle V_{\text{opt}} \rangle = 43, 73, 101, 141, 206 \text{ km s}^{-1}$; Di Paolo & Salucci 2018). For the uncertainties on the $f_b(x)$ see the text and Appendix D.

3. The Mass Distribution in Disk Systems by Exploiting the URC

The URC compacts the structural properties of rotating systems (Persic et al. 1996; Salucci et al. 2007). As a starting point, all galaxies of a given sample are binned in different groups/families according to their V_{opt} (in the case of our samples) and then coadded in terms of $x \equiv r/R_{\text{opt}}$, their radial normalized coordinate. Galaxies inside a certain limited range of V_{opt} all have, approximately, the same baryonic and DM distribution, once they are expressed in normalized radial coordinate x . For the present samples, the DD galaxies are grouped in a single bin (Karukes & Salucci 2017) and the LSB galaxies are grouped in five bins (according to their increasing V_{opt} ; Di Paolo & Salucci 2018).

The URC model is based on an exponential disk (Freeman 1970) for the stellar component and the Burkert density profile (Burkert 1995) for the DM halo (preferred in disk systems, see Salucci & Burkert 2000; de Blok & Bosma 2002; Karukes & Salucci 2017). For the disk component, the Tonini et al. H I disk (Tonini et al. 2006; Evoli et al. 2011) is considered in DD galaxies and a bulge component (Yegorova & Salucci 2007) is taken into account for the largest LSB galaxies (Das 2013). Let us note that, for LSBs, the gas contribution to the circular velocity can be considered negligible in view of the aim of this paper. See Appendix C.

We fit with the URC the coadded rotation curves for each of the 1 + 5 families. This provides us with $V_{\text{URC}}(r/R_{\text{opt}}, V_{\text{opt}})$ and $V_{\text{URC},b}(r/R_{\text{opt}}, V_{\text{opt}})$, i.e., the circular velocity and its baryonic component (see Appendix B for further details about the URC method).

The baryonic fraction f_b as a function of r/R_{opt} for galaxies tagged by V_{opt} is given by:

$$f_b(r/R_{\text{opt}}, V_{\text{opt}}) = \frac{V_{\text{URC},b}^2(r/R_{\text{opt}}, V_{\text{opt}})}{V_{\text{URC}}^2(r/R_{\text{opt}}, V_{\text{opt}})}. \quad (6)$$

See Figure 2. Note that, going from the inner to the external radii and from the biggest to the smallest galaxies, the baryonic component becomes less and less relevant than the DM one. It is remarkable that a very similar behavior of $f_b(r/R_{\text{opt}}, V_{\text{opt}})$ is found also in Spirals (Salucci et al. 2007; Lapi et al. 2018).

Equation (6), recast in other terms, becomes $V_{\text{URC},b}^2(r) = f_b(r, V_{\text{opt}}) V_{\text{URC}}^2(r)$ and, consequently, with Equation (1), we have for each galaxy:

$$g_b(r) = f_b(r, V_{\text{opt}}) g(r). \quad (7)$$

Then, by summarizing: in each galaxy with disk scale length $R_{\text{opt}}/3.2$, rotation curve $V(r, R_{\text{opt}})$ with V_{opt} tag value, we have: $g(r) = V^2(r)/r$ and $g_b(r) = f_b(r)g(r)$, where $f_b(r)$ is the baryonic fraction (hereafter, for simplicity, we drop the family tag V_{opt}). Notice that $g(r)$ is totally observed, $g_b(r)$ has a part derived from the baryonic component to the rotation curves obtained by the baryonic mass distribution.

4. Results

The emerging g versus g_b relationships, obtained for DD and LSB galaxies, are shown in Figure 1. We realize that the universality of the $g(g_b)$ relation, holding in normal spirals (McGaugh et al. 2016; Salucci 2018a) breaks down in our samples. The scatters of DD and LSB data with respect to the McG+16 relation are 0.17 dex and 0.31 dex respectively. This big discrepancy cannot be due to observational or systematical errors, in fact we have used high-quality rotation curves, so that the observational uncertainties on $V^2(r)$, leading to $g(r)$, are less than 20%. Systematical errors are present only on the quantities $g_b = f_b g$, due to f_b . From the modeling of the coadded rotation curves in Spirals, DD and LSBs, the quantity f_b has fitting uncertainties running from 10% at higher luminosity to 30% at lower luminosity. This implies that the uncertainties on $\text{Log } g_b$ lay in the range between 0.13 dex and at most 0.19 dex. In this work, as those discussed in previous sections, the determination of g and g_b is not an issue. It is important to note in Figure 1 that there are many points strongly discrepant with respect to the McG+16 relation along both axes: in detail 1 dex on the $\text{Log } g_b$ axis and the same value on the $\text{Log } g$ axis, where our measurements can be considered almost error-free.

Let us stress that, as a consequence of the method employed to derive g_b , we cannot have: $g_b > g$; only when we consider the fitting uncertainties on g_b , we obtain that this quantity can (slightly) overcome g on average by a value of ~ 0.1 dex at a 2σ level of uncertainty (see Appendix D). This point is irrelevant for the scope of this paper.

The data relative to the inner regions of galaxies (red data) are the closest to the equality line $\text{Log } g = \text{Log } g_b$, while data relative to more external regions (blue data) of galaxies tend to depart from the equality line toward the region covered by the McG+16 relation and then go beyond, with $\text{Log } g > \text{Log } g_b$. This behavior is intrinsically related to the mass distribution in galaxies: the higher the baryonic fraction f_b , the closer g is to g_b , and reversely the lower f_b is, the more g overcomes g_b .

5. The Universality of the GGBX Relationship

It is evident that, in both DD and LSB samples, pairs of accelerations (g, g_b) residing at different radii r/R_{opt} do not overlap. We realize that a relationship between g and g_b necessarily must involve also the position x , where the two accelerations are measured, and the Hubble type of the objects. This is shown in our new 3D relationship, Equation (8) (hereafter GGBX relation), among the $\text{Log } g - \text{Log } g_b - x$ quantities. Starting from the McG+16 relation (in order to have a straightforward comparison), we added new terms to

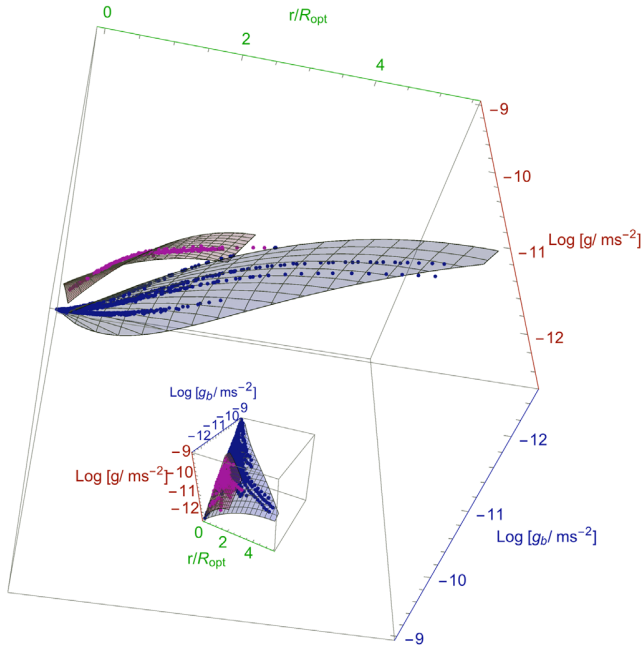


Figure 3. Relation among total acceleration g , baryonic acceleration g_b , and normalized radii r/R_{opt} . The magenta and blue points refer to DD and LSB galaxy data respectively. The surfaces are the results from the best-fit models.

find the best fitting model for LSB data. The best and simplest model that we found is:

$$\begin{aligned} \text{Log } g_{\text{LSB}}(x, \text{Log } g_b) = & (1 + a x) \text{Log } g_b \\ & + b x \text{Log} [1 - \exp(-\sqrt{g_b(x)/\tilde{g}})] + c x + d x^2, \end{aligned} \quad (8)$$

where the fitting parameters a , b , c , and d assume the best-fit values -0.95 , 1.79 , -9.01 , and -0.05 respectively. The scatter of LSB data from the fitting surface is considerably reduced, down to 0.05 dex, i.e., to a sixth of the scatter from the **McG+16** relation. Let us note that the model used in Equation (8) is just an empirical function used to fit the data that recovers $\text{Log } g \rightarrow \text{Log } g_b$ when $x \rightarrow 0$. Then the number of free parameters of the x part in the above relation expresses only our ignorance of the actual functional form of the relationship and not the fact that the $g(g_b, x)$ surface is not smooth and of negligible thickness.

In the case of DD galaxies, by simply applying translations and/or dilatations to Equation (8) along the three involved axes, we obtain the following best fitting model:

$$\begin{aligned} \text{Log } g_{\text{DD}}(x, \text{Log } g_b) \\ = \text{Log } g_{\text{LSB}}\left(\frac{x}{l} + h, \frac{\text{Log } g_b}{m} + n\right) + q. \end{aligned} \quad (9)$$

We found a perfect fit of the data when the fitting parameters l , h , m , n , q assume the best-fit values 0.49, 2.41, 0.74, 1.72, and 1.19 respectively. The scatter of DD with respect to the fitting surface is considerably reduced, with a value of 0.03 dex, i.e., about a fifth of the scatter from the **McG+16** relation.

We show in Figure 3 the DD and LSB data in the g - g_b - x space, with their best fitting surfaces from Equations (8)–(9). The result is extremely remarkable. It shows a precise relation linking the total and baryonic acceleration, the galactocentric

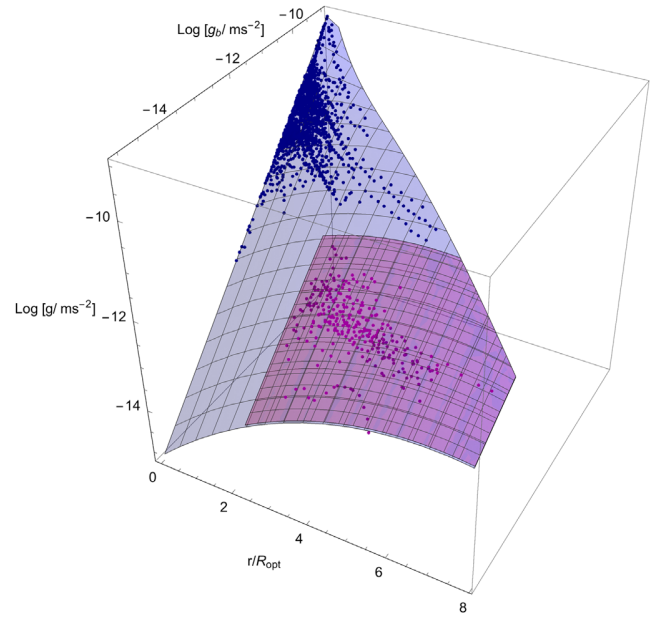


Figure 4. Relationships among the total acceleration g , the baryonic acceleration g_b , and the normalized radii r/R_{opt} for our two samples. The magenta and blue points refer to DD and LSB data, alongside their best-fit surfaces. The LSB measurements extend in the $\text{Log } g/\text{m s}^{-2}$ and $\text{Log } g_b/\text{m s}^{-2}$ range $\sim[-12.5, -9.0]$. The fitting surfaces also well represent the very low acceleration data discussed in Appendix A.

distance $x \equiv r/R_{\text{opt}}$, and even the morphology of galaxies. The scatter of both LSB plus DD data (after the translation and dilatations given by the parameters l , h , m , n , q ; see Figure 4) from the GGBX surface is only 0.05 dex, about a sixth of their scatter from the **McG+16** relation (0.29 dex); moreover, it is also lower than the scatter of 0.13 dex of the **McG+16** sample from the **McG+16** relation. The statistical significance is overwhelming, but its physical meaning is not immediate. Let us stress that the data g , g_b , x form, for LSBs and DDs, two very thin surfaces that can be overlapped through a simple coordinate transformation. Again, the number of the fitting parameters reflects our ignorance of the analytical representation of the $g(g_b, x)$ relation, not the statistical relevance of the surfaces defined by data.

5.1. Understanding the GGBX Relationship

Our relationship deviates both from the Newtonian and from the **McG+16** relationship. In particular, by considering the LSBs, i.e., our most numerous sample, we observe that:

- (i) the deviation from the Newtonian relation is more evident at larger galactocentric radii and for smaller g_b values. See the left panel of Figure 5, which shows the difference $\text{Log } g_{\text{LSB}}(x, \text{Log } g_b) - \text{Log } g_b$;
- (ii) the deviation from the **McG+16** relation is particularly evident at smaller galactocentric radii and for smaller g_b values. See the right panel of Figure 5, which shows the difference $\text{Log } g_{\text{LSB}}(x, \text{Log } g_b) - \text{Log } g_{\text{McG+16}}$.

We highlight that these results are related to the mass distribution in galaxies: any $g_b(r)$ corresponds to very different values of $g(r)$ according to the tag velocity V_{opt} (or luminosity), the normalized radius r/R_{opt} and the Hubble Type of the galaxy in question. This is a consequence of the fact that $g_b(r) = f_b(r)g(r)$ and that $f_b(r)$, related to the mass distribution

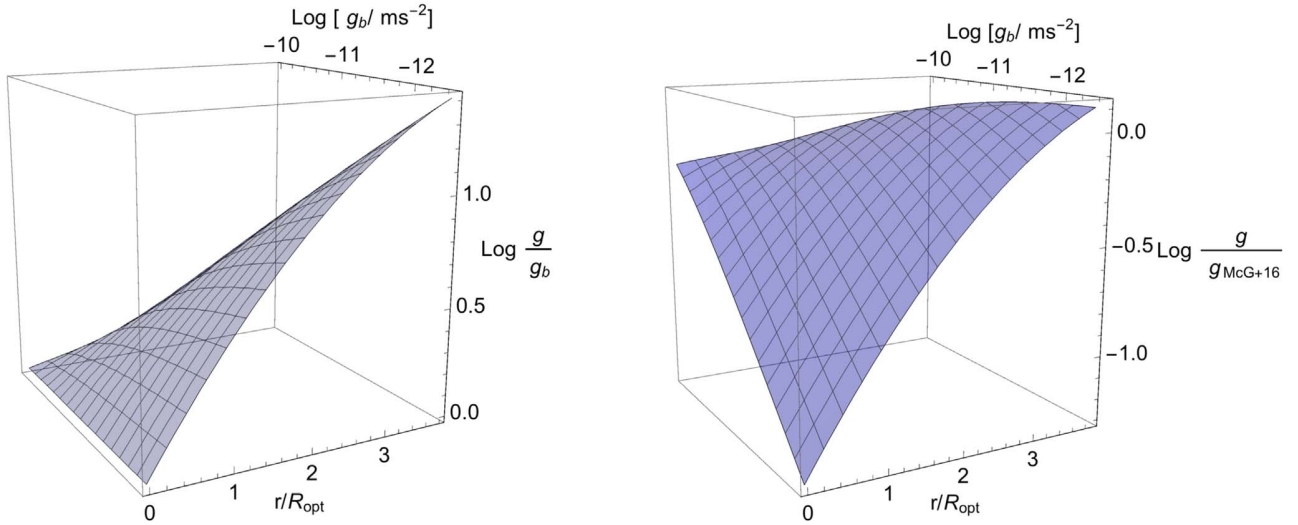


Figure 5. Surface in left panel is given by the difference between the LSBs GGBX relationship (Equation (8)) and the Newtonian value $\text{Log } g_b$. The surface in the right panel is given by the difference between the LSBs GGBX relationship and the **McG+16** relation (Equation (5)).

in galaxies, depends on the tag velocity V_{opt} (or luminosity), the normalized radius r/R_{opt} , and the Hubble Type of the galaxy in question (Figure 2).

It is worth showing how all the above results, including the disagreements with **McG+16**, are evident when we plot the GGBX relation in individual objects (see Appendix E).

In conclusion, straightforward facts are that:

- (i) the same values of the pairs (g, g_b) found in the outer region of big spirals are replicated in the inner region of small spirals, provided that approximately $r \geq R_d$. This explains the genesis of **McG+16** and **S18** findings;
- (ii) given one spiral and one LSB, both with the same V_{opt} and then very similar $f_b(x)$, they can show very different $f_b(r)$ in physical radial units. This happens because LSBs usually have much more extended R_D than spirals (see Figure 9 in Di Paolo & Salucci 2018). Thus, $f_{b,\text{LSB}}(r) > f_{b,\text{spiral}}(r)$. Then, at a fixed value of g_b , very different values of g can correspond, and vice versa. This mainly explains the failure of the **McG+16** relation in LSBs.

6. Conclusion

The two accelerations relationship (Equation (5)) by **McG+16** has attracted a great deal of interest. It is claimed and thought that it provides crucial evidence about the issue of DM. In this work, we have investigated the g_b - g relationship (found by **McG+16** for a sample dominated by normal spirals), in the recent sample of 36 Dwarf Disks and 72 LSB galaxies, whose optical velocities span from ~ 17 to $\sim 300 \text{ km s}^{-1}$, covering the full population of galaxies sizes and luminosities. We analyzed overall 1904 velocity data and modeled them by involving an exponential stellar disk, a Burkert DM halo density profile (de Blok & Bosma 2002; Karukes & Salucci 2017) and, in particular, we also considered the Tonini et al. HI disks (Tonini et al. 2006) in DD galaxies and a bulge component in larger LSB galaxies (Karukes & Salucci 2017; Di Paolo & Salucci 2018). Then, we have derived the 1904 (g_b, g) pairs in the same way as **McG+16** with the difference that the disk masses are obtained kinematically. This difference of methods,

however, leads to estimates of the disk masses that agree within their uncertainties. The great discrepancy between the **McG+16** relationship and ours does not arise from the adopted values of the stellar disk + HI disk masses.

In our objects $\text{Log } g/\text{ms}^{-2}$ lays in the range between -14.5 and -9 . On the other hand, the unbinned data $\text{Log } g/\text{ms}^{-2}$ in the **McG+16** relationship range between -11.4 and -8 . The results of our tests involving the DD and LSBs samples show empirically that the radial acceleration g in galaxies is not simply a universal function dependent on the baryonic acceleration g_b (as claimed by **McG+16** in Equation (5)), but also depends on the galactic radius expressed in normalized units r/R_{opt} .

The emerging relationship mirrors the properties of the DM in galaxies, whose fraction changes along the galactic radius, becoming more dominant on the baryonic one in the external regions, in a way that depends on the morphology and the luminosity of the galaxy (Figure 2; Persic et al. 1996).

For each sample, we have established a universal relation $g = f(g_b, x)$ (that we call the GGBX relationship), with x the normalized radius with respect to the optical radius R_{opt} . Moreover, we can go from the DD relationship to the LSB one by means of translations and/or dilatations of the three involved variables. The individual average scatter around these GGBX new surfaces (created by g, g_b, x data) is remarkably reduced with respect to that around to the **McG+16** relation, more precisely it becomes a fifth and a sixth for DD and LSB galaxy data, respectively.

Our relationship deviates both from the Newtonian and from the **McG+16** 2D relationships. In particular, the deviation from the Newtonian relation is more evident at larger galactocentric radii and for smaller g_b values, while the deviation from the **McG+16** relation is particularly evident at smaller galactocentric radii and for smaller g_b values.

It is worth saying that the results are intrinsically related to the mass distribution in galaxies, i.e., to the variation of the baryonic fraction f_b along the galactocentric radius and on the fact that it changes when we consider galaxies of different luminosity and different Hubble Type. This implies that, when considering different galaxies, a same value of g_b can be found at very different radii r and can correspond to very different

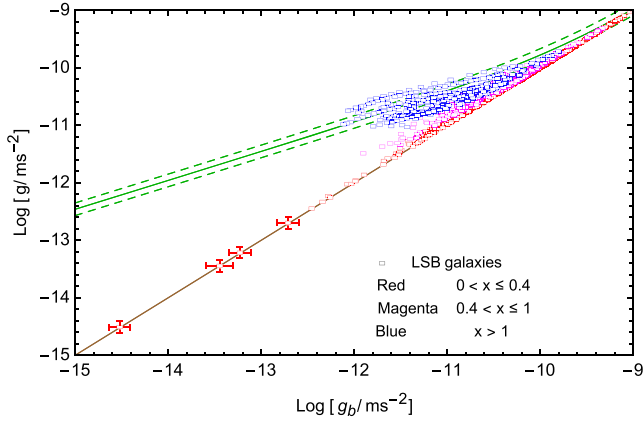


Figure 6. Relationship between the total acceleration g and its baryonic component g_b , for LSB data. $x = r/R_{\text{opt}}$. The figure is analogous to Figure 1, but also includes data through the lowest values of $\text{Log } g$ and $\text{Log } g_b$. The four “special points” with very small values of $\text{Log } g - \text{Log } g_b$ are shown with their 1σ uncertainties.

values of g . This is the main explanation of the discrepancy among LSBs, DD, and Spiral galaxies considered in [McG+16](#) and [S18](#).

In this paper a new relation among the dynamical quantities in disk galaxies has emerged. The further investigation of the origin of such a relation and the consequences in single objects will be shown in a paper in preparation by C. Di Paolo et al. (2019).

In conclusion, we find that the GGBX relationship (Equations (8)–(9)) is universal and framed in the DM + Newtonian gravity scenario. We point out that this relation stems from the properties of $V^2(x)$ and $f_b(x)$. Therefore, it does not pose issues to the Λ CDM + baryonic feedback scenario.

Crucial properties of the DM are instead unlikely to come from the $g-g_b$ relationship, in fact the DM halo density profile is $\rho(r) = 1/(4\pi Gr^2) \frac{d}{dr} [g(r)r^2(1 - f_b(r))]$ and crucially depends on quantities not present in the $g-g_b$ relationship: e.g., $dV(r)/dr$, $V^2(r) df_b(r)/dr$. Whether or not our GGBX compacts all the structural properties of DM halos will be left to a later work (C. Di Paolo et al. 2019, in preparation).

We thank F. Nesti, A. Lapi, L. Danese, and A. Erkart for useful discussions. We also thank G. Costa for help that improved the presentation of the results of this paper.

Appendix A The Extended $g-g_b$ Plane

For completeness, we show all the LSBs data in Figure 6, in order to highlight the extension of $\text{Log } g$ and $\text{Log } g_b$ values to ~ -14.5 (with the argument expressed in ms^{-2}). We highlight that, originally, we had 1605 data for the LSB galaxies. Among them, there are four “special points” that have very low values of $\text{Log } g$ and $\text{Log } g_b$, in the range $[-14.5, -12.5]$; see Figure 6. These data strongly support our result shown above, i.e., the discrepancy of LSB accelerations from the [McG+16](#) relationship; however, we keep them separate from the rest of the data because they are too few to cover the wide magnitude range (only 4 points in a range of 2 dex).

Appendix B The URC Method

The URC is derived, first, by luminosity/optical velocity and normalized radial binning of a large number of individual rotation curves that yield suitable coadded rotation curves^{5,6} $V_{\text{co-added}}(x, \lambda)$ (see for details [Persic et al. 1996](#); [Salucci et al. 2007](#)). For the present work, the DD galaxies are grouped in a single family ([Karukes & Salucci 2017](#)), the LSB galaxies are grouped in five families, each with increasing tag average velocity $\langle V_{\text{opt}} \rangle$.

The coadded curves (RCs) are very well reproduced by a suitable analytical velocity model that we call $V_{\text{URC}}(x, \lambda)$ (see [Karukes & Salucci 2017](#); [Di Paolo & Salucci 2018](#)).⁷

The URC method has been applied, so far, to Spirals, LSBs, and dwarf disks. It consists of the sum in quadrature of four terms, $V_{d,\text{URC}}$, $V_{\text{H I},\text{URC}}$, $V_{\text{bu},\text{URC}}$, and $V_{h,\text{URC}}$, each of them describing the contribution from the stellar disk, the H I gaseous disk, the central bulge, and the dark halo. Then:

$$V_{\text{co-added}}^2(x, \lambda) \simeq V_{\text{URC}}^2(x, \lambda) = V_{d,\text{URC}}^2(x, \lambda) + V_{\text{H I},\text{URC}}^2(x, \lambda) + V_{\text{bu},\text{URC}}^2(x, \lambda) + V_{h,\text{URC}}^2(x, \lambda), \quad (10)$$

where the lhs are the coadded RCs and the rhs is the analytical model with which we fit the former.

For simplicity, hereafter, we drop the tag “URC” in the model velocity components.

$V_{\text{URC}}(x, \lambda)$ fits extremely well all $V_{\text{co-added}}(x, \lambda)$ (see Figure 7) of spirals ([Persic & Salucci 1991](#); [Persic et al. 1996](#); [Salucci et al. 2007](#)), DD ([Karukes & Salucci 2017](#)), and LSB ([Di Paolo & Salucci 2018](#)), and provides us with an accurate analytical representation of the individual rotation curves.

The stellar component is described by means of the well-known exponential disk ([Freeman 1970](#)) with surface density profile $\Sigma_D(r) = \frac{M_d}{2\pi R_d^2} \exp(-r/R_d)$.

Caveat the distance of the galaxy, the gas contribution is known from observations (e.g., see [Evoli et al. 2011](#)). This component is described as follows: the total mass is obtained from the 21 cm flux and its radial distribution is given by $\Sigma_{\text{H I}}(r) = \frac{M_{\text{H I}}}{2\pi(3R_d)^2} \exp(-r/3R_d)$ ([Tonini et al. 2006](#); [Evoli et al. 2011](#); [Wang et al. 2014](#)). Then:

$$V_d^2(r) = \frac{1}{2} \frac{GM_d}{R_d} (3.2r/R_{\text{opt}})^2 (I_0 K_0 - I_1 K_1);$$

$$V_{\text{H I}}^2(r) = \frac{1}{2} \frac{GM_{\text{H I}}}{3R_d} (1.1r/R_{\text{opt}})^2 (I_0 K_0 - I_1 K_1) \quad (11)$$

where M_d is the stellar disk mass, $M_{\text{H I}}$ is the gaseous disk mass (correcting by a factor of 1.3 in order to account for the He abundance), I_n and K_n are the modified Bessel functions computed at $1.6x$ and $0.53x$ for the stellar and the gaseous disk respectively.

Let us note that, in LSBs, the gas contribution to the circular velocity is negligible for the scope of this paper (see also [Appendix C](#)).

⁵ $x = r/R_{\text{opt}}$.

⁶ λ is equal to M_k or V_{opt} , (i.e., λ is the galaxy’s family identifier).

⁷ For our objects we know the values of their R_d , so that we can express the URCs in terms of their physical radial units $V_{\text{URC}}(r)$.

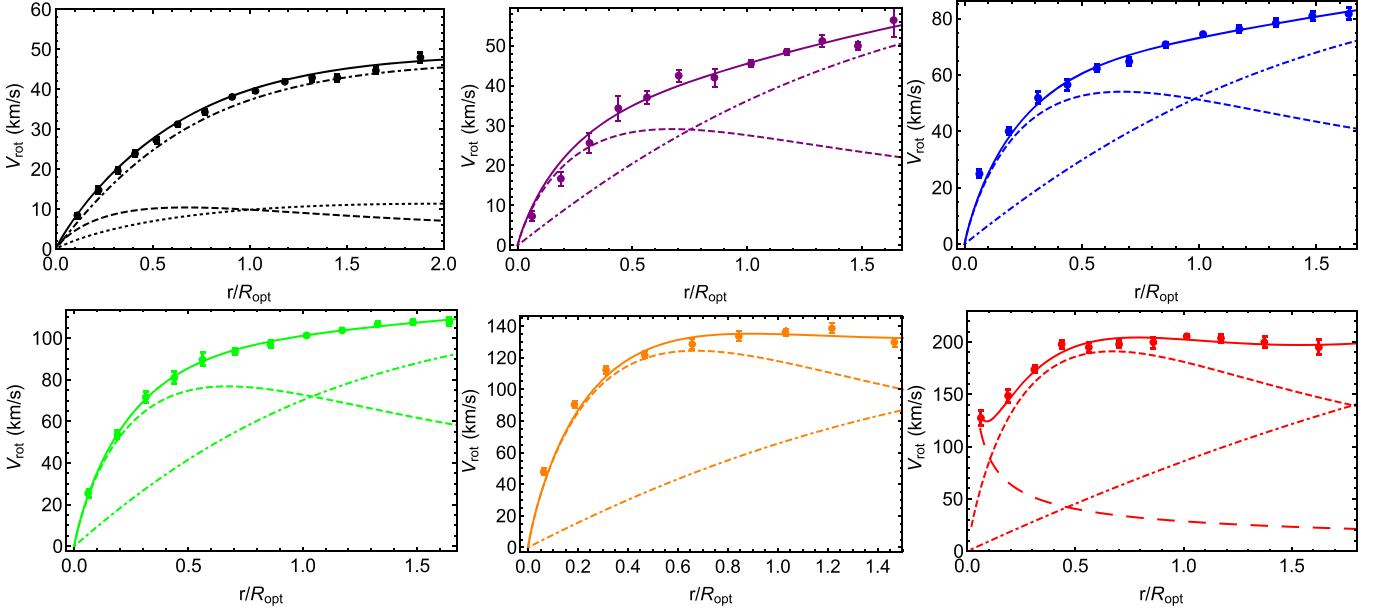


Figure 7. Best-fit URC velocity models of the coadded RCs of the unique velocity bin representative of DD galaxies (black, with $\langle V_{\text{opt}} \rangle = 40 \text{ km s}^{-1}$) and of the five velocity bins, representative of the LSBs (purple, blue, green, orange, and red with: $\langle V_{\text{opt}} \rangle = 43, 73, 101, 141, 206 \text{ km s}^{-1}$). The dashed, dotted, dotted-dashed, long-dashed, and solid lines are the stellar disk, H I disk, dark matter, bulge, and total contributions to the circular velocities, respectively.

In the largest velocity bin of LSBs, in the URC model we have included a bulge component by adopting:

$$V_{\text{bu}}^2(r) = \alpha_b V_{\text{in}}^2 (r/r_{\text{in}})^{-1}, \quad (12)$$

where V_{in} and r_{in} are values referred to the innermost circular velocity measurements and α_b is a parameter varying from 0.2 to 1 (see, e.g., Yegorova & Salucci 2007).

Therefore, for bulgeless DD galaxies we assume, as baryonic contribution, $V_b^2(r) = V_d^2(r) + V_{\text{H I}}^2(r)$, while for the LSBs we assume $V_b^2(r) = V_d^2(r)$ for the four galaxies' families (velocity bins) characterized by the smallest V_{opt} and $V_b^2(r) = V_d^2(r) + V_{\text{bu}}^2(r)$ for galaxies with the largest V_{opt} (Salucci et al. 2000; Das 2013).

For the DM halo velocity contribution we adopt the cored Burkert profile (Burkert 1995):

$$V_h^2(r) = 2\pi G \rho_0 \frac{R_0^3}{r} [\ln(1 + r/r_0) - tg^{-1}(r/r_0) + 0.5 \ln(1 + (r/r_0)^2)], \quad (13)$$

where ρ_0 is the central mass density and r_0 is the core radius.

By resumming, the coadded rotation curves $V_{\text{co-added}}$ are very well fitted by V_{URC} (see Figure 7) and the best fitting parameters M_d , α_b , ρ_0 , r_0 result all as a function of λ (V_{opt} or M_K). We direct the interested reader to Karukes & Salucci (2017) and Di Paolo & Salucci (2018).

Appendix C

The H I Component Effect on the $g-g_b$ Plane

We have investigated the $g-g_b$ plane by also including the gas component in LSB galaxies when fitting their rotation curves. For these galaxies, we assumed the contribution of the

gaseous component by means of the II relation of Equation (11) and considering the mass $M_{\text{H I}}$ as a free parameter ($M_{\text{H I}}$ includes H I + He components). The results are as follows: the gas is important only in the first velocity bin; however, the inner regions are quite dominated by the stellar component and the gas component is of limited importance. In Figure 8, we fit the first LSB coadded rotation curve (velocity bin) without/with the gas contribution. In both cases, the resulting masses of the stellar disk and of the DM halo, are similar. In fact, we have:

$$M_d = 8.8 \times 10^8 M_{\odot}; \quad r_0 = 10.7 \text{ kpc}; \\ \rho_0 = 3.7 \times 10^{-3} M_{\odot} \text{ pc}^{-3}; \quad M_{\text{vir}} = 1.0 \times 10^{11} M_{\odot}.$$

While, by considering the stellar disk + the DM halo + gaseous disk, we have:

$$M_d = 8.0 \times 10^8 M_{\odot}; \quad r_0 = 10.7 \text{ kpc}; \\ \rho_0 = 3.2 \times 10^{-3} M_{\odot} \text{ pc}^{-3}; \\ M_{\text{vir}} = 8.2 \times 10^{10} M_{\odot}; \quad M_{\text{H I}} = 1.0 \times 10^9 M_{\odot}.$$

In the above, M_d , r_0 , ρ_0 , $M_{\text{H I}}$ (the quantities obtained by fitting $V_{\text{co-add}}(x, V_{\text{opt}})$) are the stellar disk mass, the DM halo core radius, the central core mass density, the H I gaseous disk mass (including the correction for helium contribution), respectively. M_{vir} is the virial mass.

More importantly, we show in Figure 8 that the difference in the crucial quantity f_b in the two different cases is small. There is only a slightly increase at outer galactic radii in the latter case: the resulting data move further toward the equality line ($g = g_b$), making our results stronger; see Figure 9.

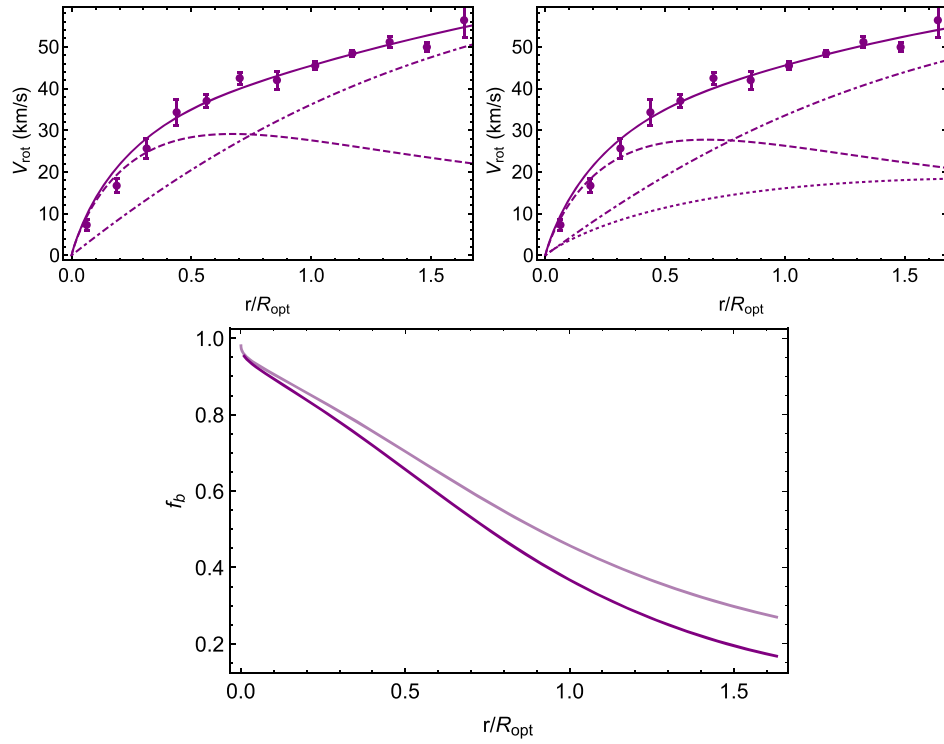


Figure 8. Upper panels: I velocity bin (family) rotation curve fitted without and with gas. The dashed, dotted–dashed, dotted, and solid lines stand for the stellar disk, the DM halo, the gaseous disk, and the total contributions to the rotation curve, respectively. Bottom panel: baryonic fraction without gas (dark purple) and with gas (light purple).

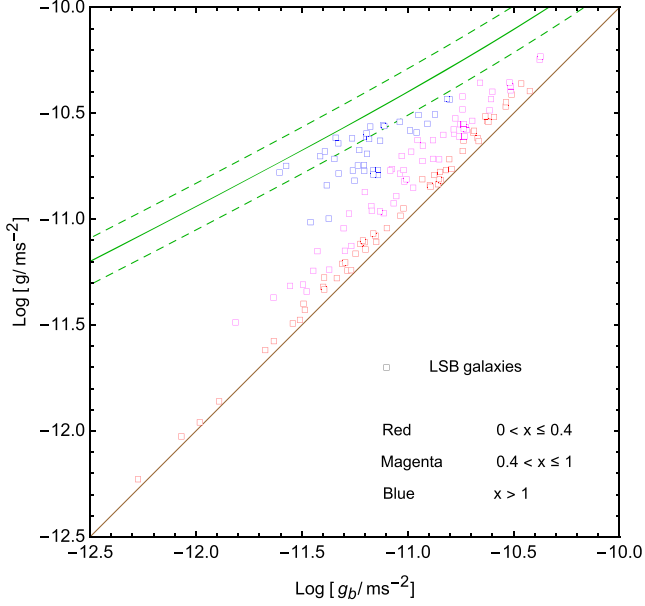
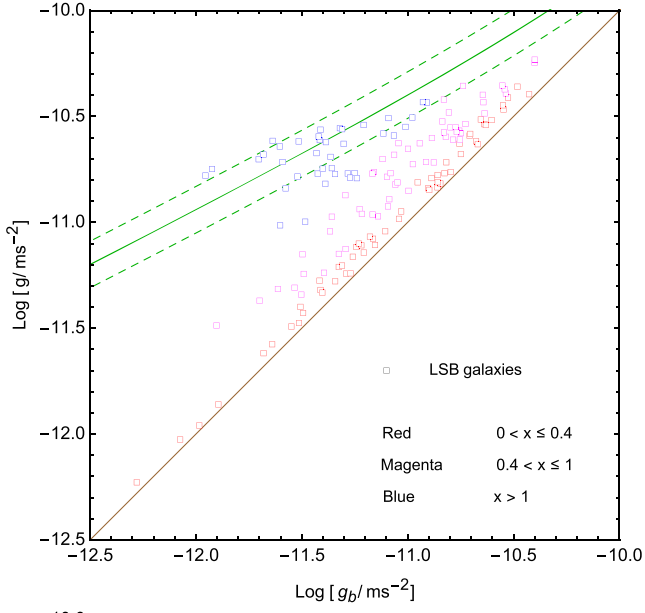


Figure 9. Data resulting from galaxies belonging to the I velocity bin (family) rotation curve fitted without gas (upper panel) and with gas (lower panel).

Appendix D

Fitting Uncertainties on f_b : The Effects on the $g-g_b$ Plane

The error induced by the kinematical estimation of the stellar mass M_d is very small. Figure 10 shows the results in the $g-g_b$ plane, taking into account $\pm 2\sigma$ fitting errors on f_b (which is the main source of error). The outcome does not change. See Figures 10 and 1.

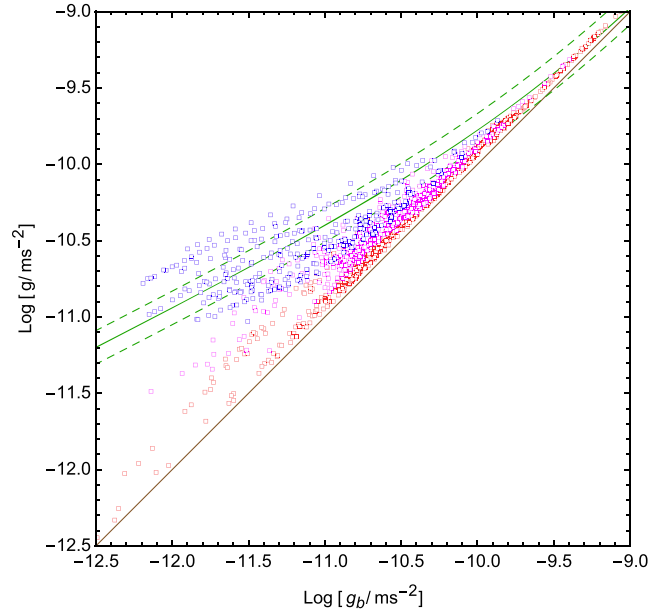
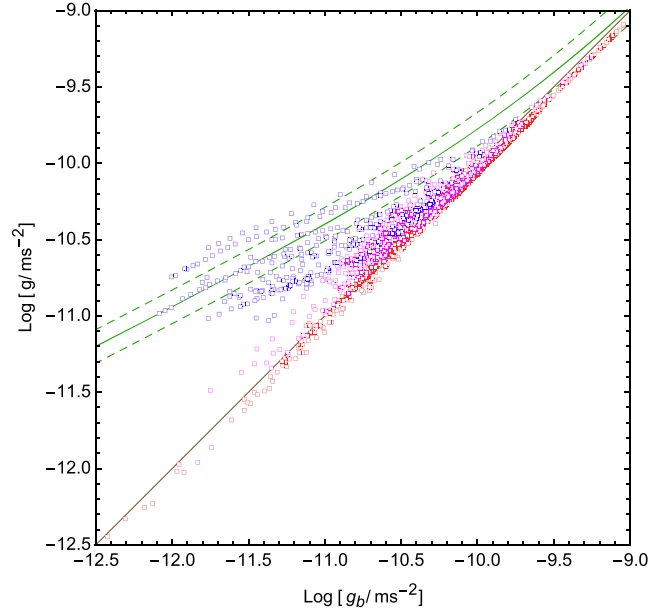


Figure 10. The $g-g_b$ relationship by assuming that f_b is 2σ higher (upper panel) and 2σ lower than the best value (lower panel).

Appendix E

The Analysis of the $g-x$ and $g-g_b$ Relations in Individual Galaxies

It is easier to understand what happens in the $g-g_b$ plane and in the $g-g_b-x$ space by analyzing a number of single galaxies. Figure 11 shows the rotation curves, its fits, g versus

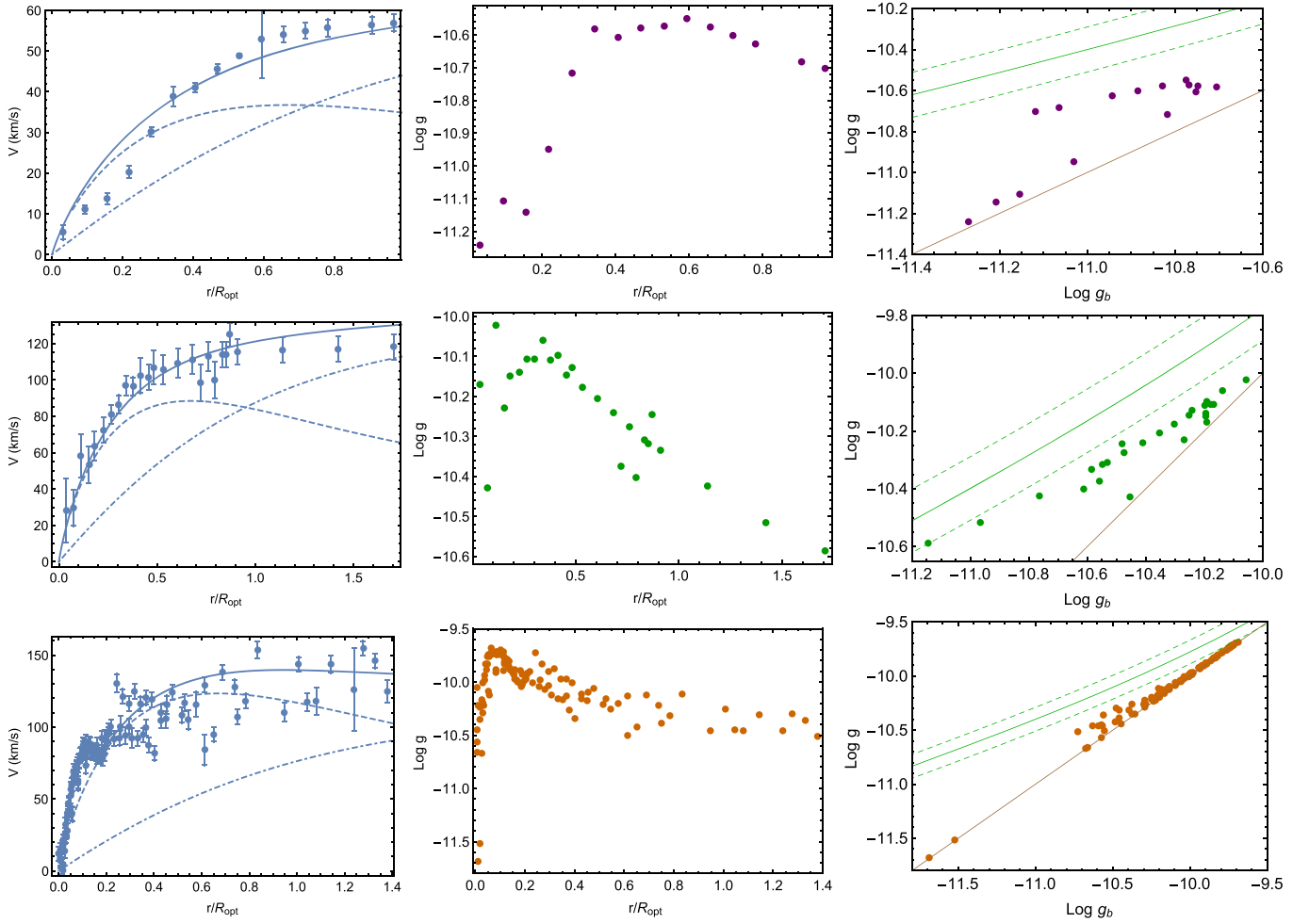


Figure 11. First, second, and third rows refer, respectively, to the galaxies UGC 1281, F568V1, and ESO 234-G013. Each row shows the galaxy’s rotation curve with the fit, the g vs. r/R_{opt} relationship, and the g vs. g_b relationship. The green and the brown lines are the McGaugh relationship (with its 1σ uncertainties) and the equality $g = g_b$ relationship, both independent on the radial coordinate r/R_{opt} .

r/R_{opt} relationship and g versus g_b relationship, for three LSBs of different size. The disagreement of present data with McG+16 relationship is evident galaxy by galaxy. Detailed explanation on this will appear on C. Di Paolo et al. (2019, in preparation).

Appendix F The LSB Sample

In Table 1, we report the list of LSB galaxies used in this work and the references of their rotation curve data and other galactic properties.

Table 1
LSB Sample

Galaxy	M (mag)	Filter	R_d (kpc)	V_{opt} (km s^{-1})	References
(1)	(2)	(3)	(4)	(5)	(6)
NGC 100	-19.68	<i>I</i>	1.2	77.2	de Blok & Bosma (2002)
NGC 247	-18.01	<i>B</i>	2.9	106.6	Carignan & Puche (1990)
NGC 959	-18.53	<i>V</i>	0.93	75.3	Kuzio de Naray et al. (2008)
NGC 2552	-18.99	<i>I</i>	1.6	104.9	Kuzio de Naray et al. (2008)
NGC 2552	-18.99	<i>I</i>	1.6	111.0	de Blok & Bosma (2002)
NGC 2552	-18.99	<i>I</i>	1.6	92.6	Swaters et al. (2003)
NGC 2552	-18.1	<i>R</i>	1.6	92.5	van den Bosch & Swaters (2001)
NGC 3274	-16.7	<i>R</i>	0.5	79.7	de Blok & Bosma (2002)
NGC 3274	-16.6	<i>R</i>	0.45	63.2	Swaters et al. (2003)
NGC 3347B	-21.76	<i>I</i>	8.1	167.0	Palunas & Williams (2000)
NGC 4395	-18.1	<i>R</i>	2.3	82.0	de Blok & Bosma (2002)
NGC 4395	-18.14	<i>R</i>	2.6	82.6	van den Bosch & Swaters (2001)
NGC 4455	-16.9	<i>R</i>	0.7	45.6	de Blok & Bosma (2002)
NGC 4455	-16.88	<i>R</i>	0.9	61.9	Marchesini et al. (2002)
NGC 4455	-16.88	<i>R</i>	0.9	51.5	van den Bosch & Swaters (2001)
NGC 5023	-19.18	<i>I</i>	0.8	78.4	de Blok & Bosma (2002)
NGC 5204	-17.3	<i>R</i>	0.66	75.2	Swaters et al. (2003)
NGC 5204	-17.28	<i>R</i>	0.66	71.0	van den Bosch & Swaters (2001)
NGC 7589	-21.9	<i>R</i>	13	224.0	Pickering et al. (1997)
UGC 628	-19.2	<i>R</i>	4.7	130.0	de Blok & Bosma (2002)
UGC 634	-17.7	<i>B</i>	3.1	95.1	van Zee et al. (1997)
UGC 731	-16.6	<i>R</i>	1.7	73.1	de Blok & Bosma (2002)
UGC 731	-16.6	<i>R</i>	1.6	73.5	Swaters et al. (2003)
UGC 731	-16.63	<i>R</i>	1.6	73.5	van den Bosch & Swaters (2001)
UGC 1230	-19.1	<i>R</i>	4.5	104.5	de Blok & Bosma (2002)
UGC 1230	-17.16	<i>NUV</i>	4.4	89.7	van der Hulst et al. (1993)
UGC 1281	-16.2	<i>R</i>	1.7	45.8	Kuzio de Naray et al. (2006)
UGC 1281	-16.2	<i>R</i>	1.7	56.9	de Blok & Bosma (2002)
UGC 1551	-19.7	<i>B</i>	2.5	55.8	Kuzio de Naray et al. (2008)
UGC 2684	-13.7	<i>B</i>	0.8	36.7	van Zee et al. (1997)
UGC 2936	-21.1	<i>R</i>	8.4	255.0	Pickering et al. (1999)
UGC 3137	-18.7	<i>R</i>	2.0	97.7	de Blok & Bosma (2002)
UGC 3174	-15.7	<i>B</i>	1.0	51.7	van Zee et al. (1997)
UGC 3371	-17.7	<i>R</i>	3.1	84.7	de Blok & Bosma (2002)
UGC 3371	-17.74	<i>R</i>	3.1	85.1	van den Bosch & Swaters (2001)
UGC 4115	-15.21	<i>V</i>	0.4	24.2	McGaugh et al. (2001)
UGC 4278	-17.7	<i>R</i>	2.3	92.6	de Blok & Bosma (2002)
UGC 5005	-17.8	<i>B</i>	4.4	95.5	de Blok & McGaugh (1997)
UGC 5272	-14.7	<i>B</i>	1.2	51.2	Kuzio de Naray et al. (2008)
UGC 5272	-14.7	<i>B</i>	1.2	46.4	de Blok & Bosma (2002)
UGC 5716	-16.3	<i>B</i>	2.0	66.4	van Zee et al. (1997)
UGC 5750	-19.5	<i>R</i>	5.6	58.5	Kuzio de Naray et al. (2006)
UGC 5750	-19.5	<i>R</i>	5.6	78.5	de Blok & Bosma (2002)
UGC 5999	-12.42	<i>R</i>	4.4	153.0	van der Hulst et al. (1993)
UGC 7178	-16.6	<i>B</i>	2.3	69.9	van Zee et al. (1997)
UGC 8837	-15.7	<i>R</i>	1.2	49.6	de Blok & Bosma (2002)
UGC 9211	-16.21	<i>R</i>	1.3	61.9	van den Bosch & Swaters (2001)
UGC 11454	-22.03	<i>R</i>	4.5	150.3	McGaugh et al. (2001)
UGC 11557	-19.7	<i>R</i>	3.1	83.7	Swaters et al. (2003)
UGC 11583	-15.48	<i>R</i>	0.31	27.9	McGaugh et al. (2001)

Note. Columns: (1) galaxy name; (2) magnitude, given for further information of the galaxies; (3) filter; (4) stellar disk scale length R_d ; (5) optical velocity V_{opt} ; (6) references. Note that some galaxies have multiple rotation curve data, that we have homogenized.

Table 2
Continued from Table 1

Galaxy	M (mag)	Filter	R_d (kpc)	V_{opt} (km s $^{-1}$)	References
(1)	(2)	(3)	(4)	(5)	(6)
UGC 11616	-21.58	<i>R</i>	4.9	133.2	McGaugh et al. (2001)
UGC 11648	-22.95	<i>KS</i>	3.8	142.2	McGaugh et al. (2001)
UGC 11748	-23.02	<i>R</i>	3.1	240.7	McGaugh et al. (2001)
UGC 11819	-20.62	<i>R</i>	5.3	154.6	McGaugh et al. (2001)
ESO 186-G055	-20.62	<i>R</i>	3.6	133.2	Pizzella et al. (2008)
ESO 206-G014	-20.32	<i>R</i>	5.2	91.3	Pizzella et al. (2008)
ESO 215-G039	-21.72	<i>I</i>	4.2	142.9	Palunas & Williams (2000)
ESO 234-G013	-21.66	<i>I</i>	3.7	139.4	Pizzella et al. (2008)
ESO 268-G044	-21.19	<i>I</i>	1.9	175.6	Palunas & Williams (2000)
ESO 322-G019	-20.41	<i>B</i>	2.5	100.7	Palunas & Williams (2000)
ESO 323-G042	-21.56	<i>I</i>	4.4	138.7	Palunas & Williams (2000)
ESO 323-G073	-21.81	<i>I</i>	2.1	165.3	Palunas & Williams (2000)
ESO 374-G003	-21.36	<i>I</i>	4.2	118.3	Palunas & Williams (2000)
ESO 382-G006	-17.03	<i>R</i>	2.3	160.0	Palunas & Williams (2000)
ESO 400-G037	-20.96	<i>I</i>	4.1	69.9	Pizzella et al. (2008)
ESO 444-G021	-19.9	<i>B</i>	6.4	107.4	Palunas & Williams (2000)
ESO 444-G047	-21.11	<i>I</i>	2.7	148.4	Palunas & Williams (2000)
ESO 488-G049	-17.94	<i>B</i>	4.4	95.3	Pizzella et al. (2008)
ESO 509-G091	-21.01	<i>I</i>	3.7	146.8	Palunas & Williams (2000)
ESO 534-G020	-21.96	<i>R</i>	17	216.6	Pizzella et al. (2008)
F561-1	-17.8	<i>B</i>	3.6	50.8	de Blok et al. (1996)
F563-V1	-16.3	<i>B</i>	2.4	27.3	de Blok et al. (1996)
F563-V2	-18.2	<i>B</i>	2.1	98.8	Kuzio de Naray et al. (2006)
F563-V2	-17.6	<i>B</i>	2.1	98.0	de Blok et al. (1996)
F565-V2	-14.8	<i>B</i>	2.0	45.2	de Blok et al. (1996)
F568-1	-18.1	<i>B</i>	5.3	130.1	Swaters et al. (2000)
F568-3	-19.14	<i>I</i>	4.0	102.6	Kuzio de Naray et al. (2006)
F568-3	-18.3	<i>B</i>	4.0	97.9	McGaugh et al. (2001)
F568-3	-18.3	<i>B</i>	4.0	101.1	Swaters et al. (2000)
F568-6	-23.6	<i>R</i>	18	297.0	Pickering et al. (1997)
F568-V1	-17.9	<i>B</i>	3.2	115.8	Swaters et al. (2000)
F571-8	-17.6	<i>B</i>	5.2	139.4	Marchesini et al. (2002)
F571-8	-17.6	<i>B</i>	5.2	140.1	McGaugh et al. (2001)
F571-V1	-11.47	<i>I</i>	3.2	72.44	de Blok et al. (1996)
F574-1	-18.4	<i>B</i>	4.3	102.3	Swaters et al. (2000)
F574-2	-17	<i>B</i>	4.5	40.0	de Blok et al. (1996)
F579-V1	-18.8	<i>B</i>	5.1	111.5	McGaugh et al. (2001)
F583-1	-16.5	<i>B</i>	1.6	68.2	Kuzio de Naray et al. (2008)
F583-1	-17.06	<i>R</i>	1.6	65.2	Marchesini et al. (2002)
F583-1	-16.5	<i>B</i>	1.6	61.3	McGaugh et al. (2001)
F583-1	-15.9	<i>B</i>	1.6	53.3	de Blok et al. (1996)
F583-4	-16.9	<i>B</i>	2.7	83.9	Kuzio de Naray et al. (2006)
F583-4	-16.9	<i>B</i>	2.7	69.0	McGaugh et al. (2001)
F730-V1	-20.27	<i>R</i>	5.8	141.6	McGaugh et al. (2001)
PGC 37759	-21.88	<i>Z</i>	6.6	139.4	Morelli et al. (2012)

References

- Burkert, A. 1995, *ApJL*, 447, L25
Carignan, C., & Puche, D. 1990, *AJ*, 100, 641
Das, M. 2013, *JApA*, 34, 19
de Blok, W. J. G., & Bosma, A. 2002, *A&A*, 385, 816
de Blok, W. J. G., & McGaugh, S. S. 1997, *MNRAS*, 290, 533
de Blok, W. J. G., McGaugh, S. S., & van der Hulst, J. M. 1996, *MNRAS*, 283, 18
Di Paolo, C., & Salucci, P. 2018, arXiv:1805.07165v1
Evoli, C., Salucci, P., Lapi, A., & Danese, L. 2011, *ApJ*, 743, 45
Freeman, K. C. 1970, *ApJ*, 160, 811
Impey, S., & Bothun, G. 1997, *ARA&A*, 35, 267
Karachentsev, I. D., Makarov, D. I., & Kaisina, E. I. 2013, *AJ*, 145, 101
Karukes, E. V., & Salucci, P. 2017, *MNRAS*, 465, 4703
Kuzio de Naray, R., McGaugh, S. S., & de Blok, W. J. G. 2008, *ApJ*, 676, 920
Kuzio de Naray, R., McGaugh, S. S., de Blok, W. J. G., & Bosma, A. 2006, *ApJS*, 165, 461
Lapi, A., Salucci, P., & Danese, L. 2018, *ApJ*, 859, 2
Lelli, F., McGaugh, S. S., & Schombert, J. M. 2016, *AJ*, 152, 157
Li, P., Lelli, F., McGaugh, S., & Schombert, J. 2018, *A&A*, 615, A3
Marchesini, D., D'Onghia, E., Chincarini, G., et al. 2002, *ApJ*, 575, 801
McGaugh, S., Lelli, F., & Schombert, J. 2016, *PhRvL*, 117, 201101
McGaugh, S. S. 1994, *ApJ*, 426, 135
McGaugh, S. S., Rubin, V. C., & de Blok, W. J. G. 2001, *AJ*, 122, 2381
Morelli, L., Corsini, E. M., Pizzella, A., et al. 2012, *MNRAS*, 423, 962
Palunas, P., & Williams, T. B. 2000, *AJ*, 120, 2884
Persic, M., & Salucci, P. 1991, *ApJ*, 368, 60

- Persic, M., Salucci, P., & Stel, F. 1996, *MNRAS*, **281**, 27
- Pickering, T. E., Impey, C. D., van Gorkom, J. H., & Bothun, G. D. 1997, *AJ*, **114**, 1858
- Pickering, T. E., van Gorkom, J. H., Impey, C. D., & Quillen, A. C. 1999, *AJ*, **118**, 765
- Pizzella, A., Corsini, E. M., Sarzi, M., et al. 2008, *MNRAS*, **387**, 1099
- Salucci, P. 2018a, *FoPh*, **48**, 1517
- Salucci, P. 2018b, in Proc. 18th Lomonosov Conf. on Elementary Particle Physics, ed. A. Studenikin (Singapore: World Scientific) arXiv:1807.08521
- Salucci, P., & Burkert, A. 2000, *ApJL*, **537**, L9
- Salucci, P., Lapi, A., Tonini, C., et al. 2007, *MNRAS*, **378**, 41
- Salucci, P., Ratnam, C., Monaco, P., & Danese, L. 2000, *MNRAS*, **317**, 488
- Swaters, R. A., Madore, B. F., & Trewhella, M. 2000, *ApJ*, **531**, L107
- Swaters, R. A., Madore, B. F., van den Bosch, F. C., & Balcells, M. 2003, *ApJ*, **583**, 732
- Tonini, C., Lapi, A., Shankar, F., & Salucci, P. 2006, *ApJL*, **638**, L13
- van den Bosch, F. C., & Swaters, R. A. 2001, *MNRAS*, **325**, 1017
- van der Hulst, J. M., Skillman, E. D., Smith, T. R., et al. 1993, *AJ*, **106**, 548
- van Zee, L., Haynes, M. P., Salzer, J. J., & Broeils, A. H. 1997, *AJ*, **113**, 1618
- Wang, J., Fu, J., Aumer, M., et al. 2014, *MNRAS*, **441**, 2159
- Yegorova, I., & Salucci, P. 2007, *MNRAS*, **377**, 507

Chapter 9

PAPER 3: “Phase-space mass bound for fermionic dark matter from dwarf spheroidal galaxies”

Phase-space mass bound for fermionic dark matter from dwarf spheroidal galaxies

Chiara Di Paolo,^{1★} Fabrizio Nesti^{2,3,4,5★} and Francesco L. Villante^{5,6★}

¹SISSA/ISAS, Via Bonomea 265, I-34136 Trieste, Italy

²Dipartimento di Fisica, Theoretical Section, Università di Trieste, Strada Costiera 11, I-34151 Trieste, Italy

³Ruđer Bošković Institute, Division of Theoretical Physics, Bijenička cesta 54, 10000 Zagreb, Croatia

⁴INFN Sez. Trieste, Via A. Valerio 2, I-34127 Trieste, Italy

⁵Dipartimento di Scienze Fisiche e Chimiche, Università dell'Aquila, Via Vetoio SNC, I-67100 L'Aquila, Italy

⁶INFN-LNGS, Via G. Acitelli 22, I-67100 Assergi (L'Aquila), Italy

Accepted 2018 January 4. Received 2017 November 14; in original form 2017 July 4

ABSTRACT

We reconsider the lower bound on the mass of a fermionic dark matter (DM) candidate resulting from the existence of known small dwarf spheroidal galaxies, in the hypothesis that their DM halo is constituted by degenerate fermions, with phase-space density limited by the Pauli exclusion principle. By relaxing the common assumption that the DM halo scale radius is tied to that of the luminous stellar component and by marginalizing on the unknown stellar velocity dispersion anisotropy, we prove that observations lead to rather weak constraints on the DM mass, which could be as low as tens of eV. In this scenario, however, the DM haloes would be quite large and massive, so that a bound stems from the requirement that the time of orbital decay due to dynamical friction in the hosting Milky Way DM halo is longer than their lifetime. The smallest and nearest satellites Segue I and Willman I lead to a final lower bound of $m \gtrsim 100$ eV, still weaker than previous estimates but robust and independent on the model of DM formation and decoupling. We thus show that phase-space constraints do not rule out the possibility of sub-keV fermionic DM.

Key words: elementary particles – neutrinos – galaxies: dwarf – dark matter.

1 INTRODUCTION

Dark matter (DM) is believed to be a main actor in cosmology, to constitute the great majority of the mass in the Universe and to rule the processes of structure formation. The so-called Λ cold dark matter (Λ CDM) paradigm, in which one assumes a cold dark matter (CDM) candidate that decouples from the primordial plasma when non-relativistic, successfully reproduces the structure of the cosmos down to scales ~ 50 kpc.

A number of serious challenges to the Λ CDM paradigm have emerged on the scale of individual galaxies and their central structure (see e.g. Weinberg et al. 2014 for a recent review). For instance, collisionless N -body simulations predict that the DM density profile of virialized objects has a negative logarithmic slope towards the centre (Flores & Primack 1994; Moore 1994; Navarro, Frenk & White 1996b, 1997; Moore et al. 1999a). Such a ‘cuspy’ distribution is not well supported by observational data of rotation curves of spiral galaxies, which are better described by haloes featuring a constant density core (Salucci & Burkert 2000). Moreover, the

number of DM subhaloes expected according Λ CDM paradigm is much larger than the observed number of satellite galaxies in the Milky Way (Klypin et al. 1999; Moore et al. 1999b), even accounting for the many recently discovered faint systems. It is still unclear whether the above problems require major changes to the Λ CDM paradigm. Models have been presented in which shallow DM cores arise naturally in a Λ CDM cosmology as a results of supernova (SN) feedback or dynamical friction (Navarro, Eke & Frenk 1996a; Governato et al. 2010, 2012; Pontzen & Governato 2012). Alternative DM candidates, however, have to be considered with utmost attention.

The hypothesis of warm dark matter (WDM) decoupling from the plasma when mildly relativistic has been advocated as a solution of the possible CDM issues. WDM introduces a non-vanishing free streaming length below which structure formation is suppressed, giving rise to the correct abundance of substructures at small scales (Colin, Avila-Reese & Valenzuela 2000; Avila-Reese et al. 2001; Bode, Ostriker & Turok 2001). Moreover, if we consider a generic fermionic dark matter (FDM) candidate, like the typical massive \sim keV warm sterile neutrino, the limit on the phase-space density provided by the Pauli exclusion principle implies that DM has a minimal velocity dispersion and, thus, resists compression. As a consequence, FDM haloes naturally produce a cored density

* E-mail: cdipaolo@sisssa.it (CDiP); fnesti@irb.hr (FN); villante@lngs.infn.it (FLV)

profile whose radius R_h (for a fixed halo mass M_h) is a decreasing function of the mass m of the DM candidate, see next section for details. Being the most DM-dominated astrophysical objects, dwarf spheroidal (dSph) galaxies are the optimal candidates to test this scenario.

The possibility to constrain the DM particle mass by determining the DM phase-space distribution was first considered in the seminal work by Tremaine & Gunn (1979). In the hypothesis of non-dissipative evolution, i.e. conservation of the maximal phase-space density, it is possible to set a strong bounds on the DM mass $m > 300\text{--}700$ eV (see e.g. Dalcanton & Hogan 2001). These bounds stem from the primordial limit of the DM phase-space density, and are not necessarily related to the fermionic nature of DM; indeed they apply also if DM can be treated as a collisionless gas collapsed via violent relaxation *à la* Lynden–Bell. However, they require the knowledge of the initial DM phase-space density (and, thus, of the DM production mechanism) and the assumption that baryonic feedback cannot alter the maximum of the DM distribution function. A more general situation was studied by Gerhard & Spiegel (1992) that pointed out the importance of constraints by dynamical friction on dSph galaxies in the Milky Way host halo, which as we will show still play the most important role.

Subsequent analyses (Bilic, Tupper & Viollier 2001; Chavanis 2002; de Vega, Salucci & Sanchez 2014) modelled truly fermionic DM cores for instance by using a Thomas–Fermi self-gravitating gas approach, suggesting that dSph galaxies host degenerate fermionic haloes while larger and less dense galaxies behave as non-degenerate classical systems. Observational data on dSph galaxies were used in Boyarsky, Ruchayskiy & Iakubovskiy (2009) to derive bounds of the order of 400 eV. Finally, in a recent analysis (Domcke & Urbano 2015) it was claimed that the velocity dispersions of the eight classical dSph galaxies of the Milky Way are well fitted by assuming DM cores composed of fully degenerate fermions with masses $m \simeq 200$ eV and allowing for a non-vanishing anisotropy of the stellar component.

The observation that kinematic properties of dSph galaxies may be connected, in a relatively simple model, to the elementary properties of the DM candidate is extremely interesting. However, there is at the moment no evidence in favour of degenerate galactic cores. If all the smallest galactic cores were to be degenerate, their masses and radii should follow a relationship $M_h \propto R_h^{-3}$, as expected for degenerate fermionic systems and univocally determined by the mass m of the DM candidate. This behaviour in the plane (R_h, M_h) is presently not observed; on the contrary, the observation that the estimated surface densities of diverse kinds of galaxies are approximately constant (Donato et al. 2009; Salucci et al. 2012), $\Sigma_0 \sim M_h/R_h^2 \sim 100 M_\odot \text{pc}^{-2}$, can only be supported by non-degenerate cores, because this relation lies almost orthogonal to the above degeneracy lines. Still, this argument cannot be used to rule out the existence of degenerate cores, because they could be present just in the smallest galaxies. These have a larger density, and therefore are candidate to support or exclude the hypothesis of fermionic DM with low mass.¹

In this paper we take a conservative attitude and determine a robust lower limit on the mass m of a fermionic DM particle from the properties of these smallest observed galaxies. We consider Will-

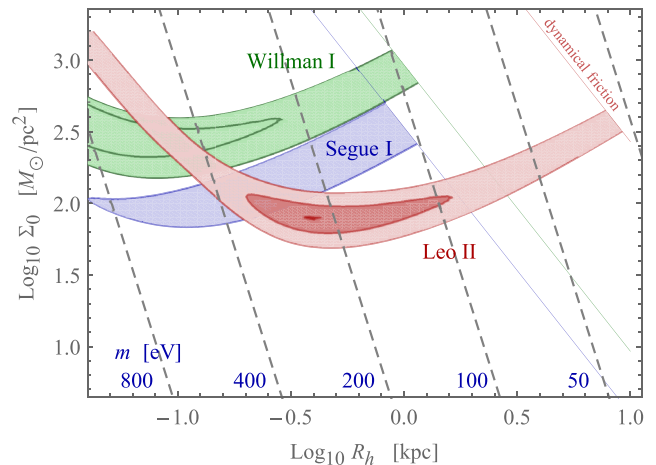


Figure 1. Plane $R_h\text{--}\Sigma_0$, describing the DM core. The shaded contours show the values of DM core sizes allowed for Willman I, Segue I, and Leo II at 68 per cent CL by the LOS velocities, and respecting the bound from the dynamical friction time.

man I (Willman et al. 2011) and Segue I (Simon et al. 2011), which are among the smallest structures for which stellar velocity measurements are available, and the ‘classical’ dSph Leo II from which restrictive bounds on m were obtained by Boyarsky et al. (2009) and Domcke & Urbano (2015). We determine bounds on the core radius R_h , mass M_h , or surface density Σ_0 of the selected galaxies by performing a fit to the stellar line-of-sight (LOS) velocity dispersion profile. The theoretical predictions are obtained through a standard Jeans analysis, including the role of the unknown velocity dispersion anisotropy of the stellar component. Moreover, we refrain from assuming that luminous matter traces the DM distribution, unlike many of the recent works, and thus leave as a free parameter the DM core radius.

We show in detail how, unless the anisotropy of stellar component will be constrained independently, the observed stellar velocity dispersion profiles lead to very poor constraints on the DM halo, and the possibility of very large \sim kpc haloes cannot be ruled out. However, such large haloes are at odds with their lifetime due to the dynamical friction within the Milky Way (Binney & Tremaine 2008). This provides a further quantitative limit on the DM halo size, allowing us to finally constrain the DM particle mass m . To facilitate the reader, our results are anticipated in Fig. 1 that contains a synthesis of our work before discussing the technical details.

The final limit that we obtain, $m \gtrsim 100$ eV, is less restrictive but more solid than previously quoted bounds (Boyarsky et al. 2009; Domcke & Urbano 2015) that rely on the assumption that the DM core radius is equal to the half-light radius, or analogously that the escape velocity from the DM core is determined by the stellar velocity dispersion. Moreover, our limit is fairly model independent because it is based only on the present phase-space density of DM particles and does not require any assumption on their initial distribution or their evolution (see e.g. Boyarsky et al. 2009 for a discussion of the model-dependent bounds that can be obtained for a dissipationless DM candidate by considering specific production mechanisms). Restrictive limits ($m \gtrsim$ few keV) on sterile neutrino mass can be also obtained from the analysis of the Ly α forest data (see e.g. Iršič et al. 2017 for a recent update). It should be noted, however, that this analysis is not directly sensitive to DM particle mass, as Ly α data essentially probe the power spectrum of density fluctuations at comoving scales \sim Mpc, by constraining the DM free

¹ It is of course also possible that the evolution of structures is such that DM, although fermionic, never forms degenerate cores; in this situation it is still or even more important to assess the values of the DM mass that allows the realization of this scenario.

streaming length. Since this quantity can be related to the particle mass only within a specific DM model, the Ly α bound cannot be applied to a generic fermionic candidate, unlike from the limit derived in this paper.

The plan of the paper is the following. In Section 2 we describe the physics relevant for degenerate fermionic DM haloes, while in Section 3 we lay down the possible strategies to constrain the mass of the DM candidate from the observational data. In Section 4 we describe the results for the Leo II, Willman I, and Segue I dwarf galaxies, by paying also attention to the possibility that some of these galaxies are instead non-degenerate. We present also a consistent estimate for the ensuing bound on the DM mass in the case of the other known dSph galaxies. In Section 5 we summarize the conclusions and possible outlook. Finally, for convenience we briefly review in Appendix A the technicalities relative to degenerate fermionic haloes, as well as the Thomas–Fermi analysis for non-exactly degenerate ones.

2 THE FDM HYPOTHESIS

We consider the equilibrium configuration for an ensemble of self-gravitating DM fermions of mass m and g internal (spin) degrees of freedom. The assumption of fermionic particles implies the upper limit for the DM phase-space distribution function that, as reviewed in Appendix A, translates into a lower limit for the DM velocity dispersion,

$$\begin{aligned} \sigma_{\text{DM}}^2 &\geq \sigma_{\text{DM,min}}^2(\rho) = \frac{1}{5} \left(\frac{6\pi^2 \hbar^3 \rho}{g m^4} \right)^{2/3} \\ &= 7.56 \left(\frac{\text{km}}{\text{s}} \right)^2 \left(\frac{g}{2} \right)^{-2/3} \left(\frac{m}{1 \text{ keV}} \right)^{-8/3} \left(\frac{\rho}{\text{M}_{\odot} \text{ pc}^{-3}} \right)^{2/3}, \end{aligned} \quad (1)$$

as a function of the mass density ρ of the system. This bound becomes effective and very stringent in the regions of high density. As a consequence, fermionic DM haloes resist compression and cannot have arbitrary size.

The strong degeneracy limit, in which the velocity dispersion is assumed to have the minimal value $\sigma_{\text{DM,min}}^2(\rho)$, represents the most compact configuration for a self-gravitating fermionic halo. The density profiles of such fully degenerate haloes are universal. They depend only on one free parameter and can be expressed (apart from a normalization factor and a scale radius that are related, see the following) in terms of the solution of the well-known Lane–Emden equation, see equation (A13). As shown in Appendix A, for our purposes the degenerate profiles are very well approximated by the function

$$\rho(r) = \rho_0 \cos^3 \left[\frac{25}{88} \pi x \right], \quad x = r/R_{\text{h}}, \quad (2)$$

where ρ_0 is the central DM halo density. The halo radius R_{h} is defined by the condition

$$\rho(R_{\text{h}}) = \rho_0/4 \quad (3)$$

and is related to the central density ρ_0 and to the properties of the DM particle by the numerical relation

$$R_{\text{h}} = 42.4 \text{ pc} \left(\frac{g}{2} \right)^{-1/3} \left(\frac{m}{1 \text{ keV}} \right)^{-4/3} \left(\frac{\rho_0}{\text{M}_{\odot} \text{ pc}^{-3}} \right)^{-1/6}. \quad (4)$$

This value represents also the minimal admissible radius for a fermionic structure since for smaller radii the gravitational potential $\phi \sim -G \rho_0 R_{\text{h}}^2$ is lower (in modulus) than $\sigma_{\text{DM,min}}^2 \sim (\rho_0/g)^{2/3} m^{-8/3}$ and the system is not stable.

Larger non-degenerate structures are admissible because they can have $\sigma_{\text{DM}}^2 \geq \sigma_{\text{DM,min}}^2$ that prevents gravitational collapse. Unlike in the completely degenerate case, their properties cannot be univocally predicted because the velocity dispersion is not determined by the mass density and not directly linked to the DM particle properties. Isothermal haloes with arbitrary level of degeneration can be studied by using the Thomas–Fermi approach as reviewed in Appendix A. Interestingly, it is found that when R_{h} is just 2–3 times larger than the minimal value (equation 4), the fermionic nature of DM particles can be neglected, i.e. the resulting structures are essentially indistinguishable from isothermal haloes obtained by assuming classical Maxwell–Boltzmann statistics and arbitrary large values of the particle mass m .

For fully degenerate fermionic structures, by using equation (4) one can predict their surface density $\Sigma_0 \equiv \rho_0 R_{\text{h}}$,

$$\frac{\Sigma_0}{\text{M}_{\odot} \text{ pc}^{-2}} = 0.584 \left(\frac{g}{2} \right)^{-2} \left(\frac{m}{1 \text{ keV}} \right)^{-8} \left(\frac{R_{\text{h}}}{100 \text{ pc}} \right)^{-5}, \quad (5)$$

as well as their mass M_{h} , defined as the mass enclosed within the radius R_{h} :

$$\frac{M_{\text{h}}}{10^7 \text{ M}_{\odot}} = 1.18 \left(\frac{g}{2} \right)^{-1/3} \left(\frac{m}{1 \text{ keV}} \right)^{-8} \left(\frac{R_{\text{h}}}{10 \text{ pc}} \right)^{-3}. \quad (6)$$

The radius, surface density, and mass of degenerate haloes are not independent quantities, being $M_{\text{h}} \simeq 2.02 \rho_0 R_{\text{h}}^3 = 2.02 \Sigma_0 R_{\text{h}}^2$ for the density profile (equation 2). For definiteness, we perform our analysis in the plane (R_{h}, Σ_0) but equivalent bounds are clearly obtained by using any couples of the three quantities R_{h} , Σ_0 , and M_{h} .

In Fig. 1 we have reported as grey dashed lines in the plane (R_{h}, Σ_0) the points relative to fully degenerate systems for selected values of the DM particle mass m and assuming $g = 2$. Equations (5) and (6) define the lower limits for surface densities and masses of fermionic DM haloes. The regions to the left of the grey lines in the plane (R_{h}, Σ_0) are not compatible with the assumption that the halo is composed of fermionic particles. Note that for fixed surface density, the smaller is the particle mass, the larger has to be the core radius. As a consequence, the observational determinations of halo radii R_{h} and surface densities Σ_0 can be translated into lower limits for the mass m of FDM candidates:

$$\frac{m}{\text{keV}} \geq 0.53 \left(\frac{g}{2} \right)^{-1/4} \left(\frac{\Sigma_0}{100 \text{ M}_{\odot} \text{ pc}^{-2}} \right)^{-1/8} \left(\frac{R_{\text{h}}}{100 \text{ pc}} \right)^{-5/8}, \quad (7)$$

and we note the reduced dependence on Σ_0 .

If galactic cores were to be commonly degenerate, one should arguably observe a clustering along the lines defined by equation (5) in the plane (R_{h}, Σ_0) , at least for the smallest structures. This clustering is presently not observed. Instead, the estimated surface densities of diverse kinds of observed galaxies appear to be approximately constant (Donato et al. 2009; Salucci et al. 2012), $\Sigma_0 \sim 100 \text{ M}_{\odot} \text{ pc}^{-2}$, a fact that can only be supported by non-degenerate cores, because this relation lies almost orthogonal to the degeneracy lines.

This argument cannot be used to rule out the fermionic nature of DM, or the occurrence of degenerate haloes, because even if all large galaxies host a non-degenerate DM halo, degenerate cores could be present in the smallest objects, of limited number and maybe even too small to be observed. Therefore, what one can do at present is to obtain a lower limit on the mass of a fermionic DM candidate from the existence of the smallest galaxies, once their properties

(radius, mass, and/or surface density) are determined. It is our aim to reassess in this way the present bound on m .

3 STRATEGIES

The standard mass estimation methods applied to dSph galaxies, like those described in Wolf et al. (2010), are not sufficient for our purposes. In fact, they provide an estimator of the mass $M_{1/2}$ enclosed inside the half-light radius $R_{1/2}$, but this radius is not necessarily representative of the DM distribution and might be in principle (much) smaller than the halo size R_h . In other words, the quantity $M_{1/2}$ represents only a lower limit on the core mass M_h but does not provide an upper constraint.

In e.g. Boyarsky et al. (2009) and Domcke & Urbano (2015) lower bounds on the mass of FDM candidates were obtained by assuming that $R_h \simeq R_{1/2}$, i.e. $M_h \simeq M_{1/2}$ and/or by assuming that the stellar velocity dispersion can be used to estimate the escape velocity from the DM core. This is only allowed if we assume that luminous matter traces DM distribution. However, this assumption may well be violated, especially in the considered scenario in which the properties of the DM distribution are not only determined by gravitational interactions but also by the fermionic nature of DM. One may also recall that for larger galaxies, like the Milky Way or elliptical galaxies, the scale lengths of stellar and dark components can differ greatly, with the dark component extending typically some factors more than the stellar one.

Along these arguments, in this work we proceed in more generality, treating R_h and M_h as independent properties of the DM halo. We only use $R_{1/2}$ and $M_{1/2}$ in a preliminary stage to select, by using the values tabulated in Wolf et al. (2010) and equation (6), the dSph galaxies Willman I (Willman et al. 2011) and Segue I (Simon et al. 2011) as the most promising candidates for constraining m . In addition to these two galaxies, which are among the smallest structures for which stellar velocity measurements are available, we also consider the ‘classical’ dSph Leo II from which restrictive bounds on m were obtained by Boyarsky et al. (2009) and Domcke & Urbano (2015).

For each galaxy, we determine the DM halo properties, core radius, and mass (or surface density) by performing a fit of the stellar LOS velocity dispersion profile as predicted by the model through the Jeans analysis, to the observed data. We also consider the role of the possible stellar velocity dispersion anisotropy. As was already suggested in the past (see e.g. Walker 2013) in most cases the poor data and the unknown anisotropy lead to very poor constraints on the DM halo, and the possibility of very large \sim kpc halo cannot be ruled out. We then consider that such large haloes would be associated with unphysically short orbital lifetimes due to the dynamical friction within the Milky Way. This fact provides a further quantitative constraint on the DM halo size, and thus allows us to constrain the DM particle mass m .

3.1 Spherical Jeans analysis

Assuming that the stellar component is virialized within the gravitational potential dominated by the DM component, the standard spherical Jeans equation

$$\left(\frac{\partial}{\partial r} + \frac{2\beta}{r} \right) (n_* \sigma_r^2) = -n_* \frac{GM(r)}{r^2} \quad (8)$$

allows one to relate the velocity dispersion profile of stars to the DM mass distribution $M(r)$. In the above, G is the Newton constant, $n_*(r)$ is the stellar number density, σ_r^2 is the radial velocity dispersion of

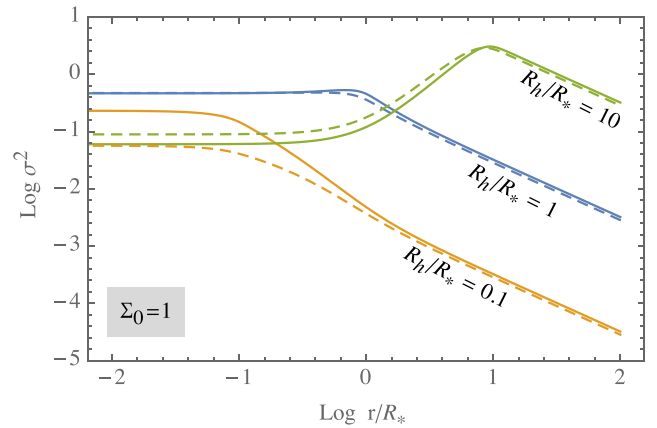


Figure 2. Stellar velocity dispersion profiles (solid) for representative DM core radii and $\beta = 0$. The dashed curves show the LOS projected velocity dispersion profiles.

stars, and $\beta \equiv 1 - \sigma_{\perp}^2/\sigma_r^2$ is its anisotropy, which in principle can depend on radius. We first discuss the case of zero anisotropy, and later comment on its role. Our final results are obtained by treating β as a nuisance parameter. A number of other aspects, like the possible co-existence of more than one stellar component, or non-complete virialization, are further factors of uncertainty that may not be easily removed.

We model the density profile of the stellar component for each dSph galaxy by means of a Plummer density profile with specific scale radius R_* :

$$n_*(r) = n_0 (1 + x^2)^{-5/2}, \quad x = r/R_*, \quad (9)$$

and the central density n_0 plays no role in the following. Clearly, the applicability of this density profile to real and poorly known galaxies is another element of uncertainty.

Equation (8) can be integrated in favour of σ_r^2 , once the DM mass distribution $M(r)$ is determined by the DM density equation (2). The resulting stellar velocity dispersion is shown in Fig. 2, for three representative cases of R_h smaller, equal or larger than the stellar scale radius R_* . The profiles shown are illustrative and are obtained by normalizing to a fixed surface density $\Sigma_0 = \rho_0 R_h = 1$. In fact, once the radius R_h is fixed, the DM central density ρ_0 or the surface density Σ_0 represents just a multiplicative constant factor for the mass function $M(r)$ and does not affect the radial dependence of σ_r^2 .

We see from Fig. 2 that if the DM halo is smaller than the Plummer radius, $R_h \leq R_*$, the stellar velocity dispersion starts to fall as soon as the DM density vanishes, reflecting the decrease of the gravitational potential. On the other hand if the DM distribution is more extended than the stellar one, $R_h \geq R_*$, the stellar velocity dispersion has to increase in the regions where the Plummer density drops. In few words, the slope of the stellar velocity dispersion $\partial \ln \sigma_r^2 / \partial \ln r$ is related to the characteristic sizes R_* and R_h of the galactic components and could, thus, be used to constrain the DM distribution.

In order to compare with observational data, one has also to consider that only the velocity dispersion *along the LOS* is measurable:

$$\sigma_{\text{los}}^2(R) = \frac{1}{\Sigma_*} \int_{R^2}^{\infty} dr^2 \frac{n_*}{\sqrt{r^2 - R^2}} \sigma_r^2 \left[1 - \beta \frac{R^2}{r^2} \right], \quad (10)$$

where $\Sigma_*(R) = \int_{R^2}^{\infty} dr^2 n_*(r)/\sqrt{r^2 - R^2}$ is the projected stellar (surface) density. In Fig. 2, we show with dashed lines the LOS

velocity dispersion for the three cases described previously. They retain the same behaviour of σ_r^2 , showing that the observed LOS velocity dispersion profile $\sigma_{\text{los}}^2(R)$ can in principle be used to constrain the size of the DM core.

3.2 Analysis for the smallest objects

In order to obtain the most restrictive bounds on the mass of the FDM particle, below we will consider Willman I (Willman et al. 2011) and Segue I (Simon et al. 2011) that are among the smallest observed galactic structures. The problem with these objects is that the number of stars for which a measure of velocity is available and which pass quality cuts is quite small (i.e. less than 50). As a consequence, it is not possible to determine the velocity dispersion in radial bins sufficiently localized to be compared directly with the profile in equation (10). One can still appreciate the characteristic signature of a large DM core, i.e. an increasing slope of the stellar dispersion velocity between $r \sim R_*$ and $r \sim R_h$, by determining the velocity dispersion in few relatively large bins with dimension $\Delta r \sim R_*$.

In order to perform such analysis, we define the *average* LOS velocity dispersion in a bin $r \in [R_1, R_2]$,

$$\overline{\sigma_{\text{los}}^2}(R_1, R_2) = \frac{1}{N_*(R_1, R_2)} \int_{R_1}^{R_2} dr 2\pi r \Sigma_*(r) \sigma_{\text{los}}^2(r), \quad (11)$$

where $N_*(R_1, R_2) = \int_{R_1}^{R_2} dr 2\pi r \Sigma_*(r)$ is the cumulative number of stars between two radii. Using equation (10), and assuming constant β , we find

$$\overline{\sigma_{\text{los}}^2} = \frac{1}{N_*(R_1, R_2)} \int_{R_1}^{R_2} dr 4\pi r^2 n_* \sigma_r^2 \mathcal{F}(r, \beta; R_1, R_2), \quad (12)$$

where the adimensional function $\mathcal{F}(r, \beta; R_1, R_2)$ is

$$\mathcal{F}(r, \beta; R_1, R_2) = \left\{ \left[\sqrt{r^2 - R_1^2} - \sqrt{r^2 - B^2} \right] \frac{(3 - 2\beta)}{3r} + \frac{\beta}{3r^3} \left[B^2 \sqrt{r^2 - B^2} - R_1^2 \sqrt{r^2 - R_1^2} \right] \right\}, \quad (13)$$

with $B = \min\{r, R_2\}$.²

For illustrative purposes, we show in Fig. 3 as solid lines the behaviour of the average LOS velocity dispersion calculated in two bins $[0, R_*]$ and $[R_*, 3R_*]$ as a function of the DM core radius R_h , for $\beta = 0$. One can observe that the average LOS dispersion velocity in the external bin overshoots the internal one as soon as $R_h/R_* \gtrsim 2$. This demonstrates that even with two single bins, and provided the uncertainties on the observed dispersion velocity are not too large, one could constrain the DM core size. For instance, if the observed dispersion velocities in two or more bins in the vicinity of $r \simeq R_*$ are approximately the same, one could rule out the possibility that DM extends much beyond the stellar component.

From the plot one can make also other remarks. Clearly, the more the DM core extends beyond the stellar component ($R_h/R_* > 1$), the less its actual density profile beyond R_h is relevant for the stellar physics, because the DM density is anyway constant in the region where the stars trace the gravitational potential. On the other hand, one can expect that if the DM core is smaller than the stellar scale ($R_h/R_* < 1$) the actual shape of the DM profile out of its core

² The number of stars in a bin $N_*(R_1, R_2)$ can be also calculated as $N_*(R_1, R_2) = \int_{R_1}^{R_2} dr 4\pi r^2 n_*(r) \mathcal{F}(r, \beta = 0; R_1, R_2)$.

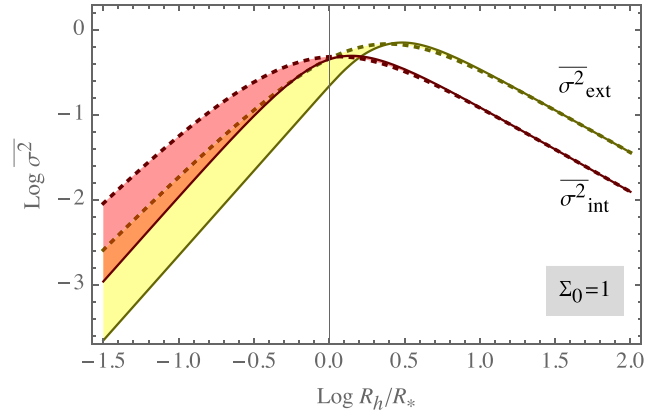


Figure 3. Averaged stellar velocity dispersion in two bins, taken here as int = $[0, r_*]$ (red) and ext = $[r_*, 3r_*]$ (yellow), for $\beta = 0$. The dashed curves show the same for a Burkert profile (non-degenerate fermions).

will influence the resulting stellar velocity dispersion. To show this effect, we have repeated the analysis for Burkert DM profiles, also reported in Fig. 3 as dashed lines, which confirms the dependence on the profile shape for $R_h < R_*$. On the other hand, for $R_h > R_*$, the solid and dashed curves are overlapping, i.e. the predicted dispersion does not depend on the shape of the DM profile, making the analysis more robust.

Unfortunately, as we shall discuss for the specific cases of Segue I and Willman I, the analysis outlined in this section is considerably hampered by the large uncertainties in each bin of the observed velocity dispersion. In addition, it is also severely limited by the unknown velocity anisotropy.

3.3 The role of anisotropy

As is well known and as we will see in detail, the unknown stellar velocity dispersion anisotropy β limits severely the possibility to extract the DM core radius R_h from observational data. Indeed, in the absence of direct information, the quantity β has to be treated as a nuisance parameter that has to be removed in order to compare a mass model with observations (see e.g. Walker et al. 2007 and Ullio & Valli 2016 for a recent critical discussion). The role of β can be understood by rewriting the Jeans equation (8) in the form

$$\frac{\partial \ln \sigma_r^2}{\partial \ln r} = -\frac{1}{\sigma_r^2} \frac{GM}{r} - \gamma_* - 2\beta, \quad (14)$$

where $\gamma_* = d \ln n_*/d \ln r$ is the slope of the stellar number density, that runs from ~ 0 near the centre to negative values out of R_* . Note that the first two terms in the right-hand side (rhs) that are related to DM and stellar distributions have opposite signs, being negative the first and positive the second. In the case of zero anisotropy, the slope of the velocity dispersion vanishes at the galactic centre, i.e. $\partial \ln \sigma_r^2 / \partial \ln r = 0$ for $r = 0$, since these two terms are both equal to zero in the origin. If the DM halo extends outside the stellar scale radius, the term γ_* starts to grow (in modulus) at $r \simeq R_*$ while $GM(r)/r\sigma_r^2$ is still negligible, and determines the positive slope of σ_r^2 observed in Fig. 2. Whereas the observed stellar velocity dispersion does not feature such a growth at large distances, one can set an upper bound on the DM core radius, that cannot be much larger than the stellar scale radius R_* .

The presence of a non-vanishing anisotropy can clearly alter this scenario. In particular, a positive β can compensate the effect of γ_*

reducing the outer slope of σ_r^2 , even in presence of a DM distribution extending well beyond the stellar radius. However, this effect is limited by the fact that the anisotropy parameter is limited to be less than 1. As a result, the case $\beta = 1$ leads to weaker upper bound on the core radius R_h , and basically the most conservative. The opposite holds for negative β values that can give quite small slope $\partial \ln \sigma_r^2 / \partial \ln r \geq 0$ even for mass models with $R_h \leq R_*$. Because a negative β is unconstrained, this limits the possibility of setting a lower bound on R_h in dSph galaxies and assessing the cusp–core problem at such short scales.

Note that, for the purpose of determining an upper limit for the core radius R_h , it is not even necessary to consider a generic $\beta(r)$ since the most relevant fact is the presence of the upper bound $\beta < 1$. In our analysis, we assume a *constant* anisotropy parameter β and we treat it as a nuisance parameter.

In order to do this, we adopt the following philosophy: for each set of DM core radius R_h and surface density Σ_0 we scan over the complete physically allowed range $-\infty < \beta \leq 1$, and if there exists a value of β that provides a good fit to the observational data, then the hypothesis of a degenerate core with those parameters cannot be rejected. Following a frequentist approach, the level of compatibility with data is assessed by defining a standard χ^2 function (see Section 4.1). This is eventually minimized with respect to β . This procedure allows us to obtain the most conservative bounds.

The comprehensive range in β that we adopt reflects our present ignorance of the dispersion anisotropy. Clearly, if in the future independent constraints on the anisotropy parameter will become available, this procedure might be improved.

It should be noted that an additional source of uncertainty is due to the slope of the density profile γ^* . As a general rule (see equation 14) the role of γ^* in the outer regions is similar to that of β : the more negative γ^* is, the stronger is the rise in the external σ_r and thus the more restrictive the bound would be. The Plummer profile that we adopt reaches quite steep values (-5) of the slope in the outer region and thus can be taken as a reasonable benchmark. Because in practice the precise slope of the density profile is extremely hard to constrain from observations, especially for the smallest objects, this additional uncertainty should be kept in mind.

3.4 Dynamical friction

The mass of dSph galaxies can be limited from above because they are subject to dynamical friction in the Milky Way DM halo. Their orbit decay with a characteristic time-scale that can be estimated from the Chandrasekhar formula (Binney & Tremaine 2008):

$$t_{\text{fric}} = \frac{10^{10} \text{ yr}}{\ln \Lambda} \left(\frac{D}{60 \text{ kpc}} \right)^2 \left(\frac{v}{220 \text{ km s}^{-1}} \right) \left(\frac{2 \times 10^{10} M_{\odot}}{M_h} \right), \quad (15)$$

where v is the velocity of the dwarf galaxy and D is its distance from the Milky Way centre. The Coulomb logarithm in the above equation is given by

$$\ln \Lambda = \ln \left(\frac{b_{\text{max}}}{b_{\text{min}}} \right), \quad (16)$$

where b_{max} and b_{min} are the maximum and minimum impact parameters. These can be estimated as (Binney & Tremaine 2008; Just et al. 2011)

$$b_{\text{max}} = - \left(\frac{d \ln \rho_{\text{MW}}}{dr} \right)^{-1} \simeq \frac{D}{\gamma}, \quad b_{\text{min}} = \max \left\{ R_h, \frac{GM_h}{v_{\text{typ}}^2} \right\}, \quad (17)$$

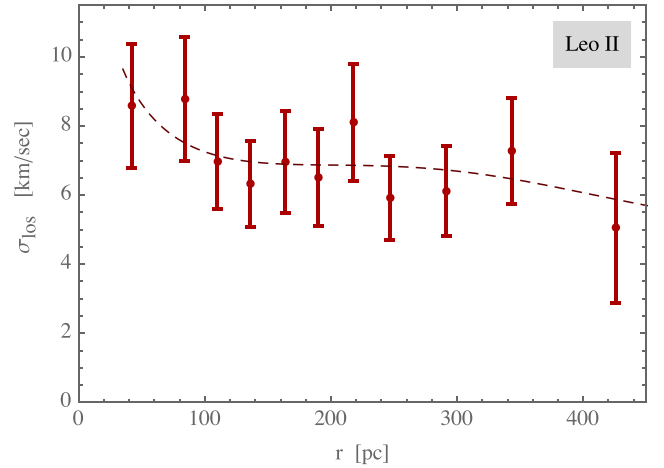


Figure 4. Stellar LOS velocity dispersions for Leo II. The dashed line represents the best fit, achieved for $\beta = 0.6$.

where v_{typ} is the virial velocity and we assumed that the Milky Way DM density scales approximately as $\rho_{\text{MW}} \propto D^{-\gamma}$ with $\gamma \simeq 2$ in the vicinity of the objects considered.³

Chandrasekhar’s formula (15) is known to fail when the mass M_h of the satellite becomes comparable to the mass of the host system that lies interior to the satellite’s orbit and/or the density of host system is constant (see e.g. Read et al. 2006). In the cases of our interest, however, none of these conditions apply and equation (15) provides a remarkably accurate description. By requiring $t_{\text{fric}} \gtrsim 10^{10}$ yr, and by considering that the typical velocity of satellites should be of the order of the Galactic virial velocities at those distances $\sim 220 \text{ km s}^{-1}$ (Nesti & Salucci 2013), one finds a bound on the mass M_h that depends on the distance of the dwarf galaxy from the Galactic Centre.

Note that the existence of an upper limit for M_h does not imply by itself the possibility to constraints the FDM scenario. It was noted, however, in Gerhard & Spergel (1992) that if the DM density of dSph galaxies can be determined from velocity dispersion data, the upper bound on M_h can be used to obtain an upper limit on R_h , thus constraining the mass m of hypothetical FDM particles.

4 RESULTS

4.1 A small classical dwarf – Leo II

As a paradigmatic case, we first analyse the case of Leo II, the smallest among the so-called ‘classical’ dSph satellite galaxies of the Milky Way. The stellar number density of Leo II is well modelled by a Plummer profile with scale length $R_* = 177$ pc. In Fig. 4 we report the observed stellar LOS velocity dispersion, $\sigma_i^2 \pm \delta \sigma_i^2$, measured in 11 bins centred at the radii r_i . We compare these data with the LOS velocity dispersion predicted in equation (10) for the fully degenerate fermionic DM halo, $\overline{\sigma_i^2} \equiv \sigma_{\text{los}}^2(r_i)$, by defining a standard χ^2 test:

$$\chi^2(R_h, \Sigma_0, \beta) = \sum_{i \in \text{bins}} \left(\frac{\sigma_i^2 - \overline{\sigma_i^2}}{\delta \sigma_i^2} \right)^2. \quad (18)$$

³ For degenerate cores, the halo radius R_h defined in equation (A14) is sufficiently close to the half-mass radius of the DM distribution.

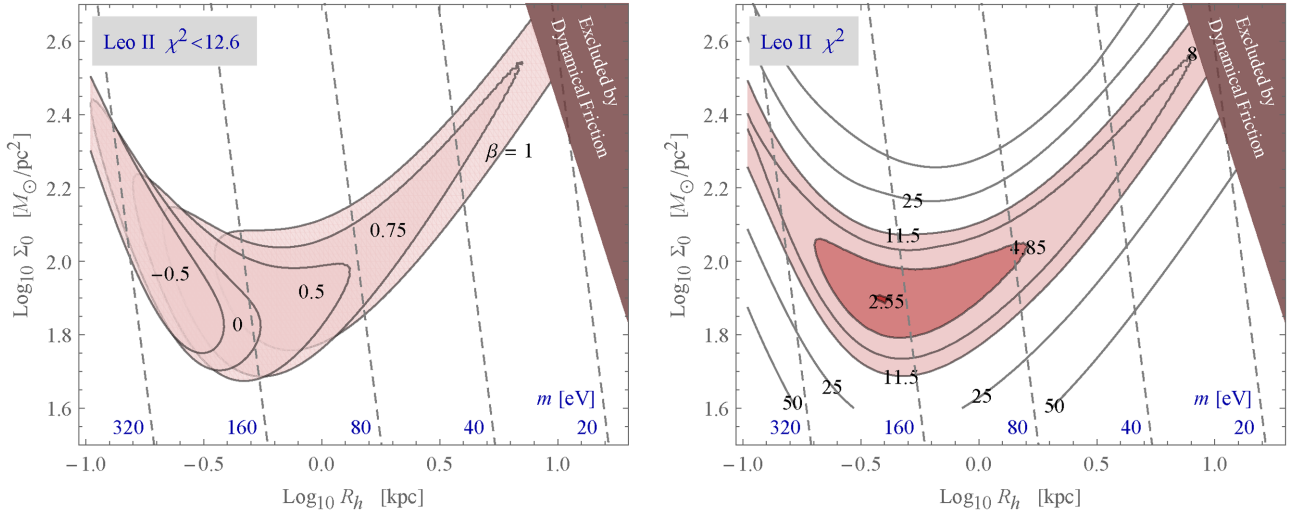


Figure 5. Leo II – left: contours of compatibility with data at 68 per cent probability ($\chi^2 \lesssim 12.6$, for 11 dof) as a function of the degenerate DM core parameters, for various values of the dispersion anisotropy β . Right: contours of best χ^2 in the plane (R_h, Σ_0) after eliminating the anisotropy β . The light shaded region is compatible with the observational data at 68 per cent CL ($\chi^2 \lesssim 11.5$, for $11 - 1 = 10$ dof). The darker shading shows the region preferred by data at 68 per cent CL ($\Delta\chi^2 = 2.3$), if one *assumes* the FDM hypothesis as true.

The model parameters are the DM core radius R_h and surface density $\Sigma_0 \equiv \rho_0 R_h$, plus the anisotropy β .

Our results are shown in Fig. 5. In the left-hand frame, we plot the χ^2 contours in the plane (R_h, Σ_0) , corresponding to 68 per cent confidence level (CL) exclusion for 11 degrees of freedom (dof), obtained by assuming fixed values of $\beta = -0.5, \dots, 1$. In the right-hand frame, we eliminate the nuisance parameter β . As discussed in Section 3.3, we use a conservative approach that does not require the introduction of a prior on the anisotropy distribution. Namely, for fixed model parameters R_h and Σ_0 , we minimize the χ^2 over the admissible range $-\infty < \beta \leq 1$; we then compare the minimal value with a χ^2 probability distribution with $11 - 1 = 10$ dof to possibly reject the assumed parameters. The light shaded area in the right-hand frame of Fig. 5 corresponds to $\chi^2 = 11.5$ that gives 68 per cent CL exclusion.⁴

The best-fitting model (which has $\chi_{\text{bf}}^2 \simeq 2.5$) is obtained with $\beta = 0.6$ and is relative to a core size $R_h \simeq 400$ pc and surface density $\Sigma_0 \simeq 75 M_\odot \text{pc}^{-2}$. It provides a very good fit to the observational data, as it is shown by the velocity dispersion profile in Fig. 4. Being this a fully degenerate halo, the couple of parameters (R_h, Σ_0) corresponds to a well-defined mass m of the FDM candidate, which for the best fit corresponds to $m \simeq 0.23$ keV, in good agreement with the value suggested by Domcke & Urbano (2015).

On the other hand, a non-degenerate fermionic core can have generic radii R_h larger than the minimal (degenerate) value as found from equation (5):

$$R_{h,\text{min}} = 90 \text{ pc} \left(\frac{g}{2}\right)^{-2/5} \left(\frac{m}{1 \text{ keV}}\right)^{-8/5} \left(\frac{\Sigma_0}{M_\odot \text{pc}^{-3}}\right)^{-1/5}, \quad (19)$$

⁴ Because we are interested in a bound on m by excluding a region of the (R_h, Σ_0) plane, we use the absolute χ^2 to determine the level of compatibility with observational data. If instead one *assumes* that the FDM hypothesis is correct, the 68 per cent CL allowed region in the plane is determined by $\Delta\chi^2 \equiv \chi^2 - \chi_{\text{bf}}^2 = 2.3$ (for 2 dof). For completeness, we show this region with dark shaded area in Fig. 5.

which is shown as grey dashed lines in Fig. 5 for selected values m . By using the inequality $R_{h,\text{min}} \leq R_h$, one would like to obtain a lower bound on the DM particle mass directly from the constraints on the halo parameters R_h and Σ_0 , as in equation (7). However, one can see that unless the anisotropy β is constrained independently, velocity dispersion data do not allow to set limits on m . In particular, for maximal values of $\beta \sim 1$, i.e. radial motion of stars, very small values of m are allowed by the data and are relative to multi-kpc haloes, as it seen in Fig. 5. This situation is most likely not realistic, being unplausible that such a huge DM halo host a stellar system of just few hundredths pc and small velocity dispersion. It is however not possible to give at this stage a quantitative support to this comment, using dispersion data alone. Indeed, in the upper right-hand part of the plots, the χ^2 becomes flattish for $R_h \gg R_*$ because the limited extent of the stellar component does not permit to constrain a much larger DM halo.

The above conclusion can be made more quantitative by producing a one-dimensional χ^2 profile as a function of m . This is shown in Fig. 6 that is built as follows.

First, we obtain the red dashed curve, relative to fully degenerate models, by expressing the core radius ($R_h = R_{h,\text{min}}$) as a function of the mass m through equation (19), and then minimizing the χ^2 with respect to Σ_0 , in addition to β . From this curve one finds directly that no lower limit on the particle mass m can be obtained, even at 68 per cent CL that would require $\chi^2 > 10.4$ (for $11 - 2 = 9$ dof). The curve also becomes flattish for $m \lesssim 50$ eV, corresponding to the fact that for small masses the DM core becomes much larger than the stellar component, whose properties can only probe the central density of the DM distribution, but not its extension. Incidentally, this also means that the stellar velocity dispersion can be equally fitted by non-degenerate cored DM profiles with the same central density, the outer profile being irrelevant.

Then, on the rising part of the red dashed curve, towards large values of m , we note that while the fit worsens progressively as the degenerate core shrinks, one cannot set an upper bound on m , because the size of a degenerate core is just a lower limit, and any good fit with a given radius can also be produced with higher m as a non-degenerate configuration. Indeed, the mass m has to play

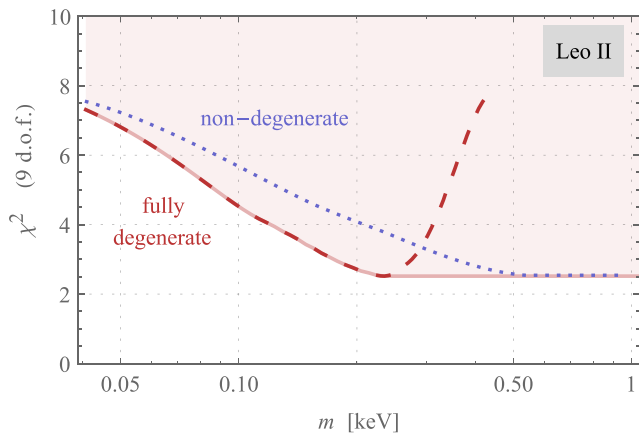


Figure 6. Leo II – the χ^2 as a function of the particle mass m with different assumptions for the DM distribution. The red dashed line is obtained, after minimization with respect to Σ_0 and β , for fully degenerate cores with radius $R_h = R_{h, \min}(m, \Sigma_0)$. The blue dotted line is similarly obtained for a non-degenerate cored (Burkert) profile with radius $R_h = 2 R_{h, \min}(m, \Sigma_0)$. The light-red solid line and the shaded region represent the overall minimal $\chi^2(m)$, obtained by considering that DM cores with generic radii $R_h \geq R_{h, \min}(m, \Sigma_0)$ are allowed for a fermionic DM candidate.

no role in the non-degenerate regime. Thus, the final χ^2 has to be thought as independent from the DM mass, i.e. flat, starting just beyond the minimum of the degenerate case. This is depicted as a light-red solid line and by the shaded region in Fig. 6.

This argument is confirmed by repeating the whole analysis with a non-degenerate cored density profile (we adopt the Burkert density profile taking a core radius two times larger than the minimal value, $R_h = 2 R_{h, \min}$, see Appendix A). This gives the blue dotted curve in Fig. 6. As expected, the non-degenerate profile leads to better fits for large masses while the χ^2 slowly converges to the degenerate case at the left-hand end of the plot. This test could be repeated by considering other admissible non-degenerate profiles, and/or different $R_h > R_{h, \min}$, and the envelope of the relative curves will produce the overall minimal χ^2 as depicted as the red solid line.

Even if stellar velocity dispersion data, taken alone, do not allow to obtain a limit on m , the mass of the DM particle can be constrained by considering that the halo decay time due to dynamical friction (equation 15) becomes unacceptably small for very large objects. Indeed, in the limit $R_h \gg R_*$ the quantity directly constrained by stellar velocity dispersion data is the halo central density $\rho_0 = \Sigma_0/R_h$. Therefore, by moving along the χ^2 flat direction at increasingly larger radii in Fig. 5, the halo mass increases as R_h^3 and eventually reaches values M_h that correspond to unacceptable friction times (equation 15). This constraint is reported in Fig. 5 by cutting the region where friction times are unphysical.

In conclusion, the interplay between dynamical friction and velocity dispersion data allows us to determine an absolute upper bound on the halo size, and thus a lower bound on the DM mass. For Leo II, this results in a very weak constraint, $m \gtrsim 25$ eV.

4.2 Smallest dwarf spheroidals: Willman I and Segue I

Let us apply the above strategies to the case of the Willman I and Segue I dSph galaxies (Simon et al. 2011; Willman et al. 2011) that are among the smallest galaxies for which LOS velocities are available. Their stellar distributions are fitted by Plummer profiles

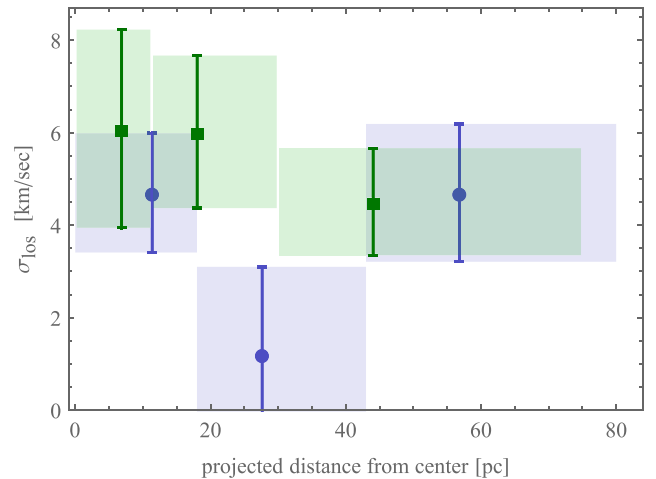


Figure 7. LOS velocity dispersion in Willman I (green squares) and Segue I (blue circles).

with very small radii, given by $R_* = 25$ and 29 pc, respectively. We use the stellar velocity data to determine the averaged LOS velocity dispersion, equation (12), in three bins with extension comparable to the Plummer radii. The results obtained are reported in Fig. 7 as a function of the projected distance from the galactic centre. We compare these observational results with the theoretical predictions by repeating the procedure adopted for Leo II, i.e. we minimize $\chi^2(R_h, \Sigma_0, \beta)$ in the full range $-\infty < \beta \leq 1$ of the anisotropy nuisance parameter.

Our results are reported in Fig. 8, where we show the contours corresponding to 68 per cent CL exclusion for $3 - 1 = 2$ dof for Willman I in the left-hand frame and for Segue I in the right-hand frame ($\chi^2 \equiv 2.3$).

We note that no significant constraint on the halo radius is obtained for Willman I. Indeed, a good fit is achieved also for $R_h \ll R_*$ by allowing the anisotropy β to be increasingly negative. The fit worsens for large core radii but the χ^2 becomes flattish beyond $R_h \sim 300$ pc, not sufficiently large to give a significant exclusion of larger halo sizes. This is clearly due to the limited radial extension of the stellar data sample, ~ 75 pc. The best fit is obtained for $R_h \simeq 30$ pc, $\Sigma_0 = 473 M_\odot \text{pc}^{-2}$ and $\beta = -0.2$ and corresponds to $\chi^2 \simeq 0$, as it is expected by considering that we have only three bins and three free parameters.

Again, even if the DM radius is not constrained, the fits provide a useful determination of the central density of the system that defines the flat direction in the plane (R_h, Σ_0) for $R_h \gg R_*$. Similarly to Leo II, by requiring that the dynamical friction decay time for Willman I is not unphysically small, we can exclude large core radii beyond $\sim \text{kpc}$ in the upper right-hand shaded region in Fig. 8 and obtain a robust lower bound on the DM mass, $m \gtrsim 80$ eV.

A similar analysis holds for Segue I, whose binned velocity dispersions are reported with blue circles in Fig. 7. The three bins show that Segue I presents a different profile with respect to other dwarfs, with the velocity dispersion rising beyond ~ 40 pc. This behaviour, which has already been noted in the literature as a possible evidence of a large DM halo (or an indication against its regularity/virialization), is consistent with the expectations from a scenario with $R_h \gg R_*$. Consistently, small radii $R_h \lesssim 40$ pc cannot be accommodated by the fit, even assuming a stellar anisotropy parameter $\beta \leq 0$. The best fit is obtained for $R_h \sim \text{few kpc}$ and no upper limits can be derived from Jeans analysis. Nevertheless, the central halo density is determined and the halo exten-

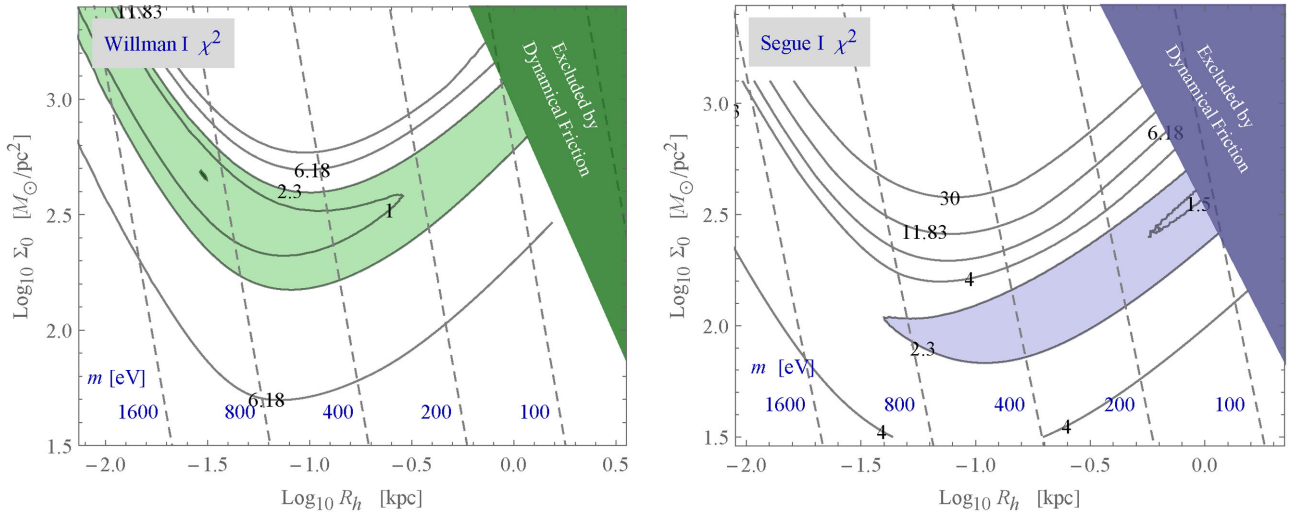


Figure 8. Contours of χ^2 , after minimizing on the free range of β . The left-hand panel is for Willman I, while the right-hand panel refers to Segue I. The light shaded regions give the region of compatibility with data at 68 per cent CL ($\chi^2 = 2.3$, 2 dof). Notice that no upper limit on the confidence interval on the radius can be placed for either galaxy.

sion is limited again by the constraint on the dynamical friction time, as shown in Fig. 8. The resulting lower bound on the DM mass is slightly better than that derived for Willman I, $m \gtrsim 100$ eV, mainly due to the fact that Segue I is closer to the galactic centre.

4.3 Other dwarfs

As a cross-check, we note that the results presented above from the Jeans analysis are indeed compatible with the fits performed in the recent work from Hayashi et al. (2016) where the authors also consider the possibility of triaxial haloes and arbitrary density profile slope at the centre. While their analysis does not consider degenerate fermionic haloes, their results confirm that for most dwarf galaxies the DM halo radius is quite poorly constrained, and haloes of few kpc size appear to be allowed by data, even if this is most likely unphysical. For our purposes, as discussed above, what drives the bound on the DM mass is the interplay of the dynamical friction constraint with the central halo density ρ_0 , which is the quantity constrained by observations in the limit of large halo size. Because this central density is largely independent on the (outer) halo shape, we can take advantage of the results of Hayashi et al. (2016) to estimate the DM mass bound for all objects presented in that work. The bound is in fact driven by the central DM density and the distance of the dwarf satellite. As we see from Table 1, by using the central fitted values of the densities, our result of Segue I and Leo II is confirmed, so that the results given in this work represent the most conservative bound around $m \gtrsim 100$ eV, with a possibly slightly stringent bound from the Triangulum II galaxy.

5 DISCUSSION AND CONCLUSIONS

In this work we have reassessed the lower bound on the mass of a FDM candidate, independently from particular models of its production or history of its clustering. The quantum nature of such light fermionic candidate implies an upper bound on the phase-space density in currently observed objects, and the knowledge of the density can be turned into a lower bound on the mass, *à la* Tremaine–Gunn. We have reconsidered the smallest dwarf spheroidal galaxies that

Table 1. Estimated lower bound on the fermionic DM mass m from a number of dSph galaxies, adopting the central densities as determined in Hayashi et al. (2016).

dSph	$\text{Log } \rho_0$ ($M_\odot \text{ pc}^{-3}$)	d_0 (kpc)	Lower bound on m
Triangulum II	0.3	30	127 eV
Segue I	-0.4	32	100 eV
Leo T	-0.6	417	26 eV
Reticulum II	-0.8	32	89 eV
Ursa Major I	-0.8	106	49 eV
Coma Berenices	-0.8	44	76 eV
Sculptor	-0.8	86	54 eV
Fornax	-1.1	147	38 eV
Ursa Major II	-1.2	32	80 eV
Leo I	-1.3	254	27 eV
Canes Venatici II	-1.4	151	34 eV
Hercules	-1.4	132	37 eV
Pisces II	-1.5	180	30 eV
Leo IV	-1.7	158	31 eV
Leo II	-1.7	233	25 eV
Draco II	-1.9	20	82 eV
Sextans	-2.	86	38 eV
Canes Venatici I	-2.2	224	22 eV
Carina	-2.2	106	33 eV
Bootes I	-2.4	66	39 eV
Leo V	-2.6	178	22 eV
Draco	-2.7	76	33 eV
Hydra II	-3.1	134	22 eV
Segue II	-3.2	35	43 eV

according to kinematical data are believed to host the largest densities of DM, thus constituting the ideal candidates to set a lower bound on the DM mass m .

Such a bound must be set in the hypothesis that the DM halo of some of these objects is composed of a completely degenerate gas of fermions, whose density profile is defined by the Lane–Emden equation. We have performed a fit of the stellar velocity dispersion predicted by the gravitational potential generated by such DM halo versus the observed stellar dispersion velocity and density profile of the Willman I, Segue I, and Leo II galaxies. In our analysis,

differently from recent works on the subject, we have not assumed that luminous matter traces the DM distribution, thus we have considered the DM core radius and surface density as free parameters. Moreover, we have taken into account the effect of the unknown anisotropy of the stellar velocity dispersion and marginalized over it.

As we have shown, the nuisance due to the stellar velocity anisotropy β seriously hampers the possibility to efficiently constrain the DM halo parameters. In practice, one finds equally acceptable haloes of very small sizes and negative β (where the total DM halo mass is determined) or very large sizes \sim few kpc and anisotropy near 1 (in which case the inner DM spatial density is determined). This latter scenario effectively corresponds to low phase-space densities, and thus no sensible lower bound on m can be given from stellar kinematical data alone. This situation is likely to persist even in the future, until a way to measure the velocity anisotropy in dSph galaxies will be available (see e.g. Read & Steger 2017), although this appears currently quite unconceivable.

New approaches have been proposed to circumvent the β -degeneracy in dSph galaxies in which subpopulations can be separated (Battaglia et al. 2008; Walker & Penarrubia 2011; Agnello & Evans 2012). These methods were applied to the Fornax galaxy in Amorisco, Agnello & Evans (2013) to exclude the Navarro–Frenk–White (NFW) profile and constrain the DM distribution. The upper bound on Fornax core radius was used by Randall, Scholtz & Unwin (2017) to infer a lower limit $m > 70$ eV for the mass of a FDM particle. Unfortunately, the likelihood distribution used to limit the core size in Amorisco et al. (2013) does not converge to zero for large core radii (see their fig. 4), as it is expected due to the fact that the stellar populations have limited extent. Therefore, while providing a robust lower bound for the core radius, even this approach cannot exclude few kpc core radii at high confidence level.

Such multi-kpc haloes are in any case unrealistic and a rationale to rule them out is provided (Gerhard & Spergel 1992) by the fact that very large haloes of known density correspond to large total halo mass, which makes their time of orbital decay due to dynamical friction in the Galactic DM halo, formula (15), unphysically small. Therefore, dynamical friction can be used to effectively limit the halo size and the interplay with the quantum bound on phase-space density leads finally to a lower bound on the fermionic DM mass m .

As it turns out from the analysis that we described, at present the most restrictive bound stems from the study of the Willman I and Segue I galaxies. Our results are put together in Fig. 1, where only the interplay between the fit to stellar data and the constraint from dynamical friction leads to a robust lower bound of $m \gtrsim 100$ eV. Thus, one is led to reopen the case for sub-keV fermionic DM, like sterile neutrinos of mass down to 100 eV.

For these two small dwarf galaxies driving the bound, the resulting DM halo can reach sizes of ~ 1 kpc, much larger than their stellar components. This does not mean that all the dSph galaxies shall have such enhanced haloes; this could likely hold only for these smallest objects that approach the fermionic degenerate regime.

As far as DM indirect detection is concerned, we note that the expected flux from DM annihilation (so-called J -factor) is enhanced in the limiting case of the extended halo sizes considered here, compensating the naturally low flux characteristic of cored haloes. At the same time, the dynamical friction upper bound on the halo sizes will slightly reduce the maximal expected J -factor in cored haloes, with respect to the analysis of e.g. Hayashi et al. (2016).

Clearly, DM masses $m = 100$ eV are at odds with bounds derived from the effect of WDM on structure formation (e.g. Lyman α) that typically forbid masses below few keV (see e.g. Iršič et al. 2017) by limiting their free streaming length. Therefore, for this scenario to be realistic, the spectrum of such DM candidates should be much colder than usual (see e.g. Drewes et al. 2017). This can be realized in models with production via decay as e.g. in Petraki & Kusenko (2008) and Domcke & Urbano (2015), or for instance in models in which DM at decoupling is overabundant and then subject to dilution by decays of other species, along the lines of e.g. Bezrukov, Hettmansperger & Lindner (2010) and Nemevsek, Senjanovic & Zhang (2012).

More theoretically, in order to attain the fermionic degeneracy that we have tested, it is also necessary that either the maximum of the primordial phase-space density saturates the occupation limit (equation A5) as it happens e.g. in relativistic decoupling, or alternatively that DM is subject to some form of dissipation or interaction, so that the phase-space density might grow during collapse. Indeed, a very interesting (and outstanding) issue is that of which collapse mechanism and time-scales could lead to degenerate fermionic haloes. While the free energy and entropy budget have been shown to be favourable (Hertel, Narnhofer & Thirring 1972; Bilic & Viollier 1997; Chavanis 2002), an assessment of the dynamics and relaxation times is still beyond reach (see Campa, Dauxois & Ruffo 2009; Chavanis, Lemou & Méhats 2015).

On the observational side, it is worth commenting that while the dSph galaxies are the smallest and most DM-dominated astrophysical objects, with a number of new dwarfs being currently discovered by present surveys, the possibility of using other types of galaxies for setting a bound on m from degeneracy is also of interest. Recently, cored halo mass modellings of disc dwarf galaxies from the Local Irregulars That Trace Luminosity Extremes, The HI Nearby Galaxy Survey (LITTLE THINGS) have been performed (see Karukes & Salucci 2017). Although the rotation curve decomposition is affected by uncertainty in the asymmetric drift gas contribution, due to their disc structure they are not subject to the dramatic anisotropy nuisance parameter of dSph galaxies and could potentially lead to a better bound on the DM mass m .

ACKNOWLEDGEMENTS

We thank Neven Bilić, Kathy Karukes, Paolo Salucci, and Piero Ullio for useful discussions. FN was partially supported by the H2020 CSA Twinning project no. 692194 ‘RBI-T-WINNING’. Results of this work were also presented in <https://indico.cern.ch/event/505065/contributions/2166456/>.

REFERENCES

- Agnello A., Evans N. W., 2012, *ApJ*, 754, L39
- Amorisco N. C., Agnello A., Evans N. W., 2013, *MNRAS*, 429, L89
- Avila-Reese V., Colin P., Valenzuela O., D’Onghia E., Firmani C., 2001, *ApJ*, 559, 516
- Battaglia G., Helmi A., Tolstoy E., Irwin M., Hill V., Jablonka P., 2008, *ApJ*, 681, L13
- Bezrukov F., Hettmansperger H., Lindner M., 2010, *Phys. Rev. D*, 81, 085032
- Bilic N., Viollier R. D., 1997, *Phys. Lett. B*, 408, 75
- Bilic N., Tupper G. B., Viollier R. D., 2001, preprint (arXiv:astro-ph/0111366)
- Binney J., Tremaine S., 2008, *Galactic Dynamics*, 2nd edn. Princeton Univ. Press, Princeton, NJ
- Bode P., Ostriker J. P., Turok N., 2001, *ApJ*, 556, 93

- Boyarisky A., Ruchayskiy O., Iakubovskiy D., 2009, *J. Cosmol. Astropart. Phys.*, 03, 005
- Campa A., Dauxois T., Ruffo S., 2009, *Phys. Rep.*, 480, 57
- Chavanis P.-H., 2002, *Phys. Rev. E*, 65, 056123
- Chavanis P.-H., Lemou M., Méhats F., 2015, *Phys. Rev. D*, 91, 063531
- Colin P., Avila-Reese V., Valenzuela O., 2000, *ApJ*, 542, 622
- Dalcanton J. J., Hogan C. J., 2001, *ApJ*, 561, 35
- de Vega H. J., Salucci P., Sanchez N. G., 2014, *MNRAS*, 442, 2717
- Domcke V., Urbano A., 2015, *J. Cosmol. Astropart. Phys.*, 01, 002
- Donato F. et al., 2009, *MNRAS*, 397, 1169
- Drewes M. et al., 2017, *J. Cosmol. Astropart. Phys.*, 01, 025
- Flores R. A., Primack J. R., 1994, *ApJ*, 427, L1
- Gerhard O. E., Spergel D. N., 1992, *ApJ*, 389, L9
- Governato F. et al., 2010, *Nature*, 463, 203
- Governato F. et al., 2012, *MNRAS*, 422, 1231
- Hayashi K., Ichikawa K., Matsumoto S., Ibe M., Ishigaki M. N., Sugai H., 2016, *MNRAS*, 461, 2914
- Hertel P., Narnhofer H., Thirring W. E., 1972, *Commun. Math. Phys.*, 28, 159
- Irsic V. et al., 2017, *Phys. Rev. D*, 96, 023522
- Just A., Khan F. M., Berczik P., Ernst A., Spurzem R., 2011, *MNRAS*, 411, 653
- Karukes E. V., Salucci P., 2017, *MNRAS*, 465, 4703
- Klypin A. A., Kravtsov A. V., Valenzuela O., Prada F., 1999, *ApJ*, 522, 82
- Moore B., 1994, *Nature*, 370, 629
- Moore B., Quinn T. R., Governato F., Stadel J., Lake G., 1999a, *MNRAS*, 310, 1147
- Moore B., Ghigna S., Governato F., Lake G., Quinn T. R., Stadel J., Tozzi P., 1999b, *ApJ*, 524, L19
- Navarro J. F., Eke V. R., Frenk C. S., 1996a, *MNRAS*, 283, L72
- Navarro J. F., Frenk C. S., White S. D. M., 1996b, *ApJ*, 462, 563
- Navarro J. F., Frenk C. S., White S. D. M., 1997, *ApJ*, 490, 493
- Nemevsek M., Senjanovic G., Zhang Y., 2012, *J. Cosmol. Astropart. Phys.*, 07, 006
- Nesti F., Salucci P., 2013, *J. Cosmol. Astropart. Phys.*, 07, 016
- Petraki K., Kusenko A., 2008, *Phys. Rev. D*, 77, 065014
- Pontzen A., Governato F., 2012, *MNRAS*, 421, 3464
- Randall L., Scholtz J., Unwin J., 2017, *MNRAS*, 467, 1515
- Read J. I., Steger P., 2017, *MNRAS*, 471, 4541
- Read J. I., Goerdt T., Moore B., Pontzen A. P., Stadel J., Lake G., 2006, *MNRAS*, 373, 1451
- Salucci P., Burkert A., 2000, *ApJ*, 537, L9
- Salucci P., Wilkinson M. I., Walker M. G., Gilmore G. F., Grebel E. K., Koch A., Martins C. F., Wyse R. F. G., 2012, *MNRAS*, 420, 2034
- Simon J. D. et al., 2011, *ApJ*, 733, 46
- Tremaine S., Gunn J. E., 1979, *Phys. Rev. Lett.*, 42, 407
- Ullio P., Valli M., 2016, *J. Cosmol. Astropart. Phys.*, 07, 025
- Walker M., 2013, in Oswald T. D., Gilmore G., eds, *Planets, Stars and Stellar Systems*. Springer Science+Business Media, Dordrecht, Vol. 5, p. 1039
- Walker M. G., Penarrubia J., 2011, *ApJ*, 742, 20
- Walker M. G., Mateo M., Olszewski E. W., Gnedin O. Y., Wang X., Sen B., Woodroffe M., 2007, *ApJ*, 667, L53
- Weinberg D. H., Bullock J. S., Governato F., Kuzio de Naray R., Peter A. H. G., 2014, *Proc. Natl. Acad. Sci. USA*, 112, 12249
- Willman B., Geha M., Strader J., Strigari L. E., Simon J. D., Kirby E., Ho N., Warren A., 2011, *AJ*, 142, 128
- Wolf J., Martinez G. D., Bullock J. S., Kaplinghat M., Geha M., Munoz R. R., Simon J. D., Avedo F. F., 2010, *MNRAS*, 406, 1220

APPENDIX A: SELF-GRAVITATING FERMIONIC GAS

We briefly review in this appendix the analysis of the equilibrium distribution of a self-gravitating gas of neutral fermions. We describe first the limiting case of complete degeneracy and then we recall the Thomas–Fermi treatment that allows to describe the transition to partially or non-degenerate case.

A1 Stability conditions for the DM halo

If we have large number of DM particles, we can assume they move in a spherically symmetric mean-field gravitational potential $\phi(r)$ that satisfies the Poisson equation:

$$\begin{aligned} \frac{d\phi}{dr} &= \frac{GM}{r^2}, \\ \frac{dM}{dr} &= 4\pi r^2 \rho, \end{aligned} \quad (\text{A1})$$

where $M(r)$ is the mass enclosed within the radius r , G is the Newton constant, and $\rho(r)$ is the matter density. For non-relativistic particles, the density can be expressed as

$$\rho = m \int dp 4\pi p^2 f(p), \quad (\text{A2})$$

where m is the particle mass and we assumed that DM distribution function $f(p)$ is isotropic. The dynamical stability of the system is expressed by the Jeans equation:

$$\frac{d}{dr}(\rho \sigma_{\text{DM}}^2) = -\rho \frac{d\phi}{dr}, \quad (\text{A3})$$

where the DM velocity dispersion σ_{DM}^2 is given by

$$\sigma_{\text{DM}}^2 = \frac{1}{3} \frac{\int dp (p^4/m^2) f(p)}{\int dp p^2 f(p)}. \quad (\text{A4})$$

If DM is composed of fermions, the distribution function $f(p)$ has an upper limit:

$$f(p) \leq \frac{g}{(2\pi\hbar)^3}, \quad (\text{A5})$$

where g represents the number of internal (spin) degrees of freedom. This automatically implies that a lower limit exists for the velocity dispersion

$$\sigma_{\text{DM}}^2 \geq \sigma_{\text{DM,min}}^2 = \frac{1}{5} \left(\frac{6\pi^2 \hbar^3 \rho}{g m^4} \right)^{2/3} \quad (\text{A6})$$

of a fermionic system of fixed density.

A2 The strong degeneracy limit

In the strong degeneracy regime, the states with energy below the Fermi energy ε are fully occupied, i.e. the distribution function $f(p)$ has the form

$$f(p) = \begin{cases} \frac{g}{(2\pi\hbar)^3} & p < p_F, \\ 0 & p > p_F, \end{cases} \quad (\text{A7})$$

where $p_F = \sqrt{2m\varepsilon}$ is the Fermi momentum. In this assumption, one obtains the expressions

$$\begin{aligned} \rho &= K \varepsilon^{3/2}, \\ \sigma_{\text{DM}}^2 &= K' \varepsilon, \end{aligned} \quad (\text{A8})$$

where $K = \sqrt{2} g m^{5/2} / (3\pi^2 \hbar^3)$ and $K' = 2/(5m)$, so that equations (A1) and (A3) can be recasted in the form

$$\frac{1}{r^2} \frac{d}{dr} \left[r^2 \frac{d\varepsilon(r)}{dr} \right] = -4\pi G m K \varepsilon(r)^{3/2}. \quad (\text{A9})$$

This equation has to be integrated with the condition $d\varepsilon(0)/dr = 0$ ensuring that the gravitational acceleration is zero at the centre. By defining

$$\xi \equiv r/\tilde{r}, \quad (\text{A10})$$

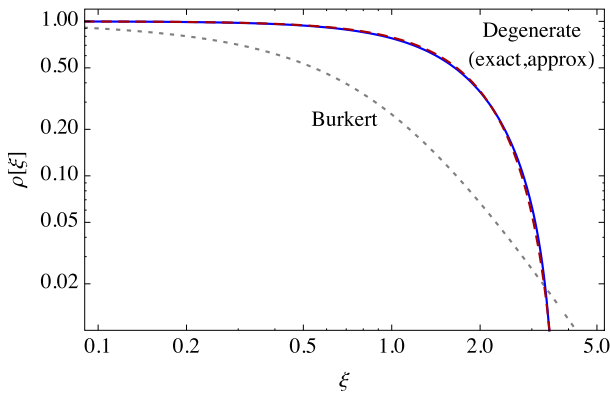


Figure A1. Density profiles for the DM haloes. Solid: the solution of the Lane–Emden equation for degenerate fermions. Dashed: its approximation adopted in the text (equation A14). Dotted: the Burkert density profile for comparison.

where the scale radius \tilde{r} is given by

$$\tilde{r} \equiv \frac{1}{\sqrt{4\pi G m K \varepsilon_0^{1/2}}} = \frac{1}{\sqrt{4\pi G m K^{2/3} \rho_0^{1/3}}}, \quad (\text{A11})$$

and by using the function $\theta(\xi)$ defined as

$$\theta(\xi) \equiv \frac{\varepsilon(\xi)}{\varepsilon_0} = \left[\frac{\rho(\xi)}{\rho_0} \right]^{2/3}, \quad (\text{A12})$$

where ε_0 (ρ_0) is the central value of the Fermi energy (density), equation (A9) can be rewritten in the form

$$\frac{1}{\xi^2} \frac{d}{d\xi} \left[\xi^2 \frac{d\theta(\xi)}{d\xi} \right] = -\theta(\xi)^{3/2}, \quad (\text{A13})$$

which is the well-known Lane–Emden equation.

Equations (A12) and (A13) show that the profiles of degenerate fermionic DM haloes are universal and depend only on the assumed central density ρ_0 and DM particle mass m . The mass distribution crucially differs from the usually adopted cusped or cored profiles. A sharp transition exists from an internal core with quite uniform density to an external region devoid of DM. For our purposes, the density profile of degenerate fermionic DM haloes can be well approximated by

$$\rho(\xi) = \rho_0 \cos^3 \left[\frac{\pi}{8} \xi \right] \quad (\text{A14})$$

for $0 \leq \xi \leq 3.65$, and $\rho(\xi) = 0$ elsewhere, see Fig. A1.

We define the halo radius by the condition $\rho(\xi_h) = \rho_0/4$ that gives $\xi_h = 2.26$ corresponding to

$$\begin{aligned} R_h &\equiv \xi_h \tilde{r} \\ &= 2.26 \left(\frac{9\pi}{27} \right)^{1/6} \frac{\hbar}{G^{1/2}} g^{-1/3} m^{-4/3} \rho_0^{-1/6} \\ &= 42.4 \text{ pc} \left(\frac{g}{2} \right)^{-1/3} \left(\frac{m}{1 \text{ keV}} \right)^{-4/3} \left(\frac{\rho_0}{M_\odot \text{ pc}^{-3}} \right)^{-1/6}. \end{aligned} \quad (\text{A15})$$

By using the above expression, we rewrite equation (A14) in the form

$$\rho(r) = \rho_0 \cos^3 \left[\frac{25}{88} \pi \frac{r}{R_h} \right], \quad (\text{A16})$$

where we used the approximate equality $\xi_h/8 \simeq 25/88$.

A3 The Thomas–Fermi model for fermionic DM

A self-consistent description of isothermal fermionic DM haloes with an arbitrary level of degeneration can be obtained by using a Thomas–Fermi approach (see Bilic et al. 2001; de Vega et al. 2014). One assumes that DM particles follow a Fermi–Dirac distribution:

$$f_{\text{FD}}(p; T, \mu) = \frac{g}{(2\pi\hbar)^3} \frac{1}{\exp[(E - \mu)/T] + 1}, \quad (\text{A17})$$

where $E = p^2/(2m)$ is the single-particle kinetic energy, T is the temperature expressed in terms of energy, and μ is the chemical potential. In the above, the density can be expressed as

$$\rho = \frac{g (2T)^{3/2} m^{5/2}}{6\pi^2 \hbar^3} I_2(\nu), \quad (\text{A18})$$

where

$$I_2(\nu) \equiv 3 \int_0^\infty dy \frac{y^2}{\exp(y^2 - \nu) + 1} \quad (\text{A19})$$

and $\nu \equiv \mu/T$ is a degeneracy parameter.

If one assumes a constant temperature, $T(r) \equiv \tilde{T}$, and that the chemical potential at each given radius includes the gravitational potential $\phi(r)$ as

$$\mu(r) = \tilde{\mu} - m\phi(r), \quad (\text{A20})$$

where $\tilde{\mu}$ is a constant, then the Jeans equation (A3) is automatically fulfilled and equations (A1) and (A2) can be recast in the form

$$\frac{1}{r^2} \frac{d}{dr} \left[r^2 \frac{d\mu(r)}{dr} \right] = -4\pi G m \rho(r), \quad (\text{A21})$$

again to be integrated with the condition $d\mu(0)/dr = 0$ for zero gravitational acceleration at the galaxy centre.

A4 The non-degenerate case

The Thomas–Fermi approach just described has the advantage of automatically implementing the upper limit (equation A5) imposed by the Pauli exclusion principle; it can thus describe the transition between classical and degenerate structures, in a continuous way. By using this approach, one is able to see that when R_h is 2–3 times larger than the minimal value in equation (A15) the fermionic nature of DM particles can be neglected, i.e. the resulting structures are essentially indistinguishable from cored isothermal haloes obtained by assuming Maxwell–Boltzmann statics and arbitrary values of the particle mass m .

This approach does not allow, however, to unambiguously predict the halo properties in the non-degenerate case. Indeed, in the classical regime (i.e. for $\nu \ll 1$) one has $I_2(\nu) \simeq \exp(\nu)$, differently from the strongly degenerate case in which $I_2(\nu) \simeq \nu^{3/2}$. Thus, the rhs of equation (A21) depends both on the temperature and the chemical potential. One obtains then a family of solutions depending on these two free parameters: the temperature \tilde{T} and the assumed chemical potential μ_0 (or, equivalently, the assumed density ρ_0) at the centre of the system. Moreover, a temperature profile, here constant, had to be assumed in the Thomas–Fermi approach in order to solve equation (A3). In a more realistic scenario, in which the temperature may vary along the galactic structure, \tilde{T} could be regarded as the central temperature; the predictions obtained in the degenerate or semidegenerate regimes are thus valid in the central core where temperature variations can be neglected, while the properties of the external region depend on the radial temperature profile. As it is natural to expect, basing on sole theoretical grounds

it is thus impossible to predict the mass distribution in regions of non-degeneration.

For this reason in the text, where we refer to non-degenerate haloes, we model them by using the observationally supported Burkert profile:

$$\rho_{\text{Bur}}(r) = \frac{\rho_0}{(1+x)(1+x^2)}, \quad x = r/R_h. \quad (\text{A22})$$

In using this profile, we require that the central density ρ_0 and core radius R_h are consistent with the assumption of non-degenerate

structure composed of fermions with mass m and g spin degrees of freedom, i.e. for each assumed value of ρ_0 , the halo radius R_h is required to be a factor of ~ 2 larger than the degenerate limit expressed by equation (A15).

This paper has been typeset from a $\text{\TeX}/\text{\LaTeX}$ file prepared by the author.

Bibliography

- [Abdallah et al., 2016] Abdallah, H. et al. (2016). Search for dark matter annihilations towards the inner galactic halo from 10 years of observations with h.e.s.s. *Phys. Rev. Lett.*, 117:111301.
- [Accardo et al., 2014] Accardo, L., Aguilar, M., Aisa, D., et al. (2014). High statistics measurement of the positron fraction in primary cosmic rays of 0.5–500 gev with the alpha magnetic spectrometer on the international space station. *Phys. Rev. Lett.*, 113:121101.
- [Ade et al., 2014] Ade, P. A. R., Aghanim, N., Armitage-Caplan, C., and others (Planck Collaboration) (22 March 2013) (2014). Planck 2013 results. I. Overview of products and scientific results. *A&A*, 571:A1.
- [Ade et al., 2016] Ade, P. A. R. et al. (2016). Planck 2015 results (XIII. Cosmological parameters). *A&A*, 594:A13.
- [Adhikari et al., 2017] Adhikari, R., Agostini, M., Ky, N., et al. (2017). A white paper on kev sterile neutrino dark matter. *JCAP*, 01:025.
- [Adriani et al., 2009] Adriani, O. et al. (2009). An anomalous positron abundance in cosmic rays with energies 1.5-100GeV. *Nat*, 458:607.
- [Aghanim et al., 2018] Aghanim, N., Akrami, Y., Ashdown, M., and others (Planck Collaboration 2018) (2018). Planck 2018 results. VI. Cosmological parameters. *arXiv:1807.06209*.
- [Alcock et al., 2000] Alcock, C. et al. (2000). The MACHO project: Microlensing results from 5.7 years of large magellanic cloud observations. *ApJ*, 542:281.
- [Arcadi, 2016] Arcadi, G. (2016). Dark Matter phenomenology of GUT Inspired simplified models. *J. Phys.: Conf. Ser.* 718 042003.
- [Arcadi et al., 2018] Arcadi, G., Dutra, M., Ghosh, P., et al. (2018). The waning of the WIMP? A review of models, searches, and constraints. *Eur. Phys. J. C*, 78:203.
- [Archambault et al., 2017] Archambault, S. et al. (2017). Dark matter constraints from a joint analysis of dwarf spheroidal galaxy observations with veritas. *Phys. Rev. D*, 95:082001.
- [Asaka et al., 2005] Asaka, T., Blanchet, S., and Shaposhnikov, M. (2005). The numsm, dark matter and neutrino masses. *Phys. Let. B.*, 631:151.

- [Asztalos et al., 2010] Asztalos, S. J., Carosi, G., Hagmann, C., et al. (2010). Squid-based microwave cavity search for dark-matter axions. *Phys. Rev. Lett.*, 104:041301.
- [Banerjee et al., 2019] Banerjee, A., Adhikari, S., Dalal, N., et al. (2019). Signatures of self-interacting dark matter on cluster density profile and subhalo distributions. *arXiv:1906.12026*.
- [Barnes and Efstathiou, 1987] Barnes, J. and Efstathiou, G. (1987). Angular momentum from tidal torques. *ApJ*, 319:575.
- [Barth, 2007] Barth, A. J. (2007). A normal stellar disk in the galaxy malin 1. *AJ*, 133:1085.
- [Bauer and Plehn, 2017] Bauer, M. and Plehn, T. (2017). Yet Another Introduction to Dark Matter. *ArXiv:1705.01987 [hep-ph]*.
- [Bayer et al., 2018] Bayer, D., Chatterjee, S., Koopmans, L. V. E., Vegetti, S., McKean, J. P., Treu, T., and Fassnacht, C. D. (2018). Observational constraints on the sub-galactic matter-power spectrum from galaxy-galaxy strong gravitational lensing. *arXiv:1803.05952*.
- [Bell et al., 2000] Bell, E. F., Barnaby, D., Bower, R. G., et al. (2000). The star formation histories of low surface brightness galaxies. *MNRAS*, 312:470.
- [Bellazzini et al., 2013] Bellazzini, B., Cliche, M., and Tanedo, P. (2013). Effective theory of self-interacting dark matter. *Phys. Rev. D*, 88:083506.
- [Benítez-Llambay et al., 2019] Benítez-Llambay, A., Frenk, C., Ludlow, A. D., and Navarro, J. (2019). Baryon-induced dark matter cores in the eagle simulations. *MNRAS*, 488:2387.
- [Bergstrom, 1999] Bergstrom, L. (1999). Non-baryonic dark matter. *Nuclear Physics B - Proceedings Supplements*, 70:31.
- [Bergstrom, 2000] Bergstrom, L. (2000). Non-baryonic dark matter: observational evidence and detection methods. *Rep. Prog. Phys.*, 63:793.
- [Bergstrom et al., 1998] Bergstrom, L., Ullio, P., and Buckley, J. (1998). Observability of gamma rays from dark matter neutralino annihilations in the milky way halo. *Astropart. Phys.*, 9:137.
- [Bernal et al., 2017] Bernal, N., Heikinheimo, M., Tenkanen, T., et al. (2017). The dawn of fimp dark matter: A review of models and constraints. *Int. J. Mod. Phys. A*, 32:1730023.
- [Bertone, 2010] Bertone, G. (2010). *Particle Dark Matter: Observations, Models and Searches*. Cambridge University Press.
- [Bertone and Hooper, 2018] Bertone, G. and Hooper, D. (2018). History of dark matter. *Rev. Mod. Phys.*, 90:045002.
- [Bertone et al., 2005] Bertone, G., Hooper, D., and Silk, J. (2005). Particle dark matter: evidence, candidates and constraints. *Phys. Rep.*, 405:279.

- [Blitz and Rosolowsky, 2004] Blitz, L. and Rosolowsky, E. (2004). The role of pressure in giant molecular cloud formation. *ApJ*, 612:L29.
- [Boddy et al., 2014] Boddy, K. K., Feng, J. L., Kaplinghat, M., et al. (2014). Strongly interacting dark matter: Self-interactions and keV lines. *Phys. Rev. D*, 90:095016.
- [Boissier et al., 2016] Boissier, S., Boselli, A., Ferrarese, L., et al. (2016). The properties of the Malin 1 galaxy giant disk. A panchromatic view from the NGVS and GUViCS surveys. *A&A*, 593:A126.
- [Boissier et al., 2003] Boissier, S., Monnier Ragainne, D., van Driel, W., et al. (2003). From spirals to low surface brightness galaxies. *Ap&SS*, 284:913.
- [Bosma, 1981a] Bosma, A. (1981a). 21-cm line studies of spiral galaxies. I - observations of the galaxies NGC 5033, 3198, 5055, 2841, and 7331. *AJ*, 86:1791.
- [Bosma, 1981b] Bosma, A. (1981b). 21-cm line studies of spiral galaxies. II. the distribution and kinematics of neutral hydrogen in spiral galaxies of various morphological types. *AJ*, 86:1825.
- [Bothun et al., 1997] Bothun, G., Impey, C., and McGaugh, S. (1997). Low-Surface-Brightness Galaxies: Hidden Galaxies Revealed. *PASP*, 109:745.
- [Bothun et al., 1987] Bothun, G., Impey, C. D., Malin, D. F., and Mould, J. R. (1987). Discovery of a Huge Low-Surface-Brightness Galaxy: A Proto-Disk Galaxy at Low Redshift? *AJ*, 94:23.
- [Bothun et al., 1993] Bothun, G., Schombert, J., Impey, C., Sprayberry, D., and McGaugh, S. (1993). The small scale environment of low surface brightness disk galaxies. *AJ*, 106:530.
- [Boyarsky et al., 2019] Boyarsky, A., Drewes, M., Lasserre, T., et al. (2019). Sterile neutrino dark matter. *Prog. Part. Nucl. Phys.*, 104:1.
- [Boyarsky et al., 2007] Boyarsky, A., Nevalainen, J., and Ruchayskiy, O. (2007). Constraints on the parameters of radiatively decaying dark matter from the dark matter halos of the milky way and Ursa Minor. *Phys. Rev. D*, 471:51.
- [Boyarsky et al., 2014] Boyarsky, A., Ruchayskiy, O., Iakubovskiy, D., and Franse, J. (2014). Unidentified line in x-ray spectra of the Andromeda galaxy and Perseus galaxy cluster. *Phys. Rev. Lett.*, 113:251301.
- [Boylan-Kolchin et al., 2012] Boylan-Kolchin, M., Bullock, J. S., and Kaplinghat, M. (2012). The Milky Way's bright satellites as an apparent failure of Λ CDM. *MNRAS*, 422:1203.
- [Bresolin and Kennicutt, 2015] Bresolin, F. and Kennicutt, R. C. (2015). Abundance gradients in low surface brightness spirals: clues on the origin of common gradients in galactic discs. *MNRAS*, 454:3664.
- [Bulbul et al., 2014] Bulbul, E., Markevitch, M., Foster, A., et al. (2014). Detection of an unidentified emission line in the stacked x-ray spectrum of galaxy clusters. *ApJ*, 789:13.

- [Bullock and Boylan-Kolchin, 2017] Bullock, J. and Boylan-Kolchin, M. (2017). Small-scale challenges to the Λ cdm paradigm. *ARAA*, 55:343.
- [Bullock et al., 2001] Bullock, J. S., Dekel, A., Kolatt, T. S., et al. (2001). A universal angular momentum profile for galactic halos. *ApJ*, 555:240.
- [Burkert, 1995] Burkert, A. (1995). The structure of dark matter halos in dwarf galaxies. *ApJ*, 447:L25.
- [Burkert, 2015] Burkert, A. (2015). The structure and dark halo core properties of dwarf spheroidal galaxies. *ApJ*, 808:158.
- [Burkholder et al., 2001] Burkholder, V., Impey, C., and Sprayberry, D. (2001). High and low surface brightness galaxies in the Local Universe. V. Optical and H I properties. *ApJ*, 122:2318.
- [Capela et al., 2013] Capela, F., Pshirkov, M., and Tinyakov, P. (2013). Constraints on primordial black holes as dark matter candidates from capture by neutron stars. *Phys. Rev. D*, 87:123524.
- [Carignan and Puche, 1990] Carignan, C. and Puche, D. (1990). HI studies of the sculptor group galaxies.IV. NGC 247. *AJ*, 100:641C.
- [Carroll et al., 1992] Carroll, S. M., Press, W. H., and Turner, E. L. (1992). The cosmological constant. *ARAA*, 30:499.
- [Carucci et al., 2015] Carucci, I., Villaescusa-Navarro, F., Viel, M., et al. (2015). Warm dark matter signatures on the 21cm power spectrum: intensity mapping forecasts for SKA. *JCAP*, 07:047.
- [Catinella et al., 2006] Catinella, B., Giovanelli, R., and Haynes, M. P. (2006). Template Rotation Curves for Disk Galaxies. *ApJ*, 640:751.
- [Cavaliere and Fusco-Femiano, 1978] Cavaliere, A. and Fusco-Femiano, R. (1978). The Distribution of Hot Gas in Clusters of Galaxies. *A&A*, 70:677.
- [Chan, 2019] Chan, M. (2019). A universal constant for dark matter-baryon interplay. *Sci. Rep.*, 9:3570.
- [Clowe et al., 2004] Clowe, D., Gonzalez, A., and Markevitch, M. (2004). Weak-lensing mass reconstruction of the interacting cluster 1e 0657-558: Direct evidence for the existence of dark matter. *ApJ*, 604:596.
- [Cohen et al., 2018] Cohen, Y., van Dokkum, P., Danieli, S., et al. (2018). The dragonfly nearby galaxies survey. v. HST/ACS observations of 23 low surface brightness objects in the fields of NGC 1052, NGC 1084, m96, and NGC 4258. *ApJ*, 868:96.
- [Copi et al., 1995] Copi, C. J., Schramm, D. N., and Turner, M. S. (1995). Big-bang nucleosynthesis and the baryon density of the universe. *Science*, 267:192.
- [Corbelli and Salucci, 2000] Corbelli, E. and Salucci, P. (2000). The extended rotation curve and the dark matter halo of M33. *MNRAS*, 311:441.

- [Cui et al., 2018] Cui, M.-Y., Pan, X., Yuan, Q., Fan, Y.-Z., and Zong, H.-S. (2018). Revisit of cosmic ray antiprotons from dark matter annihilation with updated constraints on the background model from AMS-02 and collider data. *JCAP*, 2018:024.
- [Dalcanton et al., 1997a] Dalcanton, J., Spergel, D. N., and Summers, F. (1997a). The Formation of Disk Galaxies. *ApJ*, 482:659.
- [Dalcanton et al., 1997b] Dalcanton, J. J., Spergel, D. N., Gunn, J. E., et al. (1997b). The Number Density of Low-Surface Brightness Galaxies with $23 < \mu_0 < 25$ V Mag/arcsec². *AJ*, 114:635.
- [Das, 2013] Das, M. (2013). Giant Low Surface Brightness Galaxies: Evolution in Isolation. *J Astrophys Astron*, 34:19.
- [Das et al., 2009] Das, M., Reynolds, C. S., Vogel, S. N., et al. (2009). Chandra observations of nuclear x-ray emission from low surface brightness galaxies. *ApJ*, 693:1300.
- [Davies et al., 2016] Davies, J. I., Davies, L. J. M., and Keenan, O. C. (2016). Probing the low surface brightness dwarf galaxy population of the virgo cluster. *MNRAS*, 456:1607.
- [de Block et al., 1995] de Block, W. J. G., van der Hulst, J., and Bothun, G. (1995). Surface photometry of low surface brightness galaxies. *MNRAS*, 274:235.
- [de Blok and Bosma, 2002] de Blok, W. J. G. and Bosma, A. (2002). High-resolution rotation curves of low surface brightness galaxies. *A&A*, 385:816.
- [de Blok and McGaugh, 1997] de Blok, W. J. G. and McGaugh, S. S. (1997). The dark and visible matter content of low surface brightness disk galaxies. *MNRAS*, 290:533.
- [de Blok et al., 2001] de Blok, W. J. G., McGaugh, S. S., and Rubin, V. C. (2001). High-resolution rotation curves of low surface brightness galaxies. *AJ*, 122:2381.
- [de Blok et al., 1996] de Blok, W. J. G., McGaugh, S. S., and van der Hulst, J. M. (1996). HI observations of low surface brightness galaxies: Probing low-density galaxies. *MNRAS*, 283:18.
- [de Vega et al., 2013] de Vega, H. J., Moreno, O., Moya de Guerra, E., Ramón Medrano, M., and Sánchez, N. G. (2013). Role of sterile neutrino warm dark matter in rhenium and tritium beta decays. *Nucl. Phys. B.*, 866:177.
- [de Vega and Sanchez, 2017] de Vega, H. J. and Sanchez, N. G. (2017). Equation of state, universal profiles, scaling and macroscopic quantum effects in warm dark matter galaxies. *EPJ C*, 77:81.
- [Del Popolo and Kroupa, 2009] Del Popolo, A. and Kroupa, P. (2009). Density profiles of dark matter haloes on galactic and cluster scales. *A&A*, 502:733.

- [Destri et al., 2013] Destri, C., de Vega, H. J., and Sanchez, N. G. (2013). Warm dark matter primordial spectra and the onset of structure formation at redshift z . *Phys. Rev. D*, 88:083512.
- [Di Cintio et al., 2019] Di Cintio, A., Brook, C., Macciò, A., et al. (2019). NIHAO XXI: the emergence of low surface brightness galaxies. *MNRAS*, 486:2535.
- [Di Cintio et al., 2014] Di Cintio, A., Brook, C. B., Macciò, A. V., Stinson, G. S., Knebe, A., Dutton, A. A., and Wadsley, J. (2014). The dependence of dark matter profiles on the stellar-to-halo mass ratio: a prediction for cusps versus cores. *MNRAS*, 437:415.
- [Di Paolo et al., 2018] Di Paolo, C., Nesti, F., and Villante, F. (2018). Phase-space mass bound for fermionic dark matter from dwarf spheroidal galaxies. *MNRAS*, 475:5385.
- [Di Paolo et al., 2019a] Di Paolo, C., Salucci, P., and Erkurt, A. (2019a). The universal rotation curve of low surface brightness galaxiesIV: the interrelation between dark and luminous matter. *MNRAS*, 490:5451.
- [Di Paolo et al., 2019b] Di Paolo, C., Salucci, P., and Fontaine, J. P. (2019b). The Radial Acceleration Relation (RAR): Crucial Cases of Dwarf Disks and Low-surface-brightness Galaxies. *ApJ*, 873:106.
- [Disney, 1976] Disney, M. J. (1976). Visibility of galaxies. *NAT.*, 263:573.
- [Dodelson and Widrow, 1994] Dodelson, S. and Widrow, L. M. (1994). Sterile neutrinos as dark matter. *Phys. Rev. Lett.*, 72:17.
- [Donato et al., 2009] Donato, F., Gentile, G., Salucci, P., Frigerio Martins, C. and Wilkinson, M. I., Gilmore, G., Grebel, E. K., Koch, A., and Wyse, R. (2009). A constant dark matter halo surface density in galaxies. *MNRAS*, 397:1169.
- [Drewes, 2013] Drewes, M. (2013). The phenomenology of right handed neutrinos. *Int. J. Mod. Phys. E*, 22:1330019.
- [Du et al., 2019] Du, W., Cheng, C., and Wu, H. (2019). Low surface brightness galaxy catalogue selected from the alpha.40-sdss dr7 survey and tully-fisher relation. *MNRAS*, 483:1754.
- [Duffy and van Bibber, 2009] Duffy, L. and van Bibber, K. (2009). Axions as dark matter particles. *New J. Phys.*, 11:105008.
- [Dutton et al., 2019] Dutton, A., Macciò, A., Buck, T., et al. (2019). NIHAO XX: the impact of the star formation threshold on the cusp-core transformation of cold dark matter haloes. *MNRAS*, 486:655.
- [Elbert et al., 2015] Elbert, O. D., Bullock, J. S., Garrison-Kimmel, S., Rocha, M., Oñorbe, J., and Peter, A. H. G. (2015). Dwarf galaxies in cdm and sidm with baryons: observational probes of the nature of dark matter. *MNRAS*, 453:29.

- [Ellis et al., 2012] Ellis, G. F. R., Maartens, R., and MacCallum, M. A. H. (2012). *Relativistic Cosmology*. Cambridge, Uk: Univ. Pr.
- [Evoli et al., 2011] Evoli, C., Salucci, P., Lapi, A., and Danese, L. (2011). The HI content of local late-type galaxies. *ApJ*, 743:45.
- [Faber and Gallagher, 1979] Faber, S. and Gallagher, J. (1979). Masses and mass-to-light ratios of galaxies. *ARAA*, 17:135.
- [Fall, 1983] Fall, S. (1983). Galaxy formation - some comparisons between theory and observation. in *IAU Symp. 100, Internal Kinematics and Dynamics of Galaxies*, ed. E. Athanassoula (*Besancon: Reidel*), 391.
- [Ferrero et al., 2012] Ferrero, I. Abadi, M. G., Navarro, J. F., and Sales, L. V. and Gurovich, S. (2012). The dark matter haloes of dwarf galaxies: a challenge for the cold dark matter paradigm. *MNRAS*, 425:2817.
- [Fox et al., 2011] Fox, P. et al. (2011). LEP shines light on dark matter. *Phys. Rev. D*, 84:014028.
- [Freeman, 1970] Freeman, K. C. (1970). On the disks of spiral and s0 galaxies. *ApJ*, 160:811.
- [Fune, 2018] Fune, E. (2018). Empirical velocity profiles for galactic rotation curves. *MNRAS*, 475:2132.
- [Galaz et al., 2011] Galaz, G., Herrera-Camus, R., Garcia-Lambas, D., and Padilla, N. (2011). Low surface brightness galaxies in the sdss: The link between environment, star-forming properties, and active galactic nuclei. *ApJ*, 728:74.
- [Gammaldi et al., 2018] Gammaldi, V., Karukes, E., and Salucci, P. (2018). Theoretical predictions for dark matter detection in dwarf irregular galaxies with gamma rays. *Phys. Rev. D*, 98:083008.
- [Garrett and Duda, 2011] Garrett, K. and Duda, G. (2011). Dark Matter: A Primer. *ADV ASTRON*, 2011.
- [Garrison-Kimmel et al., 2014] Garrison-Kimmel, S., Boylan-Kolchin, M., Bullock, J. S., and Kirby, E. N. (2014). Too big to fail in the local group. *MNRAS*, 444:222.
- [Gentile et al., 2005] Gentile, G., Burkert, A., Salucci, P., Klein, U., and Walter, F. (2005). High-resolution rotation curves of low surface brightness galaxies. *ApJL*, 634:L145.
- [Gentile et al., 2009] Gentile, G., Famaey, B., Zhao, H., and Salucci, P. (2009). Universality of galactic surface densities within one dark halo scale-length. *Nature*, 461:627.
- [Gentile et al., 2004] Gentile, G., Salucci, P., Klein, U., Vergani, D., and Kalberla, P. (2004). The cored distribution of dark matter in spiral galaxies. *MNRAS*, 351:903.

- [Geringer-Sameth et al., 2015] Geringer-Sameth, A., Koushiappas, S. M., and Walker, M. (2015). Dwarf galaxy annihilation and decay emission profiles for dark matter experiments. *ApJ*, 801:74.
- [Giovanelli et al., 2005] Giovanelli, R., Haynes, M. P., Kent, B., et al. (2005). The arecibo legacy fast ALFA survey. i. science goals, survey design, and strategy. *AJ*, 130:2598.
- [Goodman and Witten, 1985] Goodman, M. W. and Witten, E. (1985). Detectability of certain dark-matter candidates. *Phys. Rev. D*, 31:3059.
- [Graham et al., 2015] Graham, P., Irastorza, I., Lamoreaux, S., et al. (2015). Experimental searches for the axion and axion-like particles. *Annu. Rev. Nucl. Part. S.*, 65:485.
- [Gratier et al., 2010] Gratier, P., Braine, J., Rodriguez-Fernandez, N. J., et al. (2010). Molecular and atomic gas in the local group galaxy m 33. *A&A*, 522:A3.
- [Greco et al., 2018] Greco, J., J.E., G., Strauss, M., et al. (2018). Illuminating low surface brightness galaxies with the hyper supprime-cam survey. *ApJ*, 857:104.
- [Gunn et al., 1978] Gunn, J. E., Lee, B. W., Lerche, I., Schramm, D. N., and Steigman, G. (1978). Some astrophysical consequences of the existence of a heavy stable neutral lepton. *ApJ*, 223:1015.
- [Hinshaw et al., 2009] Hinshaw, G., Weiland, J. L., Hill, R. S., et al. (2009). Five-year wilkinson microwave anisotropy probe observations: Data processing, sky maps, and basic results. *Astrophys. J., Suppl.*, 180:225.
- [Hinz et al., 2007] Hinz, J. L., Rieke, M. J., Rieke, G. H., et al. (2007). Spitzer Observations of Low-Luminosity Isolated and Low Surface Brightness Galaxies. *ApJ*, 663:895.
- [Hoekstra and Bhuvnesh, 2008] Hoekstra, H. and Bhuvnesh, J. (2008). Weak gravitational lensing and its cosmological applications. *Annu. Rev. Nucl. Part. S.*, 58:99.
- [Honey et al., 2016] Honey, M., Das, M., Ninan, J., and Manoj, P. (2016). Near-infrared imaging of barred halo-dominated low surface brightness galaxies. *MNRAS*, 462:2099.
- [Honey et al., 2018] Honey, M., van Driel, W., Das, M., and Martin, J. M. (2018). A study of the HI and optical properties of Low Surface Brightness galaxies: spirals, dwarfs, and irregulars. *MNRAS*, 476:4488.
- [Hoof et al., 2018] Hoof, S., Geringer-Sameth, A., and Trotta, R. (2018). A global analysis of dark matter signals from 27 dwarf spheroidal galaxies using ten years of fermi-lat observations. *arXiv:1812.06986v1*.
- [Hooper and Profumo, 2007] Hooper, D. and Profumo, S. (2007). Dark matter and collider phenomenology of universal extra dimensions. *Phys. Rep.*, 453:29.

- [Hu et al., 2000] Hu, W., Barkana, R., and Gruzinov, A. (2000). Fuzzy cold dark matter: The wave properties of ultralight particles. *Phys. Rev. Lett.*, 85:1158.
- [Hui et al., 2017] Hui, L., Ostriker, J. P., Tremaine, S., and Witten, E. (2017). Ultralight scalars as cosmological dark matter. *Phys. Rev. D*, 95:043541.
- [Impey and Bothun, 1997] Impey, C. and Bothun, G. (1997). Low surface brightness galaxies. *ARAA*, 35:267.
- [Impey et al., 1996] Impey, C., Sprayberry, D., Irwin, M., and Bothun, G. (1996). Low Surface Brightness Galaxies in the Local Universe. I. The Catalog. *ApJS*, 105:209.
- [Impey and Bothun, 1989] Impey, C. D. and Bothun, G. (1989). Malin1: a quiescent disk galaxy. *ApJ*, 341:89.
- [Iovine et al., 2019] Iovine, N., Sánchez, J., and Baur, S. (2019). Combined Search for Neutrinos from Dark Matter Annihilation in the Galactic Centre using ANTARES and IceCube. *arXiv:1908.07300v1*.
- [Iršič et al., 2017] Iršič, V., Viel, M., Haehnelt, M. G., et al. (2017). New constraints on the free-streaming of warm dark matter from intermediate and small scale Lyman- α forest data. *Phys. Rev. D*, 96:023522.
- [Jungman et al., 1996] Jungman, G., Kamionkowski, M., and Griest, K. (1996). Supersymmetric dark matter. *Phys. Rep.*, 267:195.
- [Kane et al., 2015] Kane, G., Sinha, K., and Watson, S. (2015). Cosmological moduli and the post-inflationary universe: A critical review. *Int. J. Mod. Phys. D*, 24:1530022.
- [Kane and Watson, 2008] Kane, G. and Watson, S. (2008). Dark Matter and Lhc.: what is the Connection? *MPLA*, 23:2103.
- [Kang et al., 2019] Kang, S., Scopel, S., Tomar, G., et al. (2019). Present and projected sensitivities of dark matter direct detection experiments to effective wimp-nucleus couplings. *Astropart. Phys.*, 109:50.
- [Kaplinghat et al., 2015] Kaplinghat, M., Linden, T., and Yu, H. (2015). Galactic center excess in γ rays from annihilation of self-interacting dark matter. *Phys. Rev. Lett.*, 114:211303.
- [Karukes and Salucci, 2017] Karukes, E. V. and Salucci, P. (2017). The universal rotation curve of dwarf disk galaxies. *MNRAS*, 465:4703.
- [Kaviraj, 2020] Kaviraj, S. (2020). The low-surface-brightness Universe: a new frontier in the study of galaxy evolution. *arXiv e-prints*, page arXiv:2001.01728.
- [Kennedy et al., 2014] Kennedy, R., Frenk, C., Cole, S., and Benson, A. (2014). Constraining the warm dark matter particle mass with milky way satellites. *MNRAS*, 442:2487.

- [Kennicutt, 1989] Kennicutt, R. C. J. (1989). The Star Formation Law in Galactic Disks. *ApJ*, 344:685.
- [Kennicutt, 1998] Kennicutt, R. C. J. (1998). The global schmidt law in star-forming galaxies. *ApJ*, 498:541.
- [Kent, 1986] Kent, S. M. (1986). Dark matter in spiral galaxies. i. galaxies with optical rotation curves. *AJ*, 91:1301.
- [Klypin et al., 2015] Klypin, A., Karachentsev, I., Makarov, D., and Nasonova, O. (2015). Abundance of field galaxies. *MNRAS*, 454:1798.
- [Klypin et al., 1999] Klypin, A., Kravtsov, A. V., Valenzuela, O., and Prada, F. (1999). Where Are the Missing Galactic Satellites? *ApJ*, 522:82.
- [Klypin et al., 2011] Klypin, A., Trujillo-Gomez, S., and Primack, J. (2011). Dark matter halos in the standard cosmological model: Results from the bolshoi simulation. *ApJ*, 740:102.
- [Kolb and Turner, 1990] Kolb, E. W. and Turner, M. S. (1990). *The Early Universe*. Addison Wesley.
- [Kovács et al., 2019] Kovács, O., Bogdán, A., and Canning, R. (2019). Constraining the dark-matter halo mass of isolated low-surface-brightness galaxies. *ApJ*, 879:L12.
- [Kusenko, 2009] Kusenko, A. (2009). Sterile neutrinos: The dark side of the light fermions. *Phys. Rep.*, 481:1.
- [Kuzio de Naray et al., 2008] Kuzio de Naray, R., McGaugh, S. S., and de Blok, W. J. G. (2008). Mass models for low surface brightness galaxies with high-resolution optical velocity fields. *ApJ*, 676:920.
- [Kuzio de Naray et al., 2006] Kuzio de Naray, R., McGaugh, S. S., de Blok, W. J. G., and Bosma, A. (2006). High-resolution optical velocity fields of 11 low surface brightness galaxies. *ApJS*, 165:461.
- [Kuzio de Naray and Spekkens, 2011] Kuzio de Naray, R. and Spekkens, K. (2011). Do baryons alter the halos of low surface brightness galaxies? *ApJL*, 741:L29.
- [Lapi and Cavaliere, 2011] Lapi, A. and Cavaliere, A. (2011). Self-similar dynamical relaxation of dark matter halos in an expanding universe. *ApJ*, 743:127.
- [Lapi et al., 2018] Lapi, A., Salucci, P., and Danese, L. (2018). Precision scaling relations for disk galaxies in the local universe. *ApJ*, 859:19.
- [Lei et al., 2018] Lei, F., Wu, H., Du, W., et al. (2018). An $h\alpha$ imaging survey of the low-surface-brightness galaxies selected from the fall sky region of the 40% ALFALFA HI survey. *ApJS*, 235:18.
- [Lei et al., 2019] Lei, F., Wu, H., Zhu, Y., et al. (2019). An $H\alpha$ imaging survey of the low surface brightness galaxies selected from the spring sky region of the 40% ALFALFA HI survey. *ApJS*, 242:11.

- [Li et al., 2017] Li, B., Shapiro, P. R., and Rindler-Daller, T. (2017). Bose-einstein-condensed scalar field dark matter and the gravitational wave background from inflation: New cosmological constraints and its detectability by ligo. *Phys. Rev. D*, 96:063505.
- [Li et al., 2018] Li, P., Lelli, F., McGaugh, S., and Schombert, J. (2018). Fitting the radial acceleration relation to individual SPARC galaxies. *Astronomy and Astrophysics*, 615:70.
- [Li et al., 2019] Li, P., Lelli, F., McGaugh, S., Starkman, N., and Schombert, J. (2019). A constant characteristic volume density of dark matter haloes from SPARC rotation curve fits. *MNRAS*, 482:5106.
- [Liang et al., 2010] Liang, Y. C., Zhong, G. H., Hammer, F., et al. (2010). A large sample of low surface brightness disc galaxies from the sdss. II. metallicities in surface brightness bins. *MNRAS*, 409:213.
- [Lovell et al., 2014] Lovell, M. R., Frenk, C. S., Eke, V. R., Jenkins, A., Gao, L., and Theuns, T. (2014). The properties of warm dark matter haloes. *MNRAS*, 439:300.
- [López Fune, 2018] López Fune, E. (2018). Empirical velocity profiles for galactic rotation curves. *MNRAS*, 475:2132.
- [Ma, 2006] Ma, E. (2006). Verifiable radiative seesaw mechanism of neutrino mass and dark matter. *Phys. Rev. D*, 73:077301.
- [Macciò et al., 2007] Macciò, A. V., Dutton, A. A., van den Bosch, F. C., et al. (2007). Concentration, spin and shape of dark matter haloes: scatter and the dependence on mass and environment. *MNRAS*, 378:55.
- [Marchesini et al., 2002] Marchesini, D., D’Onghia, E., Chincarini, G., Firmani, C., Conconi, P., Molinari, E., and Zacchei, A. (2002). H α rotation curves: The soft core question. *ApJ*, 575:801.
- [Markevitch et al., 2004] Markevitch, M., Gonzalez, A. H., Clowe, D., et al. (2004). Direct constraints on the dark matter self-interaction cross section from the merging galaxy cluster 1e 0657-56. *ApJ*, 606:819.
- [Martin and Kennicutt, 2001] Martin, C. and Kennicutt, R. J. (2001). Star formation thresholds in galactic disks. *ApJ*, 555:301.
- [Mashchenko et al., 2006] Mashchenko, S., Couchman, H. M. P., and Wadsley, J. (2006). The removal of cusps from galaxy centres by stellar feedback in the early universe. *Nature*, 442:539.
- [Matthews and Gao, 2001] Matthews, L. and Gao, Y. (2001). CO detections of edge-on low surface brightness galaxies. *ApJ*, 549:L191.
- [Matthews et al., 2001] Matthews, L. D., van Driel, W., and Monnier-Ragaine, D. (2001). HI observations of giant low surface brightness galaxies. *A&A*, 365:1.
- [McGaugh, 1994] McGaugh, S. (1994). Oxygen abundances in low surface brightness disk galaxies. *ApJ*, 426:135.

- [McGaugh and Bothun, 1994] McGaugh, S. and Bothun, G. (1994). Structural Characteristics and Stellar Composition of Low Surface Brightness Disk Galaxies. *AJ*, 107:530.
- [McGaugh et al., 2016] McGaugh, S., Lelli, F., and Schombert, J. (2016). Radial Acceleration Relation in Rotationally Supported Galaxies. *Phys. Rev. Lett.*, 117:201101.
- [McGaugh et al., 1995] McGaugh, S. S., Bothun, G. D., and Schombert, J. M. (1995). Galaxy selection and the surface brightness distribution. *AJ*, 110:573.
- [Memola et al., 2011] Memola, E., Salucci, P., and Babic, A. (2011). Dark matter halos around isolated ellipticals. *A&A*, 534:A50.
- [Merritt et al., 2014] Merritt, A., van Dokkum, P., and Abraham, R. (2014). The discovery of seven extremely low surface brightness galaxies in the field of the nearby spiral galaxy M101. *ApJ*, 787:L37.
- [Minchin et al., 2004] Minchin, R. F., Disney, M. J., Parker, Q. A., et al. (2004). The cosmological significance of low surface brightness galaxies found in a deep blind neutral hydrogen survey. *MNRAS*, 355:1303.
- [Mishra et al., 2018] Mishra, A., Kantharia, N. G., and Das, M. (2018). Giant Low Surface Brightness Galaxies. *Bull. Soc. r. sci. Liège*, 87:365.
- [Mo et al., 2010] Mo, H., van den Bosch, F. C., and White, S. (2010). *Galaxy Formation and Evolution*. Cambridge University Press.
- [Mo et al., 1998] Mo, H. J., Mao, S., and White, S. D. M. (1998). The formation of galactic discs. *MNRAS*, 295:319.
- [Moore et al., 1999] Moore, B., Ghigna, S., Governato, F., Lake, G., Quinn, T., Stadel, J., and Tozzi, P. (1999). Dark matter substructure within galactic halos. *ApJ*, 524:L19.
- [Morelli et al., 2012] Morelli, L., Corsini, E. M., Pizzella, A., Dalla Bontà, E., Coccato, L., Méndez-Abreu, J., and Cesetti, M. (2012). Structure and dynamics of galaxies with a low surface-brightness disc - II. stellar populations of bulges. *MNRAS*, 423:962.
- [Moster et al., 2013] Moster, B., Naab, T., and White, S. (2013). Galactic star formation and accretion histories from matching galaxies to dark matter haloes. *MNRAS*, 428:3121.
- [Moster et al., 2010] Moster, B., Somerville, R., Maulbetsch, C., van den Bosch, F., Macciò, A., Naab, N., and Oser, L. (2010). Constraints on the relationship between stellar mass and halo mass at low and high redshift. *ApJ*, 710:903.
- [Mukhanov, 2005] Mukhanov, V. (2005). *Physical foundations of cosmology*. Cambridge, Uk: Univ. Pr.
- [Munoz, 2017] Munoz, C. (2017). Models of Supersymmetry for Dark Matter. *EPJ Web Conf.*, 136.

- [Naab and Ostriker, 2017] Naab, T. and Ostriker, J. (2017). Theoretical challenges in galaxy formation. *ARAA*, 55:59.
- [Navarro et al., 1997] Navarro, J., Frenk, C., and White, S. (1997). A Universal Density Profile from Hierarchical Clustering. *ApJ*, 490:493.
- [Navarro et al., 1996a] Navarro, J. F., Eke, V. R., and Frenk, C. S. (1996a). The cores of dwarf galaxy haloes. *MNRAS*, 283:L72.
- [Navarro et al., 1996b] Navarro, J. F., Frenk, C. S., and White, S. D. M. (1996b). The structure of cold dark matter halos. *ApJ*, 462:563.
- [Nebrin et al., 2019] Nebrin, O., Ghara, R., and Mellema, G. (2019). Fuzzy dark matter at cosmic dawn: new 21-cm constraints. *JCAP*, 04:051.
- [Nidever et al., 2019] Nidever, D., Olsen, K., Choi, Y., et al. (2019). Exploring the very extended low-surface-brightness stellar populations of the large magellanic cloud with SMASH. *ApJ*, 874:118.
- [Niikura et al., 2019] Niikura, H., Takada, M., Yasuda, N., et al. (2019). Microlensing constraints on primordial black holes with subaru/hsc andromeda observations. *Nat. Astron.*, 3:524.
- [Noordermeer et al., 2007] Noordermeer, E., van der Hulst, J. M., Sancisi, R., Swaters, R. S., and van Albada, T. S. (2007). The mass distribution in early-type disc galaxies: declining rotation curves and correlations with optical properties. *MNRAS*, 376:1513.
- [Nori et al., 2019] Nori, M., Murgia, R., Iršič, V., Baldi, M., and Viel, M. (2019). Lyman- α forest and non-linear structure characterization in fuzzy dark matter cosmologies. *MNRAS*, 482:3227.
- [Oh et al., 2011] Oh, S.-H., de Blok, W. J. G., Brinks, E., Walter, F., and Kenicutt, J. R. C. (2011). Dark and luminous matter in things dwarf galaxies. *AJ*, 141:193.
- [O'Neil et al., 2004] O'Neil, K., Bothun, G., van Driel, W., et al. (2004). A new HI catalog of low surface brightness galaxies out to $z = 0.1$. tripling the number of massive LSB galaxies known. *A&A*, 428:823.
- [O'Neil et al., 2000] O'Neil, K., Bothun, G. D., and Schombert, J. (2000). Red, gas-rich low surface brightness galaxies and enigmatic deviations from the tully-fisher relation. *ApJ*, 119:136.
- [O'Neil and Schinnerer, 2003] O'Neil, K. and Schinnerer, E. (2003). The first CO map of a low surface brightness galaxy. *ApJ*, 588:L81.
- [Pahwa and Saha, 2018] Pahwa, I. and Saha, K. (2018). Structural properties of faint low-surface-brightness galaxies. *MNRAS*, 478:4657.
- [Papastergis et al., 2015] Papastergis, E., Giovanelli, R., Haynes, M. P., and Shankar, F. (2015). Is there a too big to fail problem in the field? *A&A*, 574:A113.

- [Papastergis et al., 2011] Papastergis, E., Martin, A. M., Giovanelli, R., and Haynes, M. P. (2011). The velocity width function of galaxies from the 40 per cent alfalfa survey: Shedding light on the cold dark matter overabundance problem. *ApJ*, 739:38.
- [Persic and Salucci, 1991] Persic, M. and Salucci, P. (1991). The universal galaxy rotation curve. *ApJ*, 368:60.
- [Persic et al., 1996] Persic, M., Salucci, P., and Stel, F. (1996). The universal rotation curve of spiral galaxies - i. the dark matter connection. *MNRAS*, 281:27.
- [Pickering et al., 1997] Pickering, T. E., Impey, C. D., van Gorkom, J. H., and D., B. G. (1997). Neutral hydrogen distributions and kinematics of giant low surface brightness disk galaxies. *AJ*, 114:1858.
- [Plana et al., 2010] Plana, H., Amram, P., Mendes de Oliveira, C., and Balkowski, C. (2010). Mass distribution in hickson compact groups of galaxies. *AJ*, 139:1.
- [Ponomareva et al., 2017] Ponomareva, A., Verheijen, M., Peletier, R., and Bosma, A. (2017). The multiwavelength Tully-Fisher relation with spatially resolved HI kinematics. *MNRAS*, 469:2387.
- [Pontzen and Governato, 2014] Pontzen, A. and Governato, F. (2014). Cold dark matter heats up. *Nature*, 506:171.
- [Posti et al., 2018] Posti, L., Pezzulli, G., Fraternali, F., et al. (2018). Galaxy spin as a formation probe: the stellar-to-halo specific angular momentum relation. *MNRAS*, 475:232.
- [Profumo, 2017] Profumo, S. (2017). *An Introduction To Particle Dark Matter*. World Scientific Pub Co Inc.
- [Prole et al., 2019] Prole, D. J., Hilker, M., van der Burg, R. F. J., et al. (2019). Halo mass estimates from the globular cluster populations of 175 low surface brightness galaxies in the fornax cluster. *MNRAS*, 484:4865.
- [Pustilnik et al., 2011] Pustilnik, S. A., Martin, J.-M., Tepliakova, A. L., and Kniazev, A. Y. (2011). Study of galaxies in the Lynx-Cancer void. III. New extreme low surface brightness dwarf galaxies. *MNRAS*, 417:1335.
- [Read and Gilmore, 2005] Read, J. I. and Gilmore, G. (2005). Mass loss from dwarf spheroidal galaxies: the origins of shallow dark matter cores and exponential surface brightness profiles. *MNRAS*, 356:107.
- [Rees and Ostriker, 1977] Rees, M. J. and Ostriker, J. P. (1977). Cooling, dynamics and fragmentation of massive gas clouds: clues to the masses and radii of galaxies and clusters. *MNRAS*, 179:541.
- [Rhee, 1996] Rhee, M. H. (1996). *A Physical Basis of the Tully-Fisher Relation*. PhD thesis, -.
- [Ringwald, 2012] Ringwald, A. (2012). Exploring the role of axions and other wisps in the dark universe. *Phys. Dark Univ.*, 1:116.

- [Robertson and Kravtsov, 2008] Robertson, B. E. and Kravtsov, A. V. (2008). Molecular hydrogen and global star formation relations in galaxies. *The Astrophysical Journal*, 680(2):1083–1111.
- [Romanowsky and Fall, 2012] Romanowsky, A. J. and Fall, S. M. (2012). Galaxy formation - some comparisons between theory and observation. *ApJS*, 203:17.
- [Roscoe, 1999] Roscoe, D. F. (1999). An analysis of 900 optical rotation curves: dark matter in a corner? *Pramana*, 53:1033.
- [Rosenbaum and Bomans, 2004] Rosenbaum, S. and Bomans, D. J. (2004). The environment of Low Surface Brightness galaxies. *A&A*, 422:L5.
- [Rosenbaum et al., 2009] Rosenbaum, S., Krusch, E., Bomans, D. J., and Dettmar, R. J. (2009). The large-scale environment of low surface brightness galaxies. *A&A*, 504:807.
- [Ross, 1985] Ross, G. (1985). *Grand Unified Theories*. Reading, Usa: Benjamin/cummings (1984) 497 P. (Frontiers In Physics, 60).
- [Rubin et al., 1985] Rubin, V. C., Burstein, D., Ford, J. W. K., and Thonnard, N. (1985). Rotation velocities of 16 sa galaxies and a comparison of sa, sb, and sc rotation properties. *ApJ*, 289:81.
- [Rubin et al., 1980] Rubin, V. C., Ford, W. K., J., and Thonnard, N. (1980). Rotational properties of 21 sc galaxies with a large range of luminosities and radii, from NGC 4605 ($r = 4$ kpc) to UGC 2885 ($r = 122$ kpc). *ApJ*, 238:471.
- [Saburova et al., 2019] Saburova, A., Chilingarian, I., Kasparova, A., et al. (2019). UGC 1378 : a milky way sized galaxy embedded in a giant low surface brightness disc. *MNRAS*, 489:4669.
- [Salucci, 2001] Salucci, P. (2001). The constant-density region of the dark haloes of spiral galaxies. *MNRAS*, 320:L1.
- [Salucci, 2018] Salucci, P. (2018). Dark Matter in Galaxies: Evidences and Challenges. *Found Phys*, 48:1517.
- [Salucci, 2019] Salucci, P. (2019). The distribution of dark matter in galaxies. *Astron Astrophys Rev*, 27:2.
- [Salucci and Burkert, 2000] Salucci, P. and Burkert, A. (2000). Dark matter scaling relations. *ApJ*, 537:L9.
- [Salucci et al., 2007] Salucci, P., Lapi, A., Tonini, C., Gentile, G., Yegorova, I., and Klein, U. (2007). The universal rotation curve of spiral galaxies - II. the dark matter distribution out to the virial radius. *MNRAS*, 378:41.
- [Salucci et al., 2012] Salucci, P., Wilkinson, M. I., Walker, M. G., Gilmore, G. F., Grebel, E. K., Koch, A., Frigerio Martins, C., and Wyse, R. F. G. (2012). Dwarf spheroidal galaxy kinematics and spiral galaxy scaling laws. *MNRAS*, 420:2034.
- [Schmidt, 1959] Schmidt, M. (1959). The Rate of Star Formation. *ApJ*, 129:243.

- [Schneider, 1996] Schneider, P. (1996). Detection of (dark) matter concentrations via weak gravitational lensing. *MNRAS*, 283:837.
- [Schombert and McGaugh, 2014] Schombert, J. and McGaugh, S. (2014). Stellar populations and the star formation histories of LSB galaxies: III. stellar population models. *PASA*, 31:e036.
- [Schombert et al., 2013] Schombert, J., McGaugh, S., and Maciel, T. (2013). Stellar populations and the star formation histories of low surface brightness galaxies. II. H II regions. *AJ*, 146:41.
- [Schombert et al., 1992] Schombert, J. M., Bothun, G. D., Schneider, S. E., and McGaugh, S. S. (1992). A Catalog of Low Surface Brightness Galaxies. List II. *AJ*, 103:1107.
- [Schumann, 2019] Schumann, M. (2019). Direct detection of WIMP dark matter: concepts and status. *Journal of Physics G: Nuclear and Particle Physics*, 46:103003.
- [Servant and Tait, 2003] Servant, G. and Tait, T. (2003). Is the lightest Kaluza-Klein particle a viable dark matter candidate? *Nucl. Phys. B.*, 650:391.
- [Shankar et al., 2006] Shankar, F., Lapi, A., Salucci, P., et al. (2006). New relationships between galaxy properties and host halo mass, and the role of feedbacks in galaxy formation. *ApJ*, 643:14.
- [Shi et al., 2017] Shi, J., Lapi, A., Mancuso, C., et al. (2017). Angular momentum of early- and late-type galaxies: Nature or nurture? *ApJ*, 843:105.
- [Shi and Fuller, 1999] Shi, X. and Fuller, G. M. (1999). New dark matter candidate: Nonthermal sterile neutrinos. *Phys. Rev. Lett.*, 82:2832.
- [Sikivie, 1983] Sikivie, P. (1983). Experimental tests of the "invisible" axion. *Phys. Rev. Lett.*, 51:1415.
- [Simon et al., 2019] Simon, J., Birrer, S., Bechtol, K., et al. (2019). Testing the nature of dark matter with extremely large telescopes. *arXiv:1903.04742*.
- [Simon et al., 2005] Simon, J. D., Bolatto, A. D., Leroy, A., Blitz, L., and Gates, E. L. (2005). High-resolution measurements of the halos of four dark matter-dominated galaxies: Deviations from a universal density profile. *ApJ*, 621:757.
- [Sitwell et al., 2014] Sitwell, M., Mesinger, A., Ma, Y., et al. (2014). The imprint of warm dark matter on the cosmological 21-cm signal. *MNRAS*, 438:2664.
- [Spano et al., 2008] Spano, M., Marcelin, M., Amram, P., Carignan, C., Epinat, B., and Hernandez, O. (2008). GHASP: an H α kinematic survey of spiral and irregular galaxies - V. Dark matter distribution in 36 nearby spiral galaxies. *MNRAS*, 383:297.
- [Spergel and Steinhardt, 2000] Spergel, D. N. and Steinhardt, P. J. (2000). Observational evidence for self-interacting cold dark matter. *Phys. Rev. Lett.*, 84:3760.

- [Steigman and Turner, 1985] Steigman, G. and Turner, M. (1985). Cosmological constraints on the properties of weakly interacting massive particles. *Nucl. Phys. B*, 253:375.
- [Swaters et al., 2000] Swaters, R. A., Madore, B. F., and Trewhella, M. (2000). High-resolution rotation curves of low surface brightness galaxies. *ApJ*, 531:L107.
- [Swaters et al., 2003] Swaters, R. A., Madore, B. F., van den Bosch, F. C., and Balcells, M. (2003). The central mass distribution in dwarf and low surface brightness galaxies. *ApJ*, 583:732.
- [Tisserand et al., 2007] Tisserand, P., Le Guillou, L., Afonso, C., et al. (2007). The small scale environment of low surface brightness disk galaxies. *A&A*, 469:387.
- [Trachternach et al., 2006] Trachternach, C., Bomans, D. J., Habertzettl, L., and Dettmar, R. (2006). An optical search for low surface brightness galaxies in the Arecibo HI Strip Survey. *A&A*, 458:341.
- [Trevisani, 2018] Trevisani, N. . C. C. (2018). Collider searches for dark matter (atlas + cms). *universe*, 4:131.
- [Trimble, 1987] Trimble, V. (1987). Existence and Nature of Dark Matter in the Universe. *ARAA*, 25:425.
- [Trujillo and Fliri, 2016] Trujillo, I. and Fliri, J. (2016). Beyond 31 mag arcsec⁻²: The frontier of low surface brightness imaging with the largest optical telescopes. *ApJ*, 823:123.
- [Tulin et al., 2013] Tulin, S., Yu, H., and Zurek, K. M. (2013). Beyond collisionless dark matter: Particle physics dynamics for dark matter halo structure. *Phys. Rev. D*, 87:115007.
- [van den Hoek et al., 2000] van den Hoek, L. B., de Blok, W. J. G., van der Hulst, J. M., et al. (2000). The evolution of the stellar populations in low surface brightness galaxies. *A&A*, 357:397.
- [van der Hulst et al., 1993] van der Hulst, J. M., Skillman, E. D., Smith, T. R., Bothun, G. D., McGaugh, S. S., and de Blok, W. J. G. (1993). Star formation thresholds in low surface brightness galaxies. *AJ*, 106:548.
- [van der Kruit, 1987] van der Kruit, P. C. (1987). The radial distribution of surface brightness in galactic disks. *A&A*, 173:59.
- [van Zee et al., 1997] van Zee, L., Haynes, M. P., Salzer, J. J., and Broeils, A. H. (1997). A comparative study of star formation thresholds in gas-rich low surface brightness dwarf galaxies. *AJ*, 113:1618.
- [Vegetti and Koopmans, 2009] Vegetti, S. and Koopmans, L. (2009). Statistics of mass substructure from strong gravitational lensing: quantifying the mass fraction and mass function. *MNRAS*, 400:1583.

- [Vogelsberger et al., 2014] Vogelsberger, M., Zavala, J., Simpson, C., and Jenkins, A. (2014). Dwarf galaxies in Λ CDM and SIDM with baryons: observational probes of the nature of dark matter. *MNRAS*, 444:3684.
- [Vorobyov et al., 2009] Vorobyov, E. I., Shchekinov, Y., Bizyaev, D., et al. (2009). The age of blue LSB galaxies. *A&A*, 505:483.
- [Wang et al., 2014] Wang, J., Fu, J., Aumer, M., et al. (2014). An observational and theoretical view of the radial distribution of HI gas in galaxies. *MNRAS*, 441:2159.
- [Wechsler et al., 2006] Wechsler, R. et al. (2006). The dependence of halo clustering on halo formation history, concentration, and occupation. *ApJ*, 652:71.
- [Weinberg et al., 2015] Weinberg, D. H., Bullock, J. S., Governato, F., Kuzio de Naray, R., and Peter, A. H. G. (2015). Cold dark matter: Controversies on small scales. *PNAS*, 112:12249.
- [Weinberg, 1978] Weinberg, S. (1978). A new light boson? *Phys. Rev. Lett.*, 40:223.
- [Williams et al., 2016] Williams, R., Baldry, I. K., Kelvin, L. S., et al. (2016). Galaxy And Mass Assembly (GAMA): detection of low-surface-brightness galaxies from SDSS data. *MNRAS*, 463:2746.
- [Wyder et al., 2009] Wyder, T., Martin, D. C., Barlow, T., et al. (2009). The star formation law at low surface density. *ApJ*, 696:1834.
- [Wyrzykowski et al., 2011] Wyrzykowski, L., Skowron, J., and Kozowski, S. (2011). The OGLE view of microlensing towards the Magellanic Clouds IV. OGLE-III SMC data and final conclusions on MACHOs. *MNRAS*, 416:2949.
- [Yegorova and Salucci, 2007] Yegorova, I. and Salucci, P. (2007). The radial tully-fisher relation for spiral galaxies i. *MNRAS*, 377:507.
- [Zavala et al., 2009] Zavala, J., Jing, Y. P., Faltenbacher, A., Yepes, G., Hoffman, Y., Gottlöber, S., and Catinella, B. (2009). The velocity function in the local environment from Λ CDM and Λ WDM constrained simulations. *ApJ*, 700:1779.
- [Zavala et al., 2013] Zavala, J., Vogelsberger, M., and Walker, M. (2013). Constraining self-interacting dark matter with the Milky Way's dwarf spheroidals. *MNRAS*, 431:L20.
- [Zhao, 1996] Zhao, H. (1996). Analytical models for galactic nuclei. *MNRAS*, 278:488.
- [Zhong et al., 2008] Zhong, G. H., Liang, Y. C., Liu, F. S., et al. (2008). The Arecibo legacy fast ALFA survey. i. science goals, survey design, and strategy. *MNRAS*, 391:391, 986.
- [Zjupa and Springel, 2017] Zjupa, J. and Springel, V. (2017). Angular momentum properties of haloes and their baryon content in the Illustris simulation. *MNRAS*, 466:1625.

- [Zu and Mandelbaum, 2015] Zu, Y. and Mandelbaum, R. (2015). Mapping stellar content to dark matter haloes using galaxy clustering and galaxy-galaxy lensing in the sdss dr7. *MNRAS*, 454:1161.
- [Zumalacárregui and Seljak, 2018] Zumalacárregui, M. and Seljak, U. (2018). Limits on stellar-mass compact objects as dark matter from gravitational lensing of type ia supernovae. *Phys. Rev. Lett.*, 121:141101.
- [Zwaan et al., 1995] Zwaan, M. A., van der Hulst, J. M., de Blok, W. J. G., and McGaugh, S. S. (1995). The tully-fisher relation for low surface brightness galaxies: implications for galaxy evolution. *MNRAS*, 273:L35.

Acknowledgments

I thank a lot my husband Domenico and my daughter Giulia for their very precious support and for the nice time shared together in this period. Big thanks to my supervisor Paolo Salucci, who gave me the possibility to develop this work and also the opportunity to test funny experiences in the research world. I would like to thank Fabrizio Nesti, Andrea Lapi and Nicola Turini for very useful discussions about my research topic. Thanks to all the members of the astrophysics sector and to all my previous teachers for their contribution in building my cultural background. Thanks to my first math teacher in elementary school, whose interesting lessons gave me the idea of studying physics and astrophysics. I want to thank my mother for all her teachings especially about the organization in the most disparate fields of life and my father for his teaching in giving balanced relevance to events. Thanks to the whole family, especially to Ambra, Flavio, Paula and Francesco, for their help and the nice time spent together. Special thanks go to my old friends, especially to Danila, Francesca, Valeria, Veronica and Giovanna. Despite the spatial distance, I can feel them always close to me. Thanks also to my new friends, especially to Chiara & Guglielmo, Mariangela, Barbara and Deborah. They are nice people with a big heart. Thanks also to my roommates Paolo, Lara and Samuele, who shared this last period in the office with me between studies and funny discussions. I would like to thank the SISSA medialab and the SISSA press-office staff for giving me relevant opportunities in spreading science to different audiences. Special thanks to Simona Cerrato and Enrico Balli for their constant availability and for their precious advice. Thanks to the staff of the SISSA kindergarten, especially to Tea and Cristina. Thanks to the SISSA-gym people, especially to Giulia, Cristiana and Mara for sharing funny time spent in strengthening body and soul. I thank the whole SISSA administrative staff, always efficient and careful for the needs of the SISSA users. Finally, I want to thank SISSA more generally for giving me the possibility to test a multicultural environment, where people from different countries and also very different cultures live together. All this poses a good hope for a better world.